



HAL
open science

Topological rigidity of mechanical metamaterials

Marcelo Andrés Guzmán Jara

► **To cite this version:**

Marcelo Andrés Guzmán Jara. Topological rigidity of mechanical metamaterials. Condensed Matter [cond-mat]. Ecole normale supérieure de lyon - ENS LYON, 2022. English. NNT : 2022ENSL0014 . tel-03880865

HAL Id: tel-03880865

<https://theses.hal.science/tel-03880865>

Submitted on 1 Dec 2022

HAL is a multi-disciplinary open access archive for the deposit and dissemination of scientific research documents, whether they are published or not. The documents may come from teaching and research institutions in France or abroad, or from public or private research centers.

L'archive ouverte pluridisciplinaire **HAL**, est destinée au dépôt et à la diffusion de documents scientifiques de niveau recherche, publiés ou non, émanant des établissements d'enseignement et de recherche français ou étrangers, des laboratoires publics ou privés.



Numéro National de Thèse : 2022ENSL0014

THESE

en vue de l'obtention du grade de Docteur, délivré par

l'Ecole Normale Supérieure de Lyon

Ecole Doctorale N°52

Physique et Astrophysique de Lyon (PHAST)

Discipline : Physique

Soutenue publiquement le 23/09/2022, par :

Marcelo Andrés Guzmán Jara

Topological rigidity of mechanical metamaterials

Rigidité topologique des métamatériaux mécaniques

Devant le jury composé de :

Katifori, Eleni	Professeure	University of Pennsylvania	Rapporteure
Grushin, Adolfo	Chargé de recherche	Institut Néel	Rapporteur
Mao, Xiaoming	Professeure	University of Michigan	Examinatrice
Douçot, Benoît	Directeur de recherche	Sorbonne université	Examineur
Vitelli, Vincenzo	Professeur	University of Chicago	Examineur
Bartolo, Denis	Professeur des universités	ENS de Lyon	Directeur de thèse
Carpentier, David	Directeur de Recherche	ENS de Lyon	Co-encadrant de thèse

Acknowledgments

I am grateful for all the wonderful people that have turned this journey into a priceless experience.

Thank you Denis and David for this crazy ride. I am lucky to have you both as advisors. I deeply appreciate your guidance, whether it is for polishing an article, a scientific presentation, critical thinking, or just sheer motivation. Thank you for keeping up with my sometimes stubborn behavior, for making me appreciate science even deeper, for bringing the scientific aesthetics I definitely lacked, and more importantly, for the priceless help you provided when I most needed it; I will never forget that.

Many thanks to Eleni Katifori, Adolfo Grushin, Xiaoming Mao, Benoît Douçot, and Vincenzo Vitelli, for reviewing this work. It is a real honor to be evaluated by such internationally renowned scientists. Special mention to Eleni Katifori and Adolfo Grushin for taking the time of reading my manuscript and giving very valuable feedback.

To my collaborators: thank you Xiaofei and Corentin for the very pleasurable discussions, the sparkling curiosity, and the willingness to push our research to reach even greater heights. Looking forward to what we can do next!

Thanks to all the physics lab: students, teaching, and administrative staff, for the exciting and welcoming environment you create. Among them, I would like to individually thank certain members. My office mates, current and older: Alex, thank you for your invaluable friendship, for keeping up with our nonsensical italo-spanish language, and for the climbing adventures. Barbara, thank you for your unmatched sympathy, for being the role model of the office (we all wanted to have a tidy desk like yours!) and for coping with the entropy source Alex and I represented. Thomas, thank you for bringing a lot of laughs, more coffee breaks, and Ariane.

Thanks to the Bartolo team: Marine, Amélie, François, Stéphane, Nicolas, Alexandre, Camille, Alexis, Debasmita, Thibault, Benjamin. To the current members: keep up the thrilling science you are doing! I wish you the best for what's still to come. To the former members: thank you for having accepted this theoretical physicist among the experimentalists (although I did some Lego and 3D printing...). Worthy mention to Marine and Amélie for their invaluable help when I first arrived to the ENS, it was a real pleasure to have crossed your paths. Thanks to the Carpentier team: Jacquelin et Baptiste, for the friendly discussions, your curiosity, and for showing me some hardcore theoretical condensed matter physics.

Special thanks to Yeraldinne and Cristóbal. You are among the most genuine people I know; having you as friends is one of the highlights of this journey. Thank you Yeraldinne

Acknowledgments

for keeping up with our good and bad impulsive decisions, for our failed attempt at roller skating, and for being the source of our common laughter with Cristobal. Thank you Cristóbal, for paying the price of the impulsive decisions, for showing me that there are people that can laugh at greater decibels than me, and for bringing your controversial dance skills to the world. Special mention to our bike trip, the dogs, our misadventures, our minute of fame in the local newspaper, and for helping me when I most needed it.

Thank you Valentina and Ignacio, for bringing the Chilean culture with you, for the holidays in Marseille, the exquisite food, the endless determination to party (Valentina), and all the origami discussions (which Valentina knows by heart).

Extending our domain to different nations, I have to thank the wonderful moments with the VIP team, Matías, Clément, Richard, Angélique, Alex, Alex, David, Anetta, Paola, Yeraldinne, Cristóbal, Ignacio, Valentina, and all the people that have come and gone. I'm happy to see the paths you have taken; I wish you nothing but the best of luck.

Thank you Florencia (Flow!) and Sebastian. Florencia, for being a dear friend, neighbor, and unofficial office mate. Thanks for all the morning coffees, the book discussions, and the tremendous support during the covid period. Always happy to discuss health and sports with you! Thank you for lending me your office (eat the frog!), your house, your internet, your coffee machine, and much more. Sebastian, thank you for quickly becoming a very good friend, for the long conversations during coffee time, and for letting me be part of one of your most joyful moments in life. To both of you: I wish you a successful continuation, you deserve, and you will achieve, great things in life.

Thank you Lavi and Marco, you are the first friends I made in the lab. I will not forget the wonderful holidays in Italy, visiting Vincenzo and Dario, our trip to Beaujolais together with Lina, the music we played at Marco's place, and all the laughs with shared.

Thanks to all the members of the lab for the interesting pauses café: Sebastian, Florencia, Charles, Ariane, Jacquelin, Baptiste, Eric, Léo, Dario, Marco, Geoffroy, Thomas, Richard, Alex, Lavi, Ignacio, Hadi, all of you! (memory growing fragile by now, I blame the PhD).

Outside the lab: thank you Fulvia, Laura, Caroline, Charlotte, Samuel, Laure-Hélène, Clara, for turning my stay in Lyon more intense and enjoyable.

To my family, thank you mamá, papá, Carla, and Pablo, for you have been the solid foundation upon which I grow. Thank you for the incredible support, for sharing my joys, and for always bringing home to my ears.

Thank you Lucie for all the excitement and amusement you continuously bring to my life, for your incredible support, and for all the fun we have together (I could write a whole thesis about it; it would be longer than this one). Looking forward to our new adventures!

And if it was not enough, to all of you, let me repeat it once again: thank you.

Contents

1	Introduction	1
1.1	Linear response of bead and spring networks	3
1.1.1	A displacement-based approach	4
1.1.2	An elongation-based approach	5
1.1.3	The Maxwell-Calladine counting rule	5
1.1.4	Wave propagation: mechanical insulators	7
1.2	Mechanics is chiral	10
1.2.1	Schödinger-like description: combining displacements and elongations	10
1.2.2	Topology of chiral systems: the winding number	12
1.2.3	Chiral topological insulators beyond mechanics	13
1.3	Characterization of topological insulators in mechanics	14
1.4	Organization of the manuscript	18
2	Softness: Topology and geometry in mechanics	21
2.1	Introduction	21
2.2	An analogy with electrostatics	22
2.3	A new material property: the chiral polarization	23
2.4	Beyond crystals	26
2.5	Detecting zero-energy modes	27
2.6	Conclusion	29
2.7	Article	30
2.7.1	Introduction	30
2.7.2	From chiral charge to chiral polarization and Zak phases	31
2.7.3	Topology of chiral insulators	34
2.7.4	Bulk-boundary correspondence	39
2.7.5	Amorphous Chiral Insulators	40
2.7.6	Conclusion	47
2.8	Supplementary material	48
2.8.1	Bloch theory convention and Wannier states.	48
2.8.2	Chiral polarization, Zak phases and winding.	49
2.8.3	Zero energy flat-band insulators.	53
2.8.4	Basis of localised states: matrix pencil	55
2.8.5	Chiral polarization in amorphous materials.	56
2.8.6	Chiral polarization of time evolved Wannier states.	58
3	Experimental characterization of chiral materials	61
3.1	Introduction	61

3.2	Measuring the chiral polarization field	63
3.2.1	The shortcomings of spectral measurements	65
3.2.2	Bypassing the hamiltonian with local responses	65
3.2.3	Polyatomic chiral molecules and higher-order insulators	70
3.3	Experimental detection of zero-energy modes	77
3.3.1	Bulk-edge correspondence	77
3.3.2	Edge-corner	78
3.4	Conclusion	80
4	Topological stiffness of mechanical metamaterials	83
4.1	Introduction	83
4.2	Orientability	84
4.3	Elasticity of non-orientable soft surfaces	85
4.3.1	The elastic deformation bundle	87
4.3.2	Higher-dimensional non-orientable soft surfaces	88
4.3.3	Experimental measurements on soft surfaces	89
4.4	Frustrated metamaterials	90
4.4.1	Non-orientable mechanics in higher dimensions	93
4.4.2	Experimental measurements on frustrated mechanical antiferromagnets	95
4.5	Non-commutative response to heterogeneous loads	96
4.5.1	Metarings and ribbons	97
4.5.2	Metatoris and the braiding of local loads	98
4.6	Conclusions and perspectives	101
4.7	Article	104
4.8	Methods	113
4.8.1	Non-orientability of real line vector bundles beyond the Möbius bundle	113
4.8.2	Non-commutative response and non-orientable order	113
4.8.3	Mechanical sequential logic gate	116
4.9	Supplementary Videos	124
4.10	Supplementary Information	125
4.10.1	Bending mechanics of Möbius strips and non-orientable deformation bundles	125
4.10.2	Non-orientable mechanics of anti-ferromagnetic mechanical metamaterials	127
4.10.3	Non-orientable mechanics of toroidal metamaterials	132
4.10.4	Response to heterogeneous loads	135
4.10.5	Experimental Methods	141
	Bibliography	149

Introduction

Look around you. Manufactured objects surround us: the clothes you are wearing, the screen you are watching or the book you are reading. These are the results of centuries of material science knowledge, ensuring the apt properties for safeness, usefulness, and overall agreeable experience for our everyday life.

Material science has given us the mastery of everyday matter. We can characterize and tabulate the different materials found in nature by their ductility, opacity, capacitance, and magnetoresistance, among numerous features. However, the properties of raw substances are not enough to predict the final attributes of manufactured materials. Take for instance a yarn made out of cotton strings. Twisting the yarn dramatically increases the maximum supported traction force [1]. A simple geometric ingredient, the spatial arrangement of the strings, drastically changes the tensile strength of the yarn. Pushing this principle even further, we end up with the so-called metamaterials: human-engineered matter with exotic properties issued from smart patterning. Here we find optical devices displaying negative refractive indices [2, 3], fig. 1.1a, structures with finite bulk modulus yet vanishing shear modulus [4, 5], fig. 1.1b, materials that shrink laterally when compressed axially [6], fig. 1.1c, or acoustic devices controlling sound transmission [7, 8], fig. 1.1d, to name a few. A full body of literature can be found in recent reviews [9]. This exciting field pushes the boundaries of imagination, opening the door to engineering once-unthinkable properties, such as optical [11–13], mechanical [14], and acoustic [8, 15] cloaking devices, textiles with tunable mechanical properties [16], or enhanced cooling in gas turbines [17].

To characterize these exotic materials we have to expand our original toolbox to consider the smart patterning in real space. As we saw with the previous examples, we do this with geometry. But not only. Recently, global properties described by topology have emerged as additional tools to engineer metamaterials [18, 19]. Topology refers to the properties of spaces (real or abstract) that are robust to continuous deformations, for example, the number of holes a closed surface has. In physics, topology has classified electronic phases of matter escaping the previously established symmetry-breaking paradigm [20]. Boosted by novel applications, the realization of topological phases previously attributed to quantum systems [18], and recent advances in 3D printing techniques [21], the study of (topological) mechanical metamaterials has become a field by itself. Here we find the pioneering classical analogs of the (spin) quantum hall effect [22, 23], the selective buckling in architected materials [24], or the zero-edge mode trapping at topological defects [25].

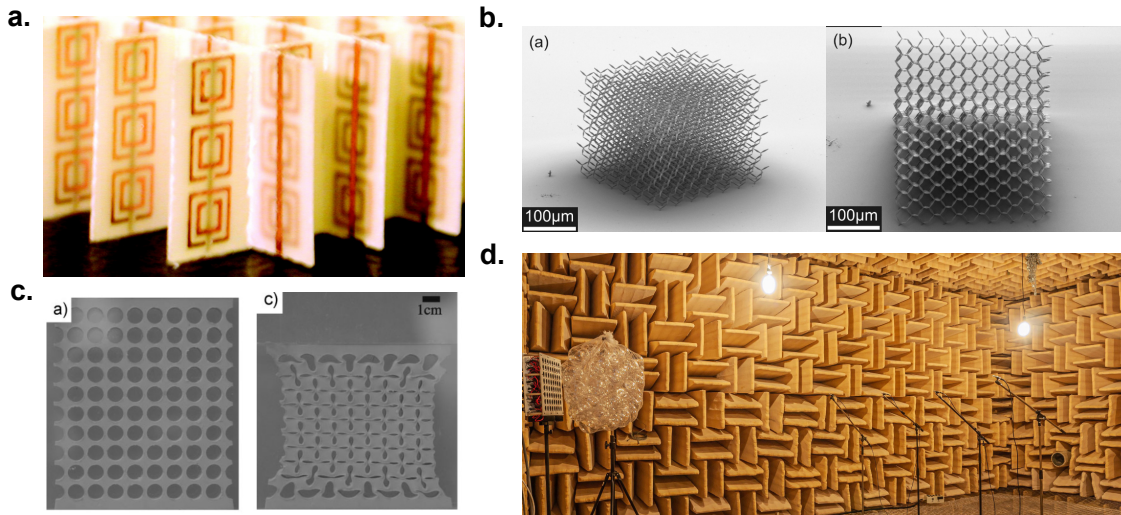


Figure 1.1: **Metamaterials.** **a.** Structured metamaterial exhibiting an effective negative index of refraction for a given frequency band. The sample corresponds to a two-dimensional array of copper strips and split ring resonators. (adapted from [2]) **b.** Electron micrograph of a polymer pentamode mechanical metamaterial. Pentamodes are special structures avoiding the coupling of compression and shear waves by making the bulk modulus as large as possible compared to the shear modulus. Due to their high flowing properties, they are often called metafluids. (adapted from [5]) **c.** (left) Square lattice of circular holes in an elastomeric matrix. (right) Above a critical load, the sample shapes into a pattern of alternating orthogonal ellipses, exhibiting a negative Poisson's ratio behavior. (adapted from [10]) **d.** Acoustic set-up able to perform far-field subwavelength imaging. At the extreme left there lies a white board with speakers on which the acoustic image is drawn. Right in front of it, an array of lossy resonant metamaterials takes the near-field features mainly issued by evanescent waves and propagates them to the far field. Far from the source, several microphones detect the far-field signal. Together with deep-learning techniques, they are able to image the sample at subwavelength resolution. (adapted from [7])

In the light of all these examples we may ask several questions: how do we rationalize the effects of geometry and topology on the properties of a mechanical material? Is there a general framework underlying them? and if so, what are the proper observables to detect these exotic features? In this thesis, we approach such questions guided by a fundamental mechanical property: rigidity. In order to build an intuition about these mechanical systems, we focus our attention on the foundations: bead-and-spring systems. Using them as guiding lines, we showcase an alternative formulation of mechanics, transparent to its topological content.

We begin this introductory chapter by revisiting the very basics of the description of bead-and-spring systems. We will show how to construct a Schrödinger-like equation describing the evolution of displacements and elongations on any mechanical network. This equation naturally leads to a Hamiltonian containing the geometrical and topological information of the network. Summarizing the state of the art in the field of topological mechanics, we will show how this Hamiltonian encodes topological properties and how

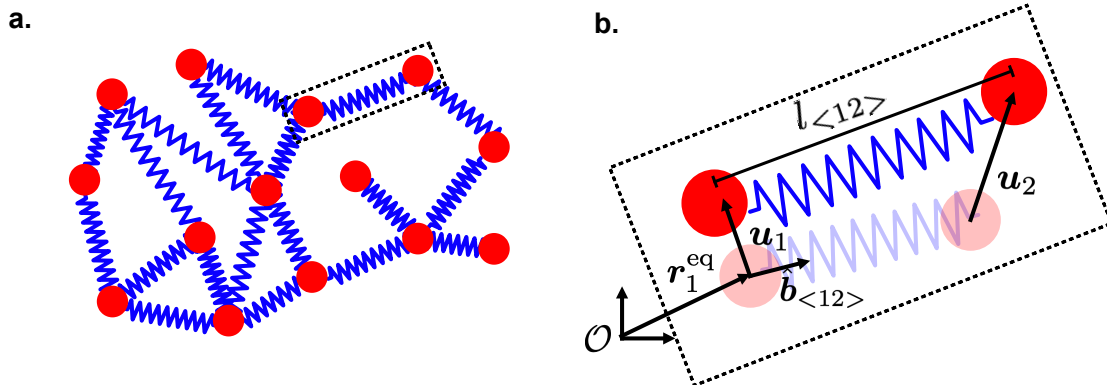


Figure 1.2: **Bead-and-spring network.** **a.** A collection of beads (red) connected by springs (blue) in two dimensions. **b.** Zoom of the marked region in **a** illustrating the definition of displacements and elongations from the equilibrium configuration (reduced opacity).

they manifest as robust edge states in different mechanical setups.

1.1 Linear response of bead and spring networks

How does a collection of beads and springs react to a slight deviation from the equilibrium configuration? This problem, being in all syllabi of undergraduate physics, reduces to a coupled harmonic oscillator for the bead displacements. The main ingredients to derive this relation stem both from geometric and constitutive relations. In what follows, inspired by the review [26], we revisit these ingredients and we will show that, by disentangling them, we will be able to naturally describe the rigidity of any mechanical network.

Starting from a network of N beads and N_c springs in d dimensions, fig. 1.2, let us denote the position of the i -th bead \mathbf{r}_i , and the length of the spring connecting beads i and j by $l_{\langle ij \rangle} = |\mathbf{r}_i - \mathbf{r}_j|$. Equilibrium, up to rigid body motions, is defined by positions \mathbf{r}_i^{eq} and lengths $l_{\langle ij \rangle}^{\text{eq}}$. Around equilibrium, we define the displacements \mathbf{u}_i and the extensions $e_{\langle ij \rangle}$ to first order:

$$\mathbf{u}_i = \mathbf{r}_i - \mathbf{r}_i^{\text{eq}}, \quad (1.1)$$

$$e_{\langle ij \rangle} = l_{\langle ij \rangle} - l_{\langle ij \rangle}^{\text{eq}} = \hat{\mathbf{b}}_{\langle ij \rangle} \cdot (\mathbf{u}_i - \mathbf{u}_j), \quad (1.2)$$

where $\hat{\mathbf{b}}_{\langle ij \rangle} = (\mathbf{r}_i^{\text{eq}} - \mathbf{r}_j^{\text{eq}})/|\mathbf{r}_i^{\text{eq}} - \mathbf{r}_j^{\text{eq}}|$ is the unit vector linking the equilibrium positions, fig. 1.2b. The perturbations of the whole system are conveniently described by collecting all the displacements into a dN -dimensional vector \mathbf{u} , and all the elongations into a N_c -dimensional vector \mathbf{e} . Equation (1.2) can then be reexpressed as a linear relation

$$\mathbf{e} = \mathcal{C}\mathbf{u}. \quad (1.3)$$

\mathcal{C} is known as the compatibility matrix [27], and its entries depend solely on the geometry and connectivity of the network.

At the mechanical level, the i -th bead feels a net force \mathbf{f}_i which is the result of the

tensions $t_{\langle ij \rangle}$ exerted by the adjacent springs:

$$\mathbf{f}_i = \sum_j \hat{\mathbf{b}}_{\langle ij \rangle} t_{\langle ij \rangle}. \quad (1.4)$$

We can recast this last equation by collecting all the forces in a dN -dimensional vector \mathbf{f} and all the tensions in a N_c -dimensional vector \mathbf{t} ,

$$\mathbf{f} = \mathcal{Q}\mathbf{t}, \quad (1.5)$$

with \mathcal{Q} known as the equilibrium matrix. Importantly, the equilibrium and compatibility matrices are transposed of each other: $\mathcal{Q} = \mathcal{C}^T$ [27].

Equations of motion

The dynamics of the displacements is then given by the total force acting on the beads:

$$\mathcal{M} \frac{d^2 \mathbf{u}}{dt^2} = -\mathbf{f} = -\mathcal{Q}\mathbf{t}, \quad (1.6)$$

with \mathcal{M} a positive definite diagonal matrix whose entries are the masses of each bead: $\mathcal{M}_{i,j} = m_i \delta_{ij}$. Equation (1.6) dictates the evolution of the displacements in terms of the tensions of the springs. To close the equations, we need the constitutive relation linking the stress to the kinematic quantities. The simplest of these relations is given by Hooke's law, which corresponds to the first-order contribution in terms of \mathbf{e} :

$$\mathbf{t} = \mathcal{K}\mathbf{e}. \quad (1.7)$$

\mathcal{K} is a positive definite diagonal matrix whose entries are the spring constants. This completes the closure relation and now we are ready to solve the dynamics of the system of beads and springs, in at least two alternative ways.

1.1.1 A displacement-based approach

Inserting eqs. (1.7) and (1.3) into Newton's equation (1.6), we end up with coupled harmonic oscillators with displacement variables playing the role of positions:

$$\mathcal{M} \frac{d^2 \mathbf{u}}{dt^2} = -\mathcal{Q}\mathcal{K}\mathcal{Q}^T \mathbf{u}. \quad (1.8)$$

In order to render the equation more symmetric, we define a mass-scaled displacement $\tilde{\mathbf{u}} = \mathcal{M}^{1/2} \mathbf{u}$, for which the equation of motion reads

$$\frac{d^2 \tilde{\mathbf{u}}}{dt^2} = -\underbrace{\tilde{\mathcal{Q}}\tilde{\mathcal{Q}}^T}_{\mathcal{D}} \tilde{\mathbf{u}}, \quad (1.9)$$

with $\tilde{\mathcal{Q}} = \mathcal{M}^{-1/2} \mathcal{Q}\mathcal{K}^{1/2}$ and the dynamical matrix \mathcal{D} being semi-positive definite. Any displacement can be described as a linear combination of the eigenstates of \mathcal{D} .

Floppy modes

The softest modes, known as floppy modes, correspond to displacements with no elastic energy. From eq. (1.9), they are determined by the nullspace of the dynamical matrix, $\ker(\mathcal{D})$. Importantly, due to the symmetric nature of \mathcal{D} , $\ker(\mathcal{D}) = \ker(\tilde{\mathcal{Q}}^T)$. It turns out that floppy modes are a result of pure geometry and connectivity; they are oblivious to the energetics of the system. Indeed, denoting a floppy mode by \mathbf{u}_{FM} and its mass-scaled version by $\tilde{\mathbf{u}}_{\text{FM}}$, a direct calculation shows that $\tilde{\mathcal{Q}}^T \tilde{\mathbf{u}}_{\text{FM}} = 0$ is equivalent to $\mathcal{Q}^T \mathbf{u}_{\text{FM}} = 0$. Therefore, floppy modes are directly obtained from the nullspace of the compatibility matrix, which encodes solely the geometry and connectivity of the network.

While the dynamical matrix seems to encode all the information of the system, from floppy modes to finite energy waves, it is, in fact, uninformative about certain zero-energy modes. To identify these lacking modes, let us look instead at how elongations evolve.

1.1.2 An elongation-based approach

By combining eqs. (1.3), (1.6), and (1.7) we get the dynamics of elongations

$$\frac{d^2 \mathbf{e}}{dt^2} = \mathcal{Q}^T \frac{d^2 \mathbf{u}}{dt^2} = \mathcal{Q}^T \mathcal{M}^{-1} \mathcal{Q} \mathcal{K} \mathbf{e}. \quad (1.10)$$

It represents, as before, coupled harmonic oscillators, this time for the elongation variables. We can render the equation more symmetric by defining a stiffness-scaled elongation $\tilde{\mathbf{e}} = \mathcal{K}^{1/2} \mathbf{e}$:

$$\frac{d^2 \tilde{\mathbf{e}}}{dt^2} = - \underbrace{\tilde{\mathcal{Q}}^T \tilde{\mathcal{Q}}}_{\bar{\mathcal{D}}} \tilde{\mathbf{e}}, \quad (1.11)$$

with $\bar{\mathcal{D}}$ a semi-positive definite dynamical matrix. All the elongations can thus be expressed as linear combinations of the normal modes of $\bar{\mathcal{D}}$.

Self-stress states

The nullspace of $\bar{\mathcal{D}}$ coincides with the nullspace of $\tilde{\mathcal{Q}}$, and it defines tensions that cost no net elastic energy, also known as self-stress states. As with floppy modes, self-stress states are merely determined by the geometry and connectivity. Let us denote a tension of zero-energy, or self-stress state, by \mathbf{t}_{SSS} and its corresponding stiffness-scaled elongation by $\tilde{\mathbf{e}}_{\text{SSS}} = \mathcal{K}^{-1/2} \mathbf{t}_{\text{SSS}}$. By definition they satisfy $\tilde{\mathcal{Q}} \tilde{\mathbf{e}}_{\text{SSS}} = 0$ which is equivalent to $\mathcal{Q} \mathbf{t}_{\text{SSS}} = 0$. From eq. (1.5), self-stress states correspond to tensions that produce no net forces, and having a null-force, they produce no work. Self-stress states are beyond the reach of the dynamical matrix \mathcal{D} , in the same way that floppy modes are not detected by $\bar{\mathcal{D}}$. Except for these zero-energy modes, both dynamical matrices give redundant information; any displacement state of finite energy is equivalently represented as an elongation state.

As we show next, the combined information of the compatibility and the equilibrium matrices leads to a general counting rule of zero-energy modes.

1.1.3 The Maxwell-Calladine counting rule

Back in the 19th century, James Maxwell realized that the number of floppy modes in a mechanical frame (beads linked by rigid struts) is a direct consequence of an excess

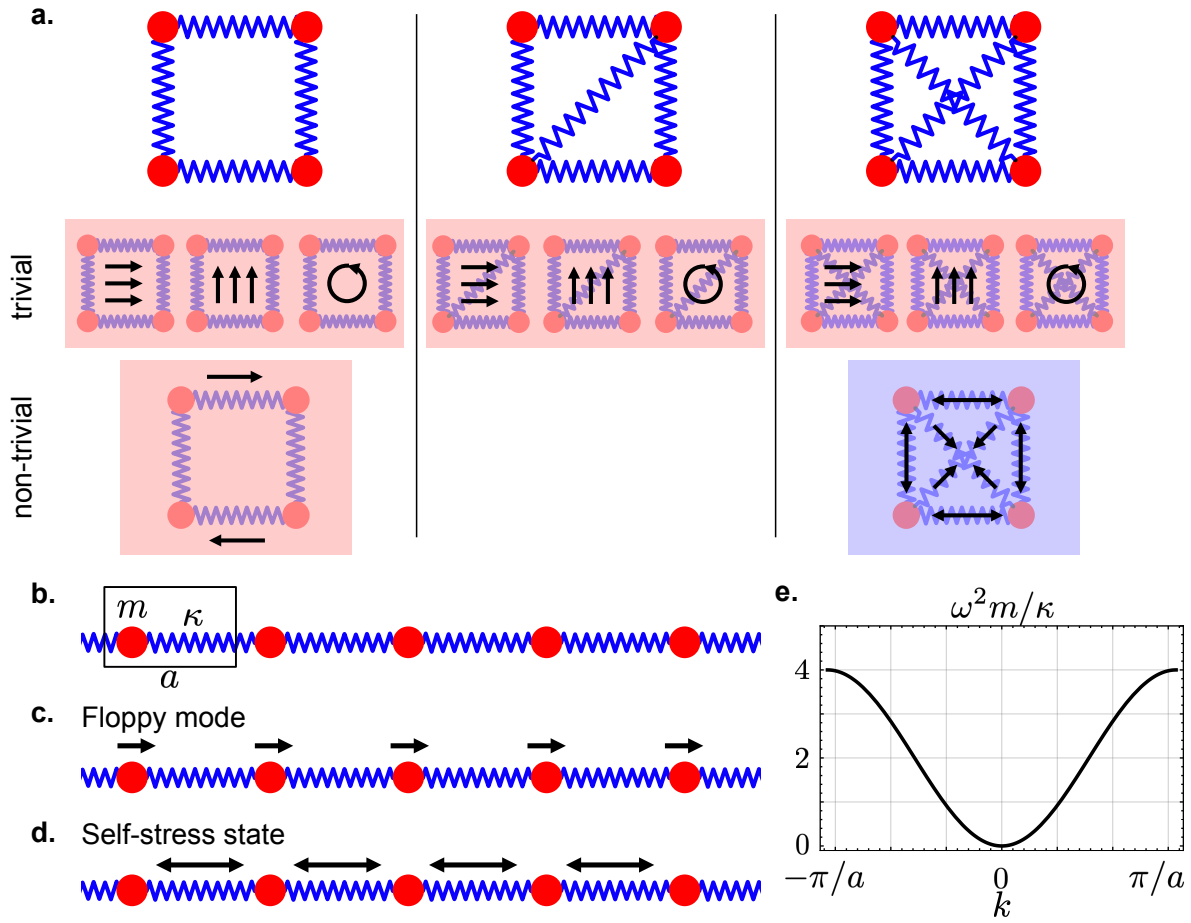


Figure 1.3: **Maxwell-Calladine index theorem.** **a.** (top) Three different frames in two dimensions. (bottom) Illustration of their zero-energy modes: floppy modes (red background) and self-stress-states (blue background). In all three cases there are three trivial floppy modes corresponding to two global translations and one global rotation. The Maxwell-Calladine index theorem (1.14) correctly predicts the amount of zero-energy modes by just counting degrees of freedom and constraints. From left to right: underconstrained, isostatic, and overconstrained frames. **b.** A periodic monoatomic chain of homogeneous beads (mass m) and springs (stiffness κ). In equilibrium, the beads are separated by a distance a . **c.** The only floppy mode of the system corresponds to a global translation. **d.** The system, being isostatic ($dN = N_c$), must have a self-stress state by virtue of the Maxwell-Calladine counting rule. It corresponds to a homogeneous compression of all the springs. **e.** The spectrum of $\mathcal{D} = \bar{\mathcal{D}}$ reveals the existence of the zero-energy modes at $k = 0$.

of degrees of freedom [28]. More than a hundred years later, Calladine, completed this observation by noticing that self-stress states arise from an excess of constraints [27]. Both statements are rationalized by the rank-nullity theorem: the rank of a matrix (number of linearly independent columns) is equal to the dimension of its nullspace plus the dimension of its domain (the total number of columns). Applying the rank-nullity theorem to both the equilibrium matrix $\mathcal{Q} \in \mathbb{R}_{dN \times N_c}$ and the compatibility matrix \mathcal{Q}^T we obtain:

$$\text{rank}(\mathcal{Q}) + \dim(\ker(\mathcal{Q})) = N_c, \quad (1.12)$$

$$\text{rank}(\mathcal{Q}^T) + \dim(\ker(\mathcal{Q}^T)) = dN, \quad (1.13)$$

where the dimensions of the nullspaces are simply the number of self-stress states N_{SSS} and the number of floppy modes N_{FM} . Finally, since $\text{rank}(\mathcal{Q}) = \text{rank}(\mathcal{Q}^T)$, we end up with the celebrated Maxwell-Calladine index theorem [27]

$$N_{\text{FM}} - N_{\text{SSS}} = dN - N_c. \quad (1.14)$$

Equation (1.14) states that the algebraic difference between floppy modes and self-stress states is given by the number of degrees of freedom minus the constraints, irrespective of the energetics.

Figure 1.3a illustrates the application of the Maxwell-Calladine index theorem on three frames of four beads and an increasing number of springs in two dimensions. All three frames possess three trivial floppy modes corresponding to rigid body motions: two translations and one rotation. In general, any free structure in d dimensions exhibits $d(d+1)/2$ rigid body motions. Besides these trivial floppy modes¹, the excess of degrees of freedom gives rise to additional non-trivial floppy modes. However, when the number of constraints exceeds the number of degrees of freedom, self-stress states appear, fig. 1.3a.

Another simple example corresponds to the periodic monoatomic chain: identical beads connected by springs in a one-dimensional array, fig. 1.3b. A quick counting reveals that there are as many degrees of freedom as constraints. Thus, by the Maxwell-Calladine counting rule (1.14), if there are zero-energy modes, there must be the same amount of floppy modes as self-stress states. This is indeed the case: the periodicity allows us to choose a unit cell and write equilibrium and compatibility matrices in momentum space:

$$Q(k) = e^{ika} - 1, \quad (1.15)$$

$$Q^\dagger(k) = e^{-ika} - 1, \quad (1.16)$$

from which we recognize a floppy mode at $k = 0$ corresponding to uniform translation, fig. 1.3c, and a self-stress states at $k = 0$ linked to a uniform tension across all the springs, fig. 1.3d. This information is also captured by the dynamical matrices $D(k) = \bar{D}(k) = \kappa/mQ(k)Q^\dagger(k) = 4\kappa \sin^2(ka/2)/m$, fig. 1.3e, with m and κ the bead mass and spring constant, respectively. In the language of electronic systems, the monoatomic chain would correspond to a conductor: we can excite waves at any arbitrary small energy. However, the first topological mechanical metamaterials were conceived in the opposite case: insulators.

1.1.4 Wave propagation: mechanical insulators

A mechanical insulator corresponds to a system that does not propagate waves in the bulk at arbitrary small energy. In other words, it has an energy gap at $E = 0$. Considering our

¹In this thesis, we consider the $d(d+1)/2$ rigid body motions as trivial floppy modes. A different convention, such as the one used in review [26], excludes them from the definition and adapts the Maxwell-Calladine counting accordingly.

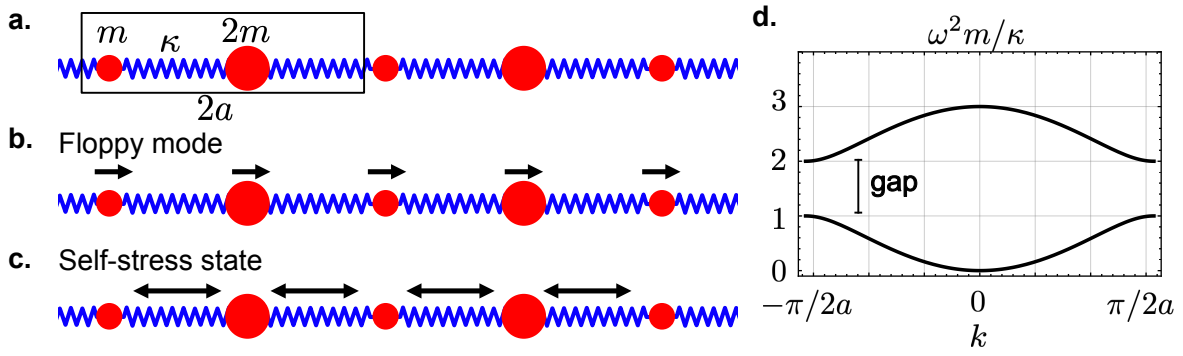


Figure 1.4: **Opening a gap in the monoatomic chain.** **a.** A diatomic chain of beads and springs. The masses of the springs alternate between m and $2m$, and the spring stiffness is κ . The system has the same floppy mode **b** and self-stress state **c** as the monoatomic chain. **d.** Dimerizing the chain opens a gap at finite energy, defining acoustic and optical branches.

previous example, how could we open a gap in the monoatomic chain? As a first attempt, we could dimerize the chain by setting alternating masses m_1 and m_2 , fig. 1.4a. Now the unit cell is twice as large, and the equilibrium matrix in momentum space reads

$$Q(k) = \begin{pmatrix} -1 & e^{-ik2a} \\ 1 & -1 \end{pmatrix}, \quad (1.17)$$

with a non-empty kernel for $k = 0$. Indeed,

$$\ker(Q(k=0)) = \ker(Q^\dagger(k=0)) = \left\{ \begin{pmatrix} 1 \\ 1 \end{pmatrix} \right\}, \quad (1.18)$$

which correspond to the same floppy mode and self-stress state as in the monoatomic chain, fig. 1.4b,c. The net effect of the dimerization is to open a gap at a finite energy, separating the acoustic from the optical branch, fig. 1.4d. Alternating the stiffness constants of the springs produces the same qualitative effect. Dimerization does not remove the zero-energy modes. This is indeed expected: zero-energy modes do not rely on the energetics; creating or removing them requires a geometrical change.

The Kane-Lubensky chain

In a pioneering paper that launched the field of topological mechanics [29], Kane and Lubensky introduced a one-dimensional array of identical beads and springs realizing a (topological) mechanical insulator, fig. 1.5a. The beads are attached to rigid bars which pivot around fixed points on the horizontal axis. Each rotor has only one angular degree of freedom. The compatibility matrix is set by the geometrical factors: the distance between two pivots a , the length of the rotor r , and the equilibrium angle θ^{eq} . Around the equilibrium configuration, the perturbations are geometrically described by the equilibrium matrix, $e_n = Q_{nm} \delta \theta_m$, which we can recast in momentum space using two beads per unit cell [30]:

$$Q^\dagger(k) = \begin{pmatrix} q_1 & q_2 \\ -q_2 e^{ik2a} & -q_1 \end{pmatrix}, \quad (1.19)$$

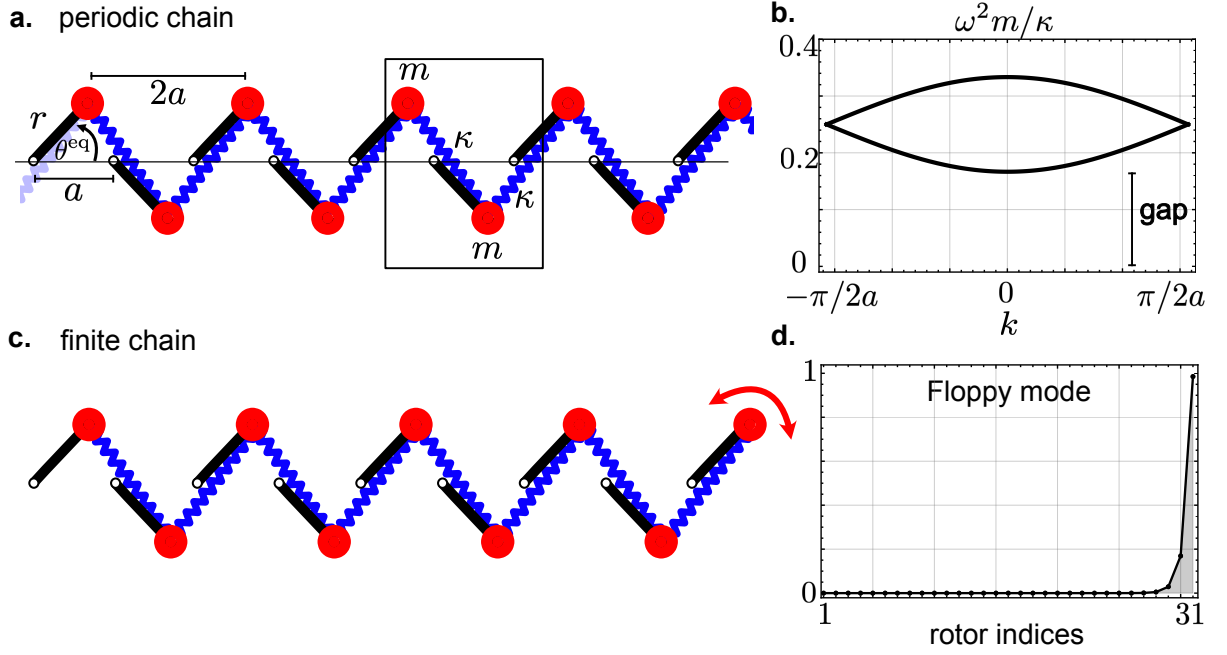


Figure 1.5: **Mechanical insulator: the Kane-Lubensky chain.** **a.** An array of beads of mass m , glued to rotors of length r , are connected by springs of stiffness κ . In equilibrium, the rotors describe an angle θ^{eq} with respect to the horizontal. The pivots of the rotors lie at a distance a from each other on a horizontal axis. In a periodic sample, the smallest repeating unit contains two beads and two springs (black rectangle). **b.** The dispersion relation from the dynamical matrix $\mathcal{D} = \bar{\mathcal{D}}$ exhibits a gap at zero energy; the chain is a mechanical insulator. Here we considered $r = 0.5a$ and $\theta^{\text{eq}} = \pi/4$. Due to the inversion symmetry, both branches meet at $k = \pm\pi/2a$. **c.** For any finite chain, the Maxwell-Calladine counting indicates the presence of at least one floppy mode. The bulk being an insulator is devoid of any zero-energy mode; the floppy mode must be localized on the edge, in this case, the right edge. **d.** The null space of the finite compatibility matrix \mathcal{Q}^T for a system of 31 rotors contains one element: a localized floppy mode. The amplitude of each bead displacement is represented as a function of the rotor index, from left to right.

with

$$q_{1/2} = r \sin \theta^{\text{eq}} (a \pm 2r \cos \theta^{\text{eq}}) / \sqrt{a^2 + 4r^2 \sin^2 \theta^{\text{eq}}}. \quad (1.20)$$

For equilibrium angles $\theta^{\text{eq}} \neq n\pi/2$, $n \in \mathbb{Z}$, the kernels of the compatibility and the equilibrium matrices are empty; there are no zero-energy modes. This is also shown by the dispersion relation of the dynamical matrices, fig. 1.5b, where a gap at $E = 0$ appears. The periodic system is an insulator.

However, for finite systems, fig. 1.5c, the Maxwell-Calladine counting rule (1.14) signals an excess of floppy modes. Not allowed in the bulk, this floppy mode must be confined to the edges. From the real space compatibility matrix, we see that this is indeed the case.

For a system of N rotors and $N - 1$ springs, the compatibility matrix reads

$$\mathcal{Q}^T = \begin{pmatrix} q_1 & q_2 & 0 & \dots & & \\ 0 & -q_1 & -q_2 & 0 & \dots & \\ 0 & 0 & q_1 & q_2 & 0 & \\ \vdots & & & \ddots & \ddots & \\ & & & 0 & -q_1 & -q_2 \end{pmatrix}, \quad (1.21)$$

whose kernel contains one element corresponding to an exponentially localized floppy mode, fig. 1.5d,

$$\mathbf{u}_{\text{FM}} = \left(\left(-\frac{q_2}{q_1} \right)^{N-1}, \left(-\frac{q_2}{q_1} \right)^{N-2}, \dots, -\frac{q_2}{q_1}, 1 \right)^T. \quad (1.22)$$

Hence the Maxwell-Calladine counting informs us about a global property: the number of zero-energy modes in the system. Mechanical insulators, on the other hand, forbid any zero-energy mode in the bulk. Moreover, we have seen that the mechanical chain displays the floppy mode at only one edge. How then can we locate the confined zero-energy modes in mechanical insulators? Here is where topology enters the game. The Kane-Lubensky chain not only is a mechanical insulator but also a topological one. To demonstrate this, we must exploit a natural symmetry enjoyed by all bead-and-spring networks: chiral symmetry.

1.2 Mechanics is chiral

The dual relations of bead-spring, displacement-elongation, force-tension, and floppy mode-self-stress state, evidence the natural sublattice symmetry present in such systems. It states the existence of two types of objects, here beads and springs, such that interactions occur exclusively between different entities. Indeed, two beads do not interact unless there is a spring in between. This natural observation manifests in the dynamics of mechanical networks. To elucidate how, let us reframe the mechanical equations (1.9) and (1.11).

1.2.1 Schödinger-like description: combining displacements and elongations

We can recast both eqs. (1.9) and (1.11) into a single second-order differential equation

$$\frac{d^2}{dt^2} \begin{pmatrix} \mathbf{u} \\ \mathbf{e} \end{pmatrix} = -\mathcal{H}^2 \begin{pmatrix} \mathbf{u} \\ \mathbf{e} \end{pmatrix}, \quad (1.23)$$

where we define

$$\mathcal{H} = \begin{pmatrix} 0 & \tilde{\mathcal{Q}} \\ \tilde{\mathcal{Q}}^T & 0 \end{pmatrix}. \quad (1.24)$$

After some algebraic manipulations, we can recast eq. (1.23) as

$$\left(i \frac{d}{dt} + \mathcal{H} \right) \left(i \frac{d}{dt} - \mathcal{H} \right) \begin{pmatrix} \mathbf{u} \\ \mathbf{e} \end{pmatrix} = 0, \quad (1.25)$$

and since the two operators commute, we obtain that the evolution of the displacements and elongations stems from a Schrödinger-like equation

$$i\frac{d}{dt}\begin{pmatrix} \mathbf{u} \\ \mathbf{e} \end{pmatrix} = \underbrace{\begin{pmatrix} 0 & \tilde{\mathcal{Q}} \\ \tilde{\mathcal{Q}}^T & 0 \end{pmatrix}}_{\mathcal{H}} \begin{pmatrix} \mathbf{u} \\ \mathbf{e} \end{pmatrix}, \quad (1.26)$$

with \mathcal{H} playing the role of the hamiltonian. This establishes the analogy with electronic systems and opens the door to study classical mechanics from the perspective of topological phases of matter.

Chiral symmetry

Equation (1.26) is the cornerstone of this thesis. The structure of the hamiltonian echoes the essential property mentioned at the beginning of the section: a chiral or sublattice symmetry. This is the symmetry that allows for a direct mapping between the Kane-Lubensky chain and the tight-binding model of an electron wave function in the polyacetylene chain [29].

In mathematical terms, chiral symmetry is formulated as an anticommutation between \mathcal{H} and the chiral operator \mathbb{C}

$$\mathbb{C}\mathcal{H} + \mathcal{H}\mathbb{C} = 0, \quad (1.27)$$

where the chiral operator reads

$$\mathbb{C} = \begin{pmatrix} 1_{dN} & 0 \\ 0 & -1_{N_c} \end{pmatrix}, \quad (1.28)$$

with identity matrices of dimensions $dN \times dN$ and $N_c \times N_c$ as entries. Due to this symmetry, the eigenstates of \mathcal{H} come by pairs. For each eigenstate $|\Psi_E\rangle$ of finite energy E , there is another eigenstate of opposite energy, $|\Psi_{-E}\rangle = \mathbb{C}|\Psi_E\rangle$. This reflects what we already knew: the information of \mathcal{D} and $\bar{\mathcal{D}}$ is redundant for finite energy states.

For zero-energy modes, however, this is no longer the case. A floppy mode, for instance, is described as a state encompassing only displacements (no elongations), $|\Psi_{E=0}^{\text{FM}}\rangle = (\mathbf{u}_{\text{FM}}, 0)$. Applying the chiral operator does not give a second zero-energy mode. Instead, we realize that zero-energy modes are eigenstates of the chiral operator

$$\mathbb{C}|\Psi_{E=0}^{\text{FM}}\rangle = +1|\Psi_{E=0}^{\text{FM}}\rangle, \quad (1.29)$$

$$\mathbb{C}|\Psi_{E=0}^{\text{SSS}}\rangle = -1|\Psi_{E=0}^{\text{SSS}}\rangle. \quad (1.30)$$

The chiral operator naturally distinguishes between the different types of zero-energy modes from their opposite eigenvalues. Moreover, $\mathbb{C}^2 = 1_{dN+N_c}$ implies that ± 1 are the only possible eigenvalues.

Maxwell-Calladine: a chiral symmetry insight

Under this chiral framework, in [31] we derive the Maxwell-Calladine counting (1.14) as a generic property of any chiral system by computing the trace of the chiral operator.

The trace, being simply the sum of the diagonal elements, accounts for the difference of degrees of freedom and constraints.

$$\mathrm{Tr}[\mathbb{C}] = \mathrm{Tr} \left[\begin{pmatrix} 1_{dN} & 0 \\ 0 & -1_{N_c} \end{pmatrix} \right] = dN - N_c. \quad (1.31)$$

Expanding the trace in the eigenbasis of \mathcal{H} , we notice that it also holds a spectral information

$$\begin{aligned} \mathrm{Tr}[\mathbb{C}] &= \sum_{E,m} \langle \Psi_{E,m} | \mathbb{C} | \Psi_{E,m} \rangle \\ &= \sum_m \langle \Psi_{0,m} | \mathbb{C} | \Psi_{0,m} \rangle \\ &= N_{\mathrm{FM}} - N_{\mathrm{SSS}}, \end{aligned} \quad (1.32)$$

with m indicating any possible degeneracy. In the second line we used the orthogonality of the eigenstates, and in the last line the fact that zero energy modes are eigenstates of \mathbb{C} . All in all, just by calculating the trace in different spaces, we arrive at the Maxwell-Calladine counting rule

$$N_{\mathrm{FM}} - N_{\mathrm{SSS}} = dN - N_c. \quad (1.33)$$

It is worth noting that as far as the description of zero-energy modes is concerned, we could have used either \mathcal{Q} or $\tilde{\mathcal{Q}}$ into the definition of \mathcal{H} without affecting the final counting.

1.2.2 Topology of chiral systems: the winding number

The Kane-Lubensky chain represents a topological insulator as studied in electronic systems [20]: an insulator in the bulk which hosts zero-energy modes at the boundaries of the sample. Importantly, the existence of these zero-energy modes is deduced from the bulk hamiltonian through topological indices. In particular, for crystalline chiral insulators, the index corresponds to the winding number $w \in \mathbb{Z}$ of \mathcal{H} expressed in momentum space [32]. To compute it, we must prescribe a unit-cell, usually the one matching the edge of the sample, and write the Hamiltonian in momentum space, $H(k)$, also known as Bloch Hamiltonian. w is then defined as the winding of the determinant of $Q(k)$:

$$\begin{aligned} w &= \frac{i}{4\pi} \int dk \mathrm{Tr} \left[\partial_k H \mathbb{C} H^{-1} \right] \\ &= \frac{1}{2\pi i} \int dk \mathrm{Tr} \left[Q^{-1} \partial_k Q \right]. \end{aligned} \quad (1.34)$$

A non-zero winding indicates the presence of localized zero-energy modes on the edges matching the unit-cell, fig. 1.6. The connection between this topological bulk-invariant and the localized zero-energy is an example of the so-called bulk-boundary correspondence, which is at the core of the use of topology in condensed matter [20, 33].

In [29], Kane and Lubensky introduced a topological polarization defined $\mathbf{R}_T = wa\hat{\mathbf{n}}$, with a the unit-cell size, and $\hat{\mathbf{n}}$ the normal of the interface. Remarkably, it has the property of pointing towards the soft edges hosting floppy modes. For suitable unit-cell choices, the topological polarization successfully indicates the presence of soft-edges in 1D Miura origamis and 2D kirigami interfaces [34], fig. 1.7a,b, and the soft edges of

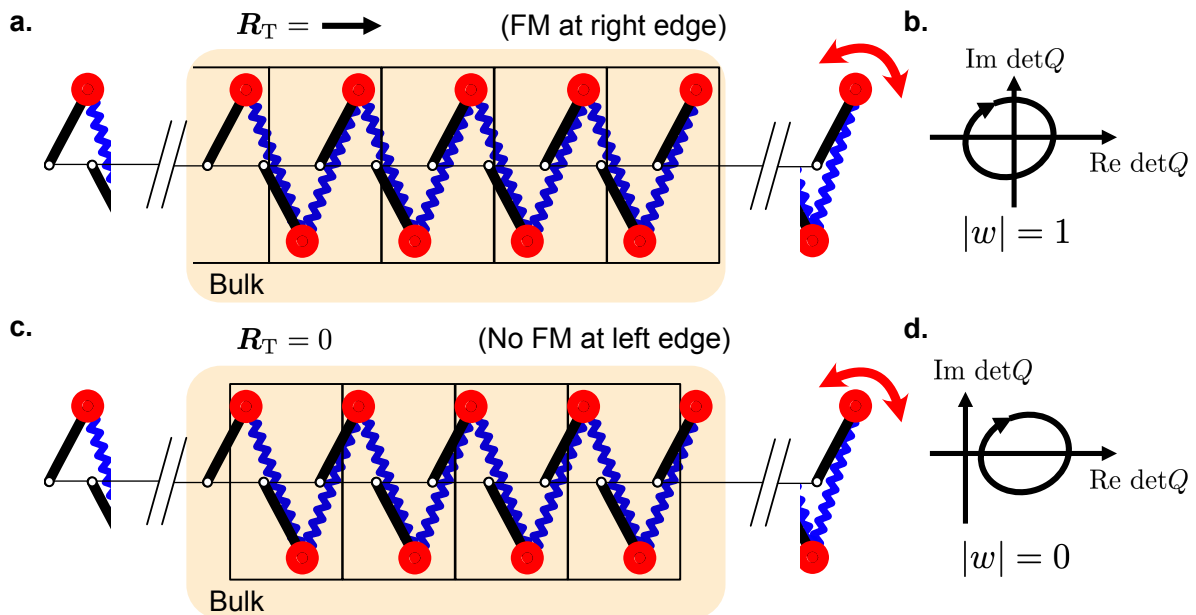


Figure 1.6: **The winding number in the Kane-Lubensky chain.** **a.** The topological polarization in the Kane-Lubensky chain is calculated from a unit-cell compatible with the right edge. The non-zero polarization points towards the right of the sample, indicating the presence of a localized floppy mode. **b.** The topological polarization is directly proportional to the winding number of the Bloch Hamiltonian $H(k)$. It corresponds to the number of times $\det Q(k)$ winds around the origin as k goes from $-\pi/a$ to π/a (a being the unit-cell size). **c.** Changing the unit-cell to the one matching the left edge leads to a null topological polarization; no zero-energy mode is localized on the left edge. This is due to the compatibility matrix not winding around the origin, **d.**

twisted-kagomé lattices [29], fig. 1.7c. In these two last examples, the Bloch Hamiltonian is computed as the Fourier transform of \mathcal{H} along a single direction perpendicular to the interface or edge.

One peculiarity of the twisted kagomé lattice is its versatile phonon band topology. With soft deformations in the frame structure, the so-called Guest-Hutchinson modes [35, 36], one can effectively guide the metamaterial through different topological states [37].

1.2.3 Chiral topological insulators beyond mechanics

We have seen that mechanics is chiral. The equation governing the dynamics of mechanical networks is characterized by a chiral hamiltonian. Importantly, eq. (1.26) is not exclusive to mechanics. Indeed, they naturally originate from quantum systems. One of the first historical chiral systems corresponds to the low-energy model characterizing the polyacetylene molecule [38], also known as the Su-Schrieffer-Heeger model or SSH model. The dimerization of this one-dimensional chain sets two distinct hopping parameters, therefore identifying two sublattices, fig. 1.8a. However, unlike mechanics, here chirality is issued from a low-energy approximation. High-energy perturbations are governed by next-nearest neighbor interactions, effectively breaking the sublattice symmetry. Figure 1.8 illustrates various examples of chiral topological insulators in different platforms,

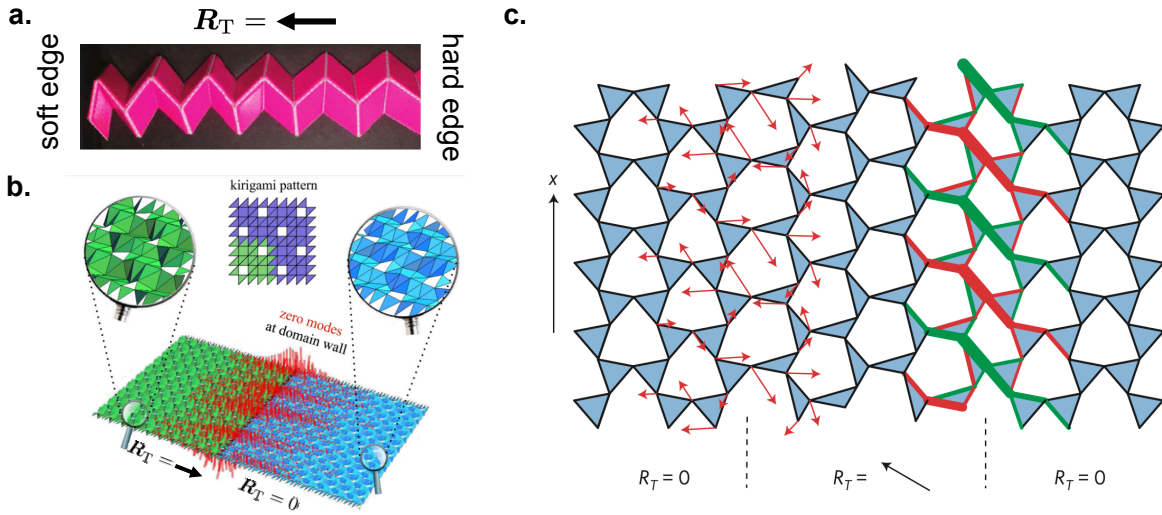


Figure 1.7: **The topological polarization in one- and two-dimensional systems.** **a.** A quasi-one-dimensional origami strip realizing a topological mechanical insulator. Due to the localized floppy mode, the left edge is much softer than the right one. The localization of the floppy mode is captured by the topological polarization. **b.** A two-dimensional kirigami sheet with a floppy mode localized on a domain wall. Its presence is predicted by the non-matching topological polarization on the left and right sides. (**a** and **b** adapted from [34]) **c.** The twisted kagomé lattice is implemented by rigid triangular plaquettes joined by the vertices. The geometry of the sample sets its topological polarization. Whenever two regions of opposite polarization meet, a zero-energy mode appears. In the example, the two domain walls present extensive zero-energy modes in the x direction. The left domain wall enjoys a floppy mode, whereas the right one, a self-stress state. (adapted from [29])

such as 2D [39,40] and 3D [41] resonators, photonic honeycomb lattices [42], topo-electrical circuits [43], and polariton micropillar arrays [44], to name a few.

1.3 Characterization of topological insulators in mechanics

We have shown that a Schrödinger-like equation (1.26) governs the evolution of displacements and elongations in a mechanical network. This reformulation unveils a natural property of mechanics: chiral symmetry, which is shared with several other systems from quantum to classical examples. This symmetry proved to be essential in classifying the topological nature of insulating phases. Carrying on the mapping with electronic systems, there are many more topological classifications of insulating phases based on different symmetries and their dimensionality [32, 45]. Does the richness of topological phases in electronic systems find its counterpart in mechanics? In this section, we show how the playground that topological mechanics has to offer goes beyond chirality. Guided by the review [46], we briefly summarize the state of the art in the field of topological mechanics.

Our starting point is the equation of motion of the displacements (1.9). Now, however,

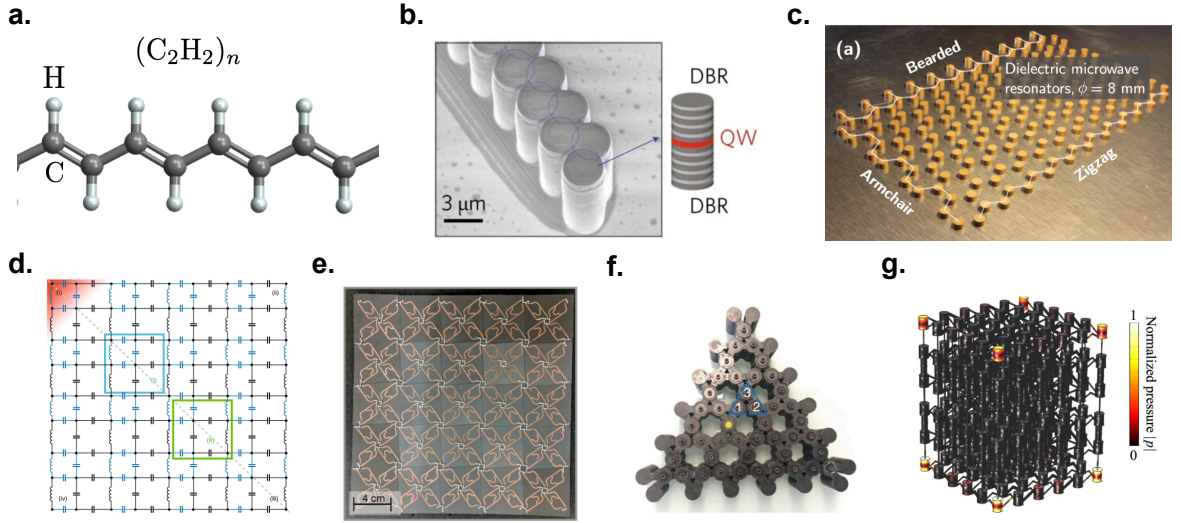


Figure 1.8: **Chiral topological insulators.** **a.** In the low energy approximation, the polyacetylene molecule is defined by a chiral tight-binding hamiltonian, known as the SSH model. Due to the alternating bonds, an electron in this molecule hops with asymmetric probabilities to the left or right carbon atoms. This effectively defines two sublattices of carbon atoms rendering the system chiral. **b.** The SSH model also applies to photonic devices. Nanowires coil around micropillars which are placed in a one-dimensional array. Due to a dimerization in the distances between the pillars, the evanescent waves couple asymmetrically with a distance-dependent strength. (adapted from [44]) **c.** Photonic implementation of a honeycomb lattice in the microwave regime. The dielectric cylinders of the lattice are coupled by an evanescent magnetic field in a regime in which the wave propagation is well described by a nearest-neighbor tight-binding model. The application of a uniaxial strain induces an anisotropy in the hopping parameters, which renders the hamiltonian chiral. (adapted from [42]) **d.** A non-dissipative linear electric circuit with weak (blue) and strong (black) bonds is effectively modeled by a chiral tight-binding hamiltonian. Each unit cell contains two capacitors and two inductors. (adapted from [43]) **e.** Reconfigurable microwave circuit in the gigahertz-frequency regime. Each unit cell is composed of four identical resonators, with different coupling rates between intracellular and extracellular cells, effectively generating a magnetic π flux threading the plaquette. (adapted from [39]) **f.** Two-dimensional acoustic meta-structure in a kagome lattice. Each site contains a resonator hosting acoustic pressure modes oscillating in the axial direction. The dimerization of the coupling strengths is achieved by changing the shape of the resonators. The system is well described by a chiral tight-binding model due to the strong confinement of the resonant modes. (adapted from [40]) **g.** Three-dimensional acoustic meta-structure designed by the same principles as in **f.** (adapted from [41])

we will include velocity-dependent forces:

$$\ddot{\mathbf{u}} = -\mathcal{D}\mathbf{u} + \mathcal{A}\dot{\mathbf{u}}, \quad (1.35)$$

where dots denote time derivatives, \mathcal{D} is the dynamical matrix, \mathcal{A} is a skew-symmetric matrix describing conservative couplings between positions and velocities, and we have dropped the tildes for simplicity. We can conveniently recast this second order differential

equation into a first order Schrödinger-like equation:

$$i \frac{d}{dt} \begin{pmatrix} \sqrt{\mathcal{D}} \mathbf{u} \\ i \dot{\mathbf{u}} \end{pmatrix} = \underbrace{\begin{pmatrix} 0 & \sqrt{\mathcal{D}} \\ \sqrt{\mathcal{D}} & i \mathcal{A} \end{pmatrix}}_{\mathcal{H}'} \begin{pmatrix} \sqrt{\mathcal{D}} \mathbf{u} \\ i \dot{\mathbf{u}} \end{pmatrix} \quad (1.36)$$

It is worth noting that the wave function depends on the displacements and their velocities. Moreover, the dynamical matrix is decomposed into square roots, $\mathcal{D} = \sqrt{\mathcal{D}} \sqrt{\mathcal{D}}$, unlike the physical decomposition used in section 1.1, given by the compatibility and equilibrium matrices, $\mathcal{D} = \mathcal{Q} \mathcal{Q}^T$. The formulation (1.36) hampers the description of zero-energy modes on mechanical networks, yet it offers an elegant insight into the topology of finite energy states.

The topological classification of electronic systems is built upon their dimensionality and three overarching symmetries [32]: particle-hole, time-reversal, and chiral symmetry. While this classification does not rely on translational invariance, the topological properties are easily introduced for translationally symmetric systems, for which the real space hamiltonian \mathcal{H}' can be expressed in Fourier space following a unit-cell convention, $H'(\mathbf{k})$. Each symmetry imposes a series of constraints on H' characterized by its (anti)commutation with some unitary or antiunitary operator:

1. Time-reversal symmetry:

$$\mathbb{T} H'(\mathbf{k}) - H'(-\mathbf{k}) \mathbb{T} = 0, \quad \mathbb{T}^2 = \pm 1, \quad (1.37)$$

with \mathbb{T} antiunitary.

2. Particle-hole symmetry:

$$\mathbb{P} H'(\mathbf{k}) + H'(-\mathbf{k}) \mathbb{P} = 0, \quad \mathbb{P}^2 = \pm 1, \quad (1.38)$$

with \mathbb{P} antiunitary.

3. Chiral symmetry:

$$\mathbb{C} H'(\mathbf{k}) + H'(\mathbf{k}) \mathbb{C} = 0, \quad \mathbb{C}^2 = 1, \quad (1.39)$$

with \mathbb{C} unitary.

Notice, however, that their meaning differs from their electronic counterparts. Time-reversal symmetry, according to the formulation (1.36) does not correspond to the reversal of time but rather to a fine-tuning of the matrices \mathcal{D} and \mathcal{A} . Here, the true time-reversal comes from the chiral symmetry: each eigenvector, of the form $(\sqrt{\mathcal{D}} \mathbf{u}, i \dot{\mathbf{u}})$, is mapped to $(\sqrt{\mathcal{D}} \mathbf{u}, -i \dot{\mathbf{u}})$ with an opposite eigenvalue. Particle-hole symmetry implies that for each eigenstate, its complex conjugate is also an eigenstate. This symmetry is directly issued from \mathcal{D} and \mathcal{A} being real matrices [46].

While there are numerous theoretical proposals for classical systems realizing topological phases [46–49], here we briefly mention some outstanding experimental examples. The first of them is the realization of mechanical Chern insulators in two dimensions (class A). They require the breaking of the time-reversal symmetry. In electronic systems, this can be achieved by imposing a net magnetic field [50]. In mechanics, however, this corresponds to having $\mathcal{A} \neq 0$. Playing with the dimensionality and engineering the \mathcal{D} and \mathcal{A}

matrices, Nash and collaborators implemented the first mechanical Chern insulator based on interacting gyroscopes on a honeycomb lattice [22], fig. 1.9a. The non-trivial topology manifests as chiral waves localized on the edges of the sample, in direct analogy with the quantum hall effect in electronic systems. Moreover, by distorting the lattice, Mitchell and collaborators show how the protection of the chiral edge waves is independent of any lattice symmetry [51].

A second example corresponds to the mechanical realization of the spin quantum Hall effect (class AII in $2D$). This phase is characterized by the spin Chern number and requires the breaking of the chiral and particle-hole symmetry, with time-reversal squaring to -1 . By coupling pendula with springs, Süsstrunk and Huber devised the sought-after mechanical analog [23], fig. 1.9b. Here the spin is given by the polarization of the oscillating pendula. The signature of this topological phase is the counter propagation of helical edge states.

Another intriguing set-up corresponds to the realization of mechanical higher-order topological insulators [52, 53]. Here the topologically protected states are localized in lower dimensions; corners in $2D$, and hinges and corners in $3D$. Their description is based on topological indices of reduced spaces [52]. In this family of topological phases, we find the experimental realization based on coupled acoustic resonators [54]. The resonators are arranged into a checkerboard lattice, fig. 1.9c. At frequencies lying in the bulk energy gap, the system responds with vibrations localized at the corners. These systems are analyzed with the help of nested Wilson loops [52], which effectively projects bulk properties into the edges. Unlike the previous examples, the topological origin of the corner states is explained by real-space symmetries, which quantize the bulk-induced edge polarizations.

In the light of all these theoretical and experimental works, a few comments are in order:

1. Equation (1.36) is based on effective models. Indeed, the decomposition $\mathcal{D} = \sqrt{\mathcal{D}}\sqrt{\mathcal{D}}$ does not stem from the physical connectivity of the system. As a result, this reformulation of mechanics is oblivious to the compatibility and equilibrium matrices, and therefore unsuited to detecting floppy modes and self-stress states.
2. Most of the experimental topological metamaterials are based on an engineering approach: given a Bloch hamiltonian $H(k)$ realizing a topological phase, we search for its mechanical realization by tweaking the interactions and finding the appropriate matrices \mathcal{D} and \mathcal{A} .
3. There is no experimental measurement of the bulk topological indices characterizing the phases. This is partly due to the previous point; there is no need to measure invariants if we already know the Hamiltonian. With some exceptions in disordered systems [51], this is also due to the lack of bulk physical observables related to these invariants.
4. Moving to chiral systems, the core of this thesis, they suffer from yet another symptom. The topological invariant itself, the winding number, is ill-suited for being a physical observable. This is evident from fig. 1.6, where the same system can be described by two opposite invariants depending on the choice of unit-cell. This problem will be further clarified, and resolved, in the next chapter.

5. Related to the two previous points, all topological invariants are defined in terms of the detailed hamiltonian. However, if a true topological observable exists, we should be able to measure it without knowing \mathcal{H} .

This thesis is aimed to characterize the rigidity of mechanical materials through their topological content in light of the chiral symmetry. To do so, we must first surmount the challenges linked to the standard topological description and the lack of physical observables. Building on the seminal work of Kane and Lubensky [29], we mix theory, experiments, and simulations, to devise a general framework able to describe distinct topological phases without relying on any Hamiltonian.

1.4 Organization of the manuscript

This thesis is organized into 4 chapters, from which this introduction, chapter 1, illustrates the state of the art in the field of mechanical materials.

Chapters 2 and 3 deal with the topological softness of mechanical systems, where floppy modes and self-stress states are the protagonists. More precisely, chapter 2 lays the theoretical framework to study chiral mechanical insulators. Exploiting chirality, we draw an analogy with electrostatic systems which helps us define a suitable observable to probe the geometry and topology of mechanical systems: the chiral polarization. This new vectorial quantity, defined in real space, does not rely on any modeling or prescribed Hamiltonian. Moreover, it univocally identifies soft regions of floppy modes and localized self-stress states. This observable proves to be useful not only in lattices but also in disordered matter. We conclude the chapter with our article "Geometry and topology tango in ordered and amorphous chiral matter" [31], where we extend our findings to all systems enjoying a chiral symmetry.

The third chapter concerns the measurement and experimental detection of the chiral polarization. Comparing different platforms in one and two dimensions, we present a robust protocol to probe the polarization in terms of local excitations. We experimentally identify the real-space structures formed by the excitations, on top of which we build the chiral polarization field. We validate our findings with experiments and simulations by correctly identifying topologically protected soft modes.

In the final chapter, we explore the topological stiffness displayed by mechanical meta-materials presenting antiferromagnetic-like interactions. Here, the main signature is the antithesis of a floppy mode: a region of the system immune to any deformation. We show that the topology linked to the elastic deformations is akin to that of non-orientable surfaces. This novel topological phase offers new platforms to study non-commutative responses and allows for the manufacturing of mechanical logic gates. We conclude the chapter with our preprint "Non-orientable order and non-commutative response in frustrated metamaterials" [55].

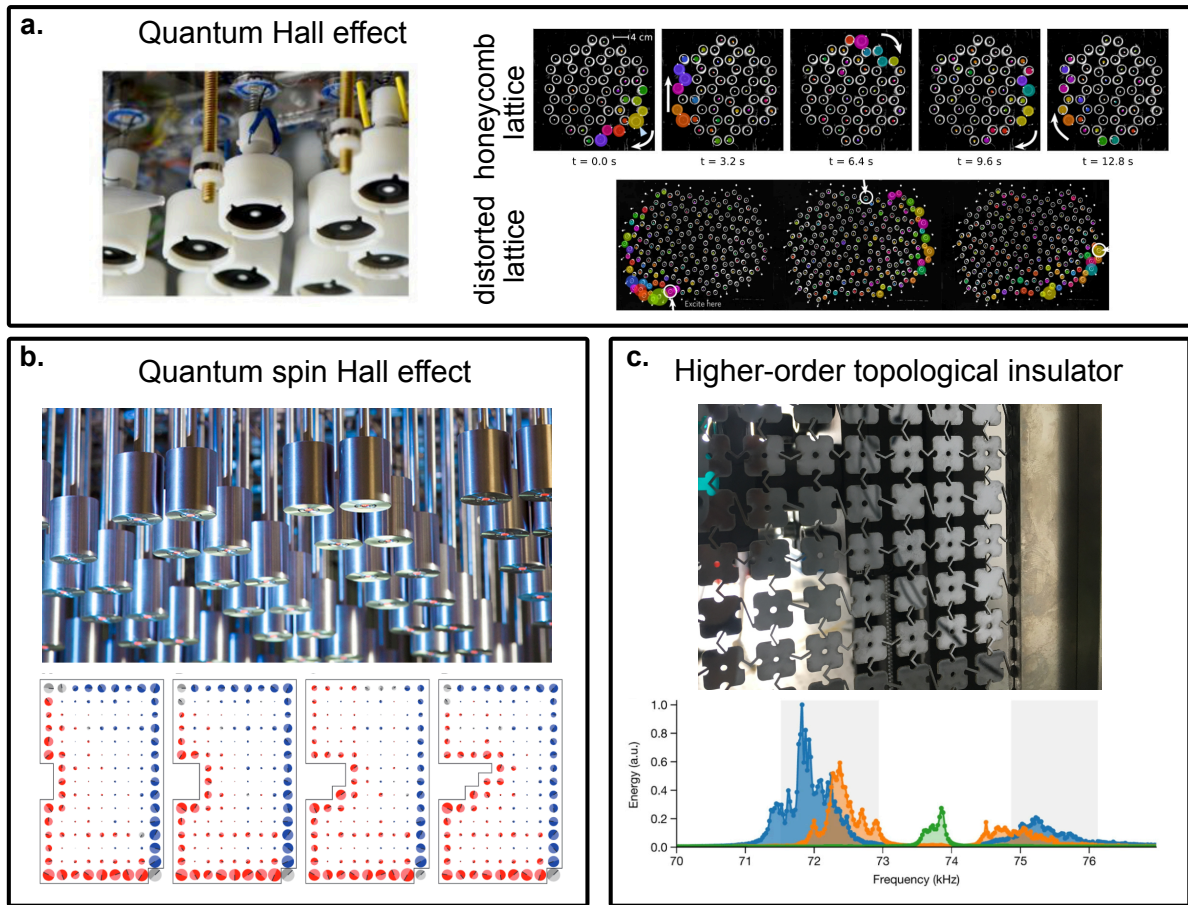


Figure 1.9: **Topological mechanics.** **a.** (left) Magnetically coupled gyroscopes as viewed from below. In the linear regime, the evolution of the gyroscopes breaks time-reversal symmetry. (top right) A lattice of 54 gyroscopes on a honeycomb lattice displays long-lived unidirectional chiral waves, akin to the quantum Hall effect. (bottom right) As with the quantum case, the localization of the chiral waves does not depend on the crystalline structure of the system. Here, a distorted lattice is excited at three different positions, each excitation leading to chiral waves confined to the edge of the sample. (adapted from [22] and [51]) **b.** (top) A system of elastically coupled pendula recreates the quantum spin Hall effect. The analog of the spin is given by the right and left polarized oscillations of the pendula. (bottom) Counterpropagating helical edge states in four different configurations with varying boundary roughness. Each image corresponds to the steady-state of the system when driving the bottom right pendulum. Red (blue) circles indicate left (right) polarized pendula, with radii proportional to their mean deflection. (adapted from [23]) **c.** (top) Higher-order topological insulator realization from a mechanical metamaterial. The out-of-plane modes of each plaquette are coupled via the bent beams. The shape of the beams realizes both negative and positive interactions among the nearest neighbors. (bottom) Spectra of the system separated by bulk (blue), edge (orange), and corner (green) contributions. At a frequency lying in the bulk and edge gap, the finite sample exhibits localized corner states which are explained by inversion and mirror symmetries. (adapted from [54])

Softness: Topology and geometry in mechanics

2.1 Introduction

Bead and spring systems exhibit a natural symmetry known as sublattice or chiral symmetry. It states that there are two types of entities - beads and springs - such that interactions occur only between different species. More explicitly, a bead does not interact directly with another bead, but rather interacts with a spring, and the spring propagates the force to the next bead. This symmetry, although present in virtually all mechanical systems, goes rather unnoticed in most mechanical textbooks.

Briefly recalling from the introduction 1, the kinematics of a collection of beads and springs, fig 2.1a, are described by the displacements of beads, $\{\mathbf{u}_i\}$, which are geometrically related to the elongation of springs, $\{e_j\}$, via the compatibility matrix: $\mathbf{e} = \mathbf{Q}^T \mathbf{u}$. In turn, the mechanics are described by the forces acting on the beads, $\{\mathbf{f}_i\}$, geometrically related to the tensions acting on the springs, $\{t_i\}$, via the equilibrium matrix: $\mathbf{f} = \mathbf{Q} \mathbf{t}$. Endowed with Hooke's law, $\mathbf{t} \propto \mathbf{e}$, the equation of motion for a bead-and-spring network corresponds to the coupled harmonic oscillator:

$$\frac{d^2 \mathbf{u}}{dt^2} = -\mathcal{D} \mathbf{u}, \quad (2.1)$$

with $\mathcal{D} = \mathbf{Q} \mathbf{Q}^T$ being the dynamical matrix. For simplicity, here and in the following the mass and spring constants are set to one. Equation (2.1) dictates the evolution of bead's displacements. From an initial state at $t = 0$ we can infer the state at any other time by just knowing \mathcal{D} , suggesting that all the relevant physical information is encoded in the dynamical matrix. However, the dynamical matrix is incapable of describing all the zero-energy modes. Displacements of zero energy (floppy modes) are directly obtained from the kernel of the dynamical matrix $\ker \mathcal{D}$ [56], yet tensions of zero energy (self-stress states), relevant for structural rigidity [57], are out of reach.

The other side of the coin consist in an elongation-based approach. The evolution of the elongations is also governed by a coupled harmonic oscillator:

$$\frac{d^2 \mathbf{e}}{dt^2} = -\bar{\mathcal{D}} \mathbf{e}, \quad (2.2)$$

with $\bar{\mathcal{D}} = \mathcal{Q}^T \mathcal{Q}$. Unlike the previous case, self-stress states are obtained from the kernel of $\bar{\mathcal{D}}$ yet floppy modes remain elusive. The limitations of both individual descriptions (2.1)(2.2) lie at the core of the natural chiral symmetry; we must track the information of both displacements and elongations to obtain the full zero-energy content. As done in the introduction this can be achieved by writing the equations of motion as a Schrödinger equation [29, 47]

$$i \frac{d}{dt} \begin{pmatrix} \mathbf{u} \\ \mathbf{e} \end{pmatrix} = \underbrace{\begin{pmatrix} 0 & \mathcal{Q} \\ \mathcal{Q}^T & 0 \end{pmatrix}}_{\mathcal{H}} \begin{pmatrix} \mathbf{u} \\ \mathbf{e} \end{pmatrix}, \quad (2.3)$$

where \mathcal{H} is the hamiltonian governing the waves of displacements and elongations in the mechanical network. This mathematical object contains *all* the physical information of the system, encompassing both floppy modes and self-stress states, fully characterizing the softness of the system. The off-block diagonal structure of the hamiltonian is the imprint of the chiral symmetry; beads interact only with springs and vice versa. In mathematical terms, the hamiltonian anticommutes with the chiral operator $\{\mathcal{H}, \mathbb{C}\} = 0$, which is defined as

$$\mathbb{C} = \begin{pmatrix} 1 & 0 \\ 0 & -1 \end{pmatrix}. \quad (2.4)$$

This mapping to quantum chiral systems was popularized by the seminal work of Kane and Lubensky [29], where they also show that mechanical systems can realize topological insulators, see fig. 2.2. Mechanically speaking, an insulator forbids any floppy mode or self-stress state in the bulk, and it is said to be topological if they exist at the edges of the sample, as opposed to a trivial insulator in which no edge states are present. These two distinct phases - topological and trivial chiral insulator - are described in the literature by a topological invariant: the winding number w of the hamiltonian(2.3) [32]. This topological quantity is defined in terms of the equilibrium matrix in momentum space, $Q(\mathbf{k})$. It takes the value $w = 1$ when edge states are present, and $w = 0$ when absent. However, this invariant has been the subject of several controversies [33, 58, 59] which boils down to its gauge-dependent nature. As discussed in the next sections, the winding number is not a material property but rather a model-dependent quantity.

Prompted by the relevance of topological mechanical metamaterials [60] and the need for a robust and unique material characterization, in this chapter, we address two fundamental questions. The first one is how to define a physical characterization of mechanical insulators. The second is how to *locally* define this observable in order to characterize disordered configurations. To answer them we contextualize and summarize our paper titled "Geometry and Topology tango in chiral materials" [31] (reproduced in section 2.7) under the light of bead-and-spring networks.

2.2 An analogy with electrostatics

It is useful to think of chiral systems as an electrostatic collection of charges. As a matter of fact, the chiral operator basically assigns a +1 eigenvalue, or charge, to every degree of freedom and a -1 charge to every constraint (spring), fig. 2.1b. While the energetics

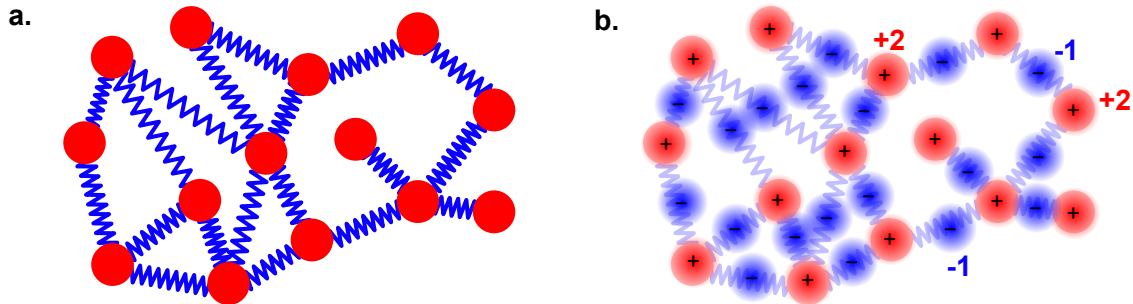


Figure 2.1: **Bead and springs are chiral systems** **a.** A collection of beads (red) connected by springs (blue) enjoy a sublattice or chiral symmetry. **b.** The chiral description of mechanics can be understood with an electrostatic analogy. Each bead possesses a positive chiral charge equal to its number of degrees of freedom, in this case, 2. Each spring has a negative chiral charge equal to the number of constraints it imposes, in this case, -1.

between real charges differ from chiral charges (no repulsion or attraction), this analogy serves as a basis to define suitable observables. For example, we can add up all the charges and compute the total chiral charge \mathcal{M} of a mechanical system:

$$\mathcal{M} = \text{Tr}[\mathbf{C}] = \text{Tr} \left[\begin{pmatrix} 1_{dN} & 0 \\ 0 & -1_{N_c} \end{pmatrix} \right] = dN - N_c, \quad (2.5)$$

with d being the dimension of the system, N the number of beads, and N_c the number of constraints (springs). Since the trace is basis-independent, a straightforward calculation in the eigenbasis of \mathcal{H} , reveals that \mathcal{M} is also a counting of zero-energy modes:

$$\begin{aligned} \mathcal{M} = \text{Tr}[\mathbf{C}] &= \sum_{E,m} \langle \Psi_{E,m} | \mathbf{C} | \Psi_{E,m} \rangle \\ &= \sum_m \langle \Psi_{0,m} | \mathbf{C} | \Psi_{0,m} \rangle \\ &= \#\text{FM} - \#\text{SSS}, \end{aligned} \quad (2.6)$$

with $\#\text{FM}$ and $\#\text{SSS}$ the number of floppy modes and self-stress states of the system, respectively. The total chiral charge is thus a rederivation of the Maxwell-Calladine counting rule presented in the introduction 1:

$$\mathcal{M} = dN - N_c = \#\text{FM} - \#\text{SSS}. \quad (2.7)$$

This constitutes our first example relating a lattice property, the number of beads and springs, to a spectral quantity, the number of zero-energy modes. This simple yet important derivation reveals the adequacy of chirality to understand mechanical systems. As we will now see, this framework is also effective in describing insulators.

2.3 A new material property: the chiral polarization

In electrostatics, a bulk dielectric is characterized by a zero total charge and the next order description falls into the polarization, describing the spatial distribution of charges.

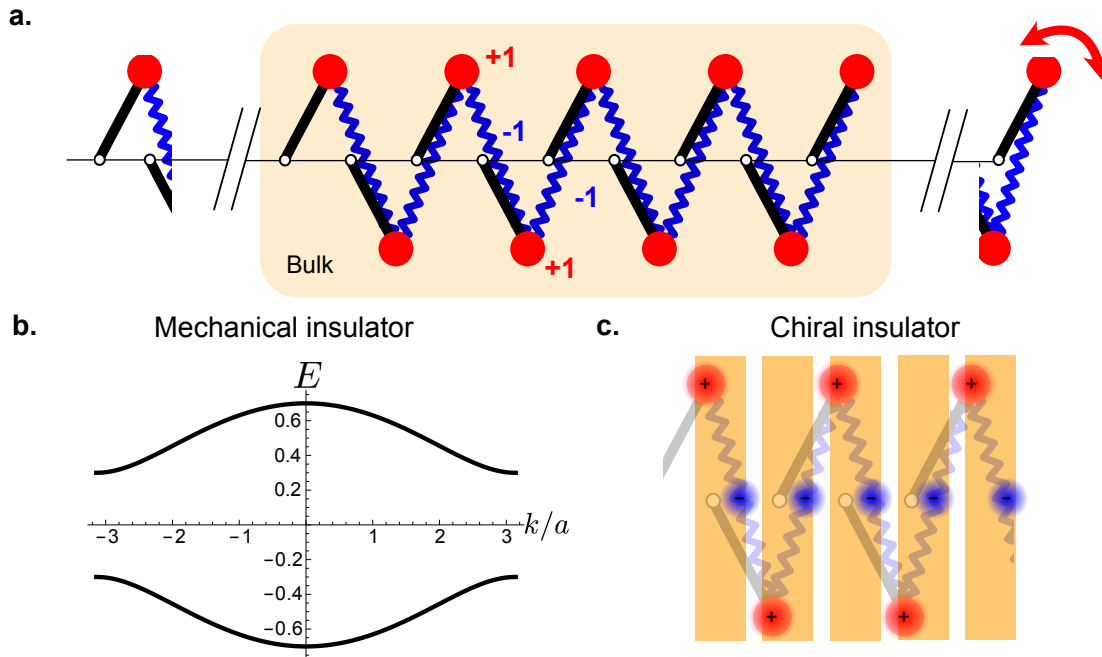


Figure 2.2: **One-dimensional mechanical insulator a.** A finite 1D chain of rotors and springs has a null chiral charge, $\mathcal{M} = 0$: Each rotor contributes $+1$ charge (one degree of freedom) whereas each spring, -1 (one constraint). As a consequence, there is one floppy mode, which is localized at the right edge of the sample. **b.** The dispersion relation obtained from the bulk of the material displays a gap: No zero-energy modes are allowed; the system is a mechanical insulator. **c.** From the chiral point of view, the bulk is also an insulator. This is easily seen when splitting the bulk into unit cells, each one containing one rotor and one spring. The chiral charge of each unit cell, and therefore of the bulk, is zero.

A mechanical insulator is defined as a system with a spectral gap, see fig. 2.2a,b. As a consequence, it has no zero-energy mode and by definition, a null chiral charge, fig. 2.2c. To characterize it, we introduce the chiral polarization. It corresponds to the weighted positions of beads and springs by the respective displacements and stresses in a chiral system,

$$\mathbf{\Pi} = 2\text{Tr}[\mathcal{C}\hat{\mathbf{x}}\mathbb{P}_{E<0}], \quad (2.8)$$

with $\hat{\mathbf{x}}$ the position operator, and $\mathbb{P}_{E<0}$ the spectral projector, which excludes any zero-energy mode. Notice that we could have taken the positive projector to define $\mathbf{\Pi}$ by virtue of the chiral symmetry.

The expression in eq. (2.8) can be greatly simplified when working with regular structures such as the mechanical chain introduced by Kane and Lubensky [29], see fig. 2.3a. It consists of a mechanical insulator in the bulk that hosts a localized floppy mode on one of the edges. It turns out that this realizes a topological insulator which, as we will see, has a topological invariant in its description.

The regularity of the insulating bulk allows us to define unit cells (of null chiral charge), fig. 2.3b, and to describe the system in terms of delocalized waves (Bloch waves) characterized by a quasi-momentum \mathbf{k} . We can then express \mathcal{H} , defined in eq. (2.3), in

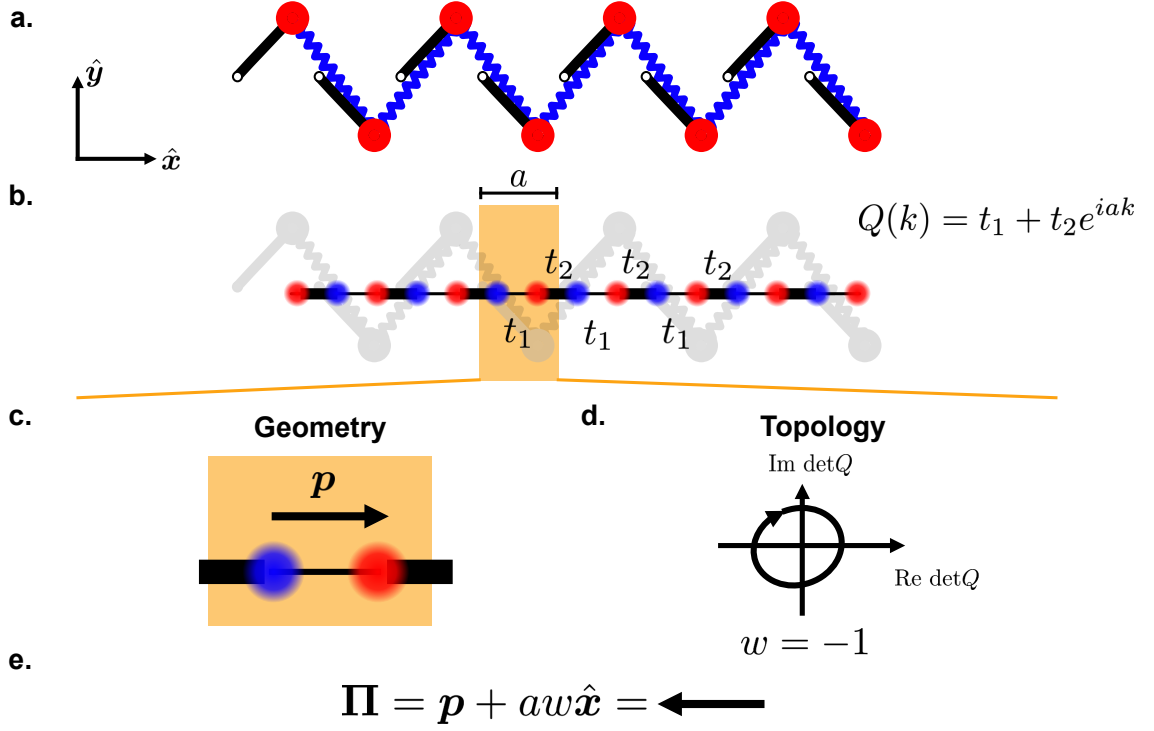


Figure 2.3: **The chiral polarization in the mechanical chain.** **a.** A periodic collection of rotors connected by spring are represented as a 1D chain of chiral charges **b.**. These charges have alternating interactions given by v and w . Employing unit cells of size a , we can write the equilibrium matrix in momentum space as $Q(k) = v + we^{iak}$. From the one-dimensional chiral chain we can extract two properties: the geometrical polarization **c** being a purely geometric property of the lattice and the unit cell, and the winding number **d**, counting the number of times $\det Q$ winds around the origin. **e** The sum of the geometry and topology results in the chiral polarization.

momentum space as a Bloch hamiltonian,

$$H(\mathbf{k}) = \begin{pmatrix} 0 & Q(\mathbf{k}) \\ Q^\dagger(\mathbf{k}) & 0 \end{pmatrix}. \quad (2.9)$$

Using this momentum representation, we can expand the trace of eq. (2.8) in the Bloch basis to elucidate the two main components of the chiral polarization. Leaving all the technical details to the article 2.7 and the supplementary information 2.8.2, we find that the chiral polarization is the sum of two terms,

$$\mathbf{\Pi} = \mathbf{p} + \Delta\gamma. \quad (2.10)$$

The first term, \mathbf{p} dubbed geometrical polarization, is the polarization of the unit cell taking into account only the chiral charges inside of it – it is the vector connecting the negative to the positive charge centers of mass. It is thus a lattice property, independent of any energetics, see fig. 2.3c. The second term, $\Delta\gamma$ is known in the literature as a geometric phase, from which the best-known example is the Berry phase [61]. Using the non-abelian Wilson loop formalism [62, 63] we link this geometrical phase to the topological invariant

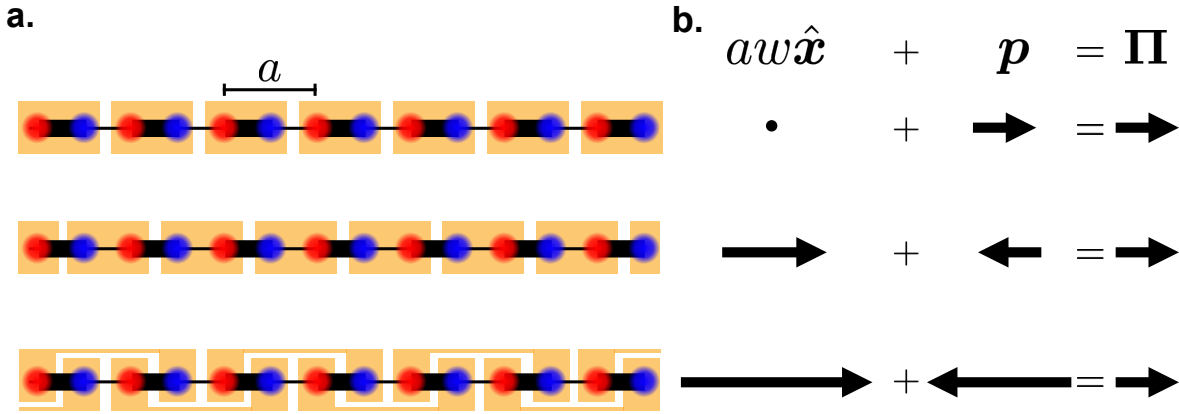


Figure 2.4: **Ambiguity of the unit cell.** **a.** Three different unit cells describe the same physical system. The first two correspond to the two possible Wigner-Seitz cells and the last one is a disjoint unit cell. Each choice, while equally valid, corresponds to different winding numbers **c** and geometrical polarizations **d**. The sum of both, the chiral polarization, is independent of the unit cell choice **e**.

describing chiral symmetric systems, the winding number of the Bloch hamiltonian [31], which in 1D reads:

$$w = \frac{1}{2\pi i} \int_{\mathcal{C}} dk \text{Tr} [\mathcal{Q}^{-1} \partial_k \mathcal{Q}]. \quad (2.11)$$

It takes integer values corresponding to the number of times the determinant of the equilibrium matrix, $\det Q(k)$, winds around the origin when traversing the momentum space, see fig. 2.3d.

We arrived then to our first major result. The chiral polarization, contrasting the spatial distribution of displacements and stresses, is thus the sum of geometry and topology:

$$\mathbf{\Pi} = \mathbf{p} + a\mathbf{w}, \quad (2.12)$$

with a being the unit-cell length.

As seen in fig. 2.3e, the chiral polarization is a non-zero vector pointing away from the localized floppy mode of the system. In the article "Geometry and topology tango in ordered and amorphous chiral matter" [31] (enclosed at the end of this chapter), we discuss in detail the relation between the geometrical polarization and the winding number in all quantum and classical chiral insulators. In short, neither of these two quantities are physical observables; none of them is gauge independent. Their very definition depends on the choice of unit cell used to describe the insulating bulk. It is the sum of the two, the chiral polarization, the material property, univocally defined as shown in fig. 2.4. But before discussing how to measure this material property, the next chapter's topic, we will generalize this definition beyond crystalline materials.

2.4 Beyond crystals

At first, it may seem that the chiral polarization, characterizing chiral topological insulators, depends on a discrete translational invariance. After all, the winding number and

the geometrical polarization that enter the relation (2.12) were defined upon a unit cell. In general, topological invariants enjoy concise expressions in momentum space [64], see eq (2.11). However, chiral insulators and their localized zero-energy states persist beyond the crystalline picture, as illustrated in fig. 2.5. Then how do we characterize a chiral material in the absence of unit cells? The total chiral polarization defined in eq. (2.8) is an average quantity; it disregards the spatial heterogeneities of the chiral charge distribution. To gain some understanding of spatial heterogeneities, we introduce the chiral polarization field.

Defining this field is not as straightforward as in dielectrics. In the latter, we have the notion of a molecule setting a length scale over which we compute the polarization. Importantly, this length scale is much smaller than the distance between molecules. As seen in fig. 2.5, in heterogeneous networks there is no length scale separation and therefore no clear notion of a molecule grouping different chiral charges. However, if such an object exists, it must take into account the spectral projector $\mathbb{P}_{E<0}$ present in the original definition (2.8).

The solution to this challenge is given by the projected position operator $\mathbb{P}_{E<0}\hat{\mathbf{x}}\mathbb{P}_{E<0}$ [65, 66]. Its eigenstates, $\{W_i\}$, known as Wannier functions in 1D, are localized due to the position operator and are distributed over the beads and springs connected by the strongest interactions due to the spectral projector. They provide our notion of molecules in mechanical systems. For each of these functions we can uniquely determine their centers and their polarizations:

$$\bar{\mathbf{x}}_i = \langle W_i | \hat{\mathbf{x}} | W_i \rangle, \quad (2.13)$$

$$\mathbf{\Pi}_i = 2 \langle W_i | \mathbf{C} \hat{\mathbf{x}} | W_i \rangle, \quad (2.14)$$

from which we define the chiral polarization field $\mathbf{\Pi}(\bar{\mathbf{x}}_i)$, illustrated in fig. 2.5e,f, able to distinguish distinct topological phases in both ordered and heterogenous systems.

It is noteworthy that in higher dimensions the different components of the projected position operator do not commute, $[\mathbb{P}_{E<0}\hat{x}_i\mathbb{P}_{E<0}, \mathbb{P}_{E<0}\hat{x}_j\mathbb{P}_{E<0}] \neq 0$ for $i \neq j$. Here we have to employ a more sophisticated technique to obtain the localized functions $\{W_i\}$. The most accepted method corresponds to finding the proper basis of $\mathbb{P}_{E<0}$ through a minimization scheme [65, 67]: starting from a basis $\{\tilde{W}_i\}$ spanning the negative energy space, we compute the gradient of the localization functional $\Omega[\{\tilde{W}_i\}]$ given by

$$\Omega[\{\tilde{W}_i\}] = \frac{1}{N} \sum_n^N \left[\langle \tilde{W}_n | \hat{\mathbf{x}}^2 | \tilde{W}_n \rangle - |\langle \tilde{W}_n | \hat{\mathbf{x}} | \tilde{W}_n \rangle|^2 \right], \quad (2.15)$$

and we update the new basis with a gradient descent protocol. In the supplementary information 2.8.5 we show an alternative method based on the diagonalization of a new projected operator. In short, we define the matrix pencil of the projected position operator as $M(\lambda_1, \lambda_2, \lambda_3) = \sum_i \lambda_i \mathbb{P}_{E<0} \hat{x}_i \mathbb{P}_{E<0}$, with $\lambda_i \in \mathbb{R}$. Depending on the parameters λ_i the eigenstates of M can be as localized as the basis $\{W_i\}$ obtained by minimizing (2.15), at a much reduced computational cost.

2.5 Detecting zero-energy modes

Not only does the chiral polarization describe distinct topological phases but also helps determine the accumulation of localized zero-energy modes, as illustrated in fig. 2.5f.

Indeed, sources of chiral polarization are a signature of floppy modes whereas sinks are linked to self-stress states. In crystalline structures, we materialize this observation in a revised bulk-boundary correspondence [31]. As shown in the article 4.7, taking the example of fig. 2.5a, the number of zero-energy modes in the boundary \mathcal{B} is given by

$$(\#FM - \#SSS)^{\mathcal{B}} = \mathcal{M}^{\mathcal{B}} + a(w_{\text{left}} - w_{\text{right}}), \quad (2.16)$$

with $\mathcal{M}^{\mathcal{B}}$ being the total chiral charge of the boundary, and $w_{\text{left/right}}$ the winding number of the left/right insulating material.

Just as in the Maxwell-Calladine relation (2.7), the zero-energy content of eq. (2.16) depends on a lattice property, $\mathcal{M}^{\mathcal{B}}$, which must now be complemented with a spectral quantity, w .

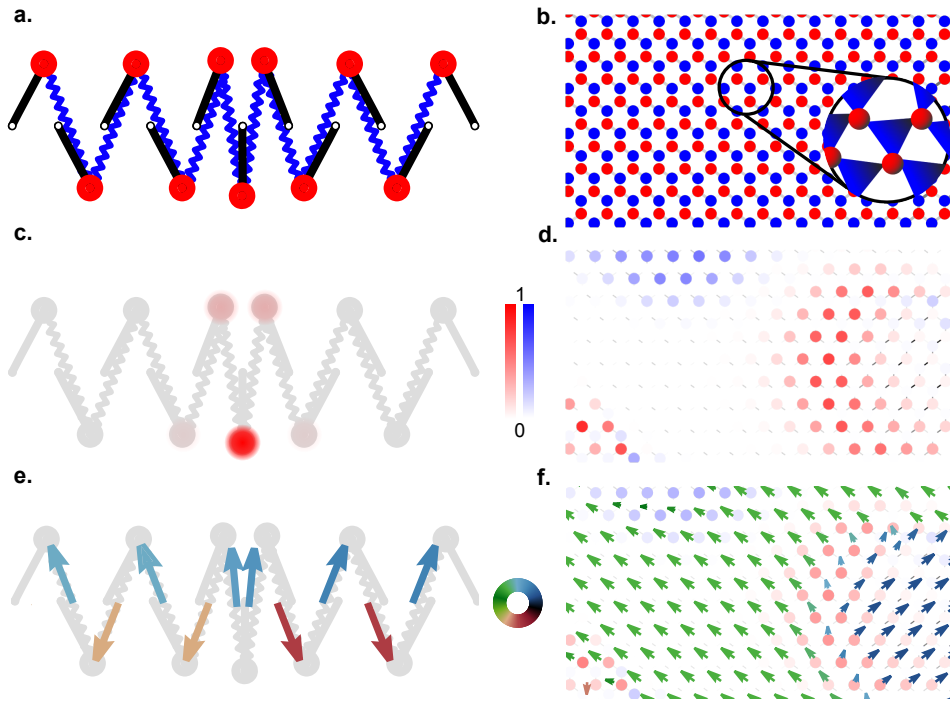


Figure 2.5: **Heterogenous chiral insulators.** Two instances of broken translational symmetry: a domain wall in a 1D mechanical chain **a** and a distorted mechanical honeycomb lattice of spheres connected by triangular plaquettes **b**. **c**, **d**. Heterogeneous insulators may exhibit zero-energy modes, in the form of floppy (red) and self-stress states (blue). The colors indicate the normalized weight of the zero-energy modes. **e**, **f**. The chiral polarization field is a local quantity encoding the weighted position of displacements and stresses. Discontinuities of this field are related to the proliferation of zero-energy modes: sources of chiral polarization correspond to floppy modes, while sinks to self-stress states. Colors indicate the local orientation of the field.

2.6 Conclusion

We have seen that a physical and local characterization of mechanical systems is achieved by the chiral polarization field: a material property describing the softness of a material. This observable encodes both the topology of the energy bands and the geometry of the subjacent lattice. In crystals, both contributions are clearly separable upon a unit cell choice. In disordered materials, they are indivisible. In both cases, the chiral polarization field carries the imprint of the very low energy modes, allowing their detection through discontinuities in the field.

In the next two sections, I replicate the article "Geometry and topology tango in ordered and amorphous chiral matter", laying out the detailed theory and the properties of this new observable, and building, step-by-step, a general description of any chiral insulator, classical or quantum.

In the next chapter, we go beyond the theoretical models and explain how to actually measure the chiral polarization in a physical setup, rendering it a useful tool to probe mechanical metamaterials.

2.7 Article

Geometry and Topology Tango in Ordered and Amorphous Chiral Matter

M. Guzmán^{*}, D. Bartolo, D. Carpentier

ENS de Lyon, CNRS, Laboratoire de Physique, Lyon, France

Abstract

Systems as diverse as mechanical structures and photonic metamaterials enjoy a common geometrical feature: a sublattice or chiral symmetry first introduced to characterize electronic insulators. We show how a real-space observable, the chiral polarization, distinguishes chiral insulators from one another and resolve long-standing ambiguities in the very concept of their bulk-boundary correspondence. We use it to lay out generic geometrical rules to engineer topologically distinct phases, and design zero-energy topological boundary modes in both crystalline and amorphous metamaterials.

2.7.1 Introduction

A century after the foundations of band theory in solids by Félix Bloch [68], physicists have discovered new states of electronic matter ranging from insulators to superconductors by exploiting the topological structure of Bloch theory [20, 69–73]. This topological revolution has built on two cornerstones: an abstract classification based on symmetries [32, 74–80], and the practical correspondence between bulk topology and the boundary states measurable in experiments [20, 69–72, 81–84]. During the past decade, these two generic principles spanned fields as diverse as photonics, acoustics, or mechanics, leading to design principles and practical realizations of maximally robust waveguides [26, 85].

Among the number of symmetries constraining wave topology, chiral symmetry has a special status. Out of the three fundamental symmetries of the overarching ten-fold classification [32, 74, 75], it is the only one naturally realized with both quantum and classical waves. It generically takes the form of a sub-lattice symmetry when waves propagate in frames composed of two connected lattices A and B , with couplings only between, A and B sites, see e.g. Fig. 2.6a. In electronic systems, the archetypal example of a chiral insulator is provided by the polyacetylene molecule described by the Su-Schrieffer-Hegger (SSH) model [38]. In mechanics, the Hamiltonian description of bead-and-spring networks is intrinsically chiral [29, 47, 86, 87]: the A sites correspond to the beads, and the B sites to the springs. In topological photonics and cold atoms chiral wave guides are among the simplest realizations of topological phases. Over the past decade, the modern theory of electronic polarization based on Zak phases and non-Abelian Wilson loops [62, 63, 88, 89] has illuminated the intimate relation between crystalline symmetries and the topology of band structures [76–80]. By contrast, the role of chiral symmetry has been overlooked.

In this article, by introducing the concept of chiral polarization we determine the zero-mode content of interfaces between topologically incompatible crystalline and amorphous chiral meta(materials)

In the bulk, the chiral charge, which measures the imbalance between the number of sites on the sub-frames A and B , predicts the number of zero-energy modes of all Hamiltonians defined on a given chiral frame. To characterize chiral insulators we define their chiral polarization $\mathbf{\Pi}$ as the spatial imbalance of the bulk waves on the two sub-frames. This material property does not rely on any crystalline symmetry and can therefore be defined locally on disordered and amorphous frames. In crystals, although akin to the time-reversal polarization of \mathbb{Z}_2 insulators [90], we show that $\mathbf{\Pi}$ is not merely set by the Bloch-Hamiltonian topology but also by the underlying frame geometry. At boundaries, we show how $\mathbf{\Pi}$ prescribes the surface chiral charge, and therefore the full zero-energy edge content of crystalline and amorphous chiral matter. Finally, we propose a series of practical protocols to experimentally measure the chiral polarization of mechanical, and photonic chiral metamaterials.

2.7.2 From chiral charge to chiral polarization and Zak phases

Introducing the concepts of chiral charge and polarization, we demonstrate that bulk properties of chiral matter are determined by an interplay between the frame topology, the frame geometry and the chiral Zak phases of Bloch Hamiltonians.

Chiral charge and chiral polarization.

We consider the propagation of waves in chiral material associated to d -dimensional frames including two sub-frames A and B . The wave dynamics is defined by a Hamiltonian \mathcal{H} . By definition, the chiral symmetry translates in the anti-commutation of \mathcal{H} with the chiral unitary operator $\mathbb{C} = \mathbb{P}^A - \mathbb{P}^B$, where \mathbb{P}^A and \mathbb{P}^B are the two orthogonal projectors on the sub-frames A and B . Simply put, in the chiral basis where \mathbb{C} is diagonal, \mathcal{H} is block off-diagonal.

In order to determine the relative weight of the wave functions of \mathcal{H} on the two sub-frames, we introduce the chiral charge

$$\mathcal{M} = \langle \mathbb{C} \rangle, \quad (2.17)$$

where the average is taken over the complete Hilbert space. Using the basis of fully localized states, we readily find that \mathcal{M} is fully prescribed by the frame topology: the chiral charge counts the imbalance between the number of A and B sites: $\mathcal{M} = N^A - N^B$. We can however also evaluate Eq. (2.17) in the eigenbasis of \mathcal{H} . Indexing by n the eigenenergies of \mathcal{H} , the eigenstates of the chiral Hamiltonian come by pairs of opposite energies related by $|-n\rangle = \mathbb{C} |n\rangle$. Chirality therefore implies that the chiral charge is solely determined by the zero modes of \mathcal{H} as $\mathcal{M} = \sum_n \langle n | \mathbb{C} | n \rangle = \langle 0 | \mathbb{C} | 0 \rangle$. Noting that the $|0\rangle$ states are eigenstates of the chiral operator with eigenvalue $+1$ when localized on the A sites and -1 when localized on the B sites, it follows that \mathcal{M} also is an algebraic count the zero modes of \mathcal{H} :

$$\mathcal{M} = N^A - N^B = \nu^A - \nu^B. \quad (2.18)$$

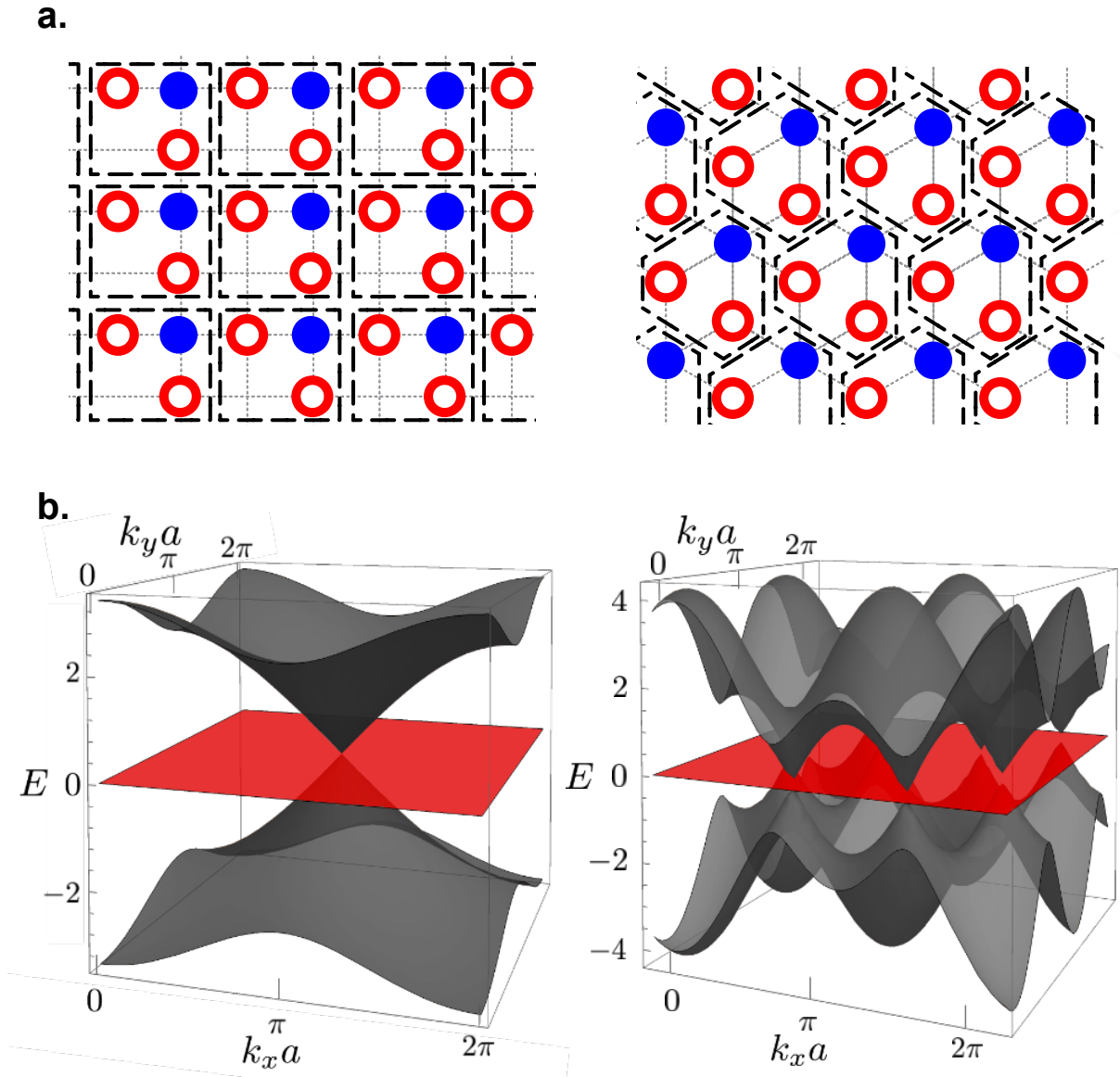


Figure 2.6: **Lattices with a finite chiral charge.** **a.** The Lieb (left) and dice (right) frames are both characterized by an imbalance between the number N^A and N^B of sites. In both cases the chiral charge per unit cell equals 1. Any Hamiltonian defined on these frames possesses a flat energy band. **b.** Illustration of two band spectra associated to chiral Hamiltonians defined on the Lieb (left) and dice (right) frames. The two band spectra are computed for tight-binding Hamiltonians with nearest neighbour coupling and a hopping parameter set to 1, see e.g. [91].

This equality is the classical result established by Maxwell and Calladine in the context of structural mechanics [27, 28] and independently discussed by Sutherland in the context of electron localization [92]. Eq. (2.18) implies that the spectral properties of \mathcal{H} are constrained by the frame topology. In particular, frames with a non-vanishing chiral charge impose *all* chiral Hamiltonian to possess flat bands. This simple prediction is illustrated in Fig. 2.6 where we show the Lieb and the dice lattices, which are both characterized by

a unit chiral charge per unit cell. All Hamiltonians defined on these lattices are therefore bound to support at least one flat band, Fig. 2.6b. No chiral insulators exist on the Lieb and dice lattices.

By contrast, in chiral insulators, no zero-energy bulk modes exist and \mathcal{M} must vanish. To probe the relative weight of the wave functions on the two sub-frames, we therefore introduce the chiral polarization vector $\Pi_j = \langle \mathbb{C}x_j \rangle_{E \neq 0}$. As the $|\pm n\rangle$ states contribute equally to Π in chiral systems, we henceforth use the definition

$$\Pi_j = 2\langle \mathbb{C}x_j \rangle_{E < 0}, \quad (2.19)$$

with $j = 1, \dots, d$ are the indices of the d crystallographic directions and where $E < 0$ indicates that the average is taken over the occupied states. This definition differs from the skew polarization introduced in [93,94] for topological insulators, and the mean chiral displacement of quantum walks [95]. Π_j does not rely on any Bloch representation and is therefore defined also in amorphous phases. We stress that, even in the crystalline case, Π_j includes geometrical content absent from the skew polarization, as it resolves the weighted positions with a sub-unit-cell resolution. This difference is simply explained by considering the mean chiral displacement (MCD) defined on a 1D lattice given a definition of a unit cell. It is defined per wavepacket ψ as $\text{MCD} = \langle \psi | \mathbb{C}x_{\text{UC}} | \psi \rangle$, with x_{UC} being the position operator at the scale of the unit cell. x_{UC} defines the positions as integer multiples of the length a of the unit cell. In contrast, equation (2.19) depends on the actual position of the sites: $x = x_{\text{UC}} + \delta x$, where δx is a sublattice correction to the unit-cell position. These differences are not mere technicalities, and will prove crucial in the next sections.

To gain more physical insight, it may be worth noting that in electronic systems, Π_j corresponds to the algebraic distance between the charge centers associated to the A and B atoms. While in mechanical networks, Π_j is the vector connecting the stress-weighted and displacement-weighted positions. A vanishing polarization indicates that the average locations of the stress and displacement coincide. Conversely, a finite chiral polarization reveals an asymmetric mechanical response discussed in [96,97]. For the sake of clarity, before revealing topologically protected zero modes in amorphous phases, we first explore the consequences of a finite chiral polarization in periodic systems such as in the paradigmatic example of the SSH model illustrated Fig. 2.7.

Chiral polarization: an interplay between Zak phases and frame geometry.

We begin with a thorough discussion of crystalline materials, defined by periodic frames and Bloch Hamiltonians. Building on previous works on the electronic polarization [62,63,88,89], we relate the chiral polarization of a crystalline material to the two Zak phases of waves projected on sub-lattices A and B when transported across the Brillouin zone. To do so, we first choose a unit cell and consider the basis of Bloch states $|\mathbf{k}, \alpha\rangle = \sum_{\mathbf{R}} e^{i\mathbf{k} \cdot \mathbf{R}} |\mathbf{R} + \mathbf{r}_\alpha\rangle$, where \mathbf{R} is a Bravais lattice vector, α labels the atoms in the unit cell and \mathbf{k} is the momentum in the Brillouin Zone (BZ). We henceforth use a convention where the Bloch Hamiltonian $H(\mathbf{k})$ is periodic in the BZ, see [88,98] and Appendix 2.8.1. More quantitatively, considering first Hamiltonians with no band crossing¹, we define the

¹In the situation where bands cross, our results should be generalized resorting to the Wilson loops of the non-commutative Berry connexion instead of the abelian Zak phase connection [99].

A sub-lattice Zak phase of the n^{th} energy band along the crystallographic direction j as

$$\gamma_j^A(n) = i \int_{\mathcal{C}_j} d\mathbf{k} \langle u_n | \mathbb{P}^A \partial_{\mathbf{k}} \mathbb{P}^A | u_n \rangle, \quad (2.20)$$

where the $|u_n(\mathbf{k})\rangle$ are the eigenstates of $H(\mathbf{k})$, and \mathcal{C}_j the non-contractible loops over the Brillouin zone defined along the d crystallographic axes. $\gamma_j^B(n)$ is defined analogously on the B sublattice. The (intercellular) Zak phase is given by the sum of $\gamma_j^A(n)$ and $\gamma_j^B(n)$ [33]. In Appendix 2.8.2, we show how to decompose the chiral polarization into a spectral and a frame contribution:

$$\Pi_j = \frac{a}{\pi} (\gamma_j^A - \gamma_j^B) + p_j, \quad (2.21)$$

where a is the lattice spacing (assumed identical in all directions), γ_j^A and γ_j^B are the sublattice Zak phases defined by

$$\gamma_j^A = \sum_{n < 0} \gamma_j^A(n). \quad (2.22)$$

In Eq. (2.21) the p_j are the components of the geometrical-polarization vector connecting the centers of mass of the A and B sites in the unit-cell:

$$\mathbf{p} = \sum_{\alpha \in A} \mathbf{r}_\alpha - \sum_{\alpha \in B} \mathbf{r}_\alpha. \quad (2.23)$$

In crystals, Eqs. 2.21 quantifies the difference between the polarity of the ground-state wave function Π and the geometric polarization of the frame \mathbf{p} . This difference is finite only when the two sublattice Zak phases differ.

2.7.3 Topology of chiral insulators

We now elucidate the relation between the chiral polarization and the band topology of chiral gapped phases defined on periodic lattices. We outline the demonstrations of our central results below and detail them in Appendix 2.8.2.

Sublattice Zak phases and winding numbers.

Computing the Wilson loop of the non-Abelian connection $\mathbf{A}_{n,m}(\mathbf{k}) = \langle u_n(\mathbf{k}) | \partial_{\mathbf{k}} | u_m(\mathbf{k}) \rangle$ along \mathcal{C}_j , we show that chirality relates the d Zak phases $\gamma_j^A + \gamma_j^B$ to the windings of the Bloch Hamiltonian as

$$\gamma_j^A + \gamma_j^B = \pi w_j + 2\pi\mathbb{Z}, \quad (2.24)$$

where $w_j = i/(4\pi) \int_{\mathcal{C}_j} d\mathbf{k} \cdot \text{Tr}[\partial_{\mathbf{k}} H C H^{-1}] \in \mathbb{Z}$. The total Zak phase is quantized but the arbitrary choice of the origin of space implies that both γ^A and γ^B are only defined up to an integer. As a matter of fact, a mere $U(1)$ gauge transformation $|u_n\rangle \rightarrow e^{i\alpha_n(\mathbf{k})} |u_n\rangle$ arbitrarily modifies $\gamma_j^A(n)$ and $\gamma_j^B(n)$ by the same quantized value: $\gamma_j^A(n) \rightarrow \gamma_j^A(n) + \pi m$, $\gamma_j^B(n) \rightarrow \gamma_j^B(n) + \pi m$, with $m \in \mathbb{Z}$. By contrast, the difference between the two sublattice Zak phases is left unchanged by the same gauge transformation which echoes

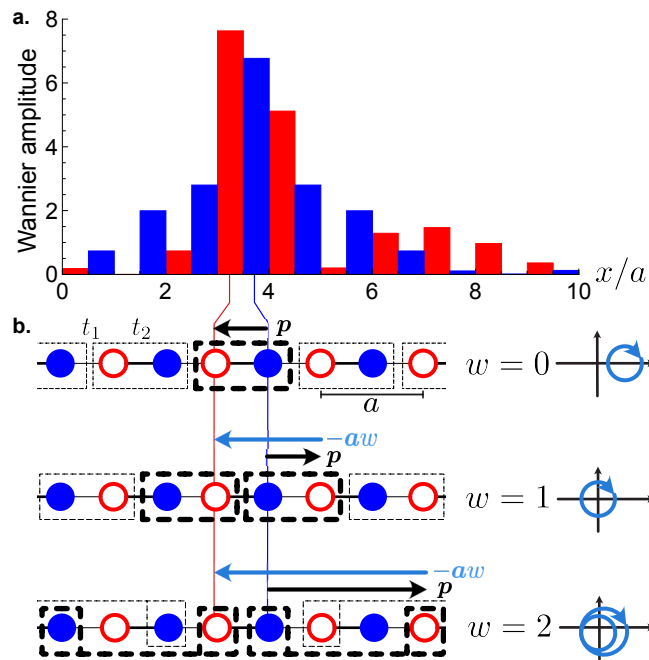


Figure 2.7: **Chiral polarization and Wannier functions.** **a.** Square of the Wannier amplitude projected into the A (red) and B (blue) sublattices for the ground state configuration of the two-band SSH model with hopping ratio $t_1/t_2 = 0.79$. a denotes the period of the 1D frame. The chiral polarization $\Pi = \langle x^A \rangle - \langle x^B \rangle$ is negative: the chain is left polarized regardless of the choice of unit cell. **b.** The winding number of the Bloch Hamiltonian encodes the chiral polarization *relative* to a given unit cell. The chiral polarization being a material property, the winding number w can therefore take any integer value when redefining the geometry of the unit cell as illustrated in the last column. Whatever the choice of the unit cell, the difference between the geometrical polarization and aw has a constant value given by the chiral polarization Π .

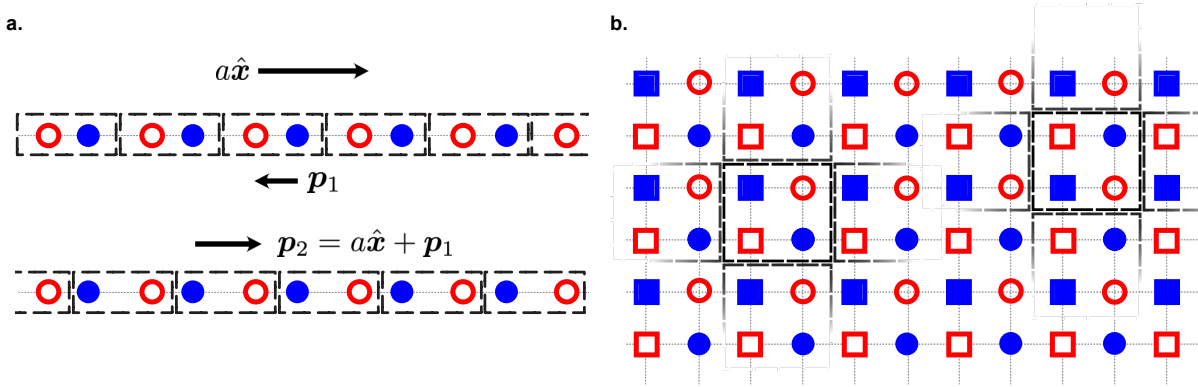


Figure 2.8: **Inferring the band topology from frame geometry.** **a.** The two-sites Wigner-Seitz cell on a 1D chiral frame have different geometrical polarizations; their difference is given by one Bravais vector. Consequently, we can always define the unit cell so that the Bloch Hamiltonian has a finite winding. **b.** All the Wigner-Seitz unit cells on the checkerboard lattice share the same (vanishing) chiral polarization. Therefore a single winding number w characterizes the Hamiltonians on this frame in virtue of Eq. (2.27). Evaluating the winding using the Wigner-Seitz cell compatible with the atomic limit of \mathcal{H} yields $w = 0$, by definition.

its independence from the space origin. Evaluating the winding of $H(\mathbf{k})$ using the Bloch eigenstates (see Appendix 2.8.1), we readily establish the essential relation²

$$\gamma_j^B - \gamma_j^A = \pi w_j \in \pi\mathbb{Z}. \quad (2.25)$$

Chirality quantizes the sublattice Zak phases of chiral insulators, even in the absence of inversion or any other specific crystal symmetry. γ_j^A and γ_j^B are however not independent. Combining Eqs. (2.24) and (2.25) we can always define the origin of space so that $\gamma_j^A = 0$ and $\gamma_j^B = \pi w_j$.

The d winding numbers of Eq. (2.25) characterize the topology of $H(\mathbf{k})$. In particular, if for a given Wigner-Seitz cell the corresponding $H(\mathbf{k})$ is associated to a finite winding ($w_j \neq 0$), then it cannot be smoothly deformed into the atomic limit defined over the same unit cell. We recall that the atomic limit of a material corresponds to a smooth deformation of the couplings to separate the energy scales so that the Wannier functions are exponentially localized, and respect the symmetries of the crystal [101]. In practice, it consists in choosing a unit cell including the strongest couplings.

The set of winding numbers is however poorly informative about the spatial distribution of the charges in electronic systems, or about the stress and displacement distributions in mechanical structures. The values of w_j are defined only up to the arbitrary choice of unit cell required to construct the Bloch theory. A well known example of this limitation is given by the SSH model, where the winding of $H_{\mathbf{k}}$ can either take the values 0 or ± 1 depending on whether the unit cell's leftmost site belongs to the A or B sublattice, see Fig. 2.7a and Appendix 2.8.2. We show in the next section, how the chiral polarization alleviates this limitation.

²Note that this difference of Zak phases was recently denoted as a chiral phase index in [100].

Disentangling Hamiltonian topology from frame geometry.

Equations (2.21) and (2.25) provide a clear geometrical interpretation of the winding number w_j as the quantized difference between the geometrical and the chiral polarization:

$$\Pi_j = (p_j - a_j w_j). \quad (2.26)$$

We can now use this relation to clarify the definition of a chiral topological insulator. The chiral polarization $\Pi_j = 2\langle \mathbb{C}x_j \rangle_{E<0}$ is a physical quantity that does not depend on the specifics of the Bloch representation. Therefore computing Π_j for two unit cells (1) and (2), we find that the windings of the two corresponding Bloch Hamiltonians $H^{(1)}(\mathbf{k})$ and $H^{(2)}(\mathbf{k})$ are related via Eq. (2.26) as

$$w_j^{(2)} - w_j^{(1)} = \frac{1}{a_j} (p_j^{(2)} - p_j^{(1)}). \quad (2.27)$$

This essential relation implies that one can always construct a Bloch representation of \mathcal{H} where $H(\mathbf{k})$ is topologically trivial, at the expense of a suitable choice of a unit cell. As a matter of fact, a redefinition of the unit cell can increase, or reduce the geometrical polarization, and therefore the winding numbers, by an arbitrary large multiple of a_j as illustrated in Fig. 2.7b.

For instance in the case of Hamiltonians with nearest neighbor couplings, applying Eq. (2.27) to Wigner Seitz unit cells ($|w_j| \leq 1$), we find that there exist as many topological classes of \mathcal{H} , as different geometrical polarizations in the Wigner-Seitz cells. This number provides a direct count of the chiral 'atomic limits' of \mathcal{H} .

Defining the topology of a chiral material therefore requires characterizing both the winding of its Bloch Hamiltonian, and the frame geometry. Remarkably, this interplay provides an insight on topological band properties from the sole inspection of the frame structure.

Inferring band topology from frame geometry.

There exists no trivial chiral phase in one dimension: one can always choose a Wigner-Seitz cell such that the Bloch representation of \mathcal{H} has a non-vanishing winding. As a matter of fact, the geometrical polarization of the Wigner-Seitz cells can only take two finite values of opposite sign depending on whether the leftmost site in a unit cell is of the A or B type, see Fig. 2.8a. Equation (2.27) therefore implies that, in $1D$, there always exists, at least, two topologically distinct gapped phases smoothly connected to two atomic limits. The two gapped phases are characterized by two distinct pairs of winding numbers defined by two inequivalent choices of unit cells. In other words all SSH Hamiltonians are topological.

Similarly, in $d > 1$ only frames having a geometrical polarization invariant upon redefinition of the Wigner-Seitz cell can support topologically trivial Hamiltonians. Equation (2.27) indeed implies that a topologically trivial Hamiltonian \mathcal{H} constrains the frame geometry to obey $p_j^{(1)} = p_j^{(2)}$ for all pairs of unit cells and in all directions j . We show a concrete example of such a frame in Fig. 2.8b.

Before discussing the crucial role of the frame topology and geometry on the bulk-boundary correspondence of chiral phases, we extend these two notions to chiral insulators

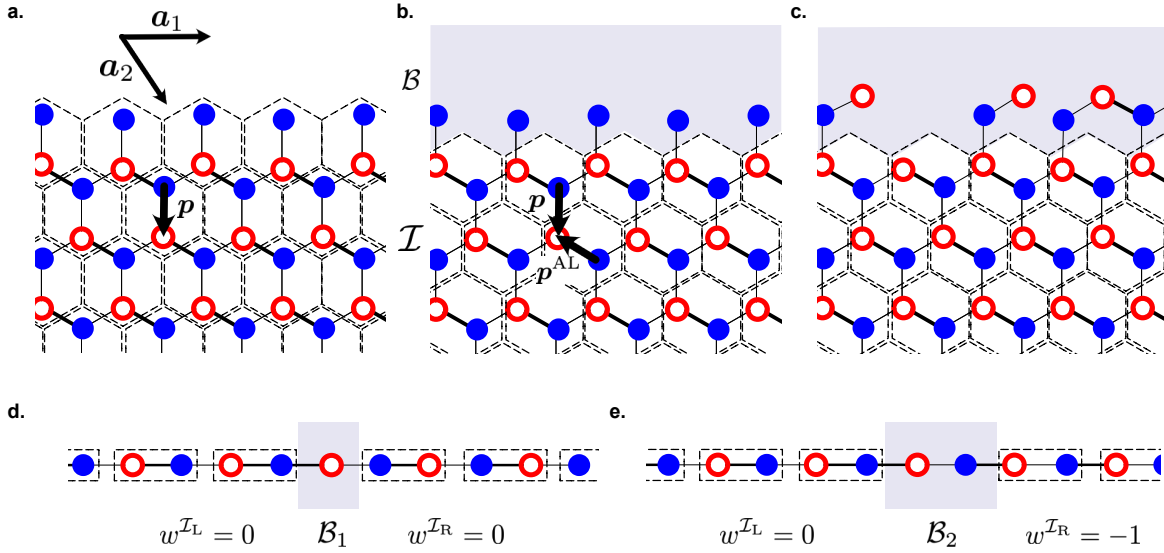


Figure 2.9: **Bulk-boundary correspondence.** **a.** A chiral crystal defined on a honeycomb frame is terminated by a clean zigzag edge incompatible with the atomic-limit Hamiltonian defined by keeping only the dominant couplings represented by thick solid lines. The dashed rectangles indicate the Wigner-Seitz cells allowing a tessellation compatible with the edge geometry. The arrow indicates the geometrical polarization \mathbf{p} . **b.** Same physical system. The crystalline bulk is now tiled using the unit cell compatible with the atomic limit. This requires a redefinition of the crystal boundary \mathcal{B} (shaded region). The arrows indicate the geometrical polarization of the new unit cell (\mathbf{p}^{AL}). The difference $\mathbf{p} - \mathbf{p}^{AL}$ is a Bravais lattice vector (\mathbf{a}_2). **c.** Same material as in (a.) and (b.) including a disordered interface \mathcal{B} bearing a non-zero chiral charge $\mathcal{M}^{\mathcal{B}}$. **d.** Two connected SSH chains. The Wigner-Seitz cell in the two materials are compatible with their atomic limits. The interface \mathcal{B}_1 separating the two materials is one-site wide. **e.** Redefining the Wigner-Seitz cell on the right hand side of the interface requires widening the boundary region. This redefinition makes the unit cell incompatible with the atomic limit. The winding of the Bloch Hamiltonian in \mathcal{I}_R takes a finite value and consequently modifies the zero-mode content of the boundary region.

with a flat band.

Chiral polarization in the presence of a net chiral charge.

It is worth noting that the chiral polarization can also be defined and computed in the presence of an additional zero-energy flat band in the gap. As detailed in the Appendix 2.8.3 section, it then takes the form

$$\Pi_j = (p_j - p_j^{\text{ZM}}) + a(\gamma_j^A - \gamma_j^B)/\pi. \quad (2.28)$$

In this case, we lose the clear decomposition Π into geometrical and topological contributions. The geometrical polarization is corrected by p^{ZM} which originates from a spectral contribution associated to the zero-energy band. Furthermore the second term on the r.h.s., the difference between two geometrical Zak phases, is not a topological winding number anymore. Despite the seemingly complex form of Eq. (2.28), we show in the next section that the chiral polarization remains an effective tool to relate spectral bulk properties to the number of zero-energy states localized at boundaries.

2.7.4 Bulk-boundary correspondence

We now establish a bulk-boundary correspondence relating the chiral polarization to the number of zero modes supported by the free surface of a chiral insulator. For the sake of clarity, we discuss the two-dimensional case without loss of generality. We consider first a crystalline insulator \mathcal{I} terminated by a clean edge $\partial\mathcal{I}$ oriented along a Bravais vector, say \mathbf{a}_1 as illustrated in Fig. 2.9a.

The bulk of the insulator can be described by different types of unit cells. As illustrated in Fig. 2.9a, in the presence of a clean edge, it is natural to choose a unit cell which allows a tessellation of the whole system. However, this unit cell is generically incompatible with the atomic limit of the Hamiltonian, and therefore does not allow a direct count of the zero energy boundary states using the simple Maxwell-Calladine count. An obvious strategy hence consists in redefining the unit cell, as in Fig. 2.9b to match the constraints of the atomic limit. This redefinition comes at the expense of leaving sites outside of the bulk tessellation. We define this ensemble of sites as the boundary region \mathcal{B} . Keeping in mind that we can smoothly deform the Hamiltonian into its atomic limit without closing the gap, we use Eq. (2.18) to count the number of zero energy states hosted by \mathcal{B} . It is given by $\mathcal{V} = \mathcal{M}^{\mathcal{B}}$. An essential geometrical observation is that the net chiral charge in \mathcal{B} can be expressed as $\mathcal{N}^{\partial\mathcal{I}}(p_2^{\text{AL}} - p_2)$, where $\mathcal{N}^{\partial\mathcal{I}}$ is the edge length expressed in number of unit cells and p_2 is the geometrical polarization of the initial unit cell. We can now make use of the invariance of the chiral polarization formalized by Eq. (2.27) to relate the geometrical count of zero modes to the winding of the Bloch Hamiltonian: $\mathcal{V} = \mathcal{N}^{\partial\mathcal{I}}(p_2^{\text{AL}} - p_2) = \mathcal{N}^{\partial\mathcal{I}} w_2^{\mathcal{I}}$. To arrive at a bulk boundary correspondence generic to all chiral insulators, we include the possibility of dealing with irregular interfaces featuring a net chiral charge $\mathcal{M}^{\mathcal{B}}$ as sketched in Fig. 2.9c. We then find

$$\mathcal{V} = \mathcal{M}^{\mathcal{B}} + \mathcal{N}^{\partial\mathcal{I}} w_2^{\mathcal{I}}. \quad (2.29)$$

Three comments are in order. Firstly, the bulk boundary correspondence defined by Eq. (2.29) reveals the geometrical implication of a nonzero winding: a finite $w_j^{\mathcal{I}}$ echoes

the impossibility to tile a periodic frame with unit cells compatible with the Hamiltonian's atomic limit. Secondly, Eq. (2.29) is readily generalized to interfaces separating two chiral insulators \mathcal{I}_L and \mathcal{I}_R , where we simply have to apply the same reasoning on each side of the interface: $\mathcal{V} = \mathcal{M}^B + \mathcal{N}^{\partial\mathcal{I}}(w^{\mathcal{I}_L} + w^{\mathcal{I}_R})$, see e.g. Figs. 2.9d and 2.9e. Thirdly, the formula given by Eq. (2.29) generalizes the Kane-Lubensky index introduced in their seminal work to count the zero-energy modes localized within isostatic mechanical networks [29]. We show that this index defines a bulk-boundary correspondence generic to all chiral insulators and even to flat band insulators such as hyperstatic lattices as further discussed in the Appendix 2.8.3.

2.7.5 Amorphous Chiral Insulators

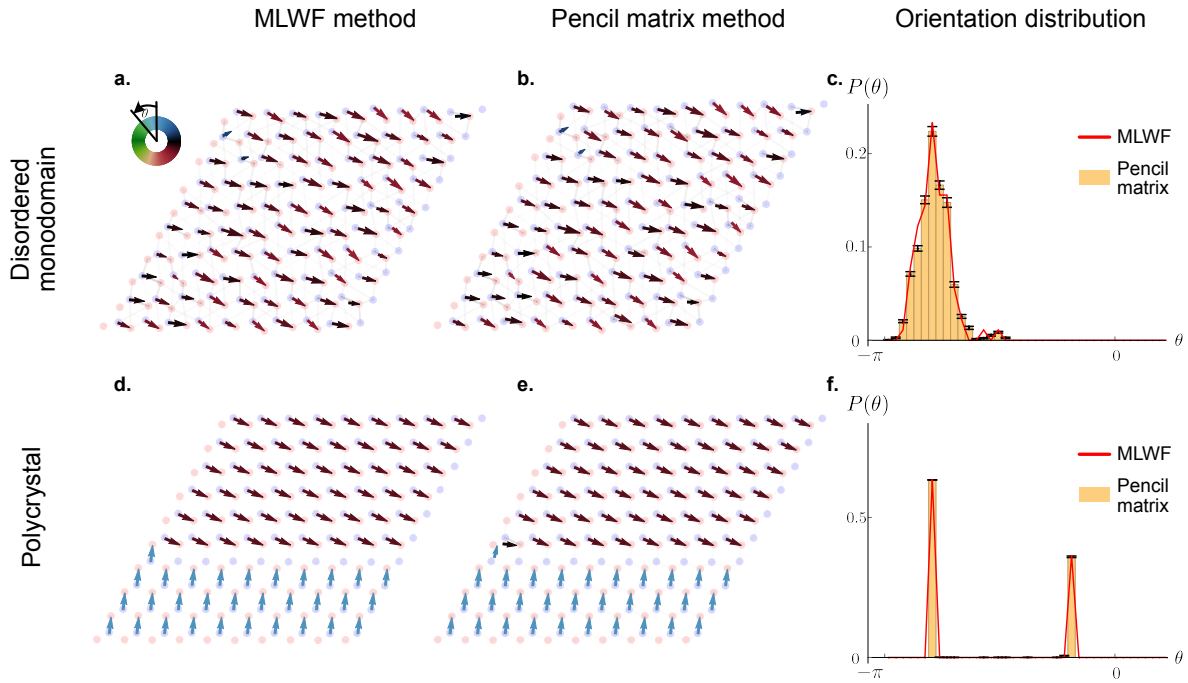


Figure 2.10: **Pencil matrix versus maximally localized Wannier functions** **a.** Single domain configuration with geometrical and spectral disorder. The chiral polarization field obtained from the maximally localized wannier functions is superposed. **b.** Chiral polarization field obtained from one realization of the pencil matrix procedure. **c.** Orientation distribution obtained from 50 values of α (bar chart), and from the maximally localized wannier functions (red solid line). **d.**, **e.**, **f.** correspond to the same information, this time for two crystalline domains.

In condensed matter, chiral symmetry is a low energy feature of electronic Hamiltonians, which is unlikely to survive to strong structural disorder. Conversely, in photonic, acoustic or mechanical metamaterials chirality is built in by design and can therefore be present both in ordered or amorphous structures [85, 102]. In mechanical metamaterials chirality is even more robust as it is inherent to any system assembled from elastically

coupled degrees of freedoms [26]. In this section, we show how to generalize our physical characterization of zero energy modes to disordered chiral metamaterials.

Over the past two years a number of experimental, numerical and theoretical works showed that crystalline symmetries are not required to define topological insulators, see e.g. [51, 103–105]. Unlike these pioneering studies where topologically inequivalent disordered phases are distinguished by abstract indices defined in real space and related to the quantification of edge currents, our framework solely based on the chiral polarization applies to chiral systems regardless of the presence or not of time reversal symmetry.

Our strategy follows from the fundamental relation: $\Pi_j = p_j - a_j w_j$ of Eq. (2.26). This relation implies a one-to-one correspondence between the chiral polarization and a topological spectral property quantized by the winding vector. The basic idea hence consists in probing the existence of topologically protected zero modes by *local* discontinuities in the chiral polarization field, even when no winding number or Zak phase can be defined. Relating topologically protected excitations to real-space singularities requires defining a local chiral polarization field $\mathbf{\Pi}(\mathbf{x})$. By definition, $\mathbf{\Pi}(\mathbf{x})$ measures the local imbalance of the wave function carried by the A and B sites. To express $\mathbf{\Pi}(\mathbf{x})$, it would be natural to consider eigenstates of the position operator $P\mathbf{x}P$ projected onto the occupied states of \mathcal{H} . However, in dimension $d > 1$, the different components of the projected position operator do not commute $[Px_jP, Px_kP] \neq 0$ for $j \neq k$, and do not possess common eigenstates. Instead, we express the polarisation in terms of the maximally localized states \widetilde{W}_m [88], which are centered on the position $\mathbf{x}_m \equiv \langle \widetilde{W}_m | \widehat{X} | \widetilde{W}_m \rangle$. These states generalize the Wannier functions in the absence of translational symmetry, see Appendix 2.8.5 for more details. We can then define the *local* chiral polarization as the weighted chiral position evaluated over \widetilde{W}_m :

$$\mathbf{\Pi}(\mathbf{x}_m) = 2 \langle \widetilde{W}_m | \mathbb{C}\widehat{X} | \widetilde{W}_m \rangle. \quad (2.30)$$

In practice, we can bypass the time consuming numerical determination of the \widetilde{W}_m by taking advantage of the matrix pencil method detailed in Appendix 2.8.4. In short, the method consists in replacing in (2.30) the \widetilde{W}_m by eigenstates of a linear combination of the projected position components $L = \sum_j \alpha_j Px_jP$; $\sum \alpha_j = 1$. The dependence on α_i of the resulting chiral polarization is a measure of the non-commutativity of the Px_j typically associated to a nonvanishing Berry curvature. In practice, as illustrated in Fig. 2.10, the difference between the actual polarization, computed from the \widetilde{W}_m , and its approximation based on the R -matrix eigenstates is smaller than the distance between neighboring sites. Given the excellent agreement found both in mono and polycrystals, we henceforth use the pencil matrix method to locally measure the chiral polarization fields in disordered and amorphous structures out of reach of conventional chiral displacement characterizations [106].

To make the discussion as clear as possible we consider separately the two possible sources of randomness in a disordered chiral insulator: (i) geometrical disorder, which affects the frame geometry leaving the interaction between the A and B sites unchanged and (ii) Spectral disorder, which alters the interactions while leaving the frame geometry unchanged.

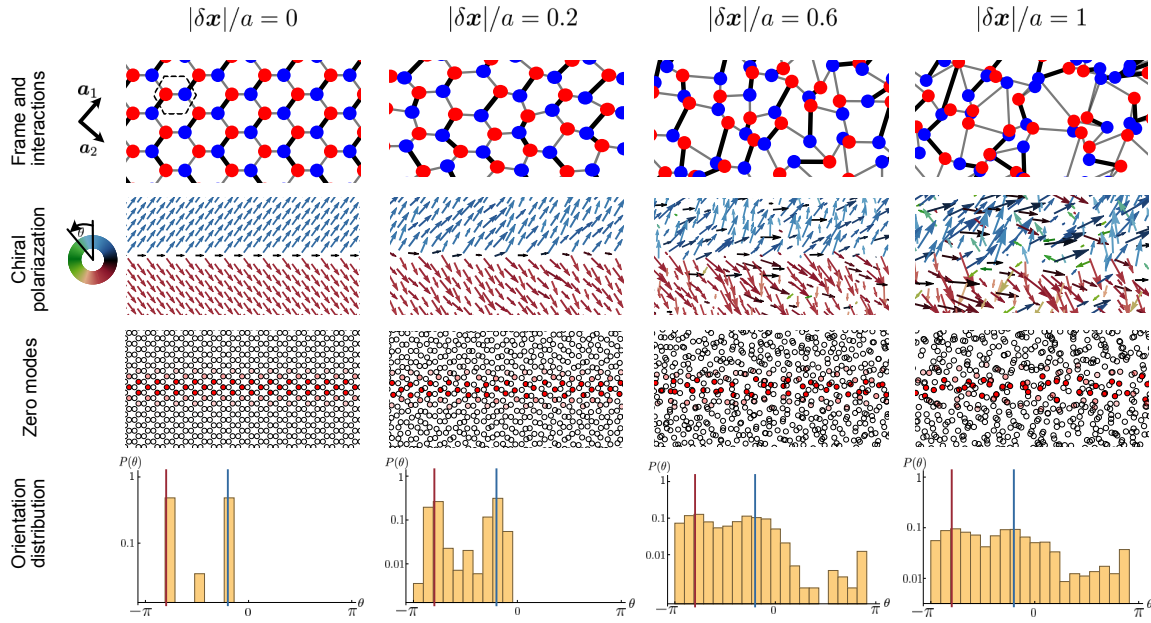


Figure 2.11: **Topological zero energy states on amorphous frames** First row: Sketch of the frame geometry for increasing positional disorder quantified by the maximal amplitude of the random displacements $|\delta\mathbf{x}|/a$. All panels show the vicinity of a boundary between two different insulators defined on the same frame but with different positions of the stronger couplings. The lines' width indicates the magnitude of the coupling strength. In all panels $t'/t = 20$. In the leftmost panel, we indicate the choice of the unit cell and of the crystallographic axes. Second row: Corresponding chiral polarization fields. The color indicates the orientation of $\mathbf{\Pi}(\mathbf{x})$ Third row: Magnitude of the zero-mode wave function. The zero mode is located at the boundary between topologically inequivalent states even on amorphous frames. Fourth row: Probability density function of the θ , the local orientation of the chiral polarization field. The distributions are peaked on the same two directions (vertical lines) regardless of the magnitude of disorder. This reveals the coexistence of two distinct topological phases robust to positional disorder.

Topological zero modes on amorphous chiral frames.

The reasoning is easily explained starting from a concrete example. Fig. 2.11 shows the interface between two topologically distinct insulators, \mathcal{I}_T and \mathcal{I}_B , living on a honeycomb frame. They correspond to distinct atomic limits of a nearest-neighbor tight binding Hamiltonians including two different hopping coefficients, see e.g. [107]. For the choice of unit cell sketched in Fig. 2.11, the winding vectors are $\mathbf{w}^{\mathcal{I}_T} = (0, 1)$ and $\mathbf{w}^{\mathcal{I}_B} = (1, 0)$. As a result the boundary region \mathcal{B} hosts one zero mode per unit cell located on the A sites. As expected from Eq. (2.26), on a homogeneous periodic frame, $\mathbf{\Pi}(\mathbf{x})$ takes two distinct values in the two regions, and is discontinuous across \mathcal{B} . Correspondingly, the distribution of the chiral polarization in the sample consists of two peaks centered on the two values associated to two topologically inequivalent phases, see Fig. 2.11 (left column).

We now disorder the frame by shifting all site positions by random displacements of maximal amplitude $|\delta\mathbf{x}|$ while preserving the magnitude of the interactions in the

corresponding Hamiltonian \mathcal{H}_D . For sufficiently large displacements, it is impossible to keep track of the original periodic lattice, see Fig. 2.11 (first row). Nonetheless, we clearly see in the third row of Fig. 2.11 that the topologically protected zero modes located in \mathcal{B} are preserved, despite the lack of crystalline symmetry and the impossibility to define a Bloch Hamiltonian and its topological winding numbers. Note that unlike in [108] both the bulk and the boundary region are homogeneously disordered. Again, the existence and location of a line of zero modes is revealed by variations of the chiral polarization field. The variations of the orientation of $\mathbf{\Pi}(\mathbf{x})$ occurs over the penetration length-scale ℓ_G set by the energy gap. The coexistence of two topologically distinct amorphous phases is signalled by a (wider) bimodal distribution of $\mathbf{\Pi}(\mathbf{x})$ peaked on the same values as in the pure case, see Fig. 2.11 (last row). This robust phenomenology is further illustrated in Supplementary Video 1, showing the evolution of the polarization field and zero-mode location as the magnitude of disorder is increased.

This observation reflects a generic feature of chiral matter. Randomizing the frame geometry cannot alter the energy gap provided that the graph defined by the coupling terms of \mathcal{H} has a fixed chiral connectivity. This observation implies that the concept of topological phase naturally applies to amorphous frames that can be continuously deformed into periodic lattices. In fact, the coexistence of different chiral insulators is effectively probed by the spatial distribution of the polarization field $\mathbf{\Pi}(\mathbf{x})$. Each peak of the distribution signals topologically inequivalent regions in amorphous chiral matter. The phase boundaries are then readily detected by jumps of the chiral-polarization vector field over ℓ_G .

Topological zero modes of disordered chiral Hamiltonians.

The case of spectral disorder is more subtle as it can trigger topological transitions. Again, we start with a concrete example. We use the same model of insulator as in the previous section. Considering the even simpler case of a perfect monocrystal, there is no zero mode in the sample. Keeping the frame unchanged we add disorder to the interactions in the form of random perturbations to the coupling parameters. We note ϵ_D the width of the Gaussian disorder distribution, ξ its correlation length and ΔE the energy gap in the pure case. When $\epsilon_D/\Delta E \ll 1$ no zero mode exists in this finite system see Fig. 2.12 first column. Consistently, the local chiral polarization hardly fluctuates in space and its distribution remains peaked around the same constant value.

By contrast as $\epsilon_D/\Delta E \sim 1$, zero energy modes emerge in the bulk. Their presence signals local the emergence of topologically inequivalent regions in the material triggered by local gap inversions. The distinct phases are revealed by the orientational distribution of $\mathbf{\Pi}(\mathbf{x})$: as disorder increases additional peaks grow at values of θ characteristic of the other two homogeneous topological insulators, Fig. 2.12 (last row). In the limit of strong disorder, the spatial extent of the coexisting phases is set by the disorder correlation length ξ as exemplified in Supplementary Movie 2. Gap closings also have a local signature in the polarization field. As $\mathbf{\Pi}(\mathbf{x}_m)$ is only defined at the generalized Wannier centers (Eq. (2.30)), $\mathbf{\Pi}(\mathbf{x}_m)$ cannot be computed at the center of a zero mode, which by definition does not support any Wannier mode. The proliferation of zero modes in the bulk is therefore signaled by an increasing number of holes in the polarization field.

The above observations do not rely on the specific model we use in Figs. 2.11 and 2.12.

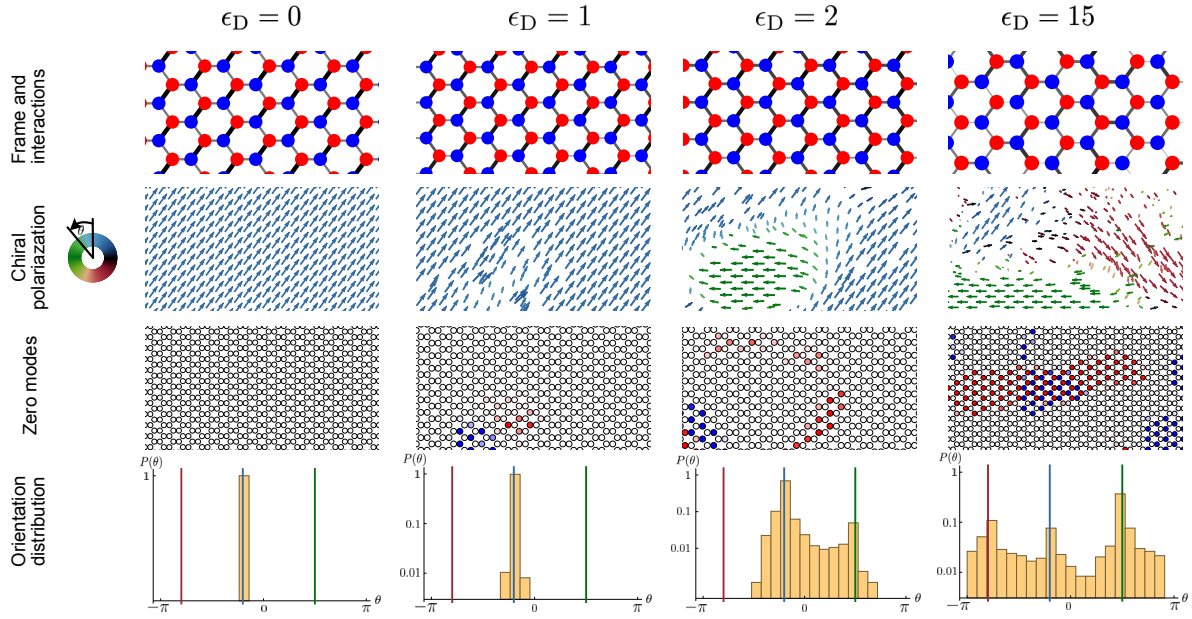


Figure 2.12: **Topological zero-energy states in the bulk of disordered chiral insulators** First row Sketch of the honeycomb frame and of the coupling strengths for increasing spectral disorder. The strengths of the couplings are represented by the width of the dark lines. Their randomness is quantified by the variance of the Gaussian couplings ϵ_D . The correlation length for all the examples is $\xi = 12a$. Second row Corresponding chiral polarization fields. The color indicates the orientation θ of $\mathbf{\Pi}(\mathbf{x})$. Third Row: Magnitude of the zero-energy modes on the A (red) and B (blue) sites. Fourth row: Probability density function of the orientation θ . Remarkably, even in the disordered cases, the distribution peaks only at values characteristic of the three phases of the homogeneous chiral Hamiltonian.

Generically, adding spectral disorder to a chiral Hamiltonian results in the nucleation of additional topological phases decorated by zero modes at their boundaries. Even in the absence of a Bloch theory, we can distinguish the topological nature of the coexisting phases by measuring their average chiral polarization. For spatially correlated disorder the spatial extent of each phase is set by the disorder correlation length ξ .

Designing topologically protected zero modes in amorphous chiral matter.

It is worth stressing that disordered chiral insulators generically support topologically protected zero-energy modes at their boundaries. Unlike crystalline topological insulators, the lower the bulk and edge symmetries the more robust the edge states.

Cutting an amorphous sample into two parts without inducing the proliferation of boundary zero modes is virtually impossible. It would require cutting bonds while preserving the connectivity between all pairs of A and B site connected by the local polarization vectors $\mathbf{\Pi}(\mathbf{x}_m)$; only this type of configurations can be continuously deformed into crystals having edges matching that of tilings generated by the unit cell of an atomic limit.

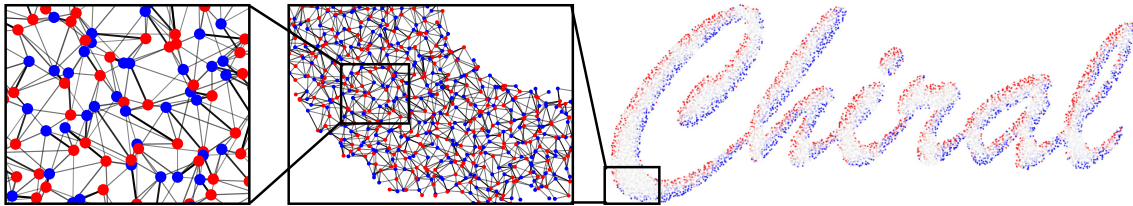


Figure 2.13: **Disordered chiral metamaterial** Macroscopic view and close ups on an amorphous frame supporting a disordered chiral insulator. The frame is defined adding a strong positional disorder to a Honeycomb lattice $|\delta\mathbf{x}| = a$. Using the same Hamiltonian as in Figs.2.11 and 2.12, we add spectral disorder corresponds to $\epsilon_D = 2$. Cutting the sample to form the word "chiral" reveals a continuous distribution of zero modes along the edge.

These cuts require extreme fine tuning in macroscopic samples and are therefore virtually impossible to achieve. This property makes the design of zero energy wave guides very robust in amorphous chiral matter. As illustrated in Fig. 2.13.

Measuring the chiral polarization.

In this section we show that the chiral polarization is not only a powerful theoretical concept, but an actual material property readily accessible to experiments. Two scenarios are possible: when the (low energy) eigenfunctions can be measured, the chiral polarization can be directly evaluated using its definition, Eq. (2.19). This technique is straightforward e.g. in mechanical metamaterials [54], where the vibrational eigenmodes can be imaged in real space in response to mechanical actuation.

Alternatively, when spectral properties are out of reach of quantitative measurements, we can infer the value of the chiral polarization from the dynamic spreading of localized chiral excitations. This approach builds and generalizes the technique pioneered in the context of periodically driven photonic quantum walk [95, 109]. For the sake of clarity we henceforth limit our discussion to 1D, two-band insulators although the reasoning applies in higher dimensions.

We introduce the dynamical chiral polarization $\Pi_\Psi(t) = \langle \Psi(t) | \mathbb{C}\hat{X} | \Psi(t) \rangle$ defined over the time-evolved states $\Psi(t) = \exp(-iHt)\Psi(0)$, where $\Psi(0)$ is a localized chiral state. Should one be able to initialize an experiment in a Wannier State $\Psi(0) = W_{n,\mathbf{R}}$, the wave function would spread as in Fig. 2.14a, but remarkably the dynamical chiral polarization $\Pi_\Psi(t)$ would be stationary and equal to Π in a homogeneous system as illustrated in Fig. 2.14a, and demonstrated in the Method section. In practice, it would be always easier to approximate the Wannier state by excitations Ψ_{AB} (resp. Ψ_{BA}) localized on two neighboring A and B sites (resp. B and A). The result of this procedure is shown in Fig. 2.14b and reveals that the long-time dynamics of $\Pi_\Psi(t)$ converges towards the chiral

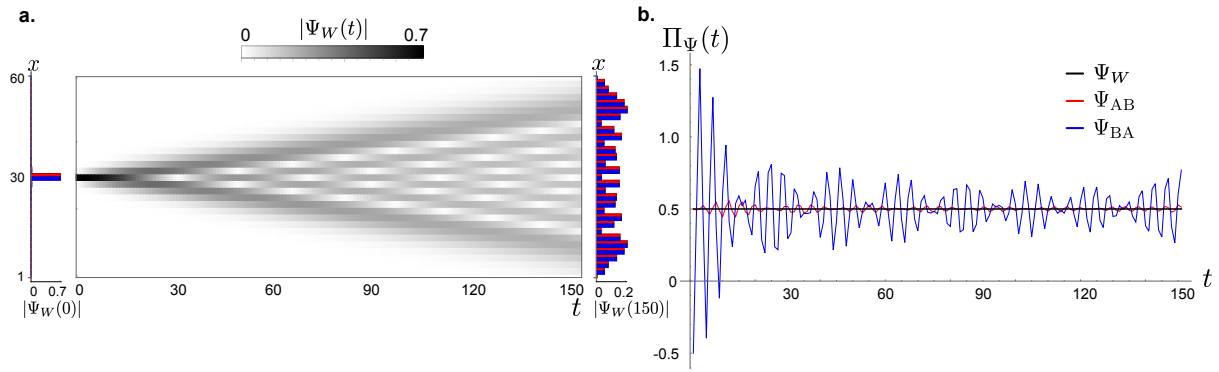


Figure 2.14: Measuring the chiral polarization in time. **a.** Left: Dynamical evolution of a Wannier state in the ground state of a two-band SSH model, with hopping ratio $t_1/t_2 = 0.1$. The state is localized in the middle of a finite system of 60 unit cells. Center: Time evolution of the wave-function amplitude. Right: The amplitude of the final state at time $t = 250$ is represented on the A (red) and B (blue) sites of the lattice. **b.** The dynamical chiral polarization $\Pi_\psi(t) = \langle \Psi(t) | \mathcal{C} \hat{X} | \Psi(t) \rangle$ corresponding to the protocol described in **a** is constant in time (black solid line). By comparison, the dynamical chiral polarization starting from a state $\Psi_{AB}(t = 0)$ (resp. $\Psi_{BA}(t = 0)$), localized on two neighboring sites A and B (resp. B and A) shows fluctuations around the static chiral polarization whose amplitude depends on the initial state. The sign $\Pi_\psi(t)$ is reversed at short time when the chiral polarization of the initial state is opposite to the static chiral polarization of the SSH chain. This results in large amplitude oscillations. The short time dynamics of Π_ψ therefore provides a direct access to the orientation of the material chiral polarization.

polarization Π . However, we stress that the essential information about the orientation of Π is already accessible at very short times and would not suffer from possible damping issues. When $\Pi_\Psi(t = 0)$ and Π have opposite signs, we observe very large amplitude oscillations reflecting the dynamic reversal of the chirality of the wave packet at short times. Conversely when $\Pi_\Psi(t = 0)$ and Π are parallel the convergence is very fast and devoid of large amplitude fluctuations.

It is worth noting that the chiral initial state $\Psi(t = 0) = \Psi_{AB}$ is an atomic-limit eigenstate. The dynamics can then be seen as the result of a quench at $t = 0$ starting from the atomic-limit Hamiltonian. The amplitude of the fluctuations in Fig. 2.14b then reveals the topological nature of the quench. As a last comment we stress that our protocol differs from the chiral displacement method introduced and used in [95, 109–111]. The mean chiral displacement depends on the unit-cell convention. As a consequence, to probe the topology of 1D systems, conventional MCD protocols require two independent measurement protocols. They effectively correspond to measuring the mean chiral displacement given two possible unit cell choices. A topological invariant is then defined by the difference between the two measurements. The Chiral polarization method, which we introduce provides a one-step characterization of the topology of a chiral phase.

2.7.6 Conclusion

We have established a generic framework to characterize, elucidate and design the topological phases of chiral insulators. In crystals, we show that the frame topology and the frame geometry act together with Bloch Hamiltonian topology to determine the zero-mode content of the bulk and interfaces. In the bulk, the frame topology fully determines the algebraic number of zero-energy modes counted by the chiral charge \mathcal{M} . Chiral insulators, however, are distinguished one another via their chiral polarization $\mathbf{\Pi}$ set both by the frame geometry and Bloch-Hamiltonian topology. At their surface, the number of zero-energy states is prescribed by the interplay between the Bloch Hamiltonian topology and the frame geometry in the bulk on one hand, and by the frame topology of the boundary on the other hand. This interplay goes beyond the bulk-boundary-correspondence principles solely based on Hamiltonian topology.

We have shown that chiral symmetry alone translates real-space properties into spectral phases without relying on any crystalline symmetry and translational invariance when expressed as a sublattice symmetry. Chiral symmetry does not merely complement the classification of topological quantum chemistry [101, 112–114] but also makes it possible to distinguish topological phases in amorphous matter. In disordered system, introducing the concept of chiral polarization field, we provide a practical platform to detect topological phases coexisting in disordered samples, and to design robust zero-mode wave guides at their boundaries.

We expect our framework to extend beyond Hamiltonian dynamics when dissipative processes obey the chiral symmetry [115]. We therefore conjecture that real-space topology, geometry and non-Hermitian operator topology should cooperate in chiral dissipative materials as diverse as cold atoms to photonics, robotic devices and active matter.

Acknowledgements

We thank J. Asboth, A. Bernevig, A. Dauphin, K. Gawedzki, A. Grushin, Y. Hatsugai, P. Massignan, A. Po, A. Schnyder and A. Vishwanath for insightful discussions.

Funding information We acknowledge support from ANR WTF, and ToRe IdexLyon breakthrough programs.

2.8 Supplementary material

2.8.1 Bloch theory convention and Wannier states.

Conventions for the Bloch decomposition.

For the sake of clarity, we first introduce the main quantities used throughout all the manuscript to describe waves in periodic lattices. We note $|\Psi_{n,\mathbf{k}}\rangle$ the Bloch eigenstates. They correspond to wavefunctions $\langle \mathbf{x} | \Psi_{n,\mathbf{k}} \rangle = \varphi_{n,\mathbf{k}}(\mathbf{x}) e^{i\mathbf{k}\cdot\mathbf{x}}$, where \mathbf{k} is the momentum in the Brillouin Zone (BZ), and where the normalized function $\varphi_{n,\mathbf{k}}$ has a periodicity of one unit cell [88]. In this article, we use the following convention to express the Bloch states as a superposition of plane waves:

$$|\Psi_{n,\mathbf{k}}\rangle = \sum_{\alpha} u_{n,\alpha}(\mathbf{k}) |\mathbf{k}, \alpha\rangle, \quad (2.31)$$

where α labels the different atoms in the crystal, and $|\mathbf{k}, \alpha\rangle$ represents the Fourier transform of the real-space position basis: $|\mathbf{k}, \alpha\rangle = \sum_{\mathbf{R}} \exp(i\mathbf{k}\cdot\mathbf{R}) |\mathbf{R} + \mathbf{r}_{\alpha}\rangle$, \mathbf{R} being a Bravais lattice vector and \mathbf{r}_{α} a site position within the unit cell. We stress that here the components $u_{n,\alpha}(\mathbf{k})$ are periodic functions of \mathbf{k} over the BZ. It is worth noting, however, that there exists multiple conventions to decompose the Bloch states as discussed e.g. in the context of graphene-like systems in [116–118]. A common alternative uses nonperiodic components over the BZ which carry an additional phase encoding the position of each atom within the unit cell: $|\Psi_{n,\mathbf{k}}\rangle = \sum_{\alpha} \tilde{u}_{n,\mathbf{k},\alpha} e^{i\mathbf{k}\cdot\mathbf{r}_{\alpha}} |\mathbf{k}, \alpha\rangle$. We will comment on the translation of our results from one convention to the other in the following.

Wannier functions.

By definition the Wannier function associated to a Bloch eigenstate is given by the inverse Fourier transform (up to a phase):

$$|W_{n,\mathbf{R}}\rangle = \Omega^{-1} \int_{\text{BZ}} d^d \mathbf{k} e^{-i\mathbf{k}\cdot\mathbf{R}} |\Psi_{n,\mathbf{k}}\rangle. \quad (2.32)$$

where Ω is the volume of the BZ. Note that for sake of clarity, we here and henceforth assume that the spectrum does not include band crossings. The technical generalization of our results to degenerated spectra is straightforward but involves some rather heavy algebra, see e.g. [88]. In addition, to ease the notation and calculations we work with orthogonal coordinates such that $\int_{\text{BZ}} dk_j = \Omega^{1/d}$, $\forall j$. The generalization to non-orthogonal lattices is straightforward and amounts to considering different geometrical factors along each reciprocal direction

Projected position operator and sublattice Zak phases.

Ignoring the distinction between the A and B sites, we can first compute the action of the position operator on the Wannier states following [88]:

$$\begin{aligned}\langle \mathbf{x} | \widehat{X} | W_{n,\mathbf{R}} \rangle &= \Omega^{-1} \int_{\text{BZ}} d^d \mathbf{k} \mathbf{x} e^{i\mathbf{k} \cdot (\mathbf{x} - \mathbf{R})} \varphi_{n,\mathbf{k}}(\mathbf{x}) \\ &= \Omega^{-1} \int_{\text{BZ}} d^d \mathbf{k} \left(-i \partial_{\mathbf{k}} e^{i\mathbf{k} \cdot (\mathbf{x} - \mathbf{R})} + \mathbf{R} e^{i\mathbf{k} \cdot (\mathbf{x} - \mathbf{R})} \right) \varphi_{n,\mathbf{k}}(\mathbf{x}) \\ &= \Omega^{-1} \int_{\text{BZ}} d^d \mathbf{k} e^{-i\mathbf{k} \cdot \mathbf{R}} \left[e^{i\mathbf{k} \cdot \mathbf{x}} (\mathbf{R} + i \partial_{\mathbf{k}}) \right] \varphi_{n,\mathbf{k}}(\mathbf{x}),\end{aligned}\quad (2.33)$$

where in the last step we applied an integration by parts, using that $|\Psi_{n,\mathbf{k}}\rangle = |\Psi_{n,\mathbf{k}+\mathbf{G}}\rangle$ with \mathbf{G} a primitive reciprocal vector. The generalization of Eq. (2.33) to the position operator projected on the sublattice $a = A, B$ is straightforward:

$$\langle \mathbf{x} | \widehat{X} \mathbb{P}^a | W_{n,\mathbf{R}} \rangle = \Omega^{-1} \int_{\text{BZ}} d^d \mathbf{k} e^{-i\mathbf{k} \cdot \mathbf{R}} \left[e^{i\mathbf{k} \cdot \mathbf{x}} (\mathbf{R} + i \partial_{\mathbf{k}}) \right] \mathbb{P}^a \varphi_{n,\mathbf{k}}(\mathbf{x}), \quad (2.34)$$

which allows us to define the average positions $\langle \mathbf{x}^a \rangle_{n,\mathbf{R}}$ restricted to the site $a = A, B$ and to the n^{th} band excitations:

$$\begin{aligned}\langle \mathbf{x}^a \rangle_{n,\mathbf{R}} &\equiv \langle W_{n,\mathbf{R}} | \mathbb{P}^a \widehat{X} \mathbb{P}^a | W_{n,\mathbf{R}} \rangle \\ &= \frac{\mathbf{R}}{\Omega} \int_{\text{BZ}} d^d \mathbf{k} \langle \varphi_{n,\mathbf{k}} | \mathbb{P}^a | \varphi_{n,\mathbf{k}} \rangle + \frac{1}{\Omega} \mathbf{\Gamma}_{\text{Zak}}^a(n),\end{aligned}\quad (2.35)$$

where $|\varphi_{n,\mathbf{k}}\rangle = e^{-i\mathbf{k} \cdot \widehat{X}} |\Psi_{n,\mathbf{k}}\rangle$, and $\mathbf{\Gamma}^a(n)$ is the vector composed of the d generalized sublattice Zak phases associated to the n -th band:

$$\Gamma_j^a(n) = i \int_{\text{BZ}} d^d \mathbf{k} \langle \varphi_{n,\mathbf{k}} | \mathbb{P}^a \partial_{k_j} \mathbb{P}^a | \varphi_{n,\mathbf{k}} \rangle \quad (2.36)$$

We can further simplify Eq. (2.35) noting that the orthonormality of the $|\varphi_{n,\mathbf{k}}\rangle$ implies $\langle \varphi_{n,\mathbf{k}} | \mathbb{P}^A + \mathbb{P}^B | \varphi_{n,\mathbf{k}} \rangle = 1$ and $\langle \varphi_{n,\mathbf{k}} | \mathbb{P}^A - \mathbb{P}^B | \varphi_{n,\mathbf{k}} \rangle = 0$, which yields $\langle \varphi_{n,\mathbf{k}} | \mathbb{P}^a | \varphi_{n,\mathbf{k}} \rangle = 1/2$. All in all, we find a simple relation between the average of the position operator and the Zak phase of the Bloch eigenstates over the BZ:

$$\langle \mathbf{x}^a \rangle_{n,\mathbf{R}} = \frac{\mathbf{R}}{2} + \frac{1}{\Omega} \mathbf{\Gamma}^a(n). \quad (2.37)$$

2.8.2 Chiral polarization, Zak phases and winding.

Chiral polarization and sublattice Zak phases.

We are now equipped to compute the chiral polarization, defined as the difference between the expected value of the projected position operators over the occupied eigenstates ($n < 0$). It readily follows from Eq. (2.37) that $\mathbf{\Pi}$ corresponds to the difference of the sublattice Zak phases:

$$\begin{aligned}\mathbf{\Pi} &\equiv 2 \sum_{n < 0} \langle \mathbf{x}^A \rangle_{n,\mathbf{R}} - \langle \mathbf{x}^B \rangle_{n,\mathbf{R}} \\ &= \frac{2}{\Omega} \sum_{n < 0} \mathbf{\Gamma}^A(n) - \mathbf{\Gamma}^B(n).\end{aligned}\quad (2.38)$$

Two comments are in order. Firstly, the sum could have been also taken over the unoccupied states ($n > 0$). As $\mathbb{C}^2 = \mathbb{I}$, the sublattice phase picked up by $|\varphi_{n,\mathbf{k}}\rangle$ is indeed the same as that of its chiral partner $|\varphi_{-n,\mathbf{k}}\rangle = \mathbb{C}|\varphi_{n,\mathbf{k}}\rangle$. Secondly, we stress that Eq. (2.38) does not depend on the specific convention of the Bloch representation. This relation, however does not disentangle the respective contributions of the frame geometry and of the Hamiltonian on the chiral polarization. To single out the two contributions, we now use the specific Bloch representation (2.31). Given this choice, the sublattice Zak phase is naturally divided into two contributions leading to

$$\Gamma^a(n) = \int_{\text{BZ}} d^d \mathbf{k} \sum_{\alpha \in a} \left(u_{n,\alpha}^* u_{n,\alpha} \mathbf{r}_\alpha + i u_{n,\alpha}^* \partial_{\mathbf{k}} u_{n,\alpha} \right). \quad (2.39)$$

The first term on the r.h.s. is the intracellular contribution to the Zak phase while the second is proportional to the sublattice intercellular Zak phase following to the definitions of [33]

$$\gamma_j^a(n) \equiv i \int_{\mathcal{C}_j} d\mathbf{k} \sum_{\alpha \in a} u_{n,\alpha}^*(\mathbf{k}) \partial_{\mathbf{k}} u_{n,\alpha}(\mathbf{k}). \quad (2.40)$$

Summing Eq.(2.39) over all occupied bands, and using the orthogonality of the chiral component $u_{n,\alpha}$ we then recover our central result:

$$\mathbf{\Pi} = \mathbf{p} + \frac{2}{\Omega^{1/d}} (\gamma^A - \gamma^B), \quad (2.41)$$

where $\mathbf{p} = \sum_{\alpha \in A} \mathbf{r}_\alpha - \sum_{\alpha \in B} \mathbf{r}_\alpha$ is the geometrical polarization of the corresponding unit-cell and $\gamma^a = \sum_{n < 0} \gamma^a(n)$. The chiral polarization is the sum of one contribution coming only from the frame geometry and one contribution characterizing the geometrical phase of the Bloch eigenstates.

Chiral polarization in different Bloch conventions.

Although the physical content of the chiral polarization does not depend on the choice of the Bloch convention, it is worth explaining how to derive its functional form for the other usual representation where $|\Psi_{n,\mathbf{k}}\rangle = \sum_{\alpha} \tilde{u}_{n,\alpha}(\mathbf{k}) e^{i\mathbf{k} \cdot \mathbf{r}_\alpha} |\mathbf{k}, \alpha\rangle$. Within this convention the vector of Zak phases take the form

$$\Gamma^a(n) = i \int_{\text{BZ}} d^d \mathbf{k} \sum_{\alpha \in a} \tilde{u}_{n,\alpha}^* \partial_{\mathbf{k}} \tilde{u}_{n,\alpha}, \quad (2.42)$$

which does not allow the distinction between the geometrical and the Hamiltonian contributions to $\mathbf{\Pi}$ when performing the sum over the occupied band in Eq. (2.38). This observation further justifies our choice for the Bloch representation.

Quantization of the intercellular Zak-phase in chiral insulators.

To demonstrate the quantization of $\gamma_j = \gamma_j^A + \gamma_j^B$, we resort to the Wilson loop formalism reviewed e.g. in Ref. [99].

Let us first recall the definition of the non-Abelian Berry-Wilczek-Zee connection along the Brillouin zone for a set of smooth vectors $|u_n(\mathbf{k})\rangle$, $n = 1, \dots, M$:

$$\mathbf{A}_{nm}(\mathbf{k}) = \langle u_n(\mathbf{k}) | \partial_{\mathbf{k}} | u_m(\mathbf{k}) \rangle. \quad (2.43)$$

The associated Wilson loop operator defined along the path \mathcal{C}_j through the Brillouin zone is given by the ordered exponential

$$W_j = \overline{\exp} \left(- \int_{\mathcal{C}_j} d\mathbf{k} \cdot \mathbf{A}(\mathbf{k}) \right) \quad (2.44)$$

The topological properties of a generic gapped chiral Hamiltonian are conveniently captured by smooth deformations yielding a flat spectrum $E = \pm 1$. The corresponding Bloch Hamiltonian is then given by

$$H = \begin{pmatrix} 0 & Q(\mathbf{k}) \\ Q^\dagger(\mathbf{k}) & 0 \end{pmatrix} \quad (2.45)$$

where $Q(\mathbf{k})$ is a nonsingular unitary matrix. Without loss of generality, we write the corresponding eigenstates as

$$|u_{\pm n}(\mathbf{k})\rangle = \frac{1}{\sqrt{2}} \begin{pmatrix} \pm Q(\mathbf{k}) |e_n^B\rangle \\ |e_n^B\rangle \end{pmatrix} \quad (2.46)$$

where the sign \pm identifies the sign of the eigenvalue $E = \pm 1$ and the normalized vectors $|e_n^B\rangle$ form a basis of the Hilbert space of Q^\dagger . The non-Abelian connection (2.43) for the negative (resp. positive) energy states then takes the simple form

$$\mathbf{A}_{nm}^-(\mathbf{k}) = \frac{1}{2} \langle e_n^B | Q^\dagger(\mathbf{k}) \partial_{\mathbf{k}} Q(\mathbf{k}) | e_m^B \rangle = \mathbf{A}_{nm}^+(\mathbf{k}) \quad (2.47)$$

It follows from the definition of the Wilson-loop operator (Eq. (2.44)) that the intercellular Zak phase for the negative energy bands $\gamma = \gamma^A + \gamma^B$ is defined in terms of the Wilson loops for the non-Abelian connection $\mathbf{A}^-(\mathbf{k})$ as

$$\gamma_j = -i \ln \det W_j^- \quad (2.48)$$

The quantization of all d intercellular Zakk phases then follows from Eqs (2.44) and (2.47):

$$\gamma_j = -i \operatorname{tr} \ln \left[\overline{\exp} \left(- \frac{1}{2} \int_{\mathcal{C}_j} d\mathbf{k} \cdot \partial_{\mathbf{k}} \ln Q(\mathbf{k}) \right) \right] \quad (2.49)$$

$$= \pi w_j \operatorname{mod} (2\pi) \quad (2.50)$$

where the $\operatorname{mod} (2\pi)$ indetermination stems from the choice of the branch cut of the complex \ln function, and where w_j is the standard winding of the chiral Hamiltonian (2.45):

$$w_j = \frac{i}{4\pi} \int_{\mathcal{C}_j} d\mathbf{k} \cdot \operatorname{tr} \left[\partial_{\mathbf{k}} H C H^{-1} \right] \in \mathbb{Z}, \quad (2.51)$$

$$= \frac{1}{2\pi i} \int_{\mathcal{C}_j} d\mathbf{k} \cdot \operatorname{tr} \left[Q^{-1} \partial_{\mathbf{k}} Q \right]. \quad (2.52)$$

We therefore conclude that the d Zak phases are topological phases defined modulo 2π .

Relating the sublattice Zak phases to the winding of the Bloch Hamiltonian.

We here demonstrate the essential relation given by Eq. (2.25). To do so, we relate the winding w_j to the sublattice Zak phases by evaluating the trace in Eq. (2.51) using the eigenstate basis. Noting that $\langle u_n | \partial_{\mathbf{k}} H(\mathbf{k}) \mathbb{C} H^{-1}(\mathbf{k}) | u_n \rangle = -2 \langle u_n | \mathbb{C} \partial_{\mathbf{k}} | u_n \rangle$, the winding takes the simple form

$$w_j = -\frac{i}{2\pi} \int_{\mathcal{C}_j} d\mathbf{k} \sum_n \langle u_n | \mathbb{C} \partial_{\mathbf{k}} | u_n \rangle. \quad (2.53)$$

Decomposing the chiral operator on the two sublattice projectors $\mathbb{C} = \mathbb{P}^A - \mathbb{P}^B$, yields

$$\pi w_j = (\gamma_j^B - \gamma_j^A) \in \pi \mathbb{Z}. \quad (2.54)$$

Quantization of the sublattice Zak phases.

Eqs. (2.50) and (2.54) shows that both the sum and the difference of the sublattice Zak phases are quantized:

$$\begin{aligned} \gamma_j^A + \gamma_j^B &= \pi w_j + 2\pi m, & m \in \mathbb{Z}, \\ \gamma_j^B - \gamma_j^A &= \pi w_j. \end{aligned} \quad (2.55)$$

It then follows that both sublattice phases γ_j^A and γ_j^B are integer multiples of π .

How does the winding number of a chiral Bloch Hamiltonian change upon unit cell redefinition?

Starting from a chiral Hamiltonian \mathcal{H} , we demonstrate below the relation between the winding numbers associated to the Bloch Hamiltonians constructed from different choices of unit cells, Eq. (2.27).

The definition of Bloch waves and Bloch Hamiltonians require prescribing a unit cell. Starting with a first choice of a unit cell geometry, say unit cell (1), we can write $H^{(1)}(\mathbf{k})$ in the chiral basis as

$$H^{(1)}(\mathbf{k}) = \begin{pmatrix} 0 & Q^{(1)} \\ Q^{\dagger(1)} & 0 \end{pmatrix}, \quad (2.56)$$

Let us now opt for a second choice of unit cell, say choice (2). The Bloch Hamiltonians $H^{(1)}$ and $H^{(2)}$ are then related by a unitary transformation

$$H^{(2)} = U^\dagger H^{(1)} U, \quad (2.57)$$

where the components of the unitary matrix are given by

$$U_{\alpha\beta} = \exp(i\mathbf{k} \cdot \mathbf{R}_\alpha^{(12)}) \delta_{\alpha\beta}, \quad (2.58)$$

where the \mathbf{R}_α^{12} are the Bravais vectors connecting the position of the atoms in the two unit-cell conventions, see Fig. 2.15 for a simple illustration. We note that, we have implicitly ignored the trivial redefinitions of the unit cell that reduce to permutations of the site indices. We can then express the winding of $H^{(2)}$ using Eq. (2.57) in the definition of

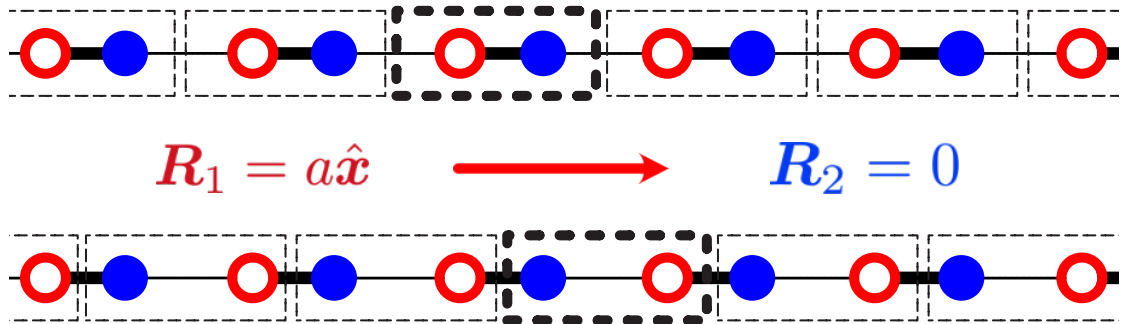


Figure 2.15: **Unit cell transformation.** We illustrate the definition of the \mathbf{R}_α vectors using the simple example of a SSH chain. For the first atom (empty symbol) $\mathbf{R}_1 = a\hat{x}$ while $\mathbf{R}_2 = 0$ for the second atom (solid symbol).

Eq. (2.51), which yields

$$w_j^{(2)} = \frac{i}{4\pi} \int_{\mathcal{C}_j} d\mathbf{k} \operatorname{tr} \left[\partial_{\mathbf{k}} (UH^{(1)}U^\dagger) \mathbb{C} (UH^{(1)}U^\dagger)^{-1} \right]. \quad (2.59)$$

Expanding the gradient, using the trace cyclic property and noting that $[\mathbb{C}, U] = 0$, we find

$$w_j^{(2)} = w_j^{(1)} - \frac{i}{2\pi} \int_{\mathcal{C}_j} d\mathbf{k} \operatorname{tr} \left[\partial_{\mathbf{k}} U \mathbb{C} U^{-1} \right]. \quad (2.60)$$

This equation relates the winding numbers of the two Bloch Hamiltonians to the winding number of the transformation matrix U , which is by definition a geometrical quantity independent of \mathcal{H} . Using Eq. (2.58) leads to the remarkable relation which relates the spectral properties of the Hamiltonian to the unit-cell geometry

$$w_j^{(1)} - w_j^{(2)} = \frac{i}{2\pi} \int_{\mathcal{C}_j} d\mathbf{k} \operatorname{tr} \left[\partial_{\mathbf{k}} U \mathbb{C} U^{-1} \right] = \frac{1}{a_j} \left(\sum_{\alpha \in A} R_\alpha - \sum_{\alpha \in B} R_\alpha \right). \quad (2.61)$$

2.8.3 Zero energy flat-band insulators.

We consider a flat-band chiral insulator, defined on a lattice with a non-vanishing chiral charge. In mechanics this situation is readily achieved adding extra bonds to further rigidify an otherwise isostatic lattice. It is characterized by a finite gap separating positive and negative energy states and by an additional flat band at $E = 0$. In such a phase, there may exist additional zero energy edge states in addition to the bulk zero-energy modes. These edge states are analogous to the topological edge modes of insulators. Our goal is here to derive a bulk-boundary correspondence for these materials and provide a count of their zero-energy edge states. We will show that this correspondence involves the specific geometry of the eigenstates as opposed to their topology in the case of genuine insulators.

To show this we first derive the expression of the chiral polarization in the presence of a finite bulk chiral charge. Our starting point is Eq. (2.38), which relates to the chiral polarization of a crystal to the sublattice Zak phases given by Eq. (2.36):

$$\mathbf{\Pi} \equiv 2 \sum_{n < 0} \langle \mathbf{x}^A \rangle_{n, \mathbf{R}} - \langle \mathbf{x}^B \rangle_{n, \mathbf{R}} = \frac{2}{\Omega} \sum_{n < 0} \mathbf{\Gamma}^A(n) - \mathbf{\Gamma}^B(n). \quad (2.62)$$

The sum over all the negative energy bands $n < 0$ is half the sum over the non-zero energy states $n \neq 0$ given by

$$\begin{aligned} \sum_{n \neq 0} \mathbf{\Gamma}^a(n) &= \int_{\text{BZ}} d^d \mathbf{k} \sum_{\alpha \in a} \sum_n u_{n, \alpha}^* u_{n, \alpha} \mathbf{r}_\alpha + \frac{2}{\Omega^{1/d}} \gamma^a \\ &= \int_{\text{BZ}} d^d \mathbf{k} \sum_{\alpha \in a} \left(1 - \sum_{n_0} u_{n_0, \alpha}^* u_{n_0, \alpha} \right) \mathbf{r}_\alpha + \frac{2}{\Omega^{1/d}} \gamma^a. \end{aligned} \quad (2.63)$$

In the last line, we single out the role of the bulk zero-energy modes indexed by n_0 . Using the above expression to evaluate the r.h.s. of Eq. (2.62), we find an expression similar to Eq. (2.41) in the main text:

$$\mathbf{\Pi} = (\mathbf{p} - \mathbf{p}_{\text{ZM}}) + \frac{2}{\Omega^{1/d}} (\gamma^A - \gamma^B). \quad (2.64)$$

A first noticeable difference with Eq. (2.41) is a spectral correction to the geometrical polarization stemming from the localized zero-energy bulk modes. This zero-mode polarization is given by

$$\mathbf{p}_{\text{ZM}} = - \int_{\text{BZ}} d^d \mathbf{k} \sum_{n_0} \left(\sum_{\alpha \in A} - \sum_{\alpha \in B} \right) u_{n_0, \alpha}^* u_{n_0, \alpha} \mathbf{r}_\alpha. \quad (2.65)$$

Three comments are in order. Firstly, we stress that while the geometrical polarization \mathbf{p} depends on the choice of origin in the presence of an excess of chiral charge, the difference $\mathbf{p} - \mathbf{p}_{\text{ZM}}$, and $\mathbf{\Pi}$, are both independent of the frame's origin. Secondly, unlike in insulators, the difference between the intercellular sublattice Zak phases, $\gamma^A - \gamma^B$ does not identify with the winding number of the Bloch Hamiltonian. In fact it is not a topological quantity: it continuously depends on the specific couplings of the Hamiltonian. Finally, we point that, by definition, the chiral polarization does not depend on the Bloch convention. A change in the Bloch convention changes the geometrical polarization, the zero-mode polarization, and the intercellular zak phases in such a way that all corrections cancel one another.

Equipped with Eq. (2.64), we now turn to the generalization of the bulk boundary correspondence for flat-band insulators. We consider a crystalline material \mathcal{S} terminated by a clean edge $\partial \mathcal{S}$ oriented along the Bravais vector \mathbf{a}_1 . This edge may host \mathcal{V}^{NT} non-trivial zero-energy modes, in addition to the (trivial) bulk zero modes associated to the flat band. The edge defines a unit cell that may not be compatible with that of the atomic limit. We can nonetheless extend the edge region such that it matches the unit-cell compatible with the atomic limit (AL). The idea being that \mathcal{V}^{NT} is fully determined by the additional chiral charge of the edge with respect to that provided by the bulk chiral charge density. Following the same reasoning as in the main text, this extra chiral charge is given by the difference of geometrical polarization and zero-mode polarization:

$$\mathcal{V}^{\text{NT}} = \mathcal{N}^{\mathcal{B}} [(p_2 - p_{\text{ZM}_2})_{\text{AL}} - (p_2 - p_{\text{ZM}_2})], \quad (2.66)$$

where \mathcal{N}^B is the boundary length expressed in units of unit-cell length. The first term is computed in the unit cell compatible with the atomic limit, and the second term is computed in the original unit cell defined by the edge $\partial\mathcal{S}$.

The invariance of the chiral polarization with respect to unit cell transformations allows the connection with the intercellular sublattice Zak phase:

$$\left(p_2 - p_{\text{ZM}_2} + \frac{2}{\Omega^{1/d}} (\gamma_2^A - \gamma_2^B)\right)_{\text{AL}} = p_2 - p_{\text{ZM}_2} + \frac{2}{\Omega^{1/d}} (\gamma_2^A - \gamma_2^B), \quad (2.67)$$

where AL denotes the terms evaluated in the unit-cell compatible with the atomic limit. All in all, the non-trivial zero-energy content of flat band insulators is given by a formula which generalizes Eq. (2.29):

$$\mathcal{V}^{\text{NT}} = \mathcal{N}^B \frac{2}{\Omega^{1/d}} [(\gamma_2^A - \gamma_2^B) - (\gamma_2^A - \gamma_2^B)_{\text{AL}}]. \quad (2.68)$$

It is worth noting that in the case of genuine insulator, $(\gamma_2^A - \gamma_2^B)_{\text{AL}} = -w_{\text{AL}} = 0$ since it corresponds to the winding number in the unit cell compatible with the AL. Once again the chiral polarization field and its relation with the geometric phases allow us to predict the existence of non-trivial zero-energy modes by observing the local discontinuities of the chiral polarization field at any interface.

2.8.4 Basis of localised states: matrix pencil

Finding a localized basis of the space of negative energy states poses several challenges when working in high-dimensional systems. In one dimension, this is an easy task that can be directly solved by finding the eigenstates of the projected position operator, $P\widehat{X}P$, where

$$P = \sum_{E < 0} |\Psi_E(\mathbf{r})\rangle \langle \Psi_E(\mathbf{r})|, \quad (2.69)$$

is the projector onto the occupied energy states and $|\Psi_E\rangle$ are the eigenstates of the real space hamiltonian \mathcal{H} .

It would be tempting to generalize this approach to two and three dimensional systems to find a common basis for the independent components of the projected position: $P\widehat{\mathbf{R}}P \equiv (P\widehat{X}P, P\widehat{Y}P, P\widehat{Z}P)$. However, in general these components do not commute. As proposed in the seminal work of Marzari and Vanderbilt [67], a workaround consists in computing the set of maximally localized Wannier functions $\{W_n\}$, which minimizes the quadratic spread:

$$\Delta r^2 = \frac{1}{Na^2} \sum_n^N \left[\langle W_n | (P\widehat{\mathbf{R}}P)^2 | W_n \rangle - |\langle W_n | P\widehat{\mathbf{R}}P | W_n \rangle|^2 \right], \quad (2.70)$$

Other minimization functions can be used to define localized states such Foster-Boys or the Edmiston-Ruedenberg criteria [119].

Here, we introduce an alternative method based on the matrix pencil of the projected positions (for a general introduction to matrix pencils see [120] and pages 375 and 461 of [121]). The matrix pencil of two matrices PXP and PYP corresponds to their linear combination $L(\alpha_1, \alpha_2) = \alpha_1 PXP + \alpha_2 PYP$, where α_i are two non-zero real coefficients [121]. When $[PXP, PYP] \neq 0$, the eigenvectors of the matrix pencil leads to

a localised basis, whose spreading is comparable to the standard Maximally Localized Wannier Functions (MLWF) at a much reduced computational cost. To illustrate this result, we study in detail the case of a chiral Halmiltonian on a 10×10 honeycomb lattice, see Fig. 2.11. We compare the MLWF and the matrix pencil methods in Fig. 2.16. We implement MLWF method using a gradient descent protocol [119]. The minimization of Ω converges slowly as shown in Fig. 2.16b. We now discuss the case of the matrix pencil method and first note that the diagonalization of L for the two limiting cases $\alpha_1 = 0$ and $\alpha_2 = 0$ corresponds to finding a basis of completely localized states along the \hat{y} and \hat{x} direction, respectively. In the general case where $\alpha_{1,2} \neq 0$, L corresponds to the position operator along the direction $\alpha_1\hat{x} + \alpha_2\hat{y}$. It is therefore convenient to parametrize this axis according to its polar angle: $L(\theta) = \cos\theta PXP - \sin\theta PYP$. Fig. 2.16c shows the spreading functional evaluated at the local basis obtained from $L(\theta)$ for different polar angles. In practice, we achieve a comparable and even better localisation with respect to the MLWF method after 200 iterations. The only values of θ for which the matrix pencil method is not effective corresponds to the crystallographic directions of the lattice, see Fig. 2.16d. As these directions are known a priori, we can safely and effectively use the matrix pencil method to compute a set of localized states. The gain in terms of computing time is obvious. Both the diagonalization of L and each minimization step of Δr^2 have a computational complexity of order N^2 , where N is the system size. Choosing a value of θ avoiding the Bravais directions allows us to find a set of localized states in one step using the matrix pencil method. It is also worth noting that this method is unrelated to the chiral symmetry of the Hamiltonians considered in the main text and applies broadly.

We now switch to disordered systems and illustrate the performance of the matrix pencil method in Figs. 2.16d, e and f. The minimization of Δr^2 for the MLWF method is more time consuming than in crystals, Fig. 2.16e. Conversely, the diagonalization time of L remains unchanged. The difference with the ordered case is visible when plotting the spreading function Ω as a function of θ . The peaks along the crystallographic directions widen, as expected, when disorder increases.

In practice, we compute the θ average of the chiral polarization associated to a set of localized eigenstates along the θ directions which yields excellent approximations of the Wannier states, see Fig. 2.10.

2.8.5 Chiral polarization in amorphous materials.

We have seen that the chiral polarization does not depend on the specifics of the unit cell: it is an intrinsic property of the material. In fact, as we show below, this framework is far more general and we can define the chiral polarization in amorphous solids.

We start by revisiting the definition of the chiral polarization in a crystal given by eq. (2.38):

$$\mathbf{\Pi} \equiv 2 \sum_{n < 0} \langle \mathbf{x}^A \rangle_{n, \mathbf{R}} - \langle \mathbf{x}^B \rangle_{n, \mathbf{R}}. \quad (2.71)$$

Strictly speaking this polarization is defined at the position \mathbf{R} . However, the discrete translational invariance of the crystal and by consequence, of the Wannier functions, makes the polarization field homogeneous. We can thus drop the \mathbf{R} indices.

The definition of the Wannier function as the inverse Fourier transform of the Bloch eigenstate cannot be used when dealing with a disordered configuration. Instead, we work

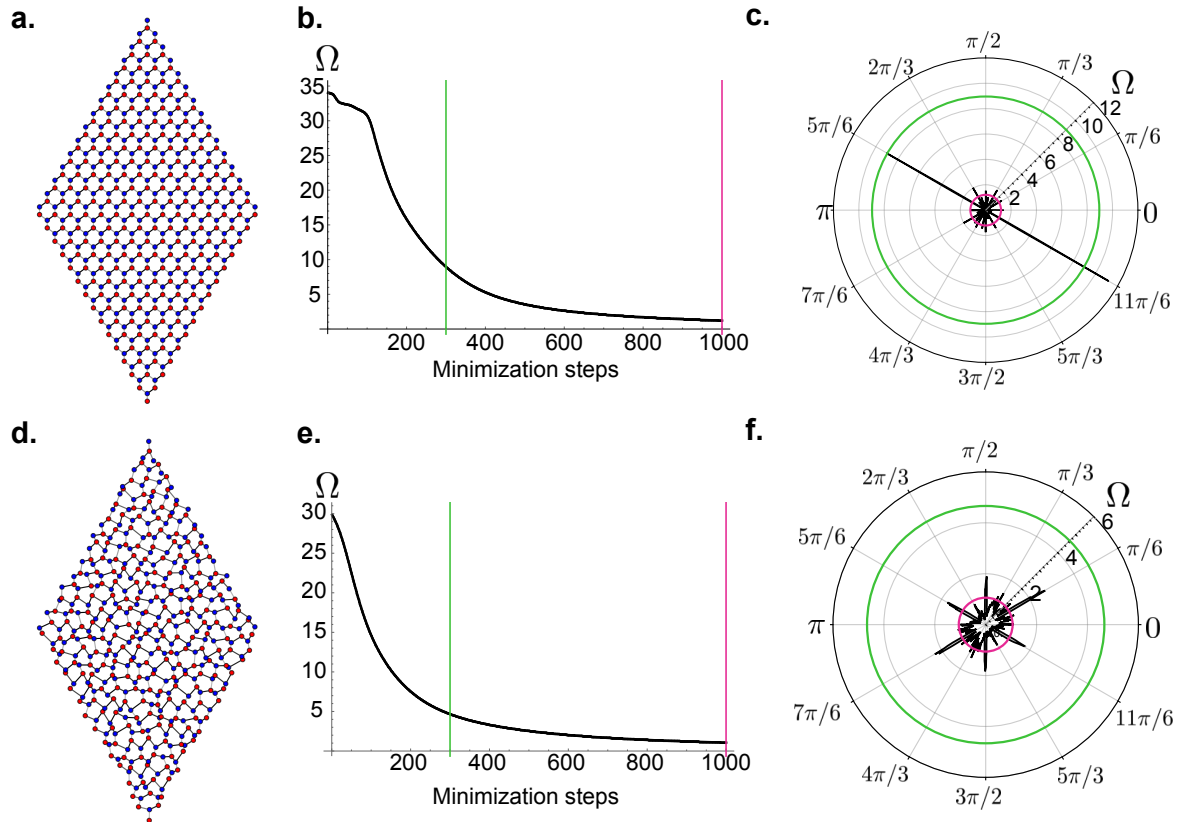


Figure 2.16: **Comparison between the matrix pencil and the MLWF method**
a. Sketch of the frame geometry for a crystalline chiral honeycomb lattice made of 15×15 unit cells. **b.** Spreading functional as a function of the amount of minimization steps for the determination of maximally localised Wannier functions. After 300 (green) and 1000 (pink) minimization steps, the spreading corresponds to $\Omega_{\text{Wannier}_{300}} \approx 8.9$ and $\Omega_{\text{Wannier}_{1000}} \approx 1.2$, respectively. **c.** Spreading functional as a function of the angle θ for the localised basis determined from the matrix pencil $L(\theta)$ (black line). In green and pink we show the spreading obtained from the wannier states after 300 and 1000 minimization steps, respectively. Except for a few given directions, notably $\theta = 11\pi/6$ and $\theta = 5\pi/6$, the matrix pencil method gives a more localised basis at a much lower computational cost. **d.**, **e.**, **f.** Same as before applied for a disordered system with $|\delta\mathbf{x}|/a = 0.2$, $\epsilon_D = 0.4$, and $\xi = 10a$. (see figs. 2.11 and 2.12)

with a another set of fully localized functions: the eigenstates of the projected position operator onto the occupied bands [99]. The projected position operator is given by $P\widehat{X}P$, where

$$P = \sum_{E < 0} |\Psi_E(\mathbf{r})\rangle \langle \Psi_E(\mathbf{r})|, \quad (2.72)$$

is the projector onto the occupied energy states (not to be confused with the projectors \mathbb{P}^a), and the $|\Psi_E\rangle$ are the eigenstates of the real space hamiltonian \mathcal{H} . Let us denote the m^{th} eigenstate of the projected position operator as \widetilde{W}_m (notice that there are as many eigenstates as occupied energy states of the Hamiltonian). This is a localized function around the center given by $\mathbf{x}_m = \langle \widetilde{W}_m | \widehat{X} | \widetilde{W}_m \rangle$, similarly to the Wannier centers. Moreover, using each localized function, we can compute the difference of the weighted positions on both sublattices, in other words, the local chiral polarization:

$$\mathbf{\Pi}(\mathbf{x}_m) = 2 \langle \widetilde{W}_m | \mathbb{C}\widehat{X} | \widetilde{W}_m \rangle \quad (2.73)$$

In a periodic frame, the eigenstates of the projected position operator reduce to a linear combination of the Wannier functions W_n : $|\widetilde{W}_m\rangle = \sum_n V_{mn} |W_n\rangle$, with $n < 0$, indicating the occupied energy bands, V a unitary matrix in the energy space, and V_{mn} a diagonal matrix in the position space. We can then rewrite the chiral polarization in eq. (2.73) as

$$\begin{aligned} \mathbf{\Pi}(\mathbf{x}_m) &= 2 \sum_{n,l} \langle W_n | V_{mn}^\dagger \mathbb{C} V_{ml} | W_l \rangle \\ &= 2 \sum_{n < 0} \langle W_n | \mathbb{C}\widehat{X} | W_n \rangle, \end{aligned} \quad (2.74)$$

where in the last line we used the fact that the V_{ml} commutes with $\mathbb{C}\widehat{X}$ and the unitarity of V . As a result, we recover the first expression defined in crystals using the Bloch formalism as given by Eq. (2.38).

2.8.6 Chiral polarization of time evolved Wannier states.

In Ref. [109], the mean chiral displacement under Hamiltonian dynamics was introduced as a measure of the Zak phase of periodic Hamiltonians in $d = 1$. This quantity characterizes a representation of a Hamiltonian associated to a given unit cell definition, and corresponds to the long-time displacement of an initially fully localized state, measured in units of the unit-cell size. As a consequence, several choices of unit cells were necessary to fully characterize the dynamics of a given (meta)material [95]. The chiral polarization which we extensively use in this article is an intrinsic (meta)material property, unlike the mean chiral displacement and the skew polarization. It is defined in real space, and does not rely on any underlying frame periodicity, Eq. (2.21) In the specific case of periodic frames $\mathbf{\Pi}$ crucially resolves the chiral imbalance of wave packets with a sub-unit-cell resolution.

In this method section, we show how $\mathbf{\Pi}$ relates to the dynamics of a maximally localized Wannier state spreading in the bulk of a chiral crystal. To do so we consider the time evolution of a wave function $|\psi_n(t)\rangle = U(t) |W_{n,\mathbf{R}}\rangle$ starting from a of a Wannier state in

band n , initially localized at \mathbf{R} , with an evolution operator $U(t) = \exp(-iHt)$. Using the notations introduced in Eq. (2.32), the position at time t is given by

$$\begin{aligned} & \langle \mathbf{x} | \widehat{X} | \psi_n(t) \rangle \\ &= \Omega^{-1} \int_{\text{BZ}} d^d \mathbf{k} \mathbf{x} e^{i\mathbf{k} \cdot (\mathbf{x} - \mathbf{R})} e^{-iE_n(\mathbf{k})t} \varphi_{n,\mathbf{k}}(\mathbf{x}) \end{aligned} \quad (2.75)$$

$$= \Omega^{-1} \int_{\text{BZ}} d^d \mathbf{k} e^{-i\mathbf{k} \cdot \mathbf{R}} \left[e^{i\mathbf{k} \cdot \mathbf{x}} (\mathbf{R} + \mathbf{v}_n(\mathbf{k})t + i\partial_{\mathbf{k}}) \right] \varphi_{n,\mathbf{k}}(\mathbf{x}), \quad (2.76)$$

where $\mathbf{v}_n(\mathbf{k}) = \partial_{\mathbf{k}} E_n(\mathbf{k})$ is the group velocity in the energy band n . We can also generalize Eq. (2.37) to define the instantaneous average positions restricted to the $a = A, B$ sublattices which read

$$\langle \mathbf{x}^a(t) \rangle_{n,\mathbf{R}} \equiv \langle \psi_n(t) | \mathbb{P}^a \widehat{X} \mathbb{P}^a | \psi_n(t) \rangle \quad (2.77)$$

$$= \oint_{\mathbf{k}} \frac{1}{2} (\mathbf{R} + \mathbf{v}_n(\mathbf{k})t) + \frac{1}{\Omega} \Gamma_{\text{Zak}}^a(n) \quad (2.78)$$

$$= \frac{1}{2} \mathbf{R} + \frac{1}{\Omega} \Gamma_{\text{Zak}}^a(n) \quad (2.79)$$

$$= \langle \mathbf{x}^a(t=0) \rangle_{n,\mathbf{R}}. \quad (2.80)$$

This result indicates that the chiral polarization of each Wannier state is a stationary quantity although they all evolve in time. When summed over (half of) the spectrum, we recover the static definition of the chiral polarization

$$\mathbf{\Pi}(t) = \text{Tr}(U^{-1}(t) \mathbb{C} \widehat{X} U(t)) \quad (2.81)$$

$$= \sum_n \langle \psi_n(t) | \mathbb{C} \widehat{X} | \psi_n(t) \rangle \quad (2.82)$$

$$\begin{aligned} &= 2 \sum_{n < 0} \langle \mathbf{x}^A(t) \rangle_{n,\mathbf{R}} - \langle \mathbf{x}^B(t) \rangle_{n,\mathbf{R}} \\ &= \frac{2}{\Omega} \sum_{n < 0} \Gamma_{\text{Zak}}^A(n) - \Gamma_{\text{Zak}}^B(n). \end{aligned} \quad (2.83)$$

We note that the trace operation in Eq. (2.81) can be evaluated using any basis of the Hilbert space, such as the ensemble of states fully localized on the A and B sites.

Experimental characterization of chiral materials

3.1 Introduction

"To measure is to know", a phrase traced back to Lord Kelvin [122], applies to most, if not all, experimental knowledge. The fact that measurement precedes knowledge is a fundamental tenet in the characterization of materials. Measuring the young modulus tells about the elasticity of a solid, as viscosity informs about the flowing properties of a liquid. Importantly, these measurements are done *without* knowing the molecular or atomic structure of the materials. After all, if we knew the microscopic details and their electronic interactions, i.e. if we had a model, in principle, we would not necessitate a measurement; we could directly predict their properties, either theoretically or through simulations. We measure what we do not know. We measure to characterize. Nonetheless, much of the characterization of topological chiral materials seems to escape this principle. With the advent of topology in physics, most of the research literature has focused, legitimately, on demonstrating the connection between topological invariants and edge-states. Examples go from microwave systems [42] to electrical circuits [43] and acoustic setups [40, 54]. Rather than measuring topological invariants, the quest was focused on experimentally proving the bulk-boundary correspondence: experimental measurement of edge-states given that the system is modeled by a hamiltonian characterized by a non-trivial topological number.

With the connection established, recent theoretical and experimental efforts have moved towards detecting topological invariants from bulk measurements, i.e. detecting the topology without the topologically protected edge states. Here we can find at least two different trends. The first one, mainly theoretical, deals with the introduction of local markers such as the local Chern marker [123], the Bott index [124], and the real space extension of topological invariants [93] originally defined in momentum space. A local real space property, as discussed in the previous chapter, allows for the detection of domain walls between distinct topological phases and the generalization to non-crystalline systems. They, however, still rely on a given hamiltonian. The second trend, mainly experimental, is the detection of topological invariants from dynamical measurements [109, 125, 126], encompassing quantum Chern insulators, and 1D chiral in-

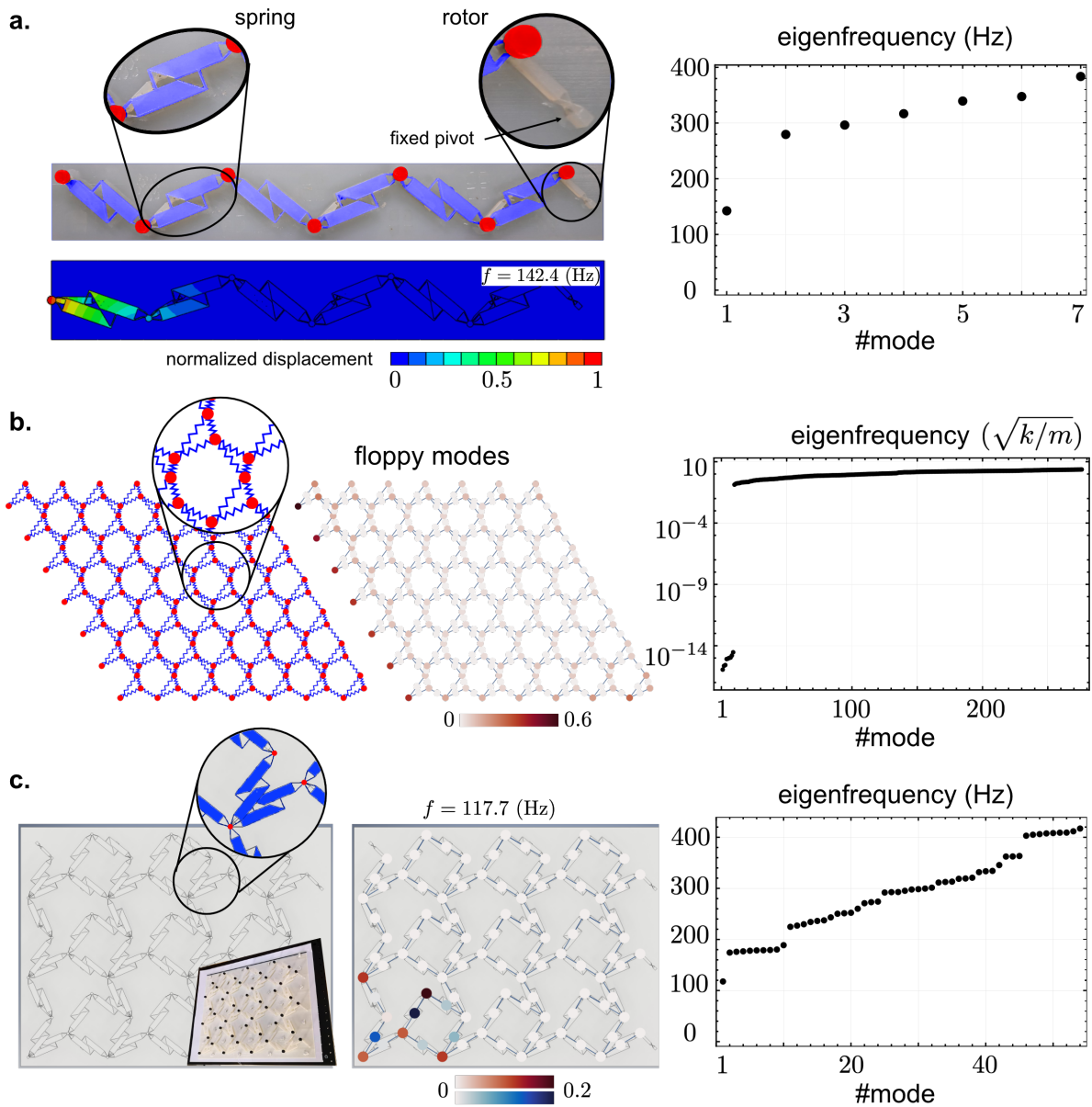


Figure 3.1: **Mechanical metamaterials with topologically protected zero-energy modes.** **a.** (top left) A 3D printed array of seven rotors connected by springs. Using FEM simulations, we determine the lowest energy mode which is localized on the left edge of the sample (bottom left). The linear spectrum (right) shows that the localized edge mode is spectrally separated from the bulk modes. **b.** (left) Illustration of a bead and spring twisted kagomé lattice made of 7×7 unit cells. The beads have mass m and the stiffness of the spring is k . The dynamical matrix \mathcal{D} governing the linear response of the system has a zero-energy mode localized on the left edge of the sample [29] which is characterized by the magnitude of the normalized displacements in red (middle). The edge mode is spectrally decoupled from the bulk modes (right). **c.** (left) A two-dimensional 3D printed collection of beads and springs made out of the same units as in **a.** The lowest energy mode, obtained from FEM simulations, is confined to the bottom right corner (middle). Here the magnitude of displacements and elongations is normalized and represented by red and blue colors, respectively. The corner mode is spectrally separated from both bulk and edge modes (right).

ulators. Here the detection relates to a global property, restricting its utility to single topological phases of matter.

The focus of my manuscript is chiral matter, from which mechanics is one example. The attempts to characterize topological chiral phases are based on either computing the winding number in real space [93] or detecting it through the long-time dynamics [109]. Yet, from chapter 2, we know that the winding number is ill-defined as a material property as it relies on the model we choose to describe the system.

In this chapter, I tackle the challenge of experimentally characterizing a chiral material, such as the ones illustrated in fig 3.1. They all represent mechanical insulators hosting localized zero-energy states. Can we predict their existence without resorting to any a priori modeling, i.e. without a predefined low-energy hamiltonian? I will show that the answer is yes. This task, as we will see, is fulfilled by the dynamical measurement of a local quantity in real space: the chiral polarization field.

This chapter is divided into two main parts. In the first one, I show how to measure the chiral polarization field. I elucidate the experimental limitations of computing the field from chiral eigenmodes and propose a protocol based on time-averaging local responses. I validate this method by comparing theory, finite element simulations (FEM), and experiments on one- and two-dimensional mechanical metamaterials. In the second part, I extract the information of the chiral polarization field to predict the existence of localized zero-energy modes. I devise a general hierarchical procedure to determine not only the type of zero-mode, floppy mode or self-stress state, but also to determine the dimensionality in which it is confined. I conclude by discussing the reach of this new protocol and future perspectives on the study of higher-order chiral moments.

3.2 Measuring the chiral polarization field

Chapter 2 laid out the theory of the chiral polarization, a material property that describes chiral systems and locates zero-energy modes. In particular, when working with mechanical networks, the chiral polarization informs about the softness of the material by identifying regions of floppy modes and self-stress states. The chiral polarization field is, in theory, the right tool to classify chiral systems. Its magnitude and orientation reveal the spatial distribution of displacement and stress perturbations, whereas the field itself reveals the underlying lattice of chiral molecules.

However, the definition of the chiral polarization argues against its practicality:

$$\mathbf{\Pi} = 2\text{Tr} [\mathcal{C}\hat{\mathbf{x}}\mathbb{P}_{E<0}]. \quad (3.1)$$

Computing $\mathbf{\Pi}$ requires the full knowledge of the low-energy eigenstates dictating the evolution of displacements and elongations. In what follows I will circumvent the need for a hamiltonian by looking at the response to local perturbations. This will render the chiral polarization an accessible physical quantity and informative about the nature of unknown materials.

But first, what do we need to compute this field? The foundational elements are displacements *and* elongations, the basis of chiral mechanics; whatever it is that we measure, it would ultimately boil down to these two quantities. More precisely, we will use the information of displacements and elongations to compute the chiral polarization in

two steps: first, we determine the chiral molecules, grouping chiral charges with strong interactions, and second, we compute the chiral polarization on each molecule.

Chiral molecules

Each chiral molecule is defined by a local function $|W_i\rangle$ satisfying two properties:

1. The set of all local functions defining the chiral molecules span the subspace of negative energy of the chiral hamiltonian \mathcal{H} . In other words, the projector into this subspace is given by:

$$\mathbb{P}_{E<0} = \sum_i^N |W_i\rangle \langle W_i|. \quad (3.2)$$

2. They are short-ranged [65]:

$$\lim_{|\bar{\mathbf{x}}_i - \mathbf{r}| \rightarrow \infty} \langle \bar{\mathbf{x}}_i - \mathbf{r} | W_i \rangle = 0, \quad (3.3)$$

with $\bar{\mathbf{x}}_i$ being the center of the function, defined as

$$\bar{\mathbf{x}}_i = \langle W_i | \hat{X} | W_i \rangle. \quad (3.4)$$

In other words, $|W_i\rangle$ decays to zero when the distance from its center increases.

In periodic crystals, functions satisfying properties (3.2) and (3.3) are termed Wannier functions. They are usually defined as the inverse Fourier transform of the negative energy Bloch eigenstates, i.e. the eigenstates of the chiral Hamiltonian \mathcal{H} expressed in momentum space. Different terminologies such as hybrid Wannier functions [66] or maximally localized Wannier functions [65] are employed in the literature alluding to their degree of localization. Here, for simplicity, we name Wannier function any $|W_i\rangle$ satisfying properties (3.2) and (3.3), regardless of the dimensionality, boundaries, and crystallinity of the system.

Chiral Polarization

Once the Wannier functions are known, per each one of them we define the chiral polarization

$$\mathbf{\Pi}_i = 2 \langle W_i | \mathcal{C} \hat{X} | W_i \rangle. \quad (3.5)$$

Finally, we introduce the map $\bar{\mathbf{x}}_i \mapsto \mathbf{\Pi}_i$, giving the sought-after chiral polarization field.

Therefore, to determine the field, we must first specify the set of Wannier functions. Mathematically speaking, determining these local functions corresponds to finding the suitable basis of a given vectorial space: the negative (or positive) energy space. This space is naturally expressed in terms of the eigenstates of the chiral hamiltonian, $\mathcal{H} |\Psi_E\rangle = E |\Psi_E\rangle$. Thus, one straightforward procedure to obtain the $|W_i\rangle$ functions would be to first measure the eigenstates of \mathcal{H} with negative energy, $\{\Psi_{E<0}\}$, and then use a linear transformation in order to get the desired basis [31, 65]. We could directly construct the

projected position operator, $\mathbb{P}_{E<0}\hat{X}\mathbb{P}_{E<0}$, where $\mathbb{P}_{E<0} = \sum_{E<0} |\Psi_E\rangle\langle\Psi_E|$, and diagonalize it. The eigenstates of the projected position operator will be the sought-after localized functions. Details on alternative localization procedures based on functional minimization and dealing with the intricacies of higher-dimensional systems are found in chapter 2.

3.2.1 The shortcomings of spectral measurements

In a nutshell, obtaining the low-energy eigenstates leads to the local functions defining the chiral molecules and, ultimately, the chiral polarization field. From an experimental point of view, this can be done by shaking the sample at increasing frequencies and selecting the modes with the largest responses.

While appealing in theory, this approach is doomed to failure for several experimental reasons. Although eigenenergies are easily accessible, see SI of [54] and fig 3.1, determining a set of low-energy chiral eigenstates is usually beyond experimental capabilities. Whether originating from the instruments' accuracy or the mismatch with the linear hamiltonian \mathcal{H} , the experimental eigenmodes will always contain a correction from the theoretical modes: $|\Psi_E^{\text{exp.}}\rangle = |\Psi_E^{\text{theo.}}\rangle + |\delta\Psi_E\rangle$. This unavoidable correction has two consequences. The first one is the non-orthogonality of the basis $\{\Psi_{E<0}^{\text{exp.}}\}$. The second one is its non-chirality. The non-orthogonality can be overcome by a simple orthogonalization procedure such as the Gram-Schmidt method. The non-chirality, however, is insurmountable; it persists even with very small corrections $|\delta\Psi_E\rangle$. In fact, any small yet finite correction has a projection on both $\mathbb{P}_{E<0}$ and $\mathbb{P}_{E>0}$:

$$|\delta\Psi_E\rangle = \sum_{E'} \langle\Psi_{E'}^{\text{theo.}}|\delta\Psi_E\rangle |\Psi_{E'}^{\text{theo.}}\rangle = \sum_{E'<0} \langle\Psi_{E'}^{\text{theo.}}|\delta\Psi_E\rangle |\Psi_{E'}^{\text{theo.}}\rangle + \sum_{E'>0} \langle\Psi_{E'}^{\text{theo.}}|\delta\Psi_E\rangle |\Psi_{E'}^{\text{theo.}}\rangle, \quad (3.6)$$

forbidding any representation of the negative energy space, and therefore, failing to comply with the first requirement to get the Wannier functions (3.2).

3.2.2 Bypassing the hamiltonian with local responses

Luckily there is an alternative based on dynamical measurements and discussed at the end of the article "Geometry and topology tango in ordered and amorphous chiral matter" [31]. Dynamical protocols have already been proposed to probe topological insulators and in particular, chiral systems. The Mean Chiral Displacement (MCD) [109], for example, has been used to compute the winding number in one-dimensional crystalline photonic arrays. They are equivalently defined as the long-time limit of the chiral position operator for a given initial state: $\lim_{t\rightarrow\infty} \langle\psi(t)|\mathbb{C}\hat{X}_{\text{cell}}|\psi(t)\rangle$, with \hat{X}_{cell} being the index position operator, labeling different unit cells. Their definition manifestly depends on a unit cell choice (how to label the cells), which is exactly at the root of the impracticality of the winding number as a physical observable [31]. Our approach is based on time averaging local responses: from the evolution of a localized state, we measure the center and the chiral polarization as a function of time. Notably, the time average of the signal agrees with the expected theoretical value given by a Wannier function regardless of the initial condition. This constitutes the core of the measurement strategy.

Short versus long time behavior

In short, local perturbations are a good proxy to Wannier functions. But why? There are three key observations to answer this question. First, we notice from the definition of either the Wannier center (3.4) or the chiral polarization (3.5), that they are independent of local signs. Take for example one Wannier function W_1 and another function W_2 only differing on one sign highlighted in red,

$$W_1 = \frac{1}{\sqrt{2}} \begin{pmatrix} 0 \\ \vdots \\ 0 \\ 1 \\ \mathbf{1} \\ 0 \\ \vdots \\ 0 \end{pmatrix}, \quad W_2 = \frac{1}{\sqrt{2}} \begin{pmatrix} 0 \\ \vdots \\ 0 \\ 1 \\ \mathbf{-1} \\ 0 \\ \vdots \\ 0 \end{pmatrix}. \quad (3.7)$$

These two distinct functions, orthogonal from each other, lead however to the same centers and polarizations. Indeed, considering that the only non-zero entries correspond to positions x_n and x_{n+1} , we have

$$\bar{x}_1 = \langle W_1 | \hat{X} | W_1 \rangle = \frac{1}{2}(x_n + x_{n+1}), \quad (3.8)$$

$$\bar{x}_2 = \langle W_2 | \hat{X} | W_2 \rangle = \frac{1}{2}(x_n + x_{n+1}), \quad (3.9)$$

and the same goes for the chiral polarizations, $\mathbf{\Pi}_1 = \mathbf{\Pi}_2$. Fundamentally speaking, we do not require the full information of the wannier function, but solely of its support, i.e. on which beads/springs they are defined. This explains why using the Wannier basis $\{W_i\}$ or their counterpart spanning the positive energy space $\{\mathbb{C}W_i\}$ lead to the same result.

Second, when we let a local perturbation evolve, the Hamiltonian dynamics will naturally spread the initial state to the neighboring sites. In the short time scale, the wave packet rapidly populates the neighboring sites with the strongest interactions, approaching the support of a Wannier state.

Third, in the long time scale, the wave-packet will inevitably spread to the weakly bonded neighbors yet with a small lifetime. This asymmetry in the local interactions leads to a wave spreading over the sample yet spending more time in the strongly linked sites. Inspired by the definition of the chiral polarization field, we introduce the time average perturbation center and chiral polarization for a normalized state $\Psi(t)$ as

$$\bar{\mathbf{x}} \equiv \frac{1}{T} \int^T dt \langle \Psi(t) | \hat{\mathbf{X}} | \Psi(t) \rangle \quad (3.10)$$

$$\bar{\mathbf{\Pi}} \equiv \frac{2}{T} \int^T dt \left(\langle \Psi(t) | \mathbb{C} \hat{\mathbf{X}} | \Psi(t) \rangle - \langle \Psi(t) | \mathbb{C} | \Psi(t) \rangle \langle \Psi(t) | \hat{\mathbf{X}} | \Psi(t) \rangle \right), \quad (3.11)$$

with $\hat{\mathbf{X}} = (\hat{X}, \hat{Y}, \hat{Z})$ the vector of position operators, and T the period on which we take the average signal. There is no rule of thumb to define T , the choice will depend on the system, the interactions, and the perturbation employed. Unlike the Wannier functions, $\Psi(t)$ may carry a non-null chiral charge, $\langle \Psi(t) | \mathbb{C} | \Psi(t) \rangle \neq 0$. In order to have an origin independent quantity, pretty much like in electrostatics, we must subtract the finite chiral charge contribution, represented by the last term in eq. (3.11).

Proof of concept

To validate equations (3.10) and (3.11), we first simulate the evolution of localized initial states according to the wave equation $i\partial_t\Psi = \mathcal{H}\Psi$, with \mathcal{H} being the SSH hamiltonian describing the mechanical Kane-Lubensky chain [29], fig. 3.2. It corresponds to a tight-binding hamiltonian with alternating hopping interactions $t_1 = 0.3$ and $t_2 = 1$. As time goes on, the center and the chiral polarization associated with the perturbation evolve in time, fig 3.2c,d. They display oscillatory signals with period $\sim 2\pi|t_1 - t_2|^{-1}$. Their time averages coincide with the theoretical value obtained from a Wannier function, fig. 3.2e,f. Notice that even when the perturbation gets delocalized over half the size of the sample,

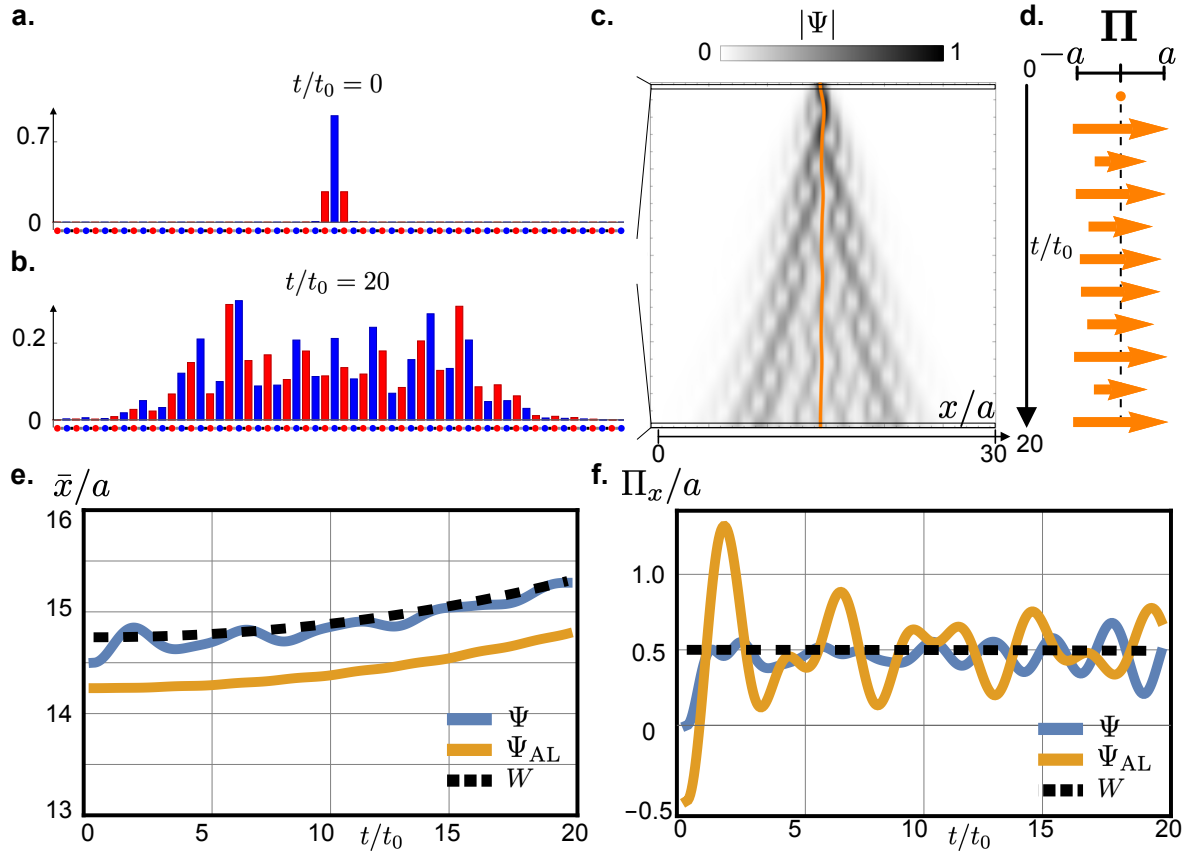


Figure 3.2: **Evolution of localized states as proxies of Wannier functions.** **a.** At $t/t_0 = 0$, a generic localized state is set at the middle of a 30 unit cell long SSH chain. Here $t_0 = \sqrt{m/k}$ corresponds to the natural time scale set by the stiffness and mass of the beads. **b.** The final state, at $t = 20t_0$, is delocalized over the sample. **c.** The initial state spreads in space while keeping its center $\bar{x}(t)$ (orange line) around the same position. **d.** The chiral polarization as a function of time oscillates in magnitude as the wave spreads across the sample. **e.** The center of the perturbation in time slightly drifts to the right of the sample while exhibiting some oscillations. The same applies to two other initial conditions: $\Psi_{AL} = (\delta_{UC=15})/\sqrt{2}$, having non-zero values only at the red and blue sites on the 15th unit cell, and a Wannier function W . **f.** Their chiral polarizations in time are oscillatory signals with well-defined time averages, agreeing with the theoretical value expected from the Wannier function.

both oscillatory signals still lead to the same results. In practice, however, several factors such as friction and onsite potentials hinder the spread of the wave function over many sites.

Comparison to simulations

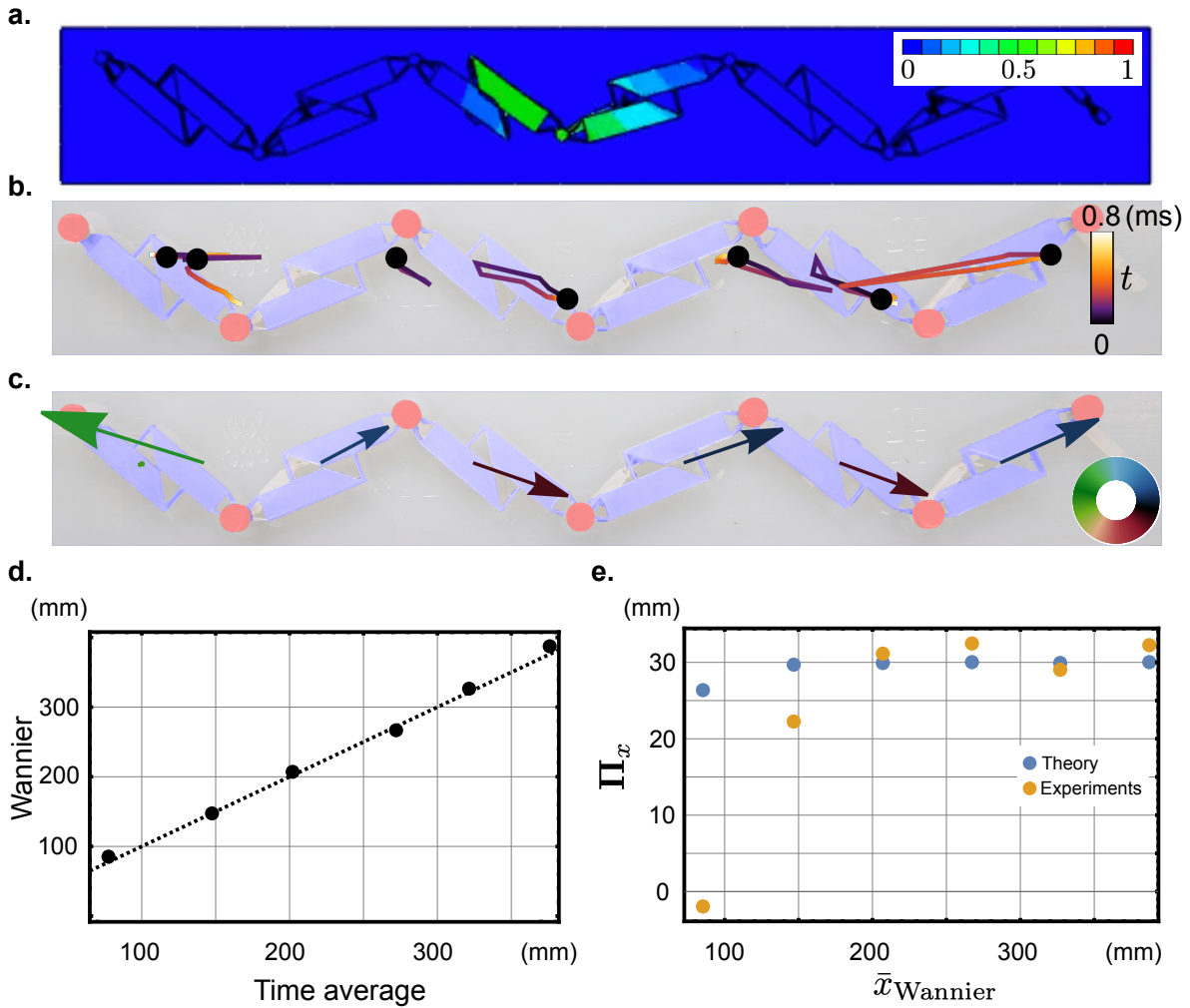


Figure 3.3: **Chiral polarization field from FEM simulations on a mechanical chain.** **a.** Mechanical chain composed of 7 nodes and 6 springs. The initial perturbation is taken as a displacement of a single node. **b.** Superposition of the centers' trajectories drawn by the perturbations over 0.8ms **c.** The time average chiral polarization field, computed over the same period, shows a right polarized bulk. At the left edge, however, the polarization points in the opposite direction. This discontinuity in the polarization field is linked to the floppy mode observed in fig. 3.1a. **d.** By pairing each center with the nearest theoretical Wannier center, we obtain an average discrepancy of 3.1%. **e.** The chiral polarization obtained both from simulations and theory (low-energy model) displays an average discrepancy of 25% mainly due to the small size of the sample. Away from the left edge hosting the floppy mode, the experimental measurements agree with the theoretical value, $\Pi_{x\text{theory}} \sim 30\text{mm}$.

Using the finite element method (FEM), we performed simulations on a mechanical chain consisting of seven nodes and six springs. Specifically, we look at the evolution of the system when subject to deformations localized on each node, fig. 3.3a. Each perturbation defines signals for both the centers and the chiral polarization, fig. 3.3b. Their time averages lead to the chiral polarization field, fig. 3.3d. We compare the results with the theoretical values obtained from the linearized model, finding a very good agreement, fig. 3.3d,e. We quantify the discrepancy as $(x_{\text{theory}} - x_{\text{experiment}})/x_{\text{theory}}$, with x the time average center. The average discrepancy over all the centers is 3.1%, leading to the expected chiral polarization field. It is worth noting, that the discrepancy of the chiral polarization increases when approaching the floppy mode, as seen in fig. 3.3e.

Beyond 1D

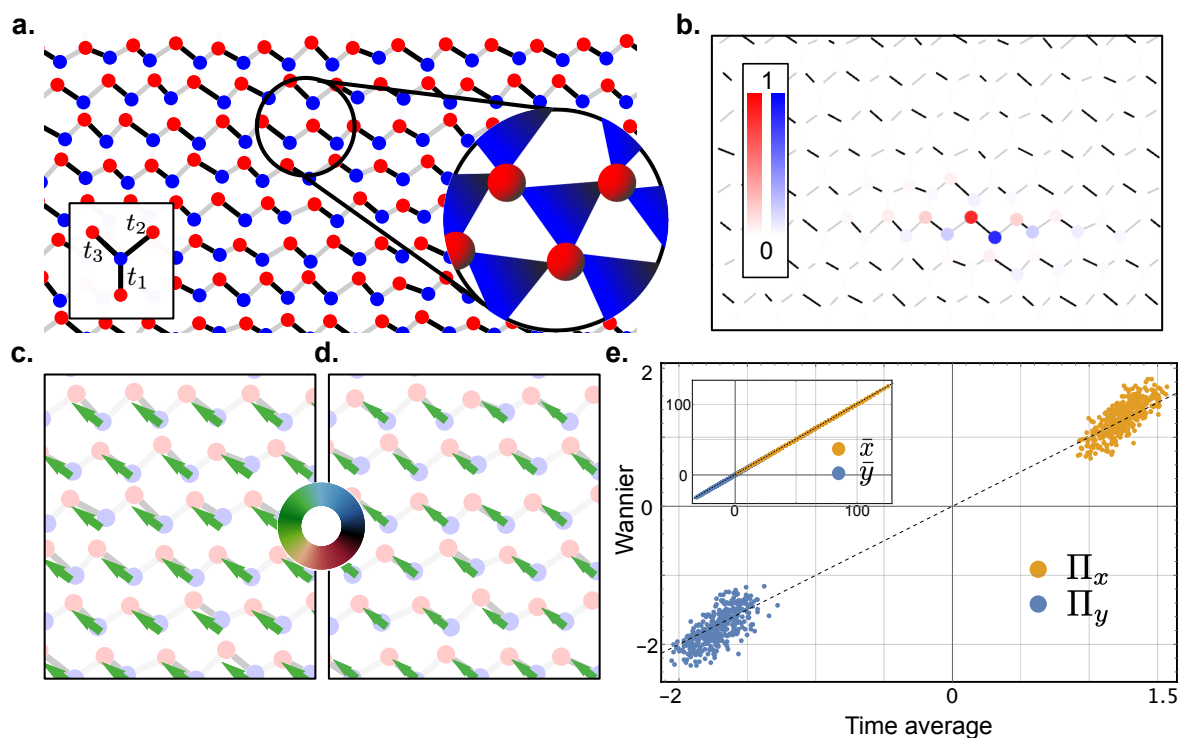


Figure 3.4: **A two-dimensional mechanical example: the mechanical honeycomb lattice.** **a.** The mechanical structure made out of beads (red) connected by triangular plaquettes (blue) is modeled by a tight-binding hamiltonian over a slightly distorted honeycomb lattice with hopping parameters t_1 , t_2 , and t_3 along the three different primitive vectors. In this example we consider $t_1 = 0.1$, $t_2 = -1$, $t_3 = 5$, directly proportional to the opacity of the links between sites. **b.** The Wannier functions define chiral molecules of one red and blue site. **c.** The chiral polarization field issued from the Wannier functions qualitatively coincides with the field, obtained from time-averaging measurements over a period $T/t_0 = 1$ (with $t_0 = \sqrt{m/k}$ the natural time-scale set by the mass and stiffness), **d.** **e.** A quantitative comparison reveals that the average discrepancies between both methods are smaller than 10% for the polarizations, and 0.4% for the centers.

We also corroborate the adequacy of the dynamical method in two-dimensional sys-

tems. Inspired by the mechanical graphene made of balls connected by triangular plaquettes [127], fig. 3.4a, we simulate the evolution of localized states with the chiral hamiltonian \mathcal{H} defined on the honeycomb lattice. It corresponds to a nearest-neighbor tight-binding hamiltonian with three hopping parameters t_1 , t_2 , and t_3 . The initial states are taken as displacements on single degrees of freedom. Theoretically, the Wannier functions span one degree of freedom and one constraint, fig. 3.4b. Both results, from the local functions and the dynamical method, reveal the same chiral polarization field, fig. 3.4c,d. The discrepancies between the two approaches is smaller than 0.4% for both components of the molecules centers $(\bar{\mathbf{x}}, \bar{\mathbf{y}})$, and 10% for the the polarizations, $(\bar{\Pi}_x, \bar{\Pi}_y)$, fig. 3.4e.

3.2.3 Polyatomic chiral molecules and higher-order insulators

Experiments, theory, and simulations validate the use of local responses to characterize mechanical systems such as the mechanical SSH model and the mechanical graphene, realizing the simplest models of chiral insulators in one and two dimensions. Their simplicity can also be seen in the chiral molecules they define. They contain only one degree of freedom (bead) and one constraint (spring), the minimum amount to ensure a null chiral charge, fig. 3.4b. More complex systems possess chiral molecules of several degrees of freedom and constraints which sometimes may not compensate, leading to hyperstatic materials [27]. We dub these examples polyatomic chiral systems.

As with electrostatics, the richer distribution of chiral charges inside these molecules may not be completely captured by the chiral polarization but require higher moments such as quadrupoles and octupoles. Here, we focus solely on the material characterization of chiral systems through the chiral polarization and we leave the natural extension to higher moments for future perspectives. As we will see, the chiral polarization field is very informative even for complex distributions of charges.

To illustrate the consequences of the polyatomicity, we begin with a toy model: the chiral checkerboard lattice depicted in fig. 3.5a. Under the proper hopping ratios, the checkerboard lattice has an energy gap and hosts zero-energy modes at the corners of the sample, fig. 3.5b. This is the simplest example of a higher-order topological insulator (HOTI) [52, 53], a family of topological materials which confine their protected edge-states to codimensions lower than $D - 1$, with D the bulk dimension. For our current purposes, the nature of the material, whether a normal topological insulator (TI) or a HOTI, will not play any role in the determination of the chiral molecules and the chiral polarization field. It will, however, have direct consequences on the prediction of the zero-energy modes discussed in the next section.

In the bulk, each Wannier function spans four sites: two degrees of freedom and two constraints. Moreover, pairs of Wannier functions are defined over the same spatial domain, fig. 3.5c. Here the map from one single Wannier function to a chiral molecule is broken. Instead, each pair of Wannier functions sharing the same support define a chiral molecule of two degrees of freedom and two constraints. If we were to define the chiral polarization field according to the Wannier functions, we would obtain the discontinuous field illustrated by fig. 3.5e,f. However, taking the average over the chiral molecule leads to a zero-field, as expected by the symmetry of the checkerboard lattice.

How then do we group the Wannier functions defining the same molecule? From fig. 3.5e, we see that the Wannier centers inside the same chiral molecule are separated

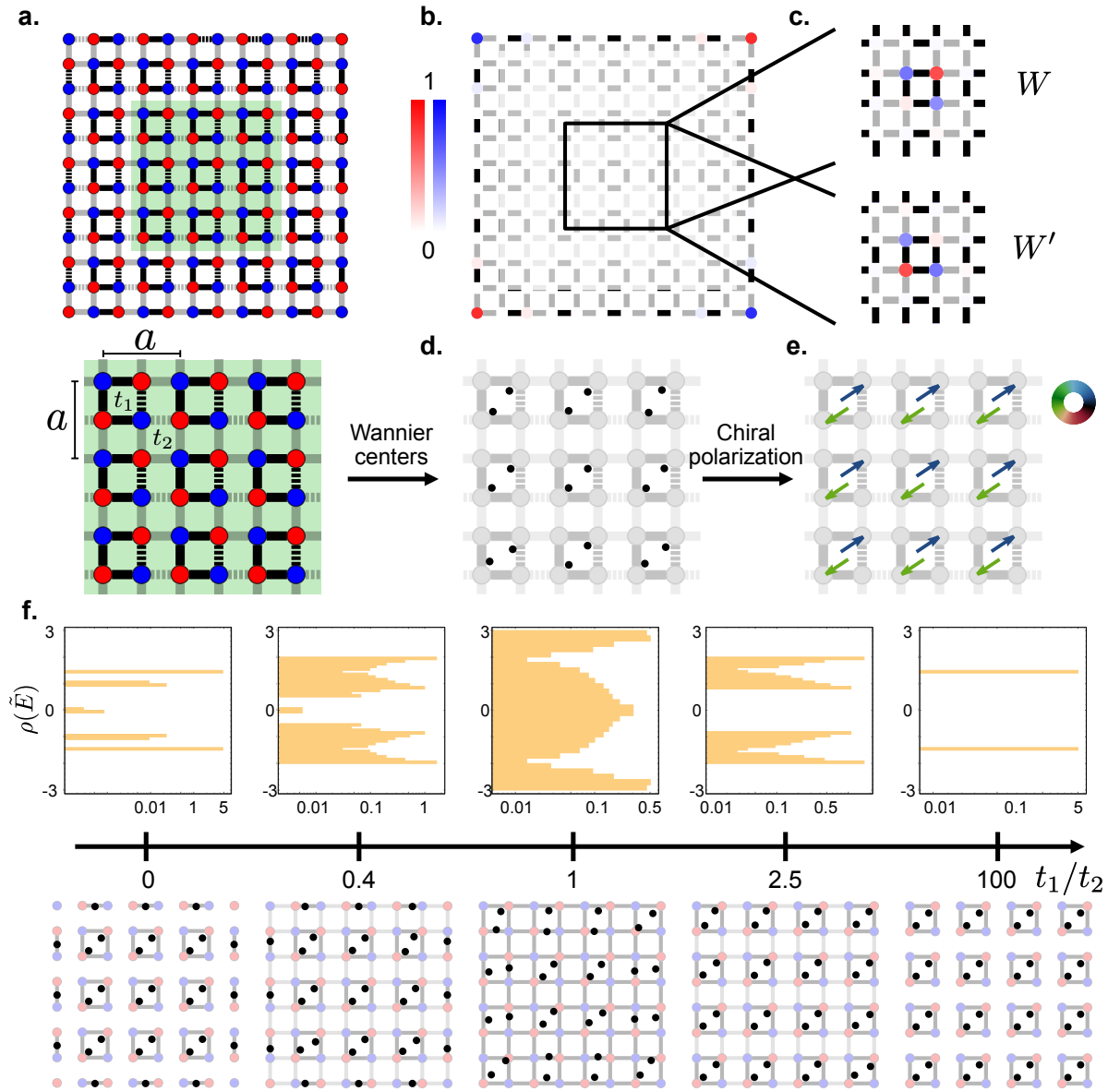


Figure 3.5: **Polyatomic chiral molecules in the checkerboard lattice.** **a.** (top) A finite checkerboard lattice enjoying a sublattice symmetry highlighted in red and blue. The strength of the hopping interactions is proportional to the opacity of the links. Solid (dashed) lines correspond to positive (negative) hopping parameters. (bottom) For illustrative purposes, we only consider two hopping parameters. The bonds around each plaquette have either a hopping strength t_1 or t_2 . The size of the unit cell is $a \times a$. **b.** For hopping values $t_1/t_2 > 1$, the system exhibits four localized zero-energy corner states. Their amplitude is characterized by the opacity of the color, with red and blue indicating the respective sublattice. **c.** In the bulk, there are pairs of orthogonal Wannier functions, W and W' , sharing the same support on the lattice; a signature of its polyatomicity. **d.** The Wannier centers of each chiral molecule are separated by a distance δ smaller than the unit cell size a . **e.** For each Wannier center we obtain a polarization. The average polarization per chiral molecule turns out to be zero in the crystalline case. **f.** (top) Density of states for the normalized eigenenergies $\tilde{E} = E/\max(t_1, t_2)$ for several hopping ratios interpolating between the cases with corner states ($t_1/t_2 < 1$) and without ($t_1/t_2 > 1$). In the transition point, $t_1/t_2 = 1$, the gap closes and the system is no longer an insulator. (bottom) The spatial distribution of the Wannier centers is independent of the energetics; it only reflects whether the system is in one phase or another.

by a finite distance δ , smaller than the lattice spacing a . This suggests a length-scale criterium: grouping local functions with $\delta < a$. We can validate this observation by tracking the changes of δ while sweeping the hopping ratio t_1/t_2 from the trivial to the topological phase, fig. 3.5f,g. While the Wannier centers rearrange when going from one phase to the other, δ remains constant regardless of the hopping parameters. The intramolecular distribution of the centers breaks the 4-fold symmetry of the lattice, which is explained by the negative and positive hopping parameters, fig. 3.5d.

This criterion also applies to the evolution of localized perturbations. As seen in fig. 3.6a, the centers of localized perturbations define noisy yet confined trajectories on the length-scale δ . Once again, the signal obtained from the perturbations is oscillatory with well-defined time averages, fig. 3.5b,c. The chiral molecule is experimentally extracted from the perturbations signals $\{\Psi_1, \Psi_2, \dots\}$ whose centers revolve around the same restricted region. From these molecules we can obtain the average signal, both in time and among the perturbations that will yield the average center and polarization. Mathematically speaking, the average centers and polarizations from eqs. (3.10) and (3.11) are defined as

$$\bar{\mathbf{r}} \equiv \sum_{\Psi \in U} \left(\frac{1}{T} \int^T dt \langle \Psi(t) | \hat{X} | \Psi(t) \rangle \right) \frac{1}{N} \quad (3.12)$$

$$\bar{\mathbf{\Pi}} \equiv \sum_{\Psi \in U} \left(\frac{1}{T} \int^T dt \left(\langle \Psi(t) | \mathbb{C} \hat{X} | \Psi(t) \rangle - \langle \Psi(t) | \mathbb{C} | \Psi(t) \rangle \langle \Psi(t) | \hat{X} | \Psi(t) \rangle \right) \right), \quad (3.13)$$

where $U = \{\Psi_1, \Psi_2, \Psi_3, \dots\}$ is the set of local perturbations defining the same chiral molecule, and $N = \dim(U)$ is the number of functions per set.

The complete picture is then obtained by perturbing all the sites, generating a whole tiling of chiral molecules and therefore probing the chiral polarization field, fig. 3.6d,e. As expected, the chiral polarization field turns out to be zero in the bulk, due to the fourfold symmetry of the checkerboard lattice. Moreover, the edges are polarized, guiding towards and away from self-stress states and floppy modes, respectively. Notice that by applying local perturbations to an unknown system, we are unaware of the distribution of zero-energy modes. It may happen that we perturb the sites comprising a zero-energy state. The trajectories of these perturbations will also define molecules and polarizations, see the bottom left and upper right corners of the checkerboard lattice in fig. 3.6d,e. However, as we will discuss in the next section, the chiral polarization will be discontinuous at these points. Finally, it is worth noting that this distilled experimental protocol does not rely on any crystalline symmetry. When working with more heterogeneous metamaterials, there is still a length scale distinction between the centers' and molecules' distances.

Comparison to experiments and simulations

Figure 3.7 illustrates the protocol carried out from the linear dynamics of the mechanical twisted kagomé lattice [29]. The initial conditions were taken as displacements on one degree of freedom at a time. Per each perturbation, the average center and polarization are computed over a period $T/t_0 = 10$, with $t_0 = \sqrt{m/k}$, fig. 3.7b. From the ensemble of trajectories over time, we can reconstruct a two-dimensional smooth density distribution

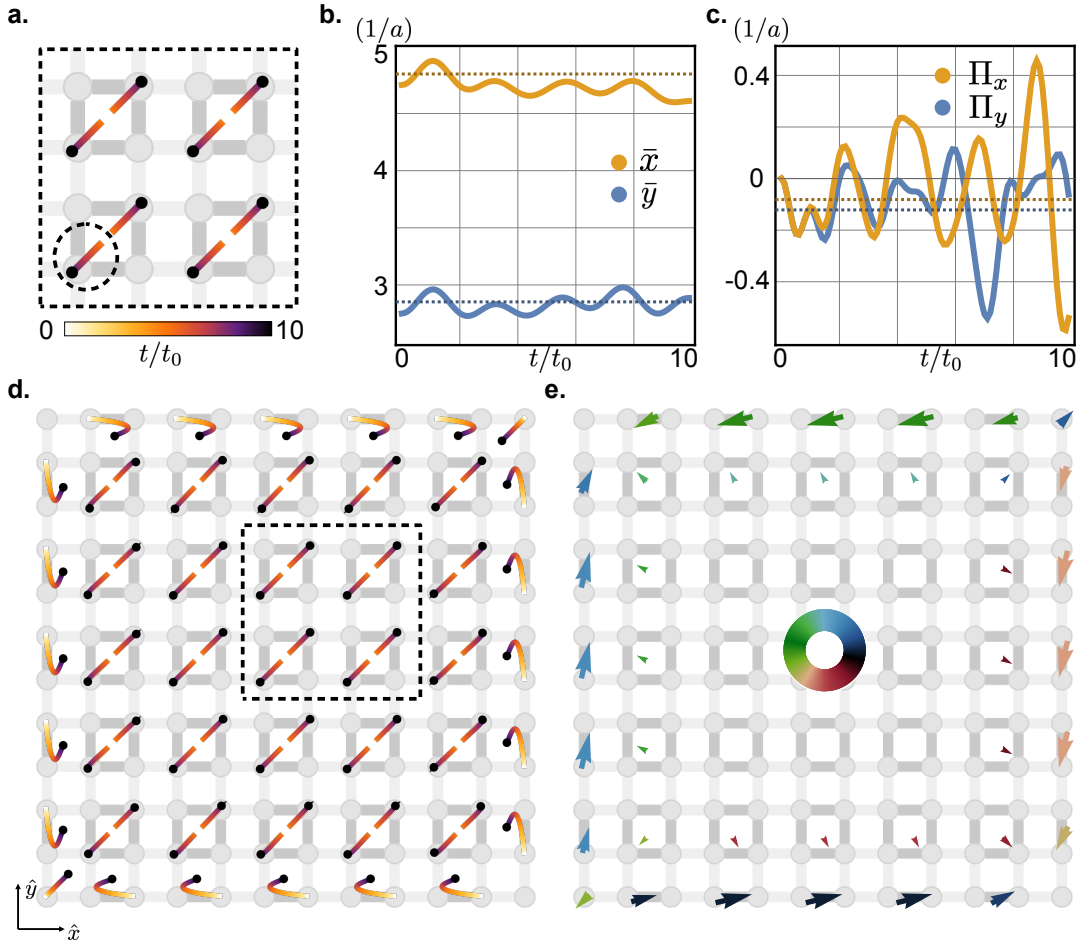


Figure 3.6: **Dynamic measurements in polyatomic systems.** **a.** Trajectories of centers from the evolution of localized states from $t/t_0 = 0$ to $t/t_0 = 10$ ($t_0 = \sqrt{m/k}$ being the natural unit set by the mass and stiffness). The initial states are fully localized on each red site of the checkerboard lattice, see fig. 3.5a. The trajectories jiggle around confined regions, in agreement with the chiral molecules defined from the Wannier functions. **b.** Vertical and horizontal components of the perturbation's center identified by the dashed circle. The oscillatory signals have well-defined time averages (dashed lines) **c.** Components of the chiral polarization in time, together with their time averages. **d.** By measuring the time averages of all the perturbations, we can identify the chiral molecules over which we compute the coarse-grained chiral polarization field, **e.** The coarse-grained polarization in the bulk is zero, in agreement with the local field of fig. 3.5. The edges are polarized, hinting at the presence of zero-energy modes.

of positions, $\bar{\rho}(\mathbf{r})$ using a kernel density estimation. We define the density as

$$\bar{\rho}(\mathbf{r}) = \frac{1}{nw} \sum_{i=1}^n K\left(\frac{\mathbf{r} - \mathbf{r}_i}{w}\right), \quad (3.14)$$

with K a kernel function which we choose as a Gaussian of unit variance, w the bandwidth, and n the number of sampling points (number of centers times number of time frames). $\rho(\mathbf{r})$ clearly distinguishes each chiral molecule, fig. 3.7c. Bulk molecules contain two

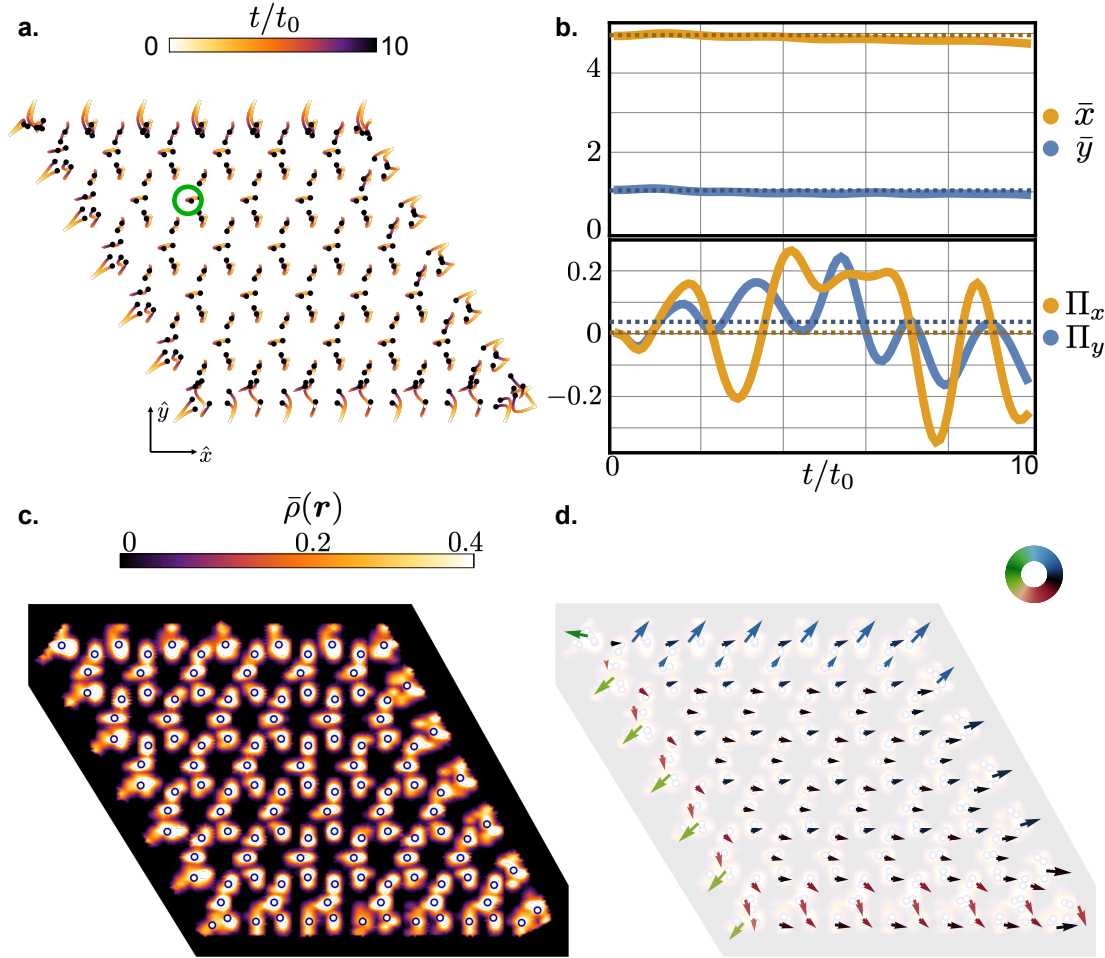


Figure 3.7: **Computing the chiral polarization field in the twisted kagomé lattice (numerics).** **a.** Superposition of the centers' trajectories issued from localized initial states from $t/t_0 = 0$ to $t/t_0 = 10$. The initial states were taken as fully localized in single nodes of one of the sublattices. **b.** Fluctuating signal of the vertical and horizontal components of a perturbation center (top) and the chiral polarization (bottom) for one of the perturbations highlighted by the green circle in **a.**. The dashed line corresponds to the time average over the shown time domain. **c.** Smooth distribution of the centers' positions $\bar{\rho}(\mathbf{r})$. The distribution is obtained from Gaussian kernels of bandwidth $\sim 0.05a$, with a the size of the unit cell. The points indicate the center of each molecule. **d.** The coarse-grained chiral polarization field reveals a uniformly polarized bulk to the right with a discontinuous polarization on the left edge.

centers over which we compute the coarse-grained chiral polarization field, fig. 3.7d. The bulk is characterized by a small yet finite uniform polarization pointing to the right. The left edge, on the other hand, is characterized by a polarization field mainly directed to the left. This discontinuity, absent on the other edges, is the signature of a localized zero-energy mode, as we will see in the next section.

More robust tests are provided by simulations using finite element methods (FEM). As a second example of a polyatomic system, we consider the 3D printed mechanical

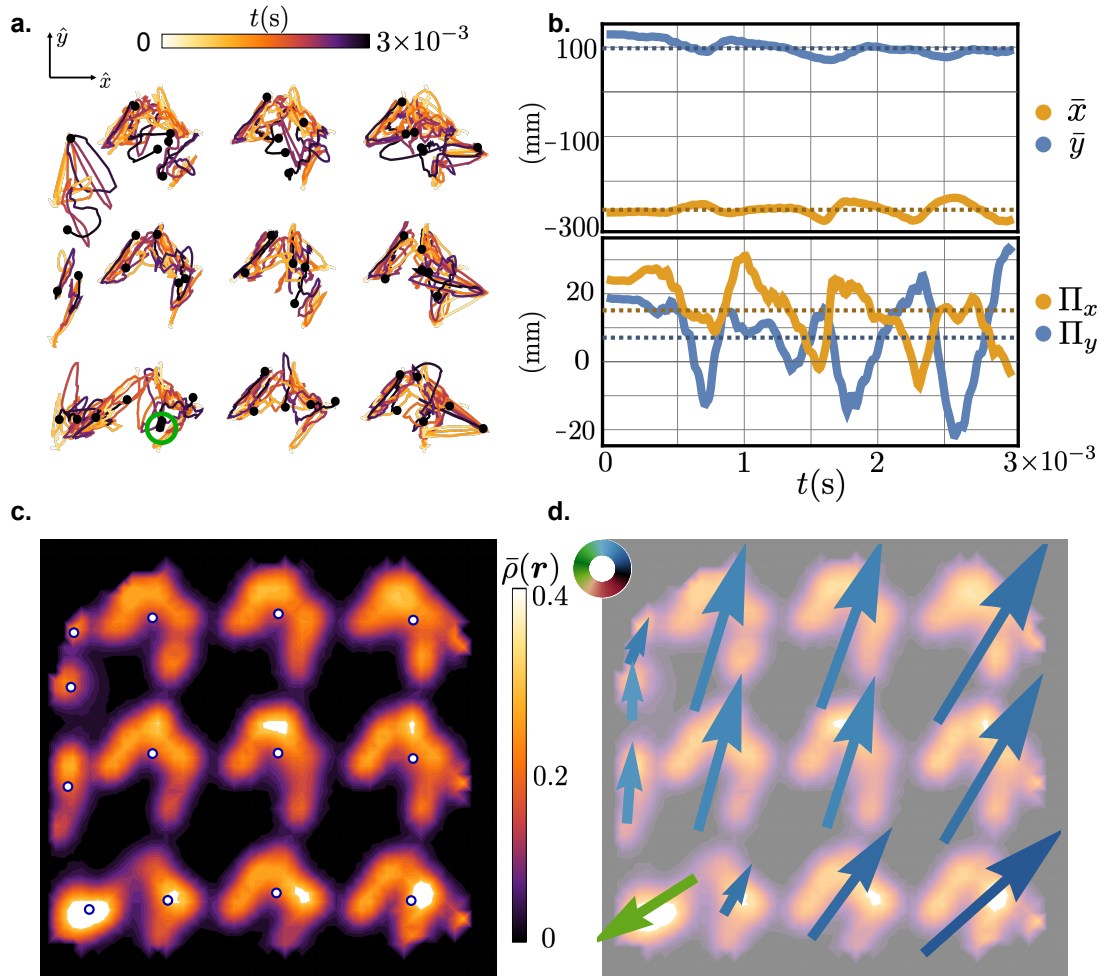


Figure 3.8: **FEM measurements of the chiral polarization in the mechanical HOTI** **a.** Superposition of the centers' trajectories issued from local perturbations from $t = 0$ s to $t = 10$ s. Each individual perturbation consisted in hammering a single node at a time. **b.** Fluctuating signal of the vertical and horizontal components of the perturbation center (top) and the chiral polarization (bottom) for the perturbation highlighted in green. The dashed line corresponds to the time average over the shown time domain. **c.** Smooth distribution of the centers' positions from $t = 0$ s to $t = 3 \times 10^{-3}$ s, $\bar{\rho}(\mathbf{r})$. The distribution is obtained from Gaussian kernels of bandwidth ~ 9 mm. The points indicate the center of each molecule. The chiral molecules defined at the edge are much smaller than those of the bulk. **d.** The coarse-grained chiral polarization field is discontinuous at the bottom-left corner.

HOTI depicted in fig. 3.1c. It shares the same building blocks used for the 3D printed Kane-Lubensky chain. The local states are prepared as displacements on each node of the sample which evolve over a time frame of 3×10^{-3} s, in which the centers and polarizations oscillate in time, fig. 3.8a,b. The ensemble of trajectories diagnoses the chiral molecules, better illustrated via the smooth distribution of positions, fig. 3.8c. In particular, the chiral molecules differ over the bulk, the left edge, and the bottom-left corner differ. The coarse-grained chiral polarization field has a clear discontinuity in the bottom left corner,

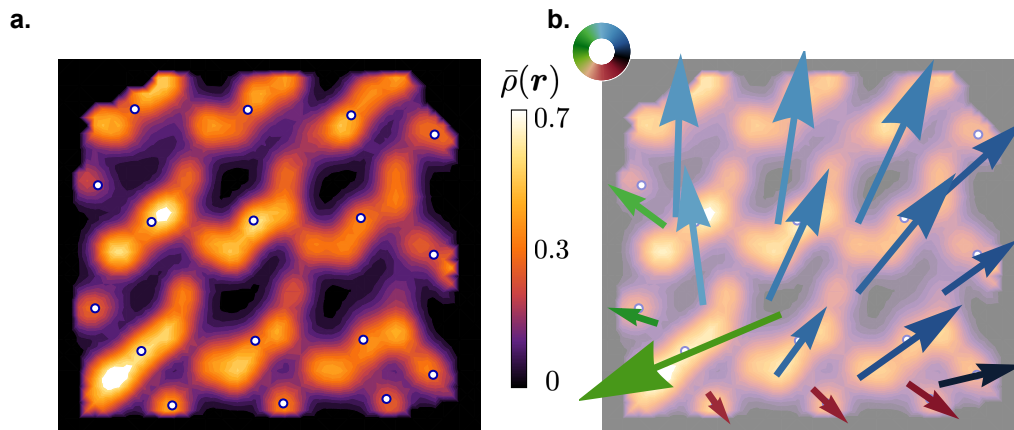


Figure 3.9: **Experimental measurements of the chiral polarization in the mechanical HOTI** **a.** Chiral molecules detected from the response to local forces exerted with a hammer on each node. The positions considered ranged from $t = 0\text{s}$ to $t = 3 \times 10^{-3}\text{s}$. The smooth distribution of centers $\bar{\rho}(\mathbf{r})$ is obtained from Gaussian kernels of bandwidth $\sim 9\text{mm}$. The points indicate the center of each molecule. **b.** Chiral polarization field calculated over each chiral molecule.

fig. 3.8d, which is the node hosting a localized floppy mode.

By individually hammering each node, we also experimentally probe the chiral molecules and the chiral polarization field, fig. 3.9, leading to the same conclusions. The morphological difference between the chiral molecules obtained through simulations and experiments can be explained by the type of perturbation applied, non-linear effects, and dissipation. Regardless, the chiral polarization field, fig. 3.9b, is qualitatively the same, exhibiting a discontinuity in the bottom left corner.

We have introduced a robust and non-invasive method to experimentally probe the chiral polarization of any mechanical metamaterial. Using localized perturbations we detect chiral molecules and therefore the coarse-grained chiral polarization field. How do we use this characterization to predict the physical properties of mechanical insulators? As expected, the answer lies in the bulk-boundary correspondence discussed in chapter 2, connecting the discontinuities of the chiral polarization field to floppy modes and self-stress states.

Importantly, the chiral polarization field is informative at different levels of precision. At the first level, by just identifying the field $\mathbf{\Pi}$ of a regular mechanical system we can significantly filter the possible distribution of zero-energy modes without knowing the exact geometry of the boundary. For example, a system that is polarized to the right, fig. 3.13a,b, can only host floppy modes on the left edge and self-stress states on the right edge, depending on how you cut the system. Floppy modes on the right edge are forbidden. This simple yet powerful observation can be of utmost utility when designing custom metamaterials. But beyond global predictions, we can be predictive at local scales.

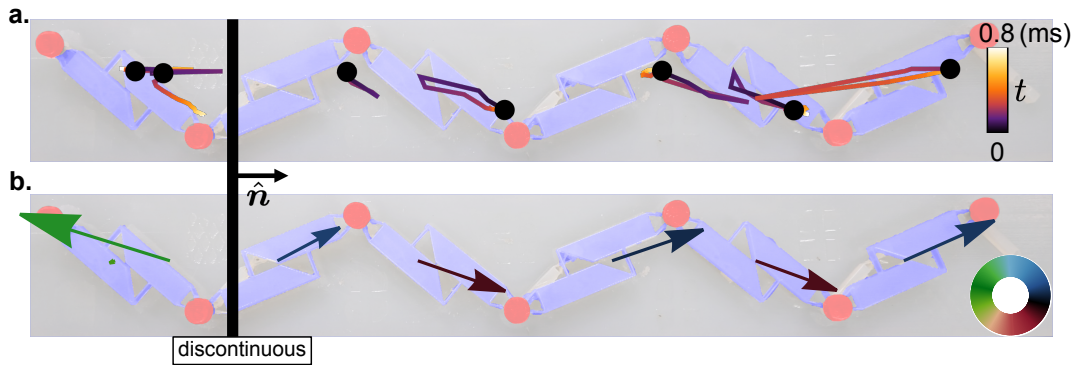


Figure 3.10: **Experimental bulk-boundary correspondence in the mechanical SSH chain.** **a.** We separate edge from bulk according to the chiral molecules defined by the centers' trajectories. The edge is characterized by a normal vector \hat{n} . **b.** The chiral polarization projected onto the normal is discontinuous. The discontinuity being a source of polarization, identifies the presence of a floppy on the left edge of the sample.

3.3 Experimental detection of zero-energy modes

As detailed in the article "Geometry and topology tango in ordered and amorphous chiral matter" [31], discontinuities in the chiral polarization field are the signature of localized zero-energy modes. In what follows I give a step-by-step recipe to predict the location of floppy modes and self-stress states in several classes of mechanical insulators.

3.3.1 Bulk-edge correspondence

The simplest class corresponds to topological insulators (TIs), widely discussed in chapter 2. For simplicity, we exemplify the cases of zero-modes localized at surfaces or edges instead of domain walls, although the reasoning remains unchanged. The first step is to separate the bulk from the edge as defined by the distribution of chiral molecules. In regular materials, the edge will be characterized by well defined normal vector \hat{n} . This is the case, for example, of the mechanical chain depicted in fig. 3.10. Once the edge is determined, we compare the chiral polarization fields projected onto the normal direction. Any discontinuity, here defined as a difference large than the unit-cell size, signals the presence of a zero-energy mode, whose nature is determined by the direction of the field. In our one-dimensional example, the field is discontinuous and the sign indicates the presence of a floppy mode. While the theory would only cover the chiral molecules issued from the Wannier functions, the experiments also probe molecules issued from zero-modes which reveal discontinuous chiral polarizations. Another example is given by the twisted kagomé lattice, fig. 3.11. Here the molecules are polyatomic and we can define at least four edges. On the left edge, the projected field is discontinuous from the one in the bulk and the sign indicated the presence of a floppy mode, as initially measured, fig. 3.1b. The same reasoning on the right edge indicates shows that the field is continuous, hinting at the absence of zero-energy modes.

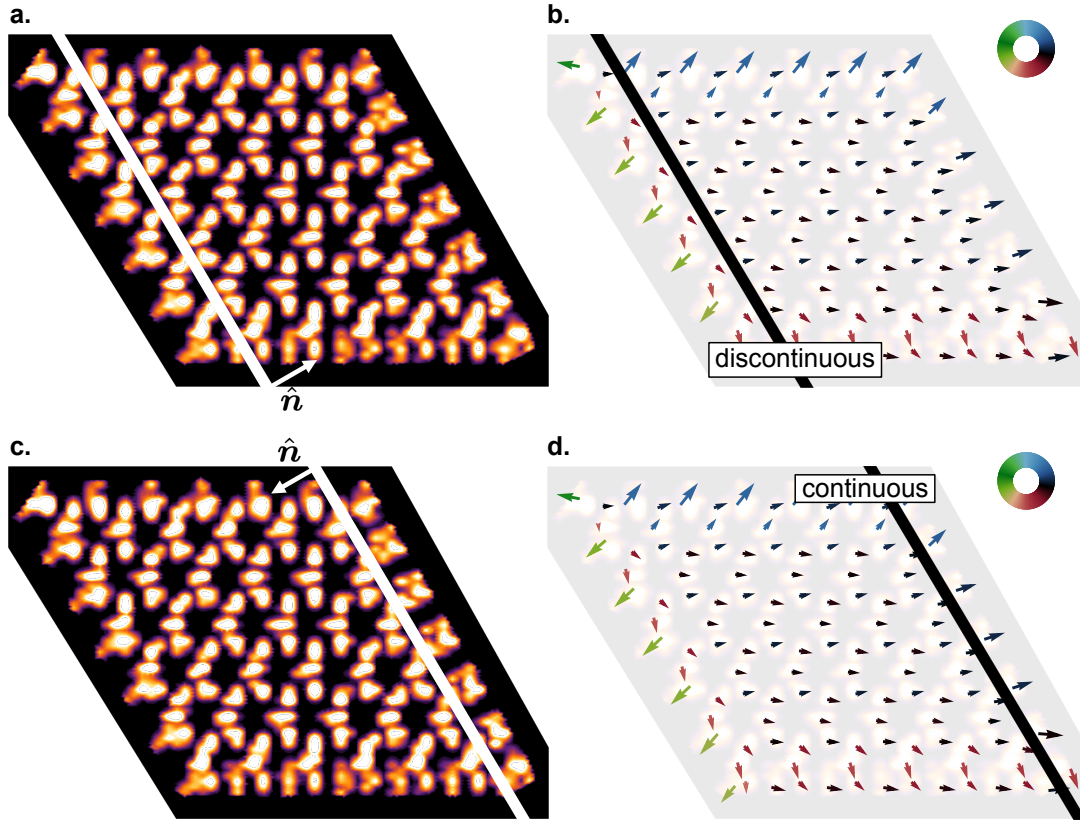


Figure 3.11: **Bulk-boundary correspondence in the twisted kagomé lattice.** **a.** We define the left of the sample with the chiral molecules. **b.** The chiral polarization projected onto the edge normal is discontinuous. The polarization pointing away from the division between bulk and edge indicates the presence of a floppy mode localized on the left edge. **c.** Definition of the right edge in the same sample. **d.** The projected chiral polarization is continuous across the bulk and the edge. There is no zero-energy mode.

3.3.2 Edge-corner

A continuum field between bulk and edge, however, can hide a more subtle distribution of zero-modes. This is the case of higher-order topological insulators (HOTIs) such as the checkerboard lattice and the mechanical system depicted in fig. 3.1c.

Theoretically speaking, the projector onto the negative energy space can be split as

$$\mathbb{P}_{E<0} = \sum_{i,\text{bulk}} |W_i\rangle \langle W_i| + \sum_{i,\text{edge}} |W_i\rangle \langle W_i|. \quad (3.15)$$

The bulk is disconnected from the corner. This observation prompts us to use the chiral polarization field of the adjacent edges to reveal the existence of any potential zero-energy corner state. The strategy then is to get the chiral polarization in the region defined by the subspace $\sum_{i,\text{edge}} |W_i\rangle \langle W_i|$. In practice, this means isolating the edge region according to the distribution of the chiral molecules, guaranteeing no overlap with the positive energy space. For example, in fig. 3.12a, c, the centers' trajectories define clear molecules both in the bulk and in the edges. Each edge has a continuous projected field with the bulk, discarding the presence of any zero-energy edge state. Each edge constitutes a new

polarized system, and we repeat the previous step: we recognize the edge of the edge, i.e. the corner, and analyze the continuity of the projected field. In our example, the field is discontinuous in the corner and the sign of the field reveals the presence of a floppy mode localized in the corner.

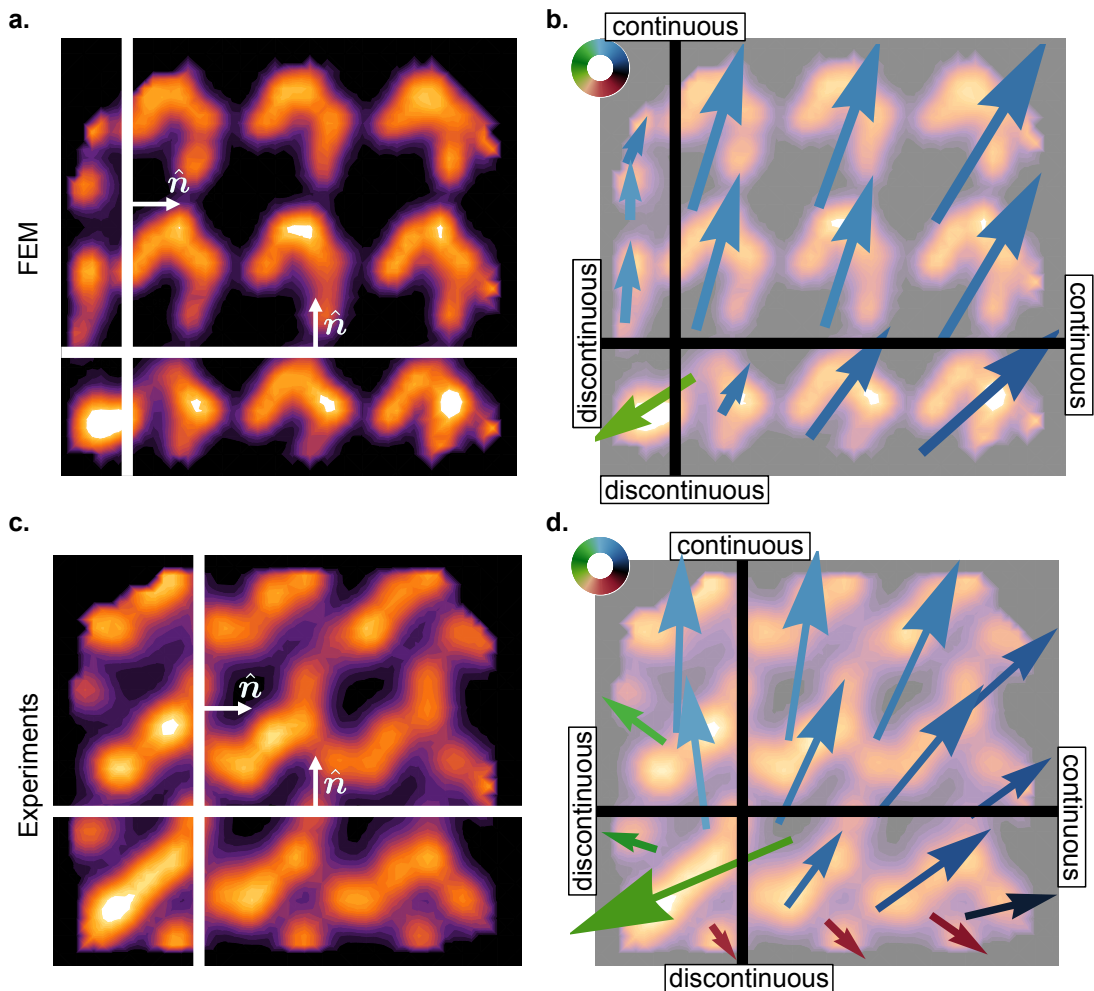


Figure 3.12: **Edge-corner correspondence in the mechanical HOTI.** **a.** Identification of left and bottom edges from the chiral molecule distribution issued by FEM simulations. **b.** While both edges have continuous projected polarizations with the bulk, the edges themselves have discontinuous fields with the bottom-left corner. The sign indicates the presence of a floppy mode localized in the corner. The same reasoning applies to the experimental data, namely, edges separated by the distribution of chiral molecules **c**, and a discontinuity in the field **d**.

The recursive workflow is illustrated in fig. 3.13c for the general case of a D -dimensional bulk insulator. A three-dimensional system, for example, can be analyzed on this recursive workflow at most three times to detect surface, hinges, and corner states. In all cases, the zero-energy modes emerge as discontinuities in the chiral polarization field over the bulk,

surfaces, or hinges.

3.4 Conclusion

We have introduced and experimentally tested a model-free characterization of mechanical chiral materials. This description relies on the response to localized perturbations as a proxy to the Wannier functions. Unlike the MCD and the skew polarization, the chiral polarization is computed in real space without any prescription of unit cells or Bloch convention. The proposed methodology has several consequences. From a conceptual point of view, it unmistakably establishes the dispensable nature of the hamiltonian in order to probe a chiral insulator. It demonstrates that measurements in chiral materials can precede the knowledge of microscopic details.

From an experimental perspective, it constitutes a robust and easy-to-apply protocol to detect and engineer zero-energy modes. Moreover, the experimental determination of the chiral polarization field is local and made in real space, allowing the detection of more complex set-ups such as domain walls or heterogeneous systems.

Theoretically speaking, we have shown that the chiral polarization, a tool originally motivated by normal TIs, can also describe chiral HOTIs. This demonstrates that more complex distributions of zero-modes do not necessarily require higher-order chiral moments such as a chiral quadrupole or octupole, or elaborated tools such as the nested Wilson loops [52, 53] or mirror-graded winding numbers [66], which rely on crystalline symmetries. The information of the chiral polarization field on surfaces and edges informs about zero-modes confined in hinges and corners, respectively. However, the higher-order moments may inform about the distribution of zero-modes from purely bulk quantities. For example, in the checkerboard lattice, we saw that the crystalline symmetry forces the bulk chiral polarization to vanish, fig. 3.6e. The natural next moment to study would be the chiral quadrupolar field:

$$\mathbb{Q} = \sum_{\Psi \in U} \left(\frac{1}{T} \int^T dt \langle \Psi(t) | \mathbb{C} \hat{X} \hat{X} | \Psi(t) \rangle \right). \quad (3.16)$$

We expect this new field to be informative about the corner states without resorting to edge polarizations. In general, though, a zero polarization field is hard to achieve without crystalline symmetries. In this case, the quadrupolar field must be corrected by the polarization and charge contribution. This natural extension to higher-order moments and their implications in the description of chiral materials is left as future work.

Finally, it is worth noting that these results directly translate to photonic systems [95, 109, 110, 128], in which local perturbations are easily induced by local lasing, electric platforms [43, 129], by probing the system with different pulses, and acoustic materials [40, 54, 130] by setting speakers at different locations. All these platforms have realizations enjoying chiral symmetry, and therefore having the chiral polarization field as a material property.

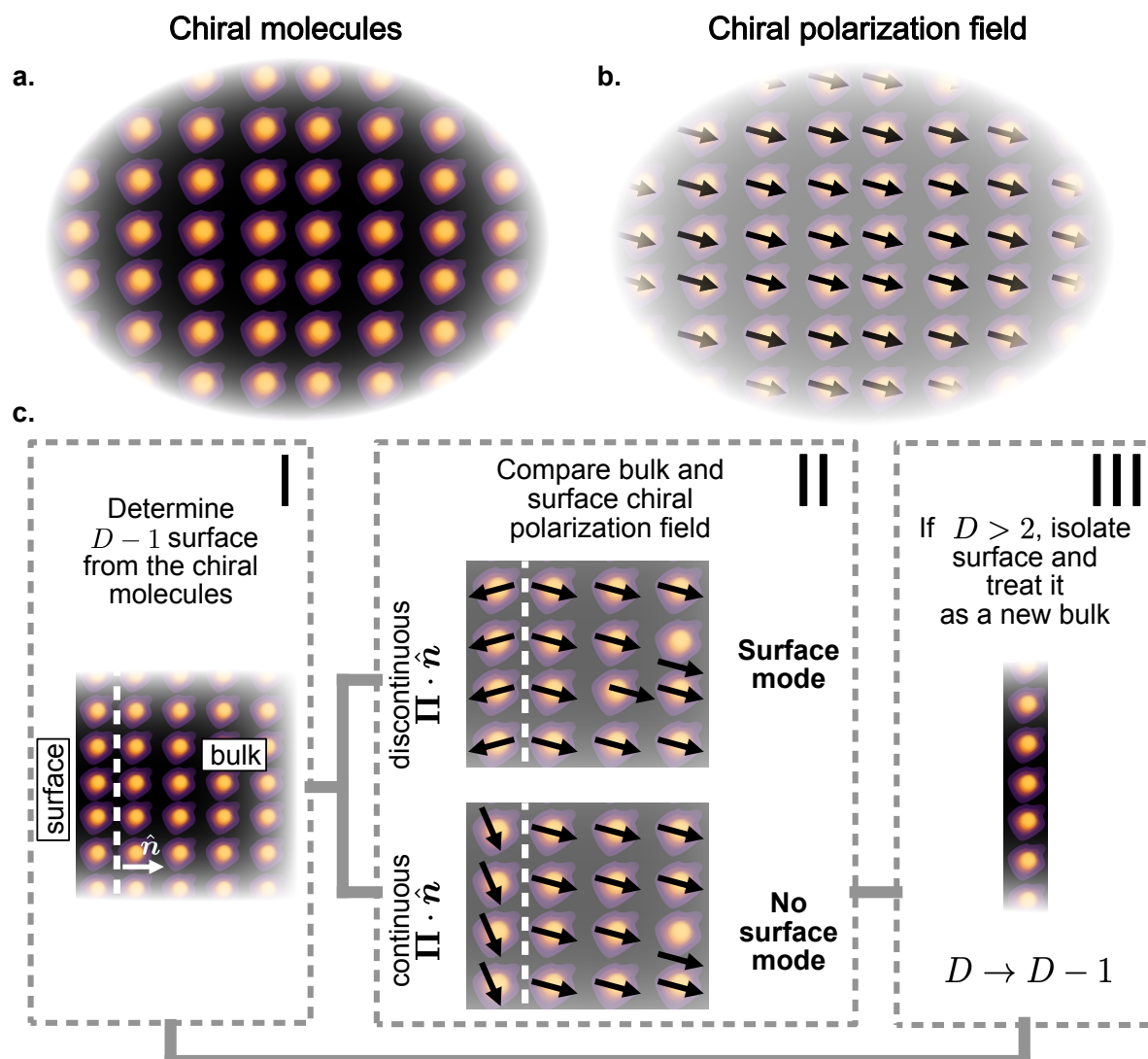


Figure 3.13: **Detection of zero-energy modes in a generic D -dimensional system**
a. To predict the existence of zero-energy states in a mechanical insulator, we first determine the chiral molecules of the D -dimensional bulk. **b.** Even before determining the edges, the coarse-grained chiral polarization field of a regular material informs about the possible distribution of zero-energy modes. In this case, floppy modes (self-stress states) may only appear at the left (right) of the sample. **c.** Diagram of the recursive workflow to detect zero-energy modes. **I:** Tessellate the bulk up to the chosen surface. Separate both regions according to the chiral molecules. The surface is characterized by a normal vector \hat{n} . **II:** Compare both the surface and the bulk chiral polarization projected to the normal. If the projection is discontinuous, there is a zero-energy mode localized on the surface. The type of zero-mode will be dictated by either the source or sink nature of the polarization at the surface. If the projection is continuous, there is no surface mode, although there may be zero-mode localized in smaller dimensions. **III:** For $D > 2$ we can further proceed by isolating the edge and analyzing it as a new bulk system of a smaller dimension $D - 1$. This new system is studied once again, beginning with step **I**.

Topological stiffness of mechanical metamaterials

4.1 Introduction

In the precedent chapters, we have analyzed and understood mechanical systems from the perspective of chirality. This broader paradigm invited both the geometry of the system and the topology of their eigenstates to characterize the softness of a mechanical network. From the elastic response of mechanical materials, we get to classify them into different topological phases. Importantly, the topology described a rather abstract space: the space of occupied eigenstates.

Real space topology, on the other hand, is easily recognizable. From a single glance, we can tell apart balloons from donuts and cylinders from Möbius strips. This prompts us to a very natural question: What are the consequences of non-trivial real-space topology on elastic bodies and their mechanical properties? Taking a (literal) twist from the previous chapter, topology will enter the game as orientability, and the central object of this chapter is the half-twisted ribbon also known as the Möbius strip. This chapter summarizes our work titled "Non-orientable order and non-commutative response in frustrated metamaterials" [55], highlighting its theoretical framework. We will see that non-orientable materials display regions which are topologically protected from any deformation. We rationalize this property by means of the topology of a mathematical space: the real deformation bundle. Non-orientability in real space will translate into the non-orientability of the real deformation bundle, which in turn will explain the existence of the vanishing deformation. We define this property as non-orientable mechanics. In subsequent sections, we bypass the need for real space non-orientability and we show that orientable mechanical antiferromagnets realize non-orientable mechanics. We exploit the consequences of non-orientable mechanics in one and two dimensions and show that it induces non-commutative mechanical responses, providing a new mechanical platform to store information. In higher dimensions, we show that we have topologically protected lines of vanishing deformation. By applying local loads we exploit the non-commutative response and we showcase how we can achieve non-commutative braiding dynamics by moving local loads.

We confront our theoretical results against experiments, confirming the robustness

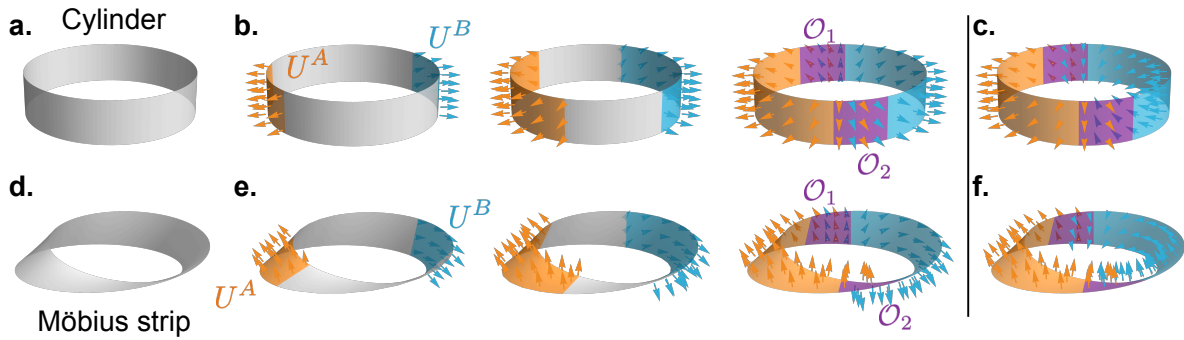


Figure 4.1: **Orientability of periodic ribbons.** **a.** A cylinder is an orientable ribbon: it can accommodate a smooth normal field over its surface. **b.** (left) On each covering, U_A in orange and U_B in blue, we locally define continuous normal fields. We extend the coverings (middle) until they overlap on the violet regions \mathcal{O}_1 and \mathcal{O}_2 (right). In this example, both overlaps disagree, $\sigma(\mathcal{O}_1) = \sigma(\mathcal{O}_2) = -1$ leading to $w_1 = 0$. **c.** Changing the normal convention of the covering U_B renders both overlap compatible, $\sigma(\mathcal{O}_1) = \sigma(\mathcal{O}_2) = 1$. The orientability remains the same, $w_1 = 0$. **d.** A Möbius strip is the simplest realization of a non-orientable surface. **e, f.** Same construction as in **b, c**. Here $w_1 = 1$ regardless of the normal conventions used on the coverings.

of non-orientable mechanics in both non-orientable ribbons and orientable mechanical metamaterials. At the end of this chapter, we enclose our article 4.7 together with its methods 4.8 and supplementary material 4.10. But first things first, what is orientability?

4.2 Orientability

Orientability is a topological property of surfaces. A surface is said to be orientable if we can define a smooth normal field on it. This is the case with spheres, torus, planes, and hollow cylinders, fig. 4.1a. Non-orientable surfaces, on the other hand, cannot accommodate any coherent normal field. In this category, we find the Möbius strip, fig. 4.1d, and the less familiar Möbius shorts, Klein bottle, and real-projective planes. Unlike orientable ribbons (hollow cylinders), characterized by two sides and two edges, a Möbius strip only has one side and one edge.

Formally speaking, non-orientability can be defined as an obstruction. Take for instance the surface of periodic orientable and non-orientable ribbons, fig. 4.1a,d. Choose two opposite poles of the surfaces, U_A and U_B , and on each one make an independent choice of normal, fig. 4.1b,e. Extend the poles with their coherent normals up to cover the whole surface. The two overlaps between the open coverings, \mathcal{O}_1 and \mathcal{O}_2 , will either agree or differ in their normal conventions. We define a function $\sigma(\mathcal{O})$ which gives +1 if the conventions agree and -1 otherwise. Orientability is then defined as $w_1 = (1 - \sigma(\mathcal{O}_1)\sigma(\mathcal{O}_2))/2$, i.e. as the parity of the non-compatible overlaps. If $w_1 = 0$, the surface is said to be orientable, and non-orientable if it equals 1. Notice that modifying the extensions of the overlaps or the normal conventions used in U_A and U_B , leaves w_1 unchanged. w_1 is a topological index indicating the obstruction to define a coherent normal vector field [131].

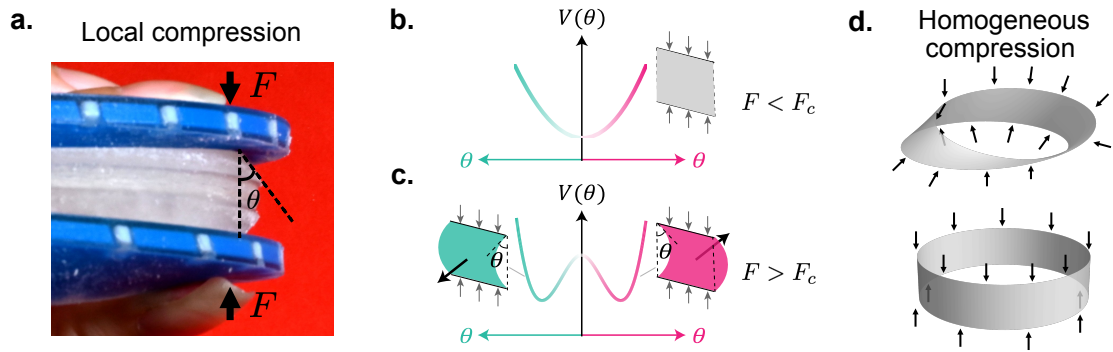


Figure 4.2: **Euler-buckling instability in elastic ribbons.** **a.** Locally compressing a ribbon produces bending deformations which locally define a normal vector. The buckling is issued from an instability. **b.** For compressible loads lower than a critical threshold, F_c , the potential describing the bending deformations is parabolic and the ground state is undeformed. **c.** Above F_c , the buckling is captured by a double-well potential. Each of the wells defines a normal. **d.** Applying homogenous compressive loads on elastic ribbons will induce buckling profiles highly dependent on their orientability.

4.3 Elasticity of non-orientable soft surfaces

Does orientability play any role in the elastic response of these ribbons? and if so, what kind of experiment would spotlight these topological differences? To answer these questions, we must consider two features of (non-)orientability:

1. It is directly inferred from the normal vector field.
2. It is a global property.

The first aspect indicates that any deformation discerning between the elasticity of orientable and non-orientable shapes must depend on the normal of the surface. This is the case, for instance, of buckling deformations. Twisting deformations, on the other hand, depending only on the tangent vector would not be affected by the orientability of the ribbon [131]. We can buckle the ribbon by applying compressive loads F to its edges, triggering the so-called Euler-buckling instability, fig. 4.2a. Above a certain threshold $F > F_c$, the lowest buckling deformation mode picks one of two directions, locally defining a normal, fig 4.2c. The second feature indicates that local measurements are not sufficient to probe orientability. Indeed, locally both the Möbius strip and the cylinder are indistinguishable; they look like flat ribbons. Orientability, or the lack of it, would be best detected from the whole deformation field.

The previous observations suggest that an appropriate experiment to probe the consequences of orientability is to look at the buckling deformation profile when applying compressive loads. Moreover, to discard any geometrical effect from local curvatures, we begin by considering homogenous loads in order to spotlight the effects of topology, fig. 4.2d. Local loads will be treated in section 4.5.

Orientability directly affects the total energy of buckling deformations. To demonstrate this, we first notice that the lowest buckling deformation mode of a ribbon can be described by one angle, $\theta(s)$ indexed by the curvilinear coordinate s of the base circle,

fig. 4.3a. As done in the precedent section, we take two coverings U_A and U_B , this time over the base circle. This is equivalent to taking the height of the ribbon to zero in fig. 4.1. On each covering, we define a continuous deformation angle $\theta_{A/B}(s)$. The energy density at position s in U_A is simply given by the standard elasticity of a ribbon near the onset of the buckling stability

$$u[\theta(s)] = \frac{K}{2}(\partial_s\theta)^2 + V(\theta), \quad (4.1)$$

with K the stiffness, $V(\theta) = V_0(\theta^2 - \theta_0^2)^2$ a quartic potential characterized by its magnitude V_0 and minima $\pm\theta_0$, and $\theta(s) = \theta_{A/B}(s)$ for $s \in U_{A/B}$. The energy over the covering U_A is then obtained by integration, $E_{U_A} = \int_{U_A} ds u[\theta(s)]$, with the same result applying to U_B . Therefore, the total energy of the ribbon is given by the integration over the two coverings minus the overlaps O_1 and O_2 :

$$\mathcal{E} = \int_{U_A} u[\theta(s)]ds + \int_{U_B} u[\theta(s)]ds - \int_{O_1} u[\theta(s)]ds - \int_{O_2} u[\theta(s)]ds. \quad (4.2)$$

We can shrink the overlap regions O_1 and O_2 to open sets of length ϵ centered around s_1 and s_2 , respectively, and take the limit $\epsilon \rightarrow 0$. In addition, we can always choose a convention in such a way that the overlap O_1 is compatible: $\theta_A(s_1) = \theta_B(s_1)$. This means that the integral over the overlap O_1 is identically zero:

$$\int_{O_1} u[\theta(s)]ds = \lim_{\epsilon \rightarrow 0} \epsilon \left\{ \frac{K}{2} \left(\frac{\theta_A(s_1) - \theta_B(s_1)}{\epsilon} \right)^2 + V(\theta_A) \right\} + O(\epsilon) = 0. \quad (4.3)$$

If the ribbon is orientable, the same reasoning applies to O_2 . On the contrary, when non-orientable, O_2 corresponds to an incompatible overlap and $\theta_A(s_2) = -\theta_B(s_2)$. The deformation profile is discontinuous and the integral does not vanish:

$$\begin{aligned} \int_{O_2} u[\theta(s)]ds &= \lim_{\epsilon \rightarrow 0} \epsilon \left\{ \frac{K}{2} \left(\frac{\theta_A(s_2) - \theta_B(s_2)}{\epsilon} \right)^2 + V(\theta_A) \right\} + O(\epsilon) \\ &= \lim_{\epsilon \rightarrow 0} \frac{2K\theta_A(s_2)^2}{\epsilon}. \end{aligned} \quad (4.4)$$

We emphasize that s_2 can be any point on the base circle, there is no a priori prescription to it. Using eqs. (4.3) and (4.4) in the total energy (4.2), and denoting $s^* = s_2$ the generic position of the overlap O_2 , the total energy of an elastic ribbon reads

$$\mathcal{E} = \int ds \left\{ \frac{K}{2}(\partial_s\theta)^2 + V(\theta) \right\} - 4Kw_1 \lim_{\epsilon \rightarrow 0} \theta^2(s^*)/\epsilon. \quad (4.5)$$

For orientable ribbons, $w_1 = 0$ and eq. (4.5) is the standard energy obtained by integration of the energy density (4.1) along the base circle. Notably, for non-orientable ribbons, $w_1 = 1$, and an extra term exists in the expression of the energy. The limit in ϵ , being divergent, constraints the deformation field to vanish at the unprescribed position s^* . Non-orientability protects the arbitrary point s^* from any finite deformation; it endows the homogeneous ribbon with a non-homogeneous effective stiffness. An alternative demonstration of this result, based on taking the continuum limit of a discrete model can be found in [131] and the supplementary information 4.10.2.

As we show next, the consequences of real-space non-orientability are directly related to the non-orientability of a different mathematical object: the elastic deformation bundle.

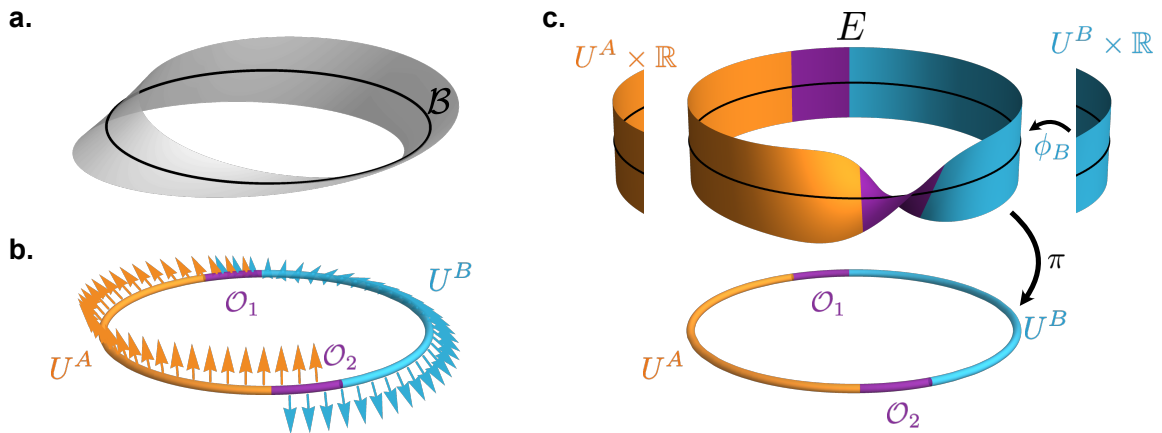


Figure 4.3: **Real line deformation bundle of the elastic Möbius strip.** **a.** The base space \mathcal{B} of the buckling deformations in a Möbius strip corresponds to a circle. **b.** Using the construction of fig. 4.1, we define two coverings, U_A (orange) and U_B (blue), and two overlaps (violet), \mathcal{O}_1 and \mathcal{O}_2 . Here, overlap \mathcal{O}_2 has two incompatible normal conventions. **c.** The total space E is constructed by the set vectorial space formed by all the fibers F . At each position s in the base circle \mathcal{B} we define a real fiber $F = \mathbb{R}$. Any subspace of E is locally homeomorphic to the product space $\mathcal{B} \times \mathbb{R}$: it defines a local trivialization $\pi^{-1}(U^B) = \phi_B(U^B \times \mathbb{R})$, where ϕ_B is a smooth mapping and π the local projection $E \rightarrow \mathcal{B}$. Globally, this is not true. E is homeomorphic to a Möbius strip and the deformation bundle is non-orientable.

4.3.1 The elastic deformation bundle

We built the total energy starting from the base circle, two coverings U_A and U_B , and two overlaps \mathcal{O}_1 and \mathcal{O}_2 . At each position s in the base circle, we assign a deformation $\theta(s)$ which in principle can take any real value. This ensemble of possible deformation at a given position is known as a real fiber F and the ensemble of fibers, indexed by s , defines the total space of deformations, or real vector bundle, E , fig. 4.3. In section 4.2 we define the orientability of surfaces as an obstruction. The same construction applies to fiber bundles. By virtue of the continuity of the deformation field, any incompatible overlap will enforce a twist in the total space E . In mathematical terms, this represents a non-orientable fiber bundle, i.e. the total space E , while locally being the product space $\mathcal{B} \times F$, has a different topological structure. Moreover, the orientability of a real fiber bundle is characterized by the same topological index introduced in eq. (4.5): the first Stiefel-Whitney index w_1 [132]. Now we can clearly understand the topological origin of the vanishing deformation point s^* . Any continuous deformation profile, depicted as a loop in the total space E , fig. 4.4a, is topologically constrained to cross the zero deformation point, regardless of the shape of the loop. Orientable fiber bundles, on the other hand, are free from this limitation, fig. 4.4b. The non-orientability of the real deformation bundle lies at the root of the topologically protected undeformable point in Möbius strips.

How does non-orientable physics generalize to higher-dimensional objects?

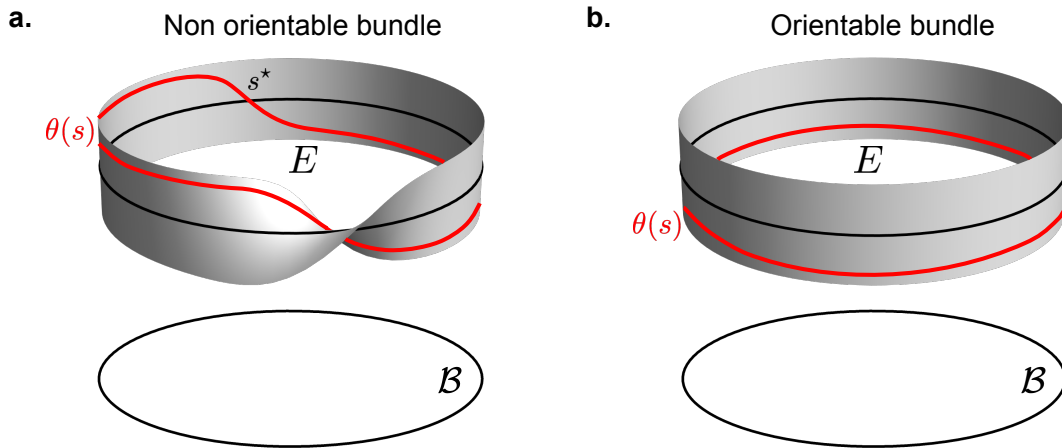


Figure 4.4: **Deformation profiles of ribbons.** **a.** A continuous deformation profile $\theta(s)$ is represented as a loop (red line) on the total space E of the deformation bundle. For non-orientable systems, the loop is constrained to cross the zero-deformation at a position s^* , regardless of its shape. **b.** This is not true for orientable systems. Moreover, on homogeneous systems, energetics will favor homogeneous profiles of finite deformation.

4.3.2 Higher-dimensional non-orientable soft surfaces

Limited by our dimensions, we cannot conceive closed non-orientable surfaces such as the Klein bottle or the Boys surface. They cannot be embedded in our three-dimensional world due to self-intersections. However, while no longer closed, a holey Klein bottle is achievable in 3D. This non-orientable object is homeomorphic to the fusion of a cylinder and a Möbius strip, also known as Möbius shorts. In other words, one can continuously deform one into the other, like a donut into a cup; they are topologically the same objects, fig. 4.5a. Its real

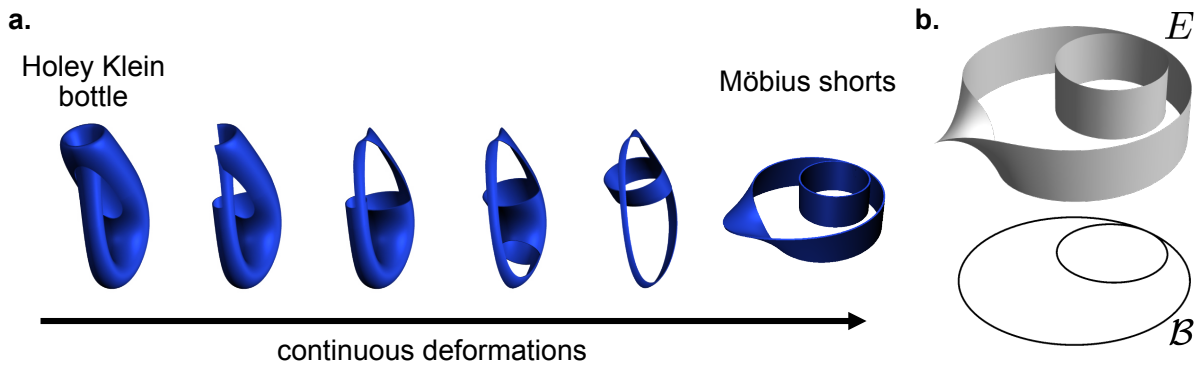


Figure 4.5: **Moebius shorts** **a.** A holey Klein bottle is an open non-orientable surface that can be realized in 3D without self-intersections. By enlarging the whole, we can continuously map it to the Möbius shorts. **b.** The deformation bundle of the Möbius shorts is non-orientable. The base space is the junction of two loops, and the total space is a Möbius shorts itself. Any deformation profile, represented as a loop in the total space, must vanish at a point s^* . While topology cannot determine the location of s^* , the energetics constrain it to be at the opposite pole of the intersection between the two surfaces.

vector bundle, easily constructed by the same principles used in the previous section, is itself a Möbius shorts, fig. 4.5b. Non-orientability manifests itself through the existence of a zero deformation point on the system. Möbius shorts of homogeneous stiffness, however, do not enjoy the spontaneous symmetry breaking displayed by the Möbius strips. Indeed, the system itself is heterogeneous and energetics will place the zero node at the furthest point from the junction between the Möbius strip and orientable ribbon.

4.3.3 Experimental measurements on soft surfaces

We tested the theory behind non-orientable mechanics thanks to our experimental collaborators Xiaofei Guo and Corentin Coulais from the University of Amsterdam. They have 3D printed both orientable and non-orientable soft ribbons of n half twists, with $n = \{0, 1, 2, 3\}$. By placing them inside a plastic bag and pumping the air, they apply a homogenous compressive load (see Methods 4.8 for details). The lowest energy configuration, as predicted, enjoys a zero-deformation point whenever the surface is non-orientable, fig. 4.6.

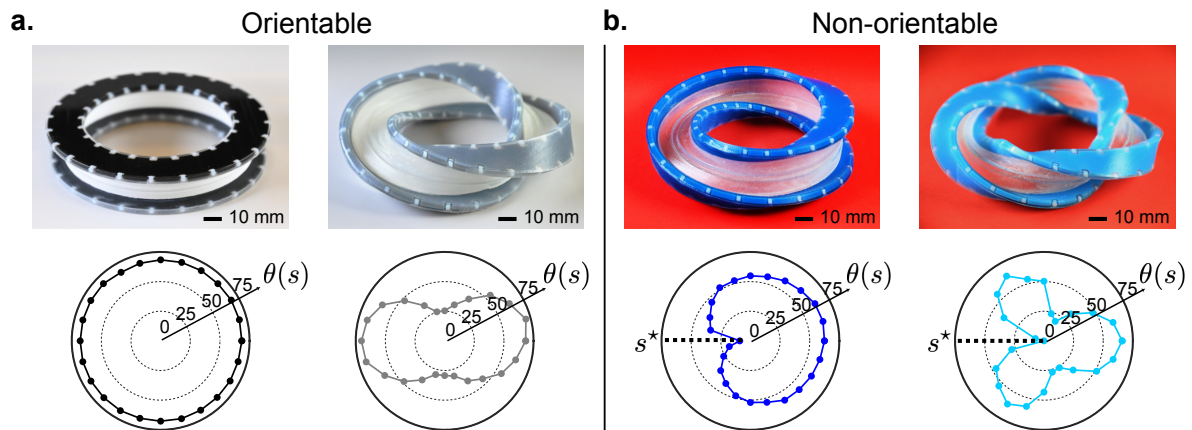


Figure 4.6: **Experimental deformation profile under homogeneous compression.** **a.** (top) two orientable 3D printed ribbons: no twist (cylinder) and two half twists. (bottom) The deformation profile of the cylinder is completely homogeneous. The local curvature of the two-half twisted ribbon induces heterogeneities. **b.** Same as before, this time for non-orientable ribbons: one and three half-twists. In both cases the deformation profile exhibits a point s^* in which the deformation field identically vanishes.

The same experimental procedure can be carried out on the Möbius shorts, for which the zero-deformation point is pinned at the furthest location away from the cylinder.

We have seen that non-orientability elastic surfaces are limited to one-dimensional or punctured two-dimensional systems. The last case, however, does not enjoy a spontaneous symmetry-breaking process since the system is intrinsically heterogeneous. Consequently, there is no degree of freedom associated with the position of the zero deformation point. As we will see in section 4.5, having this degree of freedom offers novel and exotic features for systems under heterogeneous compressions.

Notably, the local rigidity properties of non-orientable soft surfaces are ultimately rooted in the non-orientability of their elastic deformation bundles. In the next section,

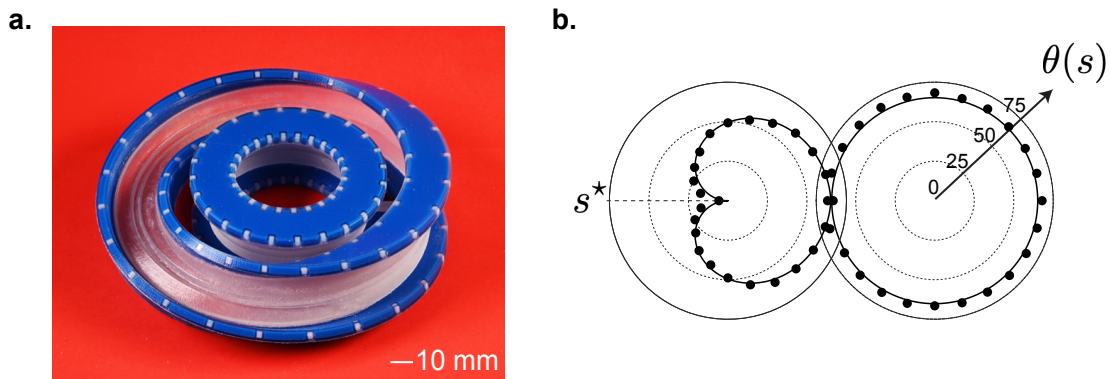


Figure 4.7: **Experimental deformation field of a Möbius shorts under homogeneous compression.** **a.** A 3D printed Möbius shorts is implemented by printing both a cylinder (inner ribbon) and a Möbius strip (outer ribbon). Both are connected at the highlighted position. For details on the manufacturing see the supplementary information 4.10.5. **b.** Deformation profile of the Möbius shorts when subject to a homogenous compressive load issued from pumping the ziplock bag. The zero-deformation point locates at the farthest point from the joint between the two ribbons.

we show that this crucial observation allows us to exploit non-orientable mechanics beyond the frame of real-space topology.

4.4 Frustrated metamaterials

Since orientable (meta)materials are the norm, one natural question to ask is whether we can bypass real space non-orientability and benefit from the advantages of non-orientable deformations bundles. Here we show that it is possible thanks to global frustration. Before explaining how globally frustrated systems realize non-orientable mechanics, we show how to devise it and reveal the similarities with the response of non-orientable surfaces.

One way to achieve global frustration is through antiferromagnetic interactions. In mechanics, this can be realized by connecting square plaquettes through their vertices, generating the metamaterial shown in fig. 4.8a [133]. Upon a local compressive load, the system buckles to one of two possible states alternating clockwise and counterclockwise rotations, fig. 4.8b,c,d. This phenomenon is in direct relation to the buckling instability of elastic ribbons, although here, the deformation profile alternates between opposite rotating units.

Gluing both ends of a finite array of plaquettes forms a metaring. Upon a homogenous compressive load, fig. 4.8e, the metaring exhibits different mechanical responses depending on the number of pairs of plaquettes, whether it is even or odd. Even-metarings display a homogeneous deformation profile, whereas odd-metarings are globally frustrated.

The low energy deformations of a metaring are captured by the shearing-bending model introduced in [133] and rederived in the supplementary information 4.10.2 to account for the global frustration. Here we briefly summarise the results and demonstrate that metarings can realize non-orientable mechanics. To do so, we first show that the parity of the metarings - either an odd or even amount of units - is in direct correspondence with

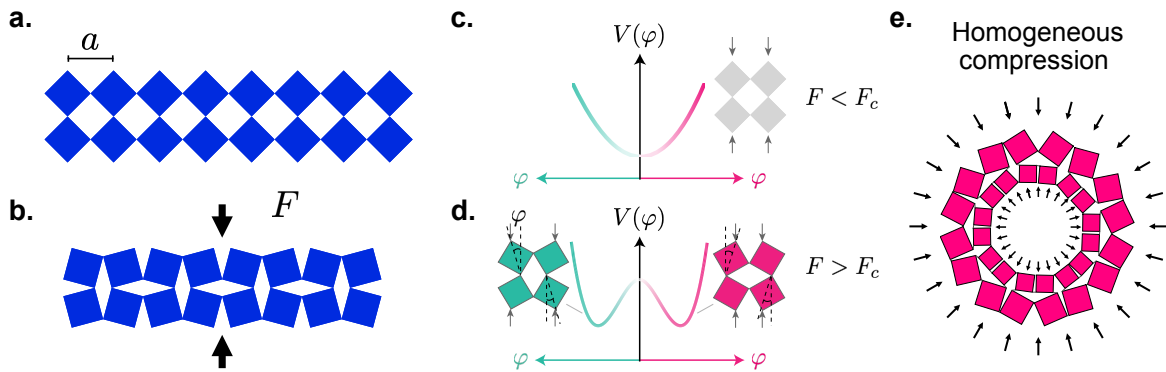


Figure 4.8: **Euler-buckling instability in frustrated metarings.** **a.** The mechanical material consists of square plaquettes connected by the vertices. **b.** When subjected to local loads, the plaquettes counter-rotate establishing an antiferromagnetic order. **c.** This phenomenon corresponds to the Buckling-Euler elasticity: below a force threshold F_c , the system remains undeformed. Above it, the ground state is described by a double-well potential. Each minimum defines two opposite directions of rotation. **d.** Local frustration arises when applying homogenous loads in an odd metaring. Antiferromagnetic order cannot be accommodated in a ring containing an odd amount of units.

the orientability of a ribbon.

Let us take the base circle, two coverings U_A and U_B , and two overlaps, \mathcal{O}_1 and \mathcal{O}_2 . Unlike orientability, which is better described by the impossibility to accommodate a continuous normal field, here the problem is better captured by accommodating alternating normals over the base circle. Each of the normals describes a positive sense of rotation and being alternate, it is suitable to describe antiferromagnetic order. On each covering, we define a staggered normal field. Both conventions will overlap in \mathcal{O}_1 and \mathcal{O}_2 . As before, the agreement on the convention on each overlap is defined by a binary function $\sigma(\mathcal{O}) = \pm 1$, taking the positive value when both conventions agree and the negative otherwise. The parity of the ring is then directly given by the parity of the conventions on the overlaps: $w_1 = (1 - \sigma(\mathcal{O}_1)\sigma(\mathcal{O}_2))/2 \in \{0, 1\}$. Even metarings are characterized by $w_1 = 0$ and can accommodate a single uniform staggered normal field. Odd metarings, on the other hand, for which $w_1 = 1$, cannot sustain such a uniform staggered normal field and there will always be at least one overlap in which the conventions disagree, fig. 4.9b,e.

In order for the antiferromagnetic metaring to display non-orientable mechanics, its elastic deformation bundle must be non-orientable. Following the same steps as in the previous section, at each point s in the base circle \mathcal{B} we assign a staggered deformation $\varphi(s)$. The ensemble of all possible deformations at position s constitutes the real fiber F , and the ensemble of fibers, the total space E . Over any sector of \mathcal{B} , for example, the covering U_A , the fibers draw a continuous section of the total space E which locally looks like the product space $\mathcal{B} \times F$. This is true everywhere by the continuity of $\varphi(s)$. Over the incompatible overlap \mathcal{O}_2 , the continuity induces a twist on the total space; the real vector bundle is non-orientable, fig. 4.10c. Frustrated metarings realize non-orientable mechanics and any continuous deformation profile is constrained to have a zero deformation point. Importantly, the soft möbius strip and the odd metaring have the same elastic deformation

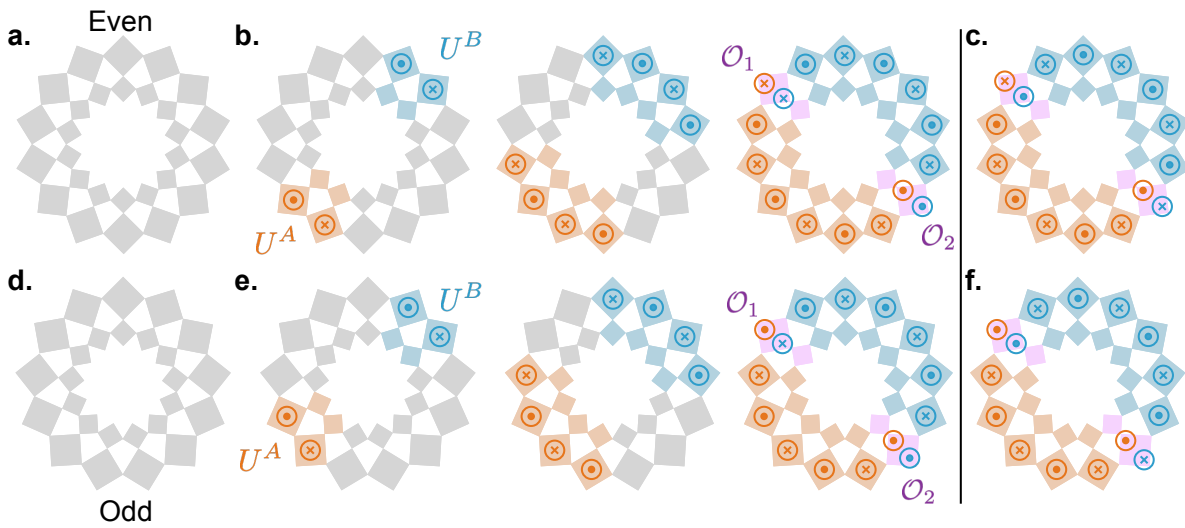


Figure 4.9: **Frustration in metarings** **a.** An even metaring can accommodate a staggered normal field over its surface. **b.** (left) On each covering, U_A in orange and U_B in blue, we locally define continuous staggered fields. We extend the coverings (middle) until they overlap on the violet regions \mathcal{O}_1 and \mathcal{O}_2 (right). In this example, both overlaps disagree, $\sigma(\mathcal{O}_1) = \sigma(\mathcal{O}_2) = -1$ leading to $w_1 = 0$. **c.** Changing the normal convention of the covering U_B renders both overlap compatible, $\sigma(\mathcal{O}_1) = \sigma(\mathcal{O}_2) = 1$. The orientability remains the same, $w_1 = 0$. **d.** Odd metarings are globally frustrated. **e, f.** Same construction as in **b, c**. Here $w_1 = 1$ regardless of the normal conventions used on the coverings.

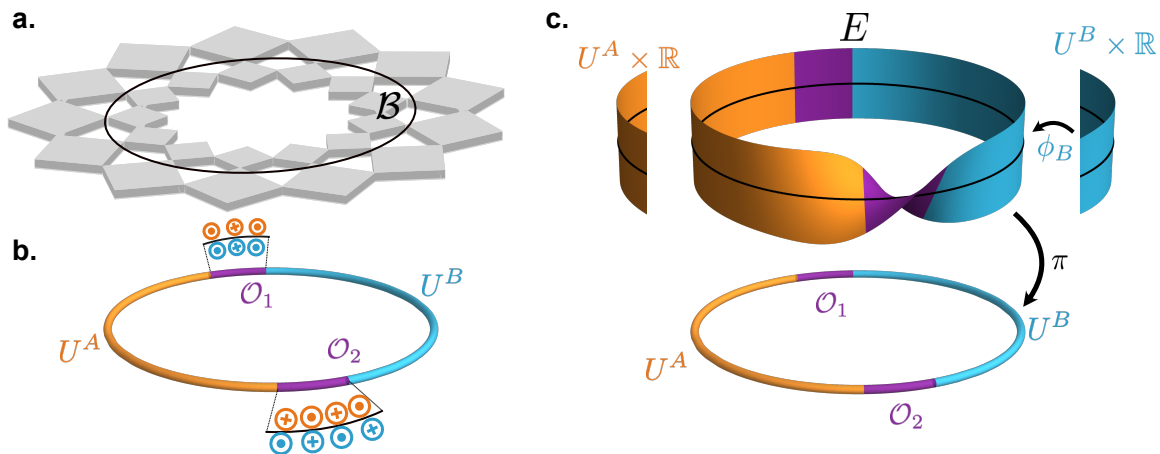


Figure 4.10: **Real line deformation bundle of a metaring** **a.** The base space \mathcal{B} of the buckling deformations of a metaring corresponds to a circle. **b.** Using the construction of fig. 4.9, we define two coverings, U_A (orange) and U_B (blue), and two overlaps (violet), \mathcal{O}_1 and \mathcal{O}_2 . Here, overlap \mathcal{O}_2 has two incompatible staggered normal conventions. **c.** The total space E is constructed by the vectorial space formed by all the fibers F . At each position s in the base circle \mathcal{B} we define a real fiber $F = \mathbb{R}$. Any subspace of E is locally homeomorphic to the product space $\mathcal{B} \times \mathbb{R}$. Globally, this is not true; deformation bundle is non-orientable.

bundle and they happen to share the same energetic description. Indeed, the energy density of a metaring near the onset of the buckling instability is generically described by

$$u[\varphi(s)] = \frac{K}{2}(\partial_s\varphi)^2 + V(\varphi), \quad (4.6)$$

where K corresponds to the stiffness and $V(\varphi) = K/\xi^2(\varphi^2 - \varphi_0^2)^2$, with ξ a characteristic length and φ_0 the deformation angle deep in the antiferromagnetic state (see the supplementary information 4.10.2 for an exhaustive derivation). The energy density of a buckled metaring is described by the same functional used for buckled soft ribbons (4.5). Having the same energy density and elastic deformation bundle, we can follow step-by-step the derivation of section 4.3, leading to the total energy

$$\mathcal{E} = \int ds \left\{ \frac{K}{2}(\partial_s\varphi)^2 + V(\varphi) \right\} - 4Kw_1 \lim_{\epsilon \rightarrow 0} \varphi^2(s^*)/\epsilon, \quad (4.7)$$

where w_1 stands for the first Stiefel-Whitney of the elastic fiber bundle. The ground state deformation of odd metarings ($w_1 = 1$) is then given by the minimization of the first integral of eq. (4.7) provided the constraint $\varphi(s^*) = 0$.

Non-orientable mechanics is within the reach of orientable objects. How then can we engineer non-orientable mechanics in higher dimensions?

4.4.1 Non-orientable mechanics in higher dimensions

To conceive higher dimensional non-orientable mechanics we must comply with two basic features of non-orientable real bundles. First, they can only be defined when their base space \mathcal{B} hosts non-contractible loops. This is the case of the unit circle S_1 in 1D and the torus $S_1 \times S_1$ in 2D. Second, when restricted to a non-contractible loop, in at least one of them, the real bundle must reduce to a Möbius bundle. Thus, the simplicity and malleability of antiferromagnetic plaquettes offer a straightforward generalization to higher-dimensional systems: frustrated toroidal metamaterials.

The natural extension of the metaring is achieved by periodically tiling the space in the orthogonal direction, creating a meta-torus. This procedure allows conceiving four distinct configurations depending on the parity along the toroidal and poloidal directions.

Prior to any energetic detail, we can directly construct the elastic fiber bundle of these higher-dimensional objects and therefore predict their topological properties. As with the metaring, we describe the local deformation of plaquettes by the staggered angle field $\varphi(s_p, s_t)$, where s_p and s_t stand for the curvilinear coordinates along the poloidal and toroidal directions, respectively. In the continuum limit, the base space \mathcal{B} corresponds to a torus. At each position (s_p, s_t) we define the real fiber F corresponding to all the possible deformations at the given point. The total space E is a four-dimensional object, which we cannot easily represent in 2D. However, building from the knowledge of one-dimensional systems, we can assert the orientability of the bundle. Let us take as an illustrative example the even-odd metatorus of fig. 4.11b. A loop lassoing the base space along the toroidal direction defines an even metaring. The deformations over this loop define a section of the total space E , which is homeomorphic to a cylinder. On the other hand, a loop along the poloidal direction defines an odd metaring and the deformations

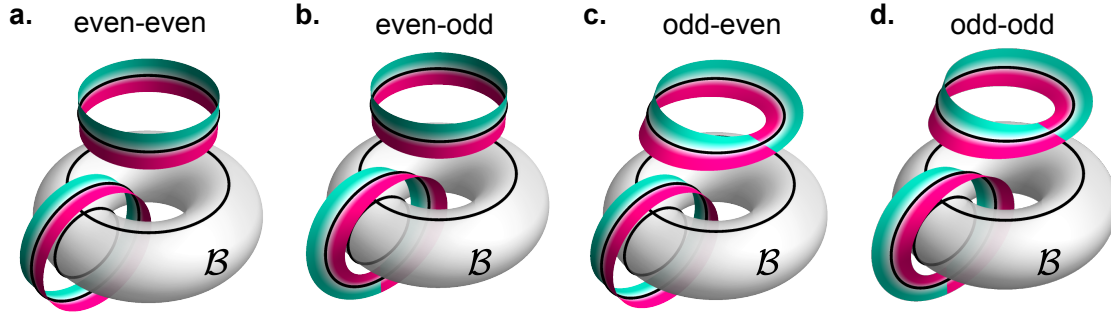


Figure 4.11: **Real deformation bundle of metatori.** The base space \mathcal{B} of the metatori is a torus. While the whole deformation bundle cannot be nicely embedded in 3D (and depicted in 2D), we can illustrate subspaces of it. The black lines correspond to different loops defined on \mathcal{B} . On each loop, we define the fibers. Whenever a subset of the fibers on a non-contractible loop defines a Möbius bundle, the whole real bundle is non-orientable. Here we use colors to better distinguish cylinders from Möbius strips. We showcase the four possible metatori: even-even **a**, even-odd **b**, odd-even **c**, and odd-odd **d**

are described by a Möbius strip. The orientability of the whole bundle is thus determined: as soon as the total space contains a section homeomorphic to a Möbius strip, the whole bundle is non-orientable. The whole catalog of metatori is depicted in fig. 4.11, from which we can infer that even-odd, odd-even, and odd-odd metatori all realize non-orientable mechanics.

Zero deformation lines

How does non-orientable mechanics manifest in higher dimensions? In this high-dimensional fiber bundle, any continuous deformation field corresponds to surface sections of the total space. From the same example of the even-odd metaring, we can see that there is a Möbius cross section per each poloidal loop characterized by its toroidal arclength s_t . Each loop constrains the deformation field to vanish at an unprescribed point $\varphi(s_t, s_p^*) = 0$, so all along the toroidal loop, there are zero deformation points. Energetics constrains these points to form a line $\mathcal{L} = \varphi(s_t, s_p^*(s_t))$ of zero deformation winding along the toroidal direction.

In homogeneous systems, the exact position of the line is picked by a spontaneous symmetry-breaking process. Any translation of \mathcal{L} along the toroidal direction forms another ground state. Its shape, however, is dictated by energetics and not the topology of the fiber bundle. Here we show that under homogenous loads, the deformation line is of minimum length. Leaving the technical details for the supplementary information 4.10, from eq. (4.7) we can generalize the total energy of a buckled metatori as

$$\mathcal{E} = \int_{T^2} ds_t ds_p \left\{ \frac{K}{2} (\nabla \varphi)^2 + V(\varphi) \right\}, \quad (4.8)$$

plus the vanishing constraint issued from orientability,

$$\varphi(\mathbf{R}^*(\sigma)) = 0, \quad (4.9)$$

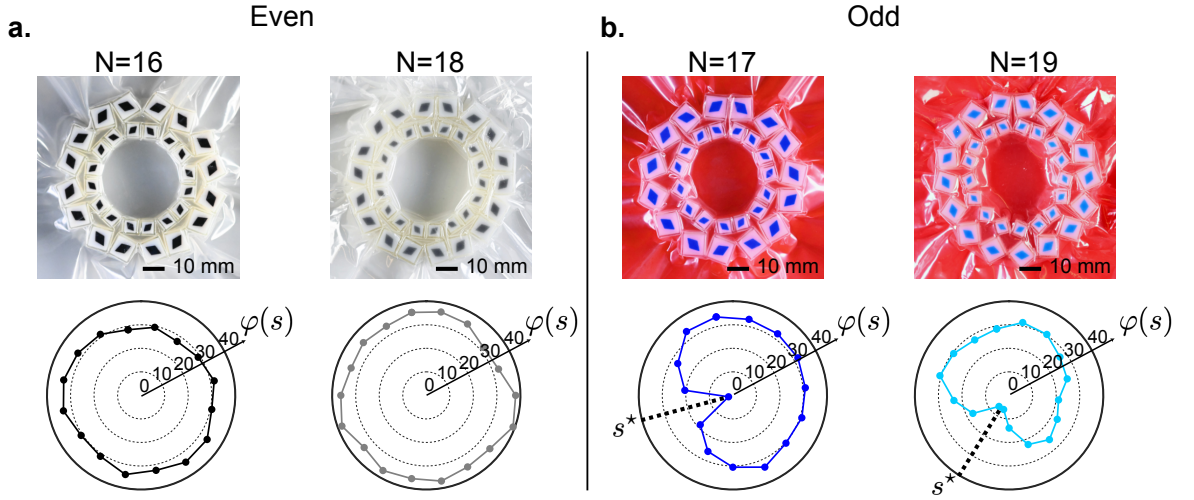


Figure 4.12: **Experimental deformation profile of homogeneously compressed metarings.** **a.** (top) two even metarings of 16 and 18 units. (bottom) The deformation profiles are roughly homogenous. **b.** Same as before, this time for odd metarings of 15 and 17 units. In both cases the deformation profile exhibits a point s^* in which the deformation field identically vanishes.

where $\mathbf{R}^*(\sigma)$ is a parametrization of \mathcal{L} with respect to its curvilinear coordinate σ . Away from the line and deep in the buckled state, the deformation field is constant. The heterogeneities are localized over a characteristic length $\xi = \sqrt{24Ka/F}$ around \mathcal{L} , thus $(\nabla\varphi)^2 \approx \varphi_0^2/\xi^2$, where φ_0 is the amplitude of the energy barrier of the quartic potential. The total energy \mathcal{E} reduces to

$$\mathcal{E} \sim 2\xi \int d\sigma \left(\frac{K}{2} \frac{\varphi_0^2}{\xi^2} + \frac{K}{\xi^2} \varphi_0^4 \right) \equiv \gamma \int d\sigma, \quad (4.10)$$

with $\gamma = K\varphi_0^2(1+2\varphi_0^2)/(2\xi)$ the effective line tension. Equation (4.10) corresponds to the effective energy of the degrees of freedom linked to the shape of \mathcal{L} . Under a homogeneous load, the energy is minimized for straight loops winding around the torus. This leads to three possible shapes depending on the parity of the metator. For the odd-even and even-odd cases, \mathcal{L} is a circle along the toroidal and poloidal directions, respectively. For the odd-odd case, \mathcal{L} is chiral and corresponds to a helix of minimum length around the torus.

4.4.2 Experimental measurements on frustrated mechanical antiferromagnets

Using once again the ziplock technique, our experimental colleagues applied a nearly uniform compressive load and determined the deformation profile of the metamaterials. For one-dimensional systems, they probe the deformation profiles of rings containing 15, 16, 17, and 18 pairs of plaquettes, fig. 4.13. For all the odd-metarings, they detected isolated undeformed plaquettes as predicted by the non-orientability of their deformation bundles. Moreover, the whole deformation profile neatly matches the one derived in

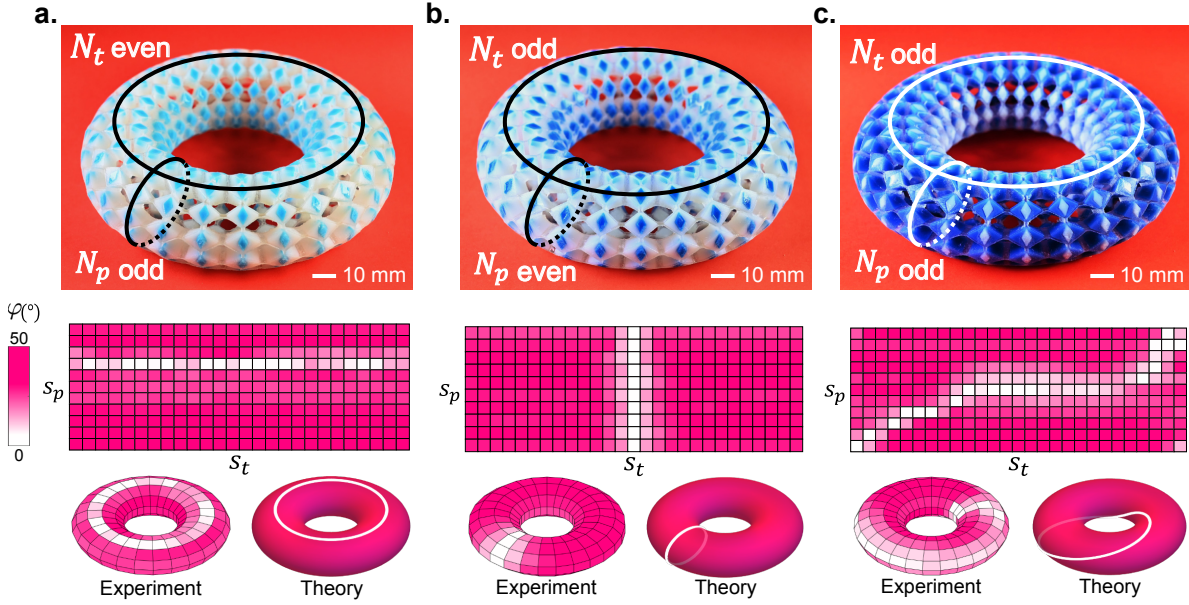


Figure 4.13: **Homogeneously compressed metatori.** Even-odd (a), odd-even (b), and odd-odd (c) 3D printed metatori. When subjected to homogenous compressions, they display zero deformation lines whose winding is dictated by the deformation bundles. These are straight lines in the first two cases, as predicted by the theory. For the odd-odd case, the experimental line deviates from the theory due to local curvature effects.

the long-ribbon limit, (see Supplementary Information 4.10). Even-metarings display a constant deformation set by the strength of the applied load.

Thanks to a refined design, they 3D printed three distinct metatori of sizes 26×11 , 27×10 , and 27×11 plaquettes (see Methods 4.8 for fabrication details). In all three cases, they observed zero-deformation lines winding along the predicted directions, fig. 4.13. It is worth mentioning that due to local curvature effects, the system is not completely homogenous, and the stiffness near the inner circle of the torus tends to be higher than the outer part. This pins the straight line in the even-odd case and induces a curved line in the odd-odd metatorus.

Non-orientable mechanics protects points and lines from any deformation under homogenous loading forces. In the next section, we will see how non-orientability also manifests upon heterogeneous loads, endowing points and lines of zero deformation with non-commutative responses.

4.5 Non-commutative response to heterogeneous loads

In a nutshell, non-orientable mechanics protect points and lines from any deformation. Their existence has a topological root, insensitive to heterogeneities in the system and the compression forces. So far we have studied homogenous compressive forces in both one and two-dimensional systems, guaranteeing a continuous set of groundstates. Heterogeneities,

as expected, pin the location of zero-deformation points in the minima of the energy landscape.

4.5.1 Metarings and ribbons

Applying a local load to either the Möbius strip or the odd metaring combines the usual elastic response and the topological constraint of a zero deformation point [55, 131]. In this section, we summarize the detailed derivations for metarings worked out in the supplementary information 4.10.4, and show that heterogeneous loads lead to multistable deformation profiles.

In the continuum limit, the energy of a free odd-metaring reads

$$\mathcal{E} = \int ds \frac{K}{2} (\partial_s \varphi)^2 + \frac{6C_b}{a^2} \varphi^2, \quad (4.11)$$

where K and C_b are elastic constants, and a the distance between two plaquettes (see SI 4.10 for the derivation from the discrete energy). The minimization of the elastic energy leads to the following equation describing the deformation profile $\varphi(s)$:

$$\lambda^2 \partial_s^2 \varphi - \varphi = 0, \quad (4.12)$$

with $\lambda^2 = a^2 K / (12C_b)$ the characteristic length of the system. Here we take into account a local compressive load as an imposed deformation on the ring, $\varphi(s=0) = \varphi(s=1) = \bar{\varphi} > 0$. The non-orientability of the deformation bundle further imposes $\varphi(s^*) = 0$. The deformation profile, is then given by

$$\varphi(s; s^*) = \begin{cases} Ae^{s/\lambda} + Be^{-s/\lambda} & s \in [0, s^*] \\ Ce^{s/\lambda} + De^{-s/\lambda} & s \in [s^*, 1] \end{cases}, \quad (4.13)$$

with

$$\begin{pmatrix} A \\ B \end{pmatrix} = \frac{\bar{\varphi}}{2 \sinh(s^*/\lambda)} \begin{pmatrix} -e^{-s^*/\lambda} \\ e^{s^*/\lambda} \end{pmatrix}, \\ \begin{pmatrix} C \\ D \end{pmatrix} = \frac{\bar{\varphi}}{2 \sinh((s^* - 1)/\lambda)} \begin{pmatrix} -e^{-s^*/\lambda} \\ e^{s^*/\lambda} \end{pmatrix}. \quad (4.14)$$

Notice that s^* is a degree of freedom of the system that is yet to be determined. To do so, we derive an effective potential by inserting $\varphi(s)$ from eq. (4.13) into the elastic energy (4.11):

$$\mathcal{U}_1(s^*) = \mathcal{E}[\varphi(s; s^*)] = \frac{K\bar{\varphi}^2}{2\lambda} \frac{\sinh(1/\lambda)}{\sinh((1-s^*)/\lambda) \sinh(s^*/\lambda)}. \quad (4.15)$$

The zero-deformation point, determined by the minimization of the effective potential \mathcal{U}_1 , is diametrically opposed to the source of deformation, $s^* = 1/2$, fig. 4.14a.

We can easily generalize this potential to N sources. In general, if $s = s^*$ is located between s_{n-1} and s_{n+1} , the exact position between both local deformations is

$$s^* = \frac{1}{2}(s_{n-1} + s_{n+1}) + \frac{1}{2}\lambda \ln \left| \frac{e^{s_{n+1}/\lambda} \bar{\varphi}_{n-1} + e^{s_{n-1}/\lambda} \bar{\varphi}_{n+1}}{e^{s_{n-1}/\lambda} \bar{\varphi}_{n-1} + e^{s_{n+1}/\lambda} \bar{\varphi}_{n+1}} \right|, \quad (4.16)$$

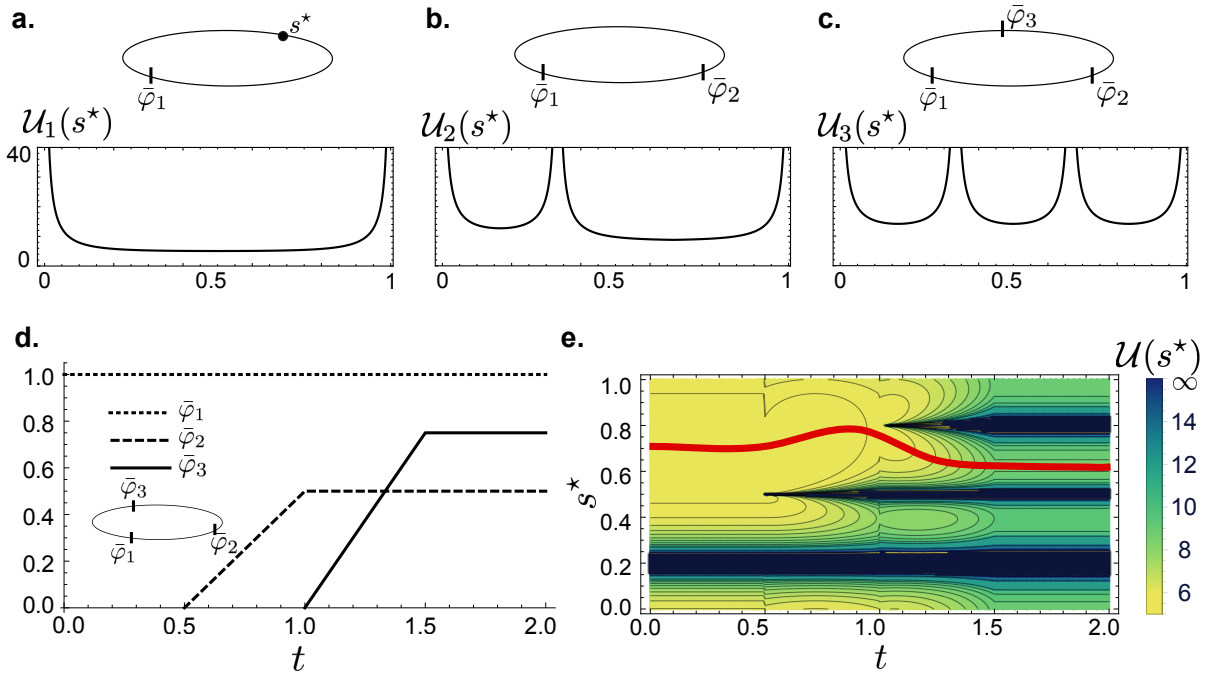


Figure 4.14: **Local response in metarings.** **a.** A single load point on a metaring induces an effective potential with only one minimum. The zero-deformation point locates diametrically opposite to the source. The number of local loads is directly related to the number of local minima. **d.** Diagram describing the sequential application of three local loads in a metaring. **e.** Color plot of the effective potential as a function of time according to the sequential application of the loads. The red line indicates the trajectory followed by the zero-deformation point.

and the effective potential is given by $\mathcal{U}_N(s^*) = \mathcal{E}(\varphi)$, which features as many minima as imposed deformations (or applied loads), fig. 4.14b,c.

A sequential application of local loads leads to the programmed selection of a minimum path, fig. 4.14d,e. As we see next, this property induces a non-commutative response in non-orientable systems.

Non-commutative response: Experimental measurements on 1D systems

Figure 4.15 illustrates the experimental application of 3 local loads, P , R , and S , on a 15-metaring, (see Methods 4.8 for experimental details). The first load P induces a zero-deformation point at its diametrically opposite location. The sequence R then S directs this point counterclockwise. On the other hand, the sequence S and then R steers the point clockwise. The trajectory of the zero-deformation node is dictated by the sequence in which the loads are applied. The sole information of the load positions cannot predict the final state of deformation.

4.5.2 Metatori and the braiding of local loads

The non-commutative response extends to higher dimensions. Unlike in homogeneous compressions where the loop \mathcal{L} minimizes its length, here the line meanders avoiding the

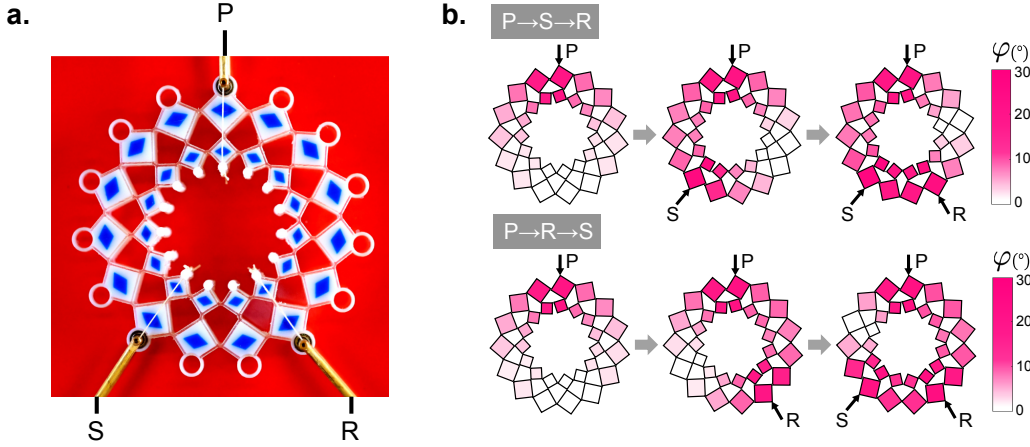


Figure 4.15: **Experimental observation of the non-commutative response on a metaring.** **a.** Three local loads, P , S , and R , are sequentially applied on an odd metaring of 15 units. **b.** The sequence $\{P, S, R\}$ steers the zero-node clockwise, whereas the sequence $\{P, R, S\}$ counterclockwise. The final deformation state depends on the history of the applied loads.

local compressions and the shape of the line gets progressively convoluted with the number of applied loads. To get some insight into the local shape of the line, we can derive an effective elasticity of \mathcal{L} when perturbed from a straight-line configuration.

Leaving the details of the calculations to the Supplementary Information 4.10.4, here we announce the methodology and the main results. We begin by considering a generic load distribution, $F(\mathbf{r}) = \sum_{\alpha} F_{\alpha} \delta(\mathbf{r} - \mathbf{r}_{\alpha})$, which leads to the total energy functional

$$\mathcal{E} = \int d^2r \left(\frac{K}{2} (\nabla \varphi)^2 + \frac{m^2}{2} \varphi^2 \right) - \int d\mathbf{r} F(\mathbf{r}) \varphi. \quad (4.17)$$

This energy must be complemented by the topological constraint issued from the non-orientability of the deformation bundle: $\varphi(\mathbf{R}^*(\sigma)) = 0$.

To obtain the effective elasticity of \mathcal{L} , we study the system subject to thermal fluctuations (Supplementary Information 4.10.4), leading to the partition function

$$\mathcal{Z} = \int \mathcal{D}\varphi \int \mathcal{D}\mathbf{R}^* \left(\prod_{\sigma} \delta(\varphi(\mathbf{R}^*(\sigma))) \right) e^{-\beta \mathcal{E}[\varphi, \mathbf{R}^*]}. \quad (4.18)$$

The effective potential is then obtained by integrating out the Gaussian fluctuations of $\varphi(\mathbf{R}^*)$, which after some lengthy calculations leads to

$$\mathcal{Z} = C_1 \int \mathcal{D}\mathbf{R}^* \exp(-\mathcal{U}[\mathbf{R}^*]), \quad (4.19)$$

where C_1 is a constant independent of $\mathbf{R}^*(s)$ and the effective potential reads

$$\mathcal{U}[\mathbf{R}^*] = \frac{\beta^2}{2} \int d\sigma d\sigma' \int d^2\mathbf{r} d^2\mathbf{r}' F(\mathbf{r}) G[\mathbf{r}, \mathbf{R}^*(\sigma)] \tilde{G}^{-1}[\mathbf{R}^*(\sigma), \mathbf{R}^*(\sigma')] G[\mathbf{R}^*(\sigma'), \mathbf{r}'] F(\mathbf{r}'). \quad (4.20)$$

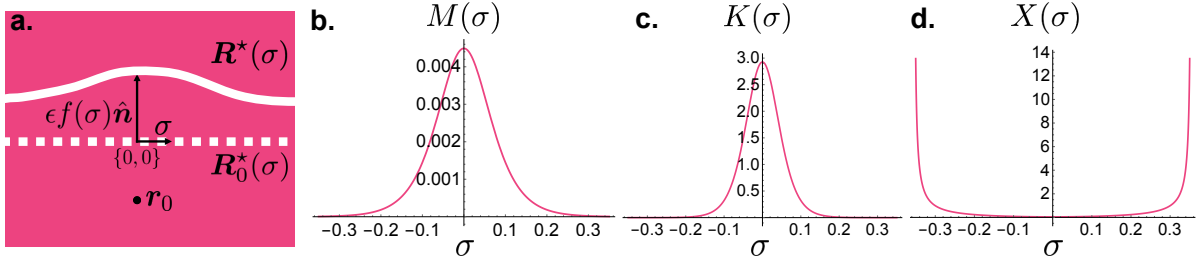


Figure 4.16: **Line repulsion from one point stress.** **a.** Sketch of the unperturbed zero line $\mathbf{R}_0^*(\sigma) = \hat{\mathbf{t}}\sigma + \mathbf{p}$ (dashed white line) and the deformed line $\mathbf{R}^*(\sigma) = \mathbf{R}_0^*(\sigma) + \epsilon f(\sigma)\hat{\mathbf{n}}$ (solid white line), where $\hat{\mathbf{t}} = \{1, 0\}$, and $\mathbf{p} = \{0, 0\}$. The point stress is applied at $\mathbf{r}_0 = \{0, -0.1\}$. **b, c, d.** Expansion terms from the one-source potential \mathcal{U}_0 for $m = 10$: effective line tension $M(\sigma)$, repulsion term $K(\sigma)$, and shift term $X(\sigma)$, respectively.

Here $G[\mathbf{r}, \mathbf{r}']$ is the Green function defined by

$$\beta(m^2 - \kappa\nabla^2)G[\mathbf{r}, \mathbf{r}'] = \delta(\mathbf{r} - \mathbf{r}'), \quad (4.21)$$

and \tilde{G}^{-1} is given by

$$\int d\sigma' G[\mathbf{R}^*(\sigma), \mathbf{R}^*(\sigma')] \tilde{G}^{-1}[\mathbf{R}^*(\sigma'), \mathbf{R}(\sigma'')] = \delta(\sigma - \sigma''). \quad (4.22)$$

It is noteworthy that eq. (4.20) is exact. However, it requires the inverse of the non-local operator \tilde{G} . To gain some physical intuition on the long wave-length limit, we can apply a series of observations and approximations:

1. In large systems, the Green's function on the torus, G , can be approximated by its counterpart defined on the plane: $G(\mathbf{r}, \mathbf{r}') = g(|\mathbf{r} - \mathbf{r}'|) = \frac{1}{2\pi\beta} K_0(m|\mathbf{r} - \mathbf{r}'|)$, with K_n the modified Bessel function of the second kind.
2. Experiments and simulations suggest that, against a single point load, the elastic energy is minimized when placing \mathcal{L} at a maximal distance from the load.
3. Based on the previous observation, we can make a perturbative analysis based on small transversal fluctuations of magnitude ϵ when applying additional local forces. We parametrize the shape of the line as $\mathbf{R}^*(\sigma) = \mathbf{R}_0^*(\sigma) + \epsilon\mathbf{R}_1^*(\sigma)$. $\mathbf{R}_0^*(\sigma) = \hat{\mathbf{t}}\sigma + \mathbf{p}$ is the original straight line, where $\hat{\mathbf{t}}$ is a unitary tangent vector, and \mathbf{p} a point of reference. The transverse fluctuations are given by $\mathbf{R}_1^*(\sigma) = f(\sigma)\hat{\mathbf{n}}$, with $\hat{\mathbf{n}}$ the normal vector.
4. In order to have a local potential \mathcal{U} , we work in the regime in which $ml \gg 1$, with l the characteristic separation between two neighboring sites.

After some tractable yet heavy calculation eq. (4.20) finally reads

$$\mathcal{U}_0[\mathbf{R}^*] = -\epsilon \int d\sigma f(\sigma) K(\sigma) X(\sigma) + \epsilon^2 \int d\sigma \left[\frac{M(\sigma)}{2} \left(\frac{df}{d\sigma} \right)^2 + \frac{K(\sigma)}{2} f^2(\sigma) \right], \quad (4.23)$$

where

$$\begin{aligned} M(\sigma) &= G_0^2, \\ K(\sigma) &= 2 \left(G_1^2 + 2G_0G_2 \right), \\ X(\sigma) &= -\frac{G_1G_0}{G_1^2 + 2G_0G_2}, \end{aligned}$$

and

$$\begin{aligned} G_0 &= g(|\hat{\mathbf{t}}\sigma + \mathbf{p} - \mathbf{r}_0|) \\ G_1 &= \frac{\hat{\mathbf{n}} \cdot (\mathbf{p} - \mathbf{r}_0)}{|\hat{\mathbf{t}}\sigma + \mathbf{p} - \mathbf{r}_0|} g'(|\hat{\mathbf{t}}\sigma + \mathbf{p} - \mathbf{r}_0|) \\ G_2 &= \left(\frac{|\hat{\mathbf{t}}\sigma + \mathbf{p} - \mathbf{r}_0|^2 - (\hat{\mathbf{n}} \cdot (\mathbf{p} - \mathbf{r}_0))^2}{4|\hat{\mathbf{t}}\sigma + \mathbf{p} - \mathbf{r}_0|^3} \right) g'(|\hat{\mathbf{t}}\sigma + \mathbf{p} - \mathbf{r}_0|) \\ &\quad + \frac{(\hat{\mathbf{n}} \cdot (\mathbf{p} - \mathbf{r}_0))^2}{4|\hat{\mathbf{t}}\sigma + \mathbf{p} - \mathbf{r}_0|^2} g''(|\hat{\mathbf{t}}\sigma + \mathbf{p} - \mathbf{r}_0|). \end{aligned} \quad (4.24)$$

To first order in ϵ , the line is repelled at a maximal distance from the source. \mathcal{L} loops are repelled by point stresses. To second order in ϵ there is a heterogeneous line tension $M(\sigma)$ and a modulation of the repulsive force from the source, $K(\sigma)$. $M(\sigma)$, $K(\sigma)$ and $X(\sigma)$ are plotted in fig. 4.35. Both M and K have a finite range. Away from the source, the line does not feel the second order correction.

As we see next, the repulsion of the line gives rise to a rich phenomenology when the positions of the loads evolve in time.

Braiding of local loads

Apart from the sequential application of local loads displayed on metarings, higher dimensional systems offer a new playground to exploit non-orientable mechanics: local braiding. Starting from the same initial distribution of loads, we can braid them along different world lines and yet get the same final distribution. This is confirmed by numerical simulations, in which we braided three local loads on a metatorus of size 49×49 , fig. 4.17. The final state of the system depends on the path taken; the zero deformation loop stores information about the load trajectories.

4.6 Conclusions and perspectives

In this chapter, we have shown that non-orientable mechanics, defined as the non-orientability of the deformation bundles, protects regions against any deformation. The most straightforward realization of non-orientable mechanics comes directly from non-orientable surfaces such as the elastic Möbius strip. We have seen that the non-orientability translates into the existence of highly stiff points in an otherwise homogeneous material.

Notably, non-orientable mechanics is not exclusive to non-orientable surfaces. We have seen that the global frustration present in antiferromagnetic mechanical systems offers a huge playground to engineer non-orientable deformation bundles. Moreover, its

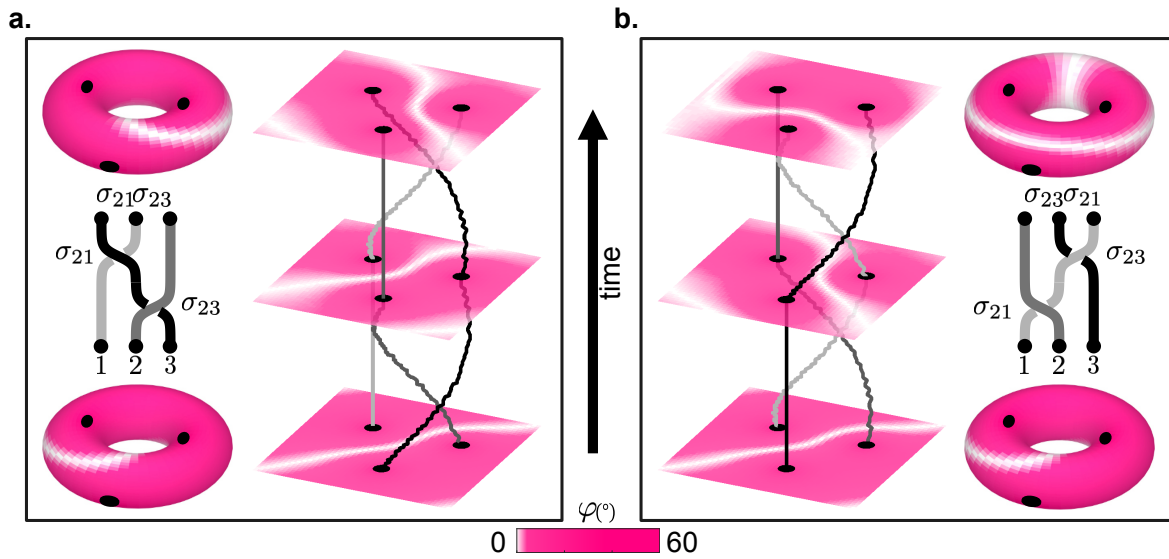


Figure 4.17: **Braiding of local loads.** Numerical simulations of an odd-odd metatorus under two different sequences of identical point loads. The points of application of the loads are continuously moved, effectively braiding their worldlines. While the initial and final load configurations are identical, the shape of the line of zero deformation explicitly depends on the braiding sequence of the load history, see Supplementary Information 4.10.5 for details on the simulation protocol).

versatility allows for the natural realization of non-orientable deformation bundles of higher dimensions. These examples are characterized by the existence of highly stiff loops whose winding is determined by the topology of the bundle, and their geometry by the detailed energetics of the system.

Antiferromagnetic mechanical metamaterials are only one platform to realize global frustration. In general, it pervades systems at all scales: molecular antiferromagnetic rings unable to accommodate their magnetic moments [134], active fluid metamaterials displaying counterrotating vortices on a ring [55, 135], and polymer beads packed in an incompatible ring-shape channel [55]. The failure to accommodate any staggered order over the whole space is captured by the non-orientability of a general parameter bundle. On the opposite coastline, we find real-space non-orientability, the original motivation of this work. Although rare and perhaps non-existent in nature, real-space non-orientability has been achieved in several chemical platforms: crystals of niobium and selenium [136], polycyclic [137] and glutamate compounds [138], carbon nanobelts [139], and even triply twisted (and beyond) Möbius strips made of monocyclic hydrocarbons [140]. However, the physical consequences of non-orientability remain rather unexplored due to the unstable and fragile nature of these objects.

Non-orientable mechanics extends well beyond one and two-dimensional base spaces. For example, a three-dimensional base space is achieved by filling the metatorus with cubic units. Beyond three dimensions, we can trick the connectivity by synthetically connecting different units simulating the connectivity of higher dimensions [141]. The same trick could be used to simulate higher-dimensional non-orientable objects such as Klein bottles and real projective planes. In higher dimensions, we expect surfaces and

volumes of zero-deformation regions. With more exotic assemblies of metamaterials we could witness the interactions of surfaces, lines, and points, offering a vast playground to explore non-commutative responses, and in general, the consequences of non-orientable fiber bundles.

4.7 Article

Non-orientable order and non-commutative response in frustrated metamaterials

Xiaofei Guo^{1,3}, Marcelo Guzmán², David Carpentier², Denis Bartolo², Corentin Coulais³,

¹Harbin Institute of Technology, China

²Univ. Lyon, ENS de Lyon, Univ. Claude Bernard, CNRS, Laboratoire de Physique, F-69342, Lyon, France

³Institute of Physics, Universiteit van Amsterdam, 1098 XH Amsterdam, The Netherlands

From atomic crystal to animal flocks, the emergence of order in nature is captured by the concept of spontaneous symmetry breaking [142–145]. This cornerstone of physics formalised by Landau theory was recently challenged by topologically ordered phases, where the number of states is not solely determined by the number of broken symmetries, but also by space topology [146]. However, topological order stems from quantum entanglement, and therefore remains essentially out of reach in classical matter [146, 147]. Here, combining experiments and theory we demonstrate a new class of classical order that escape the Landau paradigm: non-orientable order. We demonstrate this concept by designing globally frustrated mechanical metamaterials that spontaneously break a discrete symmetry under uniform load. We show that they generically feature non-orientable order parameters which we map on the deformation bundles of non-orientable soft surfaces, such as Möbius strips and Klein bottles. While Landau theory predicts a finite number of equilibria, non-orientable order implies an extensive degeneracy of mechanical ground states distinguished by topologically protected nodes and lines where deformations vanish. We then leverage non-orientable order to engineer robust mechanical memory [148–154]. Applying time-dependent local perturbations to non-orientable phases, we achieve non-commutative responses, and show that they carry an imprint of the braiding of the loads’ trajectories. Beyond mechanics, we envisage non-orientability as a robust design principle for metamaterial that can effectively store information across scales, in fields as diverse as acoustics, photonics and magnetism.

Frustration arises whenever geometry is incompatible with the symmetries of local interactions [155, 156]. It materialises in and out of equilibrium in systems ranging from electronic and synthetic spin ice [157, 158], to active flow networks [159–161], colloidal matter [162–164], and mechanical metamaterials [18, 152, 165–168].

In Fig. 4.18a, we show three experiments that span seven orders of magnitude in size, where local constraints promote antiferromagnetic, viz. staggered, order: neighbouring spins point in opposite directions, neighbouring active vortices have opposite handedness and neighbouring beads are located on alternate rows. These three experiments exemplify the concept of global frustration: the existence of a loop that lassos the whole system, and along which the local constraints cannot be satisfied all together.

In this letter, combining mechanical experiments and theory, we demonstrate that globally frustrated matter realises an uncharted class of classical order: non-orientable

order. Our goal is to reveal and explain the basic consequences of non-orientable order in classical systems.

To gain a first intuition about the concept of non-orientable order, we investigate the equilibria of one-dimensional frustrated mechanical metamaterials shown in Fig. 4.19a. These metarings are made of N pairs of coupled rotating lozenges, which are designed to promote counter rotation—or equivalently local antiferromagnetic order—in response to external loads [18, 133, 152, 165–167, 167–170]. Under sufficiently large axial compression, each pair of lozenges undergoes a structural instability and buckles with equal probability along one direction or the other (Fig. 4.19b). This transition is naturally characterised by the staggered rotation angle of the lozenges φ (Fig. 4.19b and c). In the lowest energy state, φ can take two distinct values that correspond to the local minima of a double-well energy potential $V(\varphi)$ (Fig. 4.19b and SI).

We now address the consequences of global frustration on the configurations accessible to φ in the buckled state. To see this, we apply a hydrostatic load to the metaring by placing it in a vacuum bag, see Supplementary Video 2. The system picks up a local direction of rotation, and spontaneously breaks the local symmetry $\varphi \rightarrow -\varphi$ (Fig. 4.19d). When the number of pairs of lozenges N is even, the order parameter φ is homogeneous, and antiferromagnetic order extends over the whole ring (Fig. 4.19d). Conversely, when N is odd, the translation symmetry along the curvilinear coordinate s is spontaneously broken. The magnitude of the staggered rotation $\varphi(s)$ is heterogeneous and vanishes at an unspecified point s^* (Fig. 4.19d). As a result, the buckled metaring features an extensive degeneracy of its mechanical equilibria, which are parametrised by the location of s^* . This is a remarkable result seen from the perspective of Landau theory of phase transitions: the local buckling instability breaks a discrete \mathbb{Z}_2 symmetry ($\varphi \rightarrow -\varphi$) in principle associated with no Goldstone mode and two ground states only [143]. Yet the odd metarings enjoy an extensive ensemble of ground states that spontaneously break translation symmetry.

To elucidate this counter-intuitive observation, we consider the continuum limit description of this metamaterial. Our measurements are well described by the minimal elastic energy density derived in SI:

$$\mathcal{E}[\varphi(s)] = \frac{K}{2}(\partial_s \varphi)^2 + V(\varphi), \quad (4.25)$$

where K is the elastic stiffness (see Fig 4.19e and SI). When N is even, one can define the staggered rotation field φ consistently over the whole ring and Eq. (4.25) reduces to the usual Landau theory of a scalar order parameter associated to a broken \mathbb{Z}_2 symmetry. However, when N is odd this simple picture breaks down. Whereas φ can be locally defined without ambiguity, global frustration provides an obstruction to defining φ consistently over the whole ring (see Fig. 4.19c and SI). In mathematical terms, the ensemble of all possible deformations define a real line bundle. When N is even it is trivial, *i.e.* non-vanishing configurations exist. Conversely, when N is odd, the deformation bundle cannot be globally trivialized by any smooth transformation: it is non-orientable [171]. It forms a Möbius strip bundle sketched in Fig. 4.18b and Extended Data Fig. 4.22. Non-orientability is clearly seen from the discontinuity of the colormap that measures the deformation amplitude: any smooth anti-ferromagnetic order parameter $\varphi(s)$ must vanish at least at one point s^* (see also SI for a pedagogical introduction to non-orientable bundles). In summary, non-orientable order is defined by: (i) a local breaking of a symmetry, and (ii) an order parameter, or deformation, field that lives on a non-orientable fibre bundle.

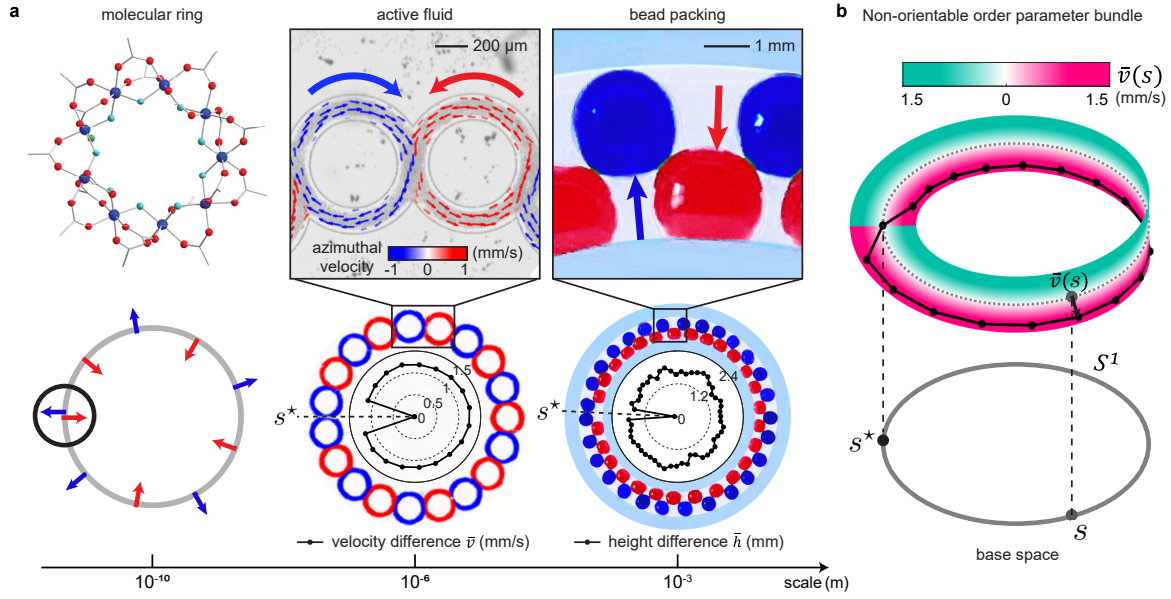


Figure 4.18: Frustration-induced non-orientable order. (a) Three examples of globally frustrated systems spanning seven orders of magnitude in scale. (Left): A molecular antiferromagnetic ring, made of chemical compound (CCDC 893835), whose 9 magnetic moments are located on Cr ions (blue). The molecular ring cannot accommodate a global antiferromagnetic order, see [134]. (Middle): An active-fluid metamaterial made of colloidal rollers flowing at constant speed in 19 connected annular microchannels. The colloids' diameter is $\sim 4.8 \mu\text{m}$. The active flow self-organises into connected “fluidic gears” which features local antiferromagnetic order. This order is however globally frustrated when the number of annuli is odd. Global frustration is clearly seen in the map of the azimuthal component of the flow in each annulus: $\mathbf{v}(\mathbf{r}) \cdot \hat{\mathbf{t}}$, where $\hat{\mathbf{t}}$ is the normalised tangent vector. In the bottom panel, the colour indicates the value of the tangent flow averaged in each annulus. The radial plot shows the variations of the difference of the spatially averaged azimuthal velocities \bar{v} between adjacent “fluidic gears”. \bar{v} vanishes at an unspecific point s^* . See also Supplementary Video 1. The experimental methods are thoroughly described in [135]. (Right): 2 mm-diameter polymer beads packed in a ring-shape channel. When confined in this quasi-one dimensional geometry, the packing realises a prototypical example of antiferromagnetic order (spheres are associated with $+1/2$ or $-1/2$ spin values, when in contact with the outer or inner walls, respectively), see [162] for a detailed analogy. When the ring perimeter is incommensurate with the length of the staggered pattern, antiferromagnetic order is globally frustrated. Frustration constrains the height difference $\bar{h}(s)$ between adjacent beads to vanish at an unspecific point s^* . (b) The primary goal of our article is to establish that the staggered order parameters of globally frustrated matter belong to non-orientable fibre bundles, and define a non-orientable order. In the basic case of frustrated 1D antiferromagnetic rings, the order parameter field belongs to a Möbius-strip bundle, which we illustrate here. All sections of the bundle, *i.e.* field configurations, vanish at least once along the base circle at an unspecified point s^* . The dark dots corresponds to the staggered velocity field $\bar{v}(s)$ of the frustrated active-fluid metamaterial defined in (a). Locally, the Möbius-strip bundle can be continuously mapped on a cylinder $S^1 \times \mathbb{R}$, but not globally. It is topologically distinct from the cylinder bundle associated to unfrustrated 1D antiferromagnetic order (see Extended Data Fig. 4.22).

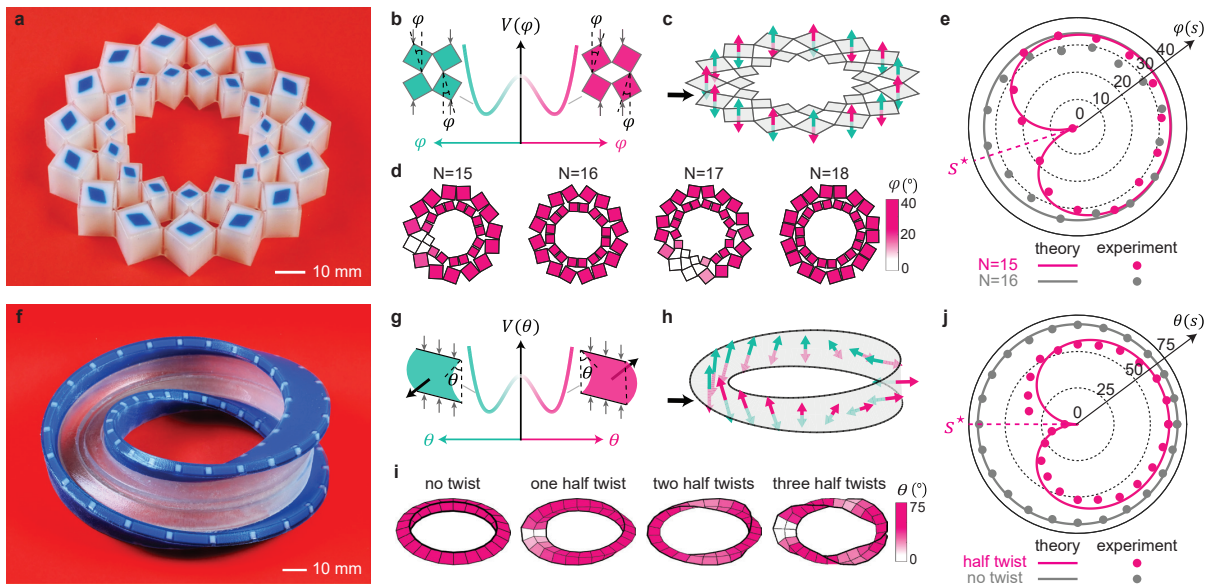


Figure 4.19: **Non-orientable order in frustrated metamaterials and flexible Möbius bands.** (a) A 3D-printed metaring, which consists of 15 pairs of lozenges. (b) Plot of the double-well potential $V(\varphi)$ whose minima correspond to the two directions of rotation (green and pink). In practice, at the onset of a mechanical instability the potential is well approximated by the normal form $V(\varphi) = K\xi^{-2}(\varphi^2 - \varphi_0^2)^2$. (c) The arrows indicate the two alternative conventions defined in (b) for the staggered-rotation vector of an odd metaring. No convention can be consistently defined over the whole ring. (d) Experimental measurements of the staggered rotation angle φ of metarings including even and odd numbers of units. Under uniform hydrostatic pressure, the deformations of odd metarings vanishes at an unspecified node. Translation symmetry is spontaneously broken. (e) Polar plot of φ for an odd metaring with 15 pairs of lozenges (pink disks) and an even metaring with 16 pairs of lozenges (gray disks). The solid lines are fits to the continuum theory detailed in SI. See also Supplementary Video 2. (f) A 3D printed Möbius band having a cross section in the shape of an I letter. The blue part is rigid in order to apply pressure while the white part is soft and can buckle. (g) Plot of the double-well potential $V(\theta)$ that distinguishes the two buckling directions of flexible bands (shown in green and pink colour). (h) The pink and green arrows represent the normal to the Möbius band corresponding to the two sign conventions defined in (g). No smooth normal vector field can be defined over the whole Möbius band. (i) Experimental measurements of the bending angle θ of twisted bands compressed by a uniform hydrostatic pressure. Under uniform hydrostatic pressure, the bending deformations of bands featuring an odd number of twists vanishes at an unspecified point. Translation symmetry is spontaneously broken. (j) Polar plot of the deformations of a Möbius band (pink) and of a cylinder (grey). The solid lines are fits to the continuum theory, see SI. See also Supplementary Video 3.

This essential result suggests an alternative strategy to engineer non-orientable order using flexible Möbius bands (Fig. 4.19f), see also [131]. To see this, we first illustrate the Euler buckling of a flat flexible band in Fig. 4.19g. It provides a canonical example of a spontaneous discrete symmetry breaking [131, 172]. Under the action of a sufficiently large axial load, a soft band can bend with equal probability along one direction or the other (Fig. 4.19g). When it is twisted into a non-orientable object such as a Möbius band, there is an intrinsic ambiguity in defining a continuous normal vector field, and hence a bending direction, over the whole band (Fig. 4.19h) [131]. In Extended Data Fig. 4.22 and in SI, we demonstrate experimentally and theoretically that whenever a twisted band is non-orientable, its bending deformations belong to a non-orientable bundle. When the band geometry is homogeneous, a zero deformation node s^* emerges at an unprescribed location, and gives rise to non-orientable order (see Fig. 4.19i, 4.19j, Extended Data Fig. 4.22 and Supplementary Video 3). Unlike the frustrated antiferromagnetic ring of Fig. 4.19a, non-orientable order originates here from the 3D shape of the Möbius band itself. However, the deformations of both structures belong to Möbius-strip bundles, sketched in Fig. 4.18b and Extended Data Fig. 4.22: the deformations of frustrated metarings and Möbius strips belong to the same topological class. We stress that although non-orientable order escapes the Landau paradigm and implies an extensive ground-state degeneracy, it is genuinely different from both the topological order quantum phases [146], as it does not involve any notion of long-range entanglement, and topological gapped phases [173] associated to topological properties distinct from non-orientability.

Two questions naturally arise from the observations of Fig. 4.18 and Fig. 4.19: (i) is it possible to engineer structures associated with non-orientable bundles distinct from a Möbius strip? (ii) if so, what would be the physical manifestations of their topology? A direct route to answer these questions consists in studying the bending mechanics of more complex non-orientable soft surfaces. In practice 2D closed manifold such as the Klein Bottle cannot be engineered in our 3D space. But we can make the so-called Möbius shorts (Fig. 4.20a) which are continuous deformations of holey Klein bottles [174]. Measuring the response of a 3D printed Möbius shorts (Fig. 4.20b) under a uniform hydrostatic load, we find again that the bending deformations $\theta(s)$ are heterogeneous and vanish at a point s^* whatever the load amplitude (Fig. 4.20c). Using the mapping between Möbius strip and metaring deformations introduced above, we can readily design a metamaterial that shares the same deformation topology as holey Klein bottles (Fig. 4.20b). It consists in connecting an odd and an even metaring at a pair of lozenges (Fig. 4.20e), as confirmed by the deformation profile showed in (Fig. 4.20f). Note that s represents the curvilinear coordinate along the base space of the order parameter bundle, which is here a curve in the shape of the figure eight (Fig. 4.20g). The order-parameter bundle is again non-orientable and therefore obstructs homogeneous deformations. However, unlike the single Möbius strip and metarings, the location of s^* is here fully determined by the heterogeneous geometry of the Möbius shorts, at the intersection between the two metarings (Fig. 4.20c and f). The orientable loop buckles homogeneously, and to minimize the elastic energy the location of s^* in the non-orientable loop is maximally distant from the intersection point (Eq. 4.25). The extensive ground state degeneracy of non-orientable order is here lost as a result of the intrinsic spatial heterogeneity of holey Klein bottles and Möbius shorts.

The above examples indicate that mapping non-orientable 2D surfaces to frustrated

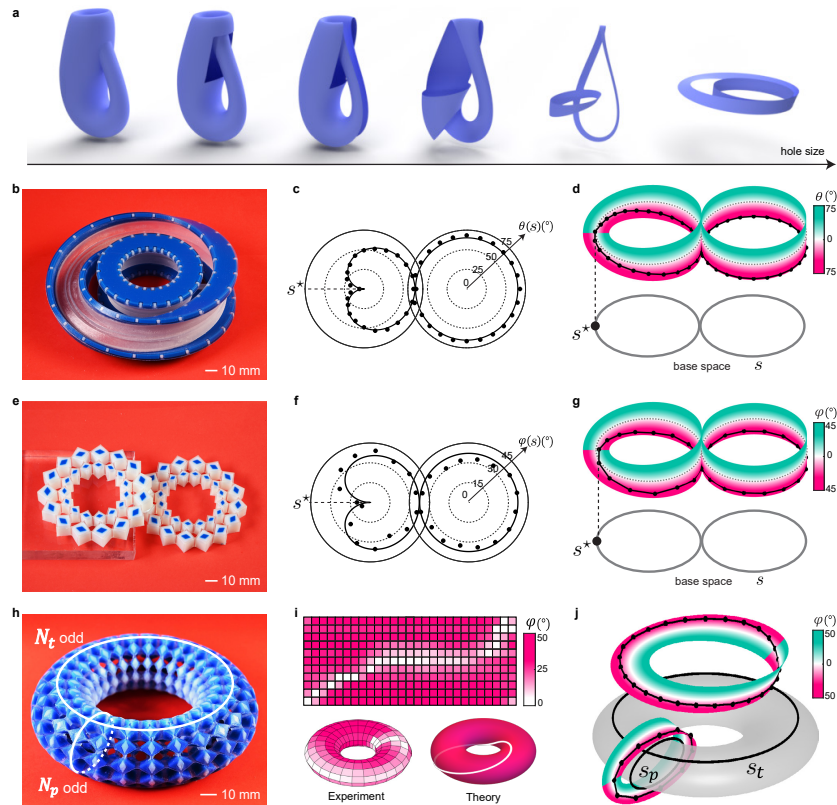


Figure 4.20: **Non-orientable mechanics of higher dimensional metamaterials.** (a) A Klein bottle is a surface topologically equivalent to a square with periodic boundary conditions along the x direction and twisted boundary conditions along the y direction: \mathbb{R}^2 / \sim with the equivalence relation $(x, y) \sim (x + 1, y)$, $(x, y + 1) \sim (-x, y)$. This abstract surface cannot be embedded in our 3D space. Punching a hole in a Klein bottle resolves this limitation: we can fabricate the resulting object. Upon decreasing the hole size, this holey Klein bottle (right) can be continuously deformed into an even simpler shape: Möbius shorts (left). (b) Picture of a 3D printed Möbius shorts composed of two rigidly connected bands: a cylinder and a Möbius band (see SI). (c) We apply a uniform hydrostatic load on 3D printed Möbius shorts. The resulting buckling deformations are heterogeneous. Their magnitude $\theta(s)$ vanish at a point s^* . s^* is located at a maximal distance from the intersection between the two bands. (d) Sketch of the order-parameter bundle (viz. the deformation bundle) of soft Möbius shorts. The black dots correspond to the experimental measurements showed in (c). (e) Two 3D printed metarings are rigidly connected at a pair of nodes. The first ring is made of an even number of lozenges, the second is made of an odd number. (f) The deformations of the connected metarings are associated with a heterogeneous staggered deformation field showing the same variations as in a buckled Möbius shorts, see (c). (g) The order-parameter bundle of two connected metarings identifies with that of soft Möbius shorts, see (d). (h) We 3D print metatorus and vary the parity of the number of lozenges in the toroidal (N_t) and poloidal (N_p) directions. We here illustrate the situation where both N_p and N_t are odd ($N_t = 27$ and $N_p = 11$). We discuss the other two possible parities in Extended Data Fig. 4.23 and SI. (i) Experimental measurements of the staggered rotation field $\varphi(s_t, s_p)$ under uniform hydrostatic pressure, and theoretical prediction of the shape of the loop of zero deformation \mathcal{L} (solid white line), see also Supplementary Video 4. (j) Sketch of the order-parameter bundle of a metatorus made of an odd number of lozenges in both directions. The gray torus is the base space, the coloured strips illustrate the twist of the bundles along the toroidal and poloidal directions. The dark dots are experimental data. They correspond to the measured staggered deformations along two orthogonal cuts along the pressurised metatorus.

metamaterials limits potential applications to complex shapes and (quasi)one-dimensional heterogeneous structures which do not enjoy the extensive ground state degeneracy offered by homogeneous non-orientable order. To circumvent this fundamental limitation, we show below how to engineer non-orientable order in homogeneous two-dimensional metamaterials which cannot be associated with any physical soft surface. A simple design strategy follows from two elementary mathematical property of non-orientable real bundles: (i) They can only be defined when their base space \mathcal{B} hosts non-contractible loops, or in mathematical terms when their fundamental group $\Pi_1(\mathcal{B})$ is non-trivial (such as the unit circle S_1 in Fig. 4.18). The simplest 2D surface enjoying a nontrivial fundamental group is the torus $\mathcal{B} = S^1 \times S^1$. (ii) When restricted to a non-contractible loop, the order parameter bundle must reduce to the Möbius bundle sketched in Fig. 4.18b (see Methods and [171]).

The design strategy then becomes clear. We generalise non-orientable order to higher-dimensional bodies, by constructing frustrated toroidal metamaterials showed in Fig. 4.20h and Extended Data Fig. 4.23. We frustrate the local symmetry breaking of their ground states by tuning the parity of the number of lozenges N_p and N_t along the poloidal and/or toroidal directions. When we place a metatorus in a vacuum bag to apply a uniform hydrostatic compression, we observe the emergence of a zero-deformation loop \mathcal{L} , as illustrated in Fig. 4.20i. When N_p and N_t have opposite parities, \mathcal{L} winds along the direction where the number of lozenges is even, whereas it wind along both directions when both N_p and N_t are odd (as confirmed by experiments showed in Fig. 4.20i, Extended Data Fig. 4.23). When both N_p and N_t are odd the zero loop takes an unanticipated helix shape, which spontaneously breaks both translation and mirror symmetry along both directions (see Fig. 4.20i). In all cases, the spontaneous breaking of translation symmetry results in an extensive degeneracy of the number of equilibria.

To explain how non-orientability determines the topology of the zero-deformation loops, we note that global frustration prevents the emergence of a uniform ground state. Taking the continuum limit and noting s_t and s_p the two principal coordinates on the torus, we find that when N_p and N_t are both odd, for any s_t , there must exist a point $s_p^*(s_t)$ where φ vanishes. Equivalently for any s_p , there must exist a point $s_t^*(s_p)$ where φ vanishes. The resulting set of points \mathcal{L} where $\varphi(s_p, s_t) = 0$ is therefore a loop, which must wind once along each directions. In more technical terms, \mathcal{L} is the composition of the two generators of the fundamental group $\Pi_1(S_1 \times S_1)$. The existence of a non-contractible zero loop reveals the non-orientability of the staggered order parameter $\varphi(s_p, s_t)$. Restricting the base space to a non-contractible loop intersecting \mathcal{L} , and following the reasoning used to describe the 1D metaring, we readily find that the restricted deformations defines a Möbius line bundle, see Fig. 4.20j, Extended Data Fig. 4.23, Methods and SI. We stress that there exist no physical soft-surface whose the buckling modes provide an analogue of the frustrated metatori deformations. The abstract manifold defined by a deformation configuration $\varphi(s_p, s_t)$ has no realisation in our 3D world.

The topology of the deformation bundle determines the winding direction of the \mathcal{L} loops. However, neither the shape nor the response of \mathcal{L} loops to perturbations are determined by non-orientability. Both are set by the specific form of the elastic energy of the metatori. To gain quantitative insight on the morphology of the zero loops, we write a minimal model for the elasticity of the metatori by generalising Eq. (4.25) to two dimensions, see SI for details. In the vicinity of \mathcal{L} , the magnitude of the staggered

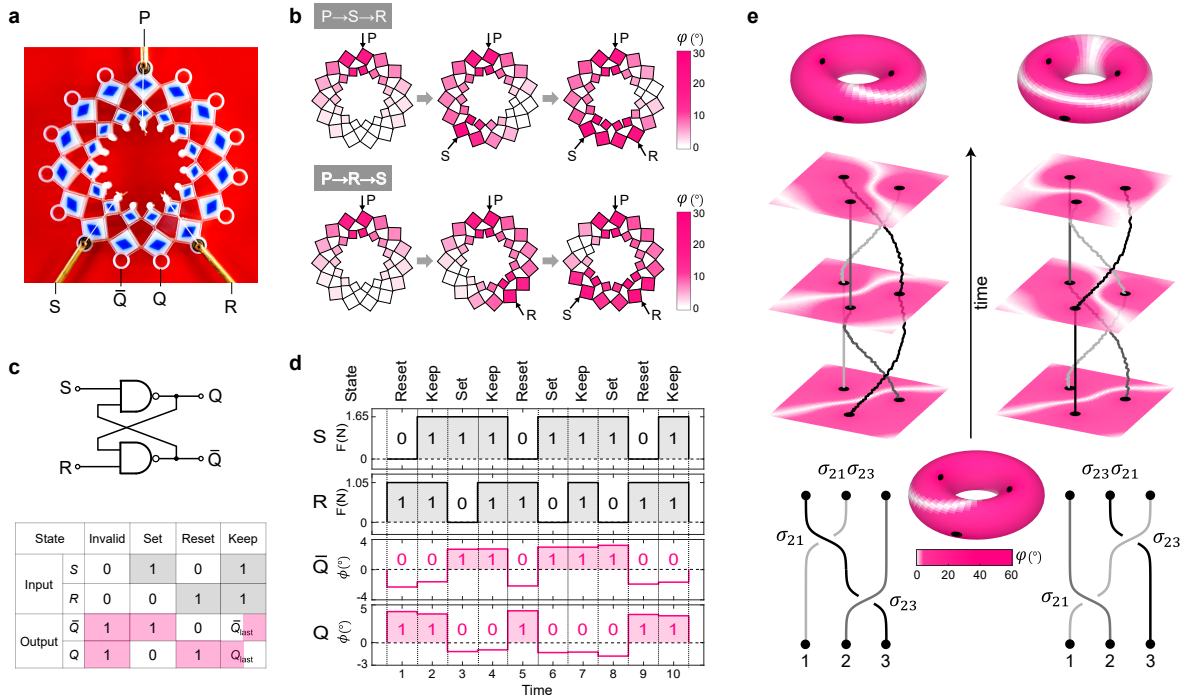


Figure 4.21: **Non-commutative mechanics and mechanical memory.** (a) Picture of an odd metaring under point loads P, S and R (see SI for details). (b) Measurements of the staggered-rotation field φ for two sequences of loading P \rightarrow S \rightarrow R (top) and P \rightarrow R \rightarrow S (bottom), see also Extended Data Fig. ?? and Supplementary Video 5. (c) Circuit diagram (top) and value table (bottom) of a Set-Reset latch. (d) Correspondence between the input loads S and R (black) and output rotations (pink) plotted as function of time for the metaring showed in (a), see also Supplementary Video 6. (e) Numerical simulations of an odd-odd metatorus under two different sequences of identical point loads. The points of application of the loads are continuously moved, effectively braiding their worldlines. While the initial and final load configurations are identical, the shape of the line of zero deformation explicitly depend on the braiding sequence of the load history, see also Supplementary Video 7 and SI for details on the simulation protocol).

deformations is small over a length ξ (see Fig. 4.19). We can then approximate the total elastic energy cost of these deformations by $E = \gamma \int d\sigma$, where σ is the curvilinear coordinate along \mathcal{L} . This is the energy of an elastic string having a finite line tension $\gamma \sim K\varphi_0^2(1 + 2\varphi_0^2)/(2\xi)$. Minimising this energy functional, we therefore find that \mathcal{L} is the loop of minimal length satisfying the winding constraints imposed by non-orientability, in agreement with our experimental measurements reported in Fig 4.20i, Extended Data Fig. 4.23 and SI. For odd-odd metatori, the minimisation of the loop length predicts two mirror configurations winding once around the torus, which explains the spontaneous breaking of parity symmetry upon uniform hydrostatic compression (Fig. 4.20i).

We have shown how frustrated metamaterials generically achieve non-orientable order beyond one dimension. We now show that the topologically protected zero-nodes and zero-lines provide the elementary units of robust mechanical memory. Storing, reading and erasing mechanical information require the deformations to depend on the history of the loading sequence [148–154, 175]. One strategy consists in applying multiple loads

to a material having a non-commutative response, i.e. deformations that depends on the sequential order of the loads. To achieve this property, we apply point loads to odd metarings (Fig. 4.21a).

Applying a first load P results in a zero-node at the diametrically opposite location (Fig. 4.21b). Applying two subsequent loads S and R steers the zero-node counterclockwise when S is applied first, or clockwise when R is applied first (Fig. 4.21b). In other words, the state of deformations cannot be inferred from the sole knowledge of the load positions, but depends on their sequential order.

To realise the write, read, and erase operations, we demonstrate a one-bit digital memory akin to a Set-Reset latch [176] exemplified in Fig. 4.21c. We define two loads (S and R) and two rotation angles (\bar{Q} and Q) as input and output signals respectively (Fig. 4.21a). The sequential loading steps and measurements shown in Fig 4.21d realise all the Set-Reset latch operations shown in Fig 4.21c. We also stress that the read, write and erase operations can be performed sequentially without mechanical resetting [148].

This basic example of non-commutative response stems from non-orientable order, which guarantees the presence of a single zero-node s^* . When more than one point load is applied, the zero-node can be located at multiple stable positions that cannot be captured by linear and commutative response, see Methods, Extended Data Fig. 4.24, 4.25, 4.26, 4.27 and SI for details.

In two dimensions, we show how to tailor the morphology of \mathcal{L} loops, see (Fig. 4.21e). Identical sets of local loads result in dramatically different deformation states that reflect the full braiding history of their worldlines. We apply two load sequences associated with two non-commuting braiding operations and find that the zero-deformation loops protected by non-orientable order store information about the load trajectories. We therefore expect non-orientable order to offer an avenue to perform computational tasks based on source braiding alternative to the holonomic computing paradigm [175, 177, 178].

Acknowledgments. We thank Jasper van Wezel, Martin van Hecke, Anne Meeussen, Li Ma and Yair Shokef for insightful discussions and suggestions, Daan Giesen for technical assistance and Amélie Chardac, Camille Jorge and Romane Braun for help with the active matter and packing experiments. X.G. acknowledgdes financial support from the China Scholarship Council. D.B. and D.C. acknowledge support from IDEXLYON ToRe and ANR WTF grants. C.C. acknowledges funding from the European Research Council via the Grant ERC-StG-Coulais-852587-Extr3Me.

All the codes and data supporting this study are available on the public repository <https://doi.org/10.5281/zenodo.5730508>.

4.8 Methods

4.8.1 Non-orientability of real line vector bundles beyond the Möbius bundle

The simplest vector bundle discussed in this manuscript correspond to the Möbius bundle, a non-orientable real line bundle defined over the unit circle. To design 2D and 3D materials featuring non-orientable order we need to consider non-orientable real line bundles defined on higher-dimensional base space \mathcal{B} . Let us consider a real line bundle $E \xrightarrow{\pi} \mathcal{B}$ defined over a base space \mathcal{B} . This bundle is non-trivial (E cannot be continuously mapped on $\mathcal{B} \times \mathbb{R}$) if it is non-orientable. Equivalently, no homogenous field (order parameter, deformation, etc) can be consistently defined over \mathcal{B} , they must vanish at least at a point [171].

How do we detect the non-orientability of a real line bundle? The simplest procedure consists in assigning to each non-contractible loop \mathcal{C} of the base space \mathcal{B} a number \mathbb{Z}_2 : 0 if the line bundle restricted to \mathcal{C} is a cylinder, 1 if it realizes a Möbius bundle (see SI for an introduction to the Möbius bundle). Given that orientability is a topological property, this index does not depend on smooth deformations of the line \mathcal{C} , and is a property of each homotopy class of loops. This orientability index is thus a homomorphism from the fundamental group of \mathcal{B} $\pi_1(\mathcal{B})$ to \mathbb{Z}_2 from which the first Stiefel-Whitney class $w_1(E)$ is deduced [171]. Non-orientable order thus only exists on manifolds that feature non-contractible loops, *i.e.* for which the fundamental group $\pi_1(\mathcal{B})$ is non-trivial.

The simplest 1D examples are the circle S^1 (Fig. 4.18b in the Main Text), or several circles intersecting at a point (Fig. 4.20d in the Main Text). The simplest 2D case correspond to the torus (Fig. 4.20j in the Main Text) considered in this article.

Note that while non-orientability is detected from considerations along one-dimensional loops, it encodes a genuine higher dimensional topological property. This contrasts with the concept of weak topological gapped phases, where the topological index characterising an insulating phase in d dimensions is extended in $d + 1$ dimensions by a stacking procedure.

4.8.2 Non-commutative response and non-orientable order

Intuitive explanation

As explained in the Main Text, non-orientable order requires two ingredients: (i) spontaneous local symmetry breaking, (ii) deformation fields that live on a non-orientable fibre bundle. Both play essential roles in achieving non-commutative response.

(i) *Spontaneous local symmetry breaking.* First, let us consider a single pair of lozenges under sufficiently large axial compressive loads. The lozenges can buckle with equal probability along one direction or the other (Extended Data Fig. 4.24a) and therefore spontaneously break the left-right symmetry. However, if the lozenges are already twisted, axial compressive loads can only increase the amplitude of rotation and can not reverse the sign of the lozenges' orientation (Extended Data Fig. 4.24b). As a consequence, the sign of the rotation strongly depends on the previous deformation of the structure. This property gives the system sequential memory and therefore offers the possibility to achieve

a non-commutative response, i.e. different loading sequences lead to different states of deformation.

However, local symmetry breaking by itself is not enough to achieve a non-commutative response. An obvious example is provided by a ring made of an even number of pairs of lozenges. When we apply the first axial compressive load P , antiferromagnetic order—adjacent squares rotating in opposite directions—extends over the whole ring (Extended Data Fig. 4.24c). No matter how many subsequent axial compressive loads are applied, and what the loading sequence is, the sign of the lozenges' rotation remains the same (Extended Data Fig. 4.24c). In other words, different loading sequences do not alter the ultimate deformations. Even metarings do not achieve non-commutative response, see Extended Data Fig. 4.24d for the data from experiments.

The trivial result of the even metaring indicates that, to achieve the non-commutative response, the sign of the rotation is required to be changeable during the loading process. Our strategy to achieve non-commutative response is introducing a frustration into the system using a non-orientable fibre bundle, and then changing the sign of the rotation by moving the position of the frustration.

(ii) *Non-orientable fibre bundle.* As mentioned in the Main Text, the deformation field of the odd metaring lives on a non-orientable fibre bundle. When a load P is applied, antiferromagnetic order extends simultaneously on both sides of the point P . However, due to the geometric frustration caused by the non-orientable bundle, antiferromagnetic order cannot extend across the whole ring. Therefore a zero-node must exist at a location s^* . In this simple case s^* corresponds to a maximal distance from P as a result of energy minimisation (Extended Data Fig. 4.24e (top left)).

The lozenge where the second load S is applied has already experienced a counterclockwise rotation, in response to the first point load P (Extended Data Fig. 4.24e (top left)). Therefore, the S load amplifies the counterclockwise rotation of the lozenge and pushes the zero-node s^* away from S to minimise the deformation gradients, and therefore the overall elastic energy. When s^* crosses the lozenge located at the position R , the sign of the lozenge's rotation is reversed accordingly (Extended Data Fig. 4.24e (top middle)). Therefore, the third load R pushes the zero-node s^* further to the right-hand side of the ring as exemplified in Extended Data Fig. 4.24e (top right).

However, when we change the loading sequence to $P \rightarrow R \rightarrow S$, the zero-node s^* is pushed along a different path towards the left-hand side of the ring as shown in Extended Data Fig. 4.24e (bottom). As a result, the two loading sequences $P \rightarrow S \rightarrow R$ and $P \rightarrow R \rightarrow S$ result in different states of deformation. This phenomenon can also be described as a non-commutative response, i.e. $P + S + R \neq P + R + S$ (Extended Data Fig. 4.24f).

In summary, spontaneous local symmetry breaking gives the system sequential memory. The non-orientable fibre bundle provides the possibility to achieve multiple states of deformation. The combination of these two ingredients leads to a non-commutative mechanical response.

A continuum theory perspective on non-commutative response

We now present a deeper link between non-orientable order and non-commutative response using continuum theory. The existence of a non-orientable fibre bundle implies that there exists an odd number of zero-nodes in the deformation field along the ring. So, in principle

an odd metaring could have three or more zero-nodes. But in this letter, we only focus on the low energy level, where an odd(even) metaring features 1(0) zero-node.

Let us start with the trivial case of the even metaring. When applying N axial compressive point loads, they compartmentalise the ring into N sectors. For each sector $[s_n, s_{n+1}]$, we have a solution $\varphi_n(s) = A_n e^{s/\lambda} + B_n e^{-s/\lambda}$, with

$$\begin{pmatrix} A_n \\ B_n \end{pmatrix} = \begin{pmatrix} e^{s_n/\lambda} & e^{-s_n/\lambda} \\ e^{s_{n+1}/\lambda} & e^{-s_{n+1}/\lambda} \end{pmatrix}^{-1} \begin{pmatrix} \bar{\varphi}_n \\ \bar{\varphi}_{n+1} \end{pmatrix}, \quad (4.26)$$

where λ is the elastic penetration length (see Eq. S20 in SI). Let us consider the case where three point loads P , S and R are applied. Using the principle of minimum potential energy, we can calculate the boundary values of all sectors, $\bar{\varphi}_P$, $\bar{\varphi}_S$ and $\bar{\varphi}_R$ (see SI for details), and compute the full deformation field (Extended Data Fig. 4.25a). We notice that there exists only one set of stable equilibria, φ and $-\varphi$. The selection of the sign of rotation, φ or $-\varphi$ is random, but is fixed when the first load is applied. We therefore describe the pair of equilibria φ and $-\varphi$ as the same state of deformation. No matter what the loading sequence is, the even metaring always reaches the same and only possible state of deformation. Therefore, an even metaring cannot achieve non-commutative response. For sake of clarify we henceforth use φ to represent the magnitude of the staggered angle.

Let us now consider the case of odd metarings. The deformation field of the odd metaring lives on a non-orientable fibre bundle. Non-orientability implies that the bundle is non-trivial, which guarantees the existence of point s^* where $\varphi(s^*) = 0$.

The zero-node s^* and the N point loads compartmentalise the ring into $N + 1$ sectors. The deformations in each sector still conform to the function Eq.(4.26). Importantly, s^* can be located in any interval $[s_{n-1}, s_{n+1}]$:

$$s_n^* = \frac{1}{2}(s_{n-1} + s_{n+1}) + \frac{1}{2}\lambda \ln \left| \frac{e^{s_{n+1}/\lambda} \bar{\varphi}_{n-1} + e^{s_{n-1}/\lambda} \bar{\varphi}_{n+1}}{e^{s_{n-1}/\lambda} \bar{\varphi}_{i-1} + e^{s_{n+1}/\lambda} \bar{\varphi}_{n+1}} \right|, \quad (4.27)$$

so there exist N possible locations for s^* . Under three point loads P , S and R , the zero-node s^* can be located in any of the three intervals: $s_1^* \in [s_P, s_R]$, $s_2^* \in [s_R, s_S]$ or $s_3^* \in [s_S, s_P]$. For each s_n^* , using the minimum potential energy principle, we can calculate the corresponding boundary values $[\bar{\varphi}_P^n, \bar{\varphi}_S^n, \bar{\varphi}_R^n]$ and compute the full deformation field (Extended Data Fig. 4.25b). There are $N = 3$ possible solutions, which makes it possible to achieve a non-commutative response. We stress that the existence of multiple solutions is intimately linked to the nonlinearity introduced by the spontaneous symmetry breaking.

We proved that odd metarings can enjoy multiple stable equilibria. Now the question is: which equilibrium does the system select? The answer depends on the loading history. The location of the zero-node s^* tends to move continuously during the loading process (Extended Data Fig. 4.25c), otherwise the system would need to overcome a huge energy barrier to jump from one equilibrium state to another. When the loading sequence is $P \rightarrow S \rightarrow R$ (resp. $P \rightarrow R \rightarrow S$), the zero-node moves continuously to the location s_3^* (resp. s_1^*) (Extended Data Fig. 4.25c). Different loading sequences lead to different states of deformation: odd metarings enjoy non-commutative response.

It is also worth noting that the zero-node can end its journey at s_2^* . However this cannot be realised by merely switching the load sequences, like applying PSR , PRS , SPR and so on. More steps are required to reach this state, for instance, by applying the sequence $P \rightarrow 0.985S \rightarrow 0.99R \rightarrow 0.015S \rightarrow 0.01R$, see Extended Data Fig. 4.25d.

Non-commutative conditions

In the above, we have presented some specific examples of non-commutative response. However, this feature is not systematic, and require some operating conditions which we describe in details below. The non-commutative response requires two conditions : (i) the system must have more than one stable equilibrium states, (ii) under different loading sequences, the topologically-protected zero-nodes must end in different sectors of the metaring. (Extended Data Fig. 4.26 a and b). These two conditions are controlled by three parameters: (i) the amplitude of the loads, (ii) the locations of the loads, (iii) the loading sequence.

These three parameters have infinite combinations. So, in practice, we only discuss the role of the locations of the point loads. We consider load of equal amplitudes applied sequentially. So the loading sequence of the three loads have six possible permutations. Given this protocol, the condition for non-commutative response is that the length of each sector is smaller than the half length of the whole loop, i.e. $\max[l_{PS}, l_{SR}, l_{RP}] < L/2$, see Extended Data Fig. 4.26 for detailed discussion. Importantly, although three stable equilibria exist, only two possible states can be reached by the six load permutations (Extended Data Fig. 4.26). Reaching the third equilibrium state required applying a different protocol as exemplified in the previous section.

4.8.3 Mechanical sequential logic gate

In this section, we use the same setup as the previous section to realise a mechanical sequential logic gate, see Fig. 4.21a in the Main Text and SI for detailed technical information. We apply three axial compressive point loads P , S and R on the ring. The load P is a pre-load and always exists during the whole process. Loads S and R are two binary inputs. The inputs are 1 when a load is applied and 0 otherwise. The rotation angles \bar{Q} and Q are two outputs. They can be binarized by assigning the values 1 for clockwise rotations and 0 for counterclockwise rotations. The mechanical logic gate we build can achieve the same value table as the Set-Reset latch, one of the most typical sequential circuits (Fig. 4.21c in the Main Text). Unlike combinational circuits, the outputs of sequential circuits do not only depend on the inputs, but also the outputs of the previous steps. The sequential circuits have memory. This memory is embodied as the state 'Keep' in our mechanical logic gate. When all three loads are applied, i.e. the inputs $SR = 11$, the logic gate is at the state 'Keep', and the outputs keep the output values from the previous step. The state 'Keep' also reflects the non-commutative response of the metaring (the same loads (input) can lead to different states of deformation (outputs)), see Extended Data Fig. 4.27.

Importantly, the mechanical sequential logic gate works under continuous input signals without any mechanical reset. This property requires the unloading process to conform to the value table. For example, when we change the inputs from $SR = 11$ (Keep) to $SR = 01$ (Reset), i.e. unload the force S , no matter what the outputs of the previous step are, the outputs must be reset as $\bar{Q}Q = 01$. To satisfy this condition, we adjust the magnitude of the loads, so that the system features only one stable equilibrium state (see SI for detailed information). As the system always reaches the same equilibrium, it therefore gives the same outputs. Similarly, the inputs $SR = 10$ (Set) also requires constant outputs $\bar{Q}Q = 10$. By applying a continuous load signal on the setup we build,

we checked that the setup indeed conforms to the value table during either the loading process or the unloading process. The result is shown in Fig. 4.21d of the Main Text.

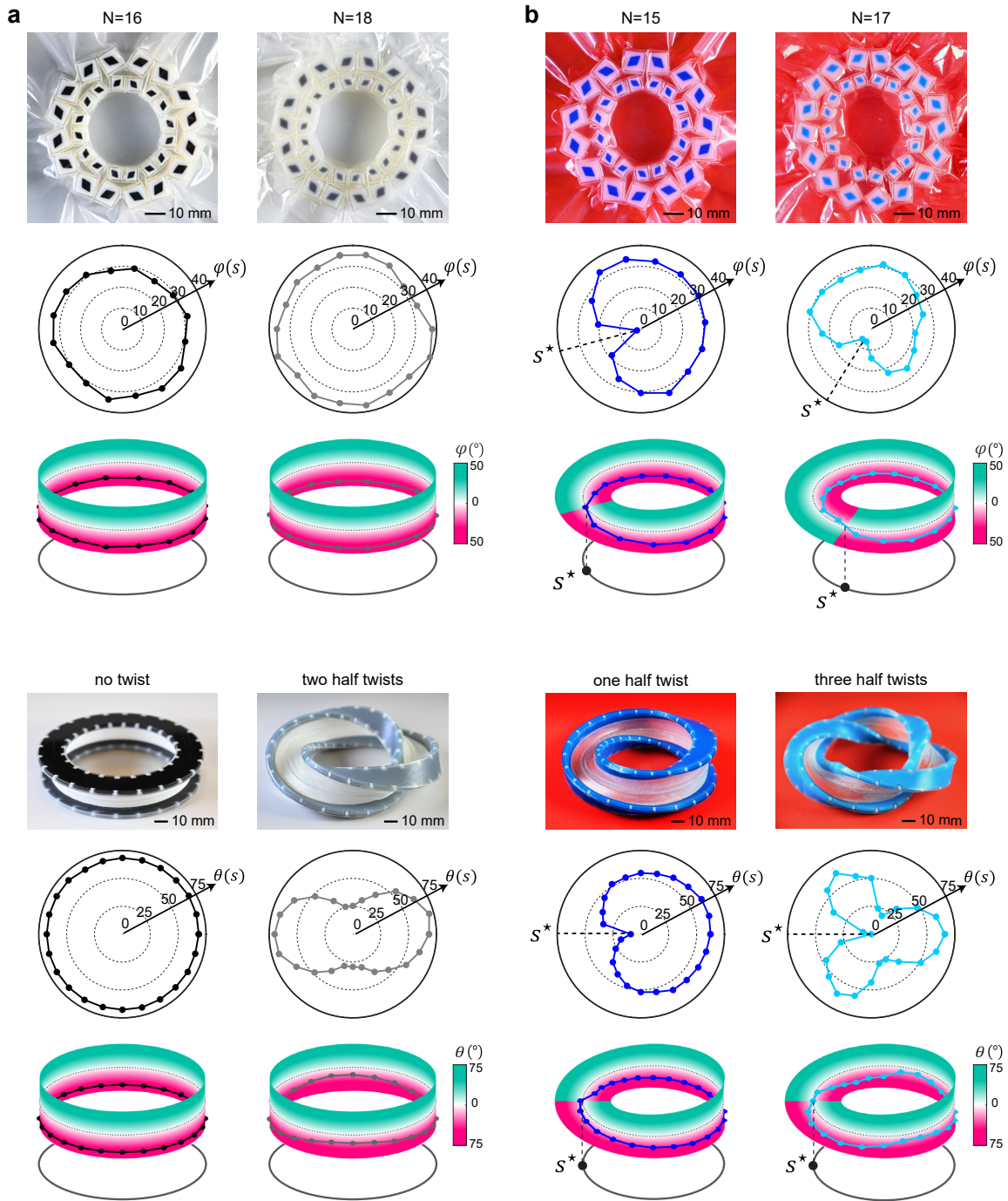


Figure 4.22: Metarings and twisted bands under hydrostatic compression. From top to bottom, we show pictures of the compressed specimen (top), polar plots of the deformations (middle) and the corresponding order-parameter bundles (bottom). **(a)** Metarings with an even number of pairs of lozenges and twisted bands with an even number of half twists live on a cylinder bundle. The order parameters $\varphi(s)$ and $\theta(s)$ do not vanish under hydrostatic compression. **(b)** Metarings with an odd number of pair of lozenges and twisted bands with an odd number of half twists live on a Möbius bundle. The order parameters $\varphi(s)$ and $\theta(s)$ vanish at one point s^* under hydrostatic compression. The inhomogeneous bending angles of twisted bands are due to the inhomogeneous geometry of the bands.

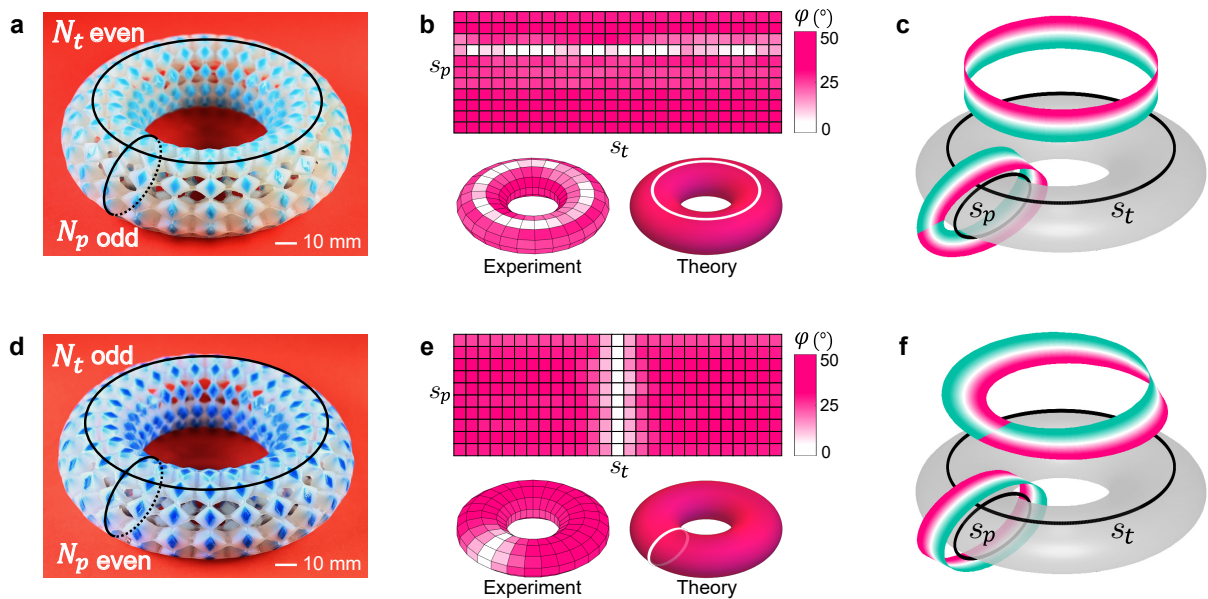


Figure 4.23: **Non-orientable mechanics of toroidal metamaterials.** We vary the parity of the number of lozenges in the toroidal (N_t) and poloidal (N_p) directions: **(a-c)** $N_t = 26$ and $N_p = 11$; **(d-f)** $N_t = 27$ and $N_p = 10$. **(a, d)** 3D printed metatortori. **(b, e)** Experimental measurements of the staggered rotation field $\varphi(s_t, s_p)$ under hydrostatic pressure, and theoretical prediction of the shape of the loop of zero deformation \mathcal{L} (solid white line), see also Supplementary Video 4. **(c, f)** Non-orientable bundles of the staggered-rotation fields. The gray tori represent the base space. The coloured strips illustrate the twist of the bundles along the toroidal and poloidal directions.

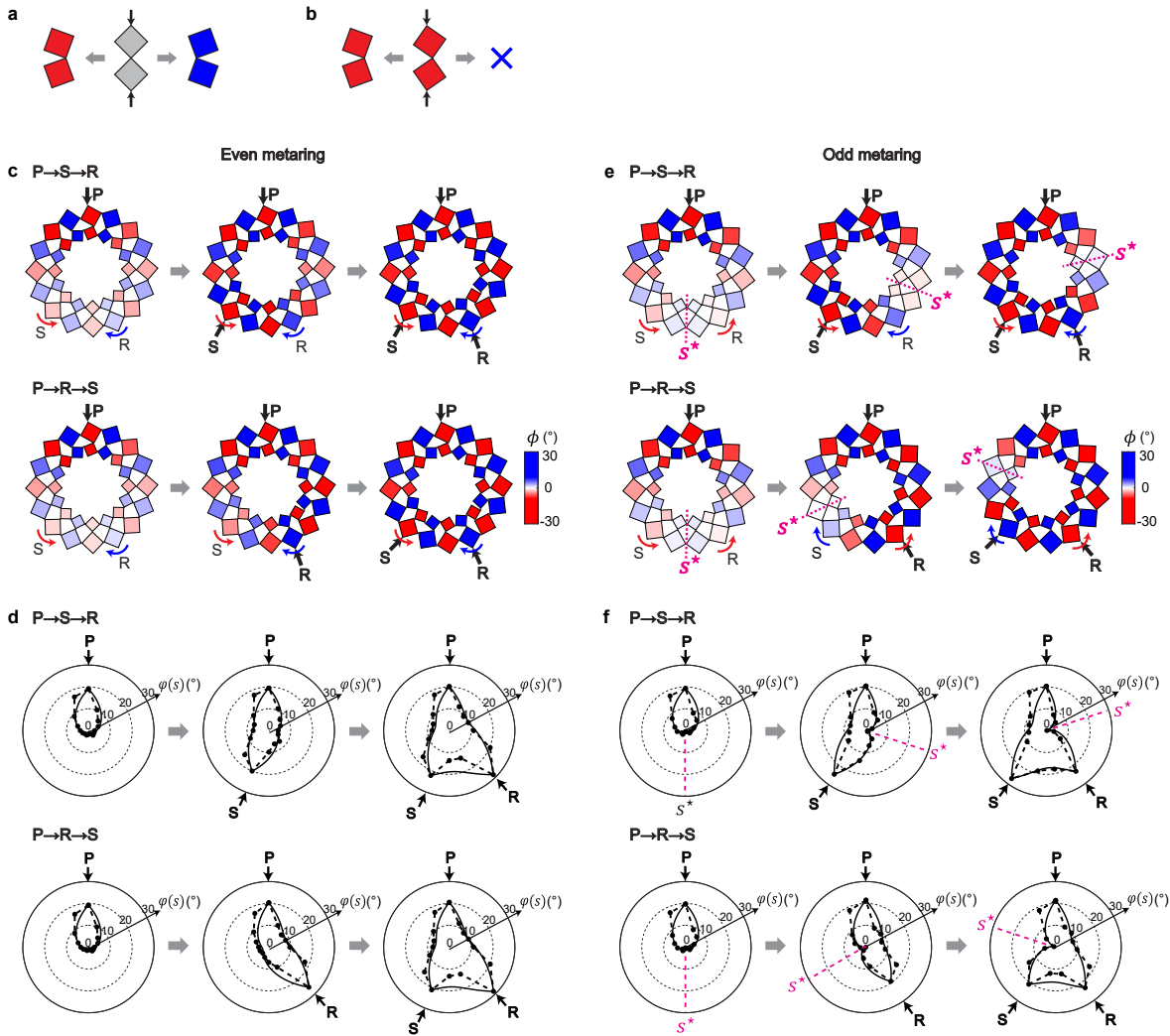


Figure 4.24: **Non-commutative response with non-orientable order.** (a) A pair of lozenges buckles with equal probability along one direction or the other under axial compression and therefore spontaneously break the left-right symmetry. (b) For a pair of twisted lozenges, axial compressive loads can only increase the amplitude of rotation and can not reverse the sign of the lozenges' orientation. (c-d) Under two different the loading sequences $P \rightarrow S \rightarrow R$ and $P \rightarrow R \rightarrow S$, an even metaring (16 pairs of lozenges) displays the same response. The sign of the lozenges' rotation remains the same no matter what loading sequence is applied. (c) Reconstructed metarings. (d) Polar plots of the staggered rotation angle φ . (e-f) Under two different the loading sequences $P \rightarrow S \rightarrow R$ and $P \rightarrow R \rightarrow S$, an odd metaring (15 pairs of lozenges) displays different responses. (e) Reconstructed metarings. (f) Polar plots of the staggered rotation angle φ . Left row: Under a point load P a zero-node s^* appears at the maximum distance from P . Middle row: The second load S (R) pushes the zero-node s^* away from S (R). The sign of the rotation of lozenges located at position R (S) is reversed while applying the load S (R). Right row: The third load R (S) pushes the zero-node s^* further to the right side (left side) of the ring.

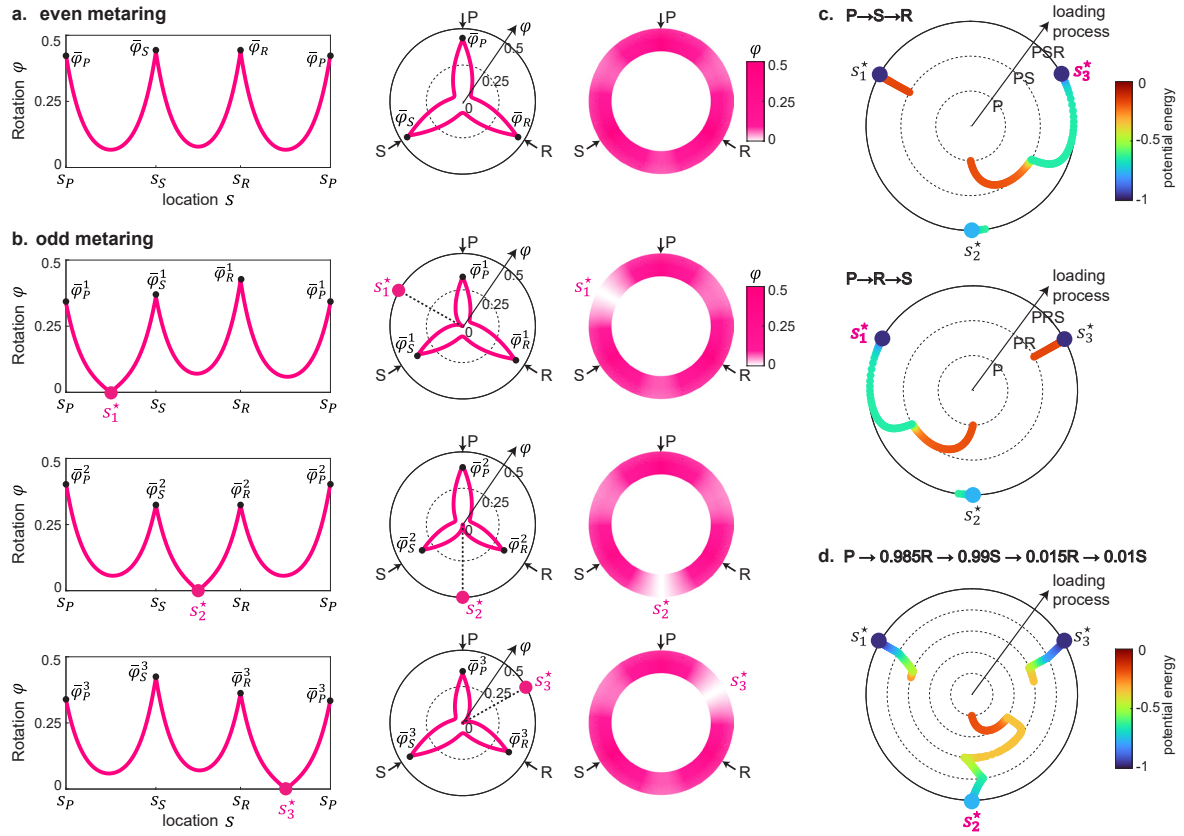


Figure 4.25: **Stable equilibria and the moving path of the zero-node s^* of metarings in continuum theory.** (a) The deformation plots of an even metaring under three point loads P , R and S in continuum theory. There is only one stable equilibrium. (b) The deformation plots of an odd metaring under three point loads P , R and S in continuum theory. There are three possible stable equilibria. Each stable equilibria corresponds to a zero node s^* in different intervals: $s_1^* \in [s_P, s_R]$, $s_2^* \in [s_R, s_S]$ or $s_3^* \in [s_S, s_P]$. (c) Under the loading sequence $P \rightarrow S \rightarrow R$, the zero-node continuously move to the location s_3^* . (d) Under the loading sequence $P \rightarrow R \rightarrow S$, the zero-node continuously move to the location s_1^* . (e) Under the loading sequence $P \rightarrow 0.985R \rightarrow 0.99S \rightarrow 0.015R \rightarrow 0.01S$, the zero-node continuously move to the location s_2^* . We take $s_P = 0$, $s_R = 0.34$, $s_S = 0.66$, $\bar{F}_P = \bar{F}_S = \bar{F}_R = 366.7$, $K = 12$ and $\lambda = 0.0667$ in all cases, see SI for details.

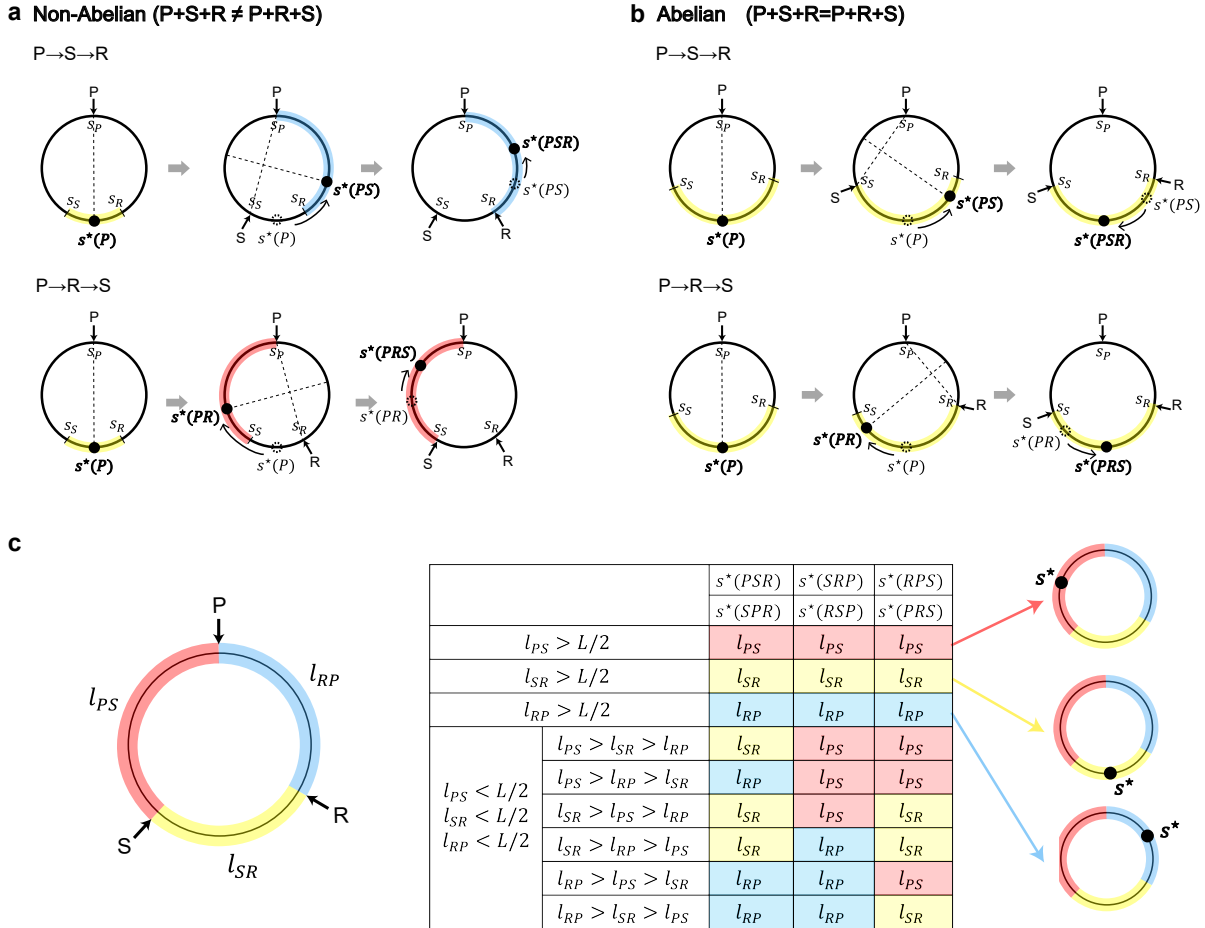


Figure 4.26: **Conditions of non-commutative mechanics of an odd metaring in response to three local loads.** (a) A case where the points of applications of the loads P , R , S leads to non-commutative response. Under two different load sequences, the third load pushes the zero-nodes s^* towards into two distinct sectors. (b) A case where the points of applications of the loads P , R , and S do not allow for a non-commutative response. Under two different loading sequences, the third load pushes the zero-nodes s^* back towards the same sector. (c) Conditions for non-commutative responses based on the relative sizes of the sectors l_{PS} , l_{SR} and l_{RP} , and on the sequential order of the loads P , R and S , and location of the zero-node s^* resulting from six different loading sequences. The zero-node can be located at three different possible locations: in the sector l_{PS} , l_{SR} and l_{RP} . L is the length of the whole loop.

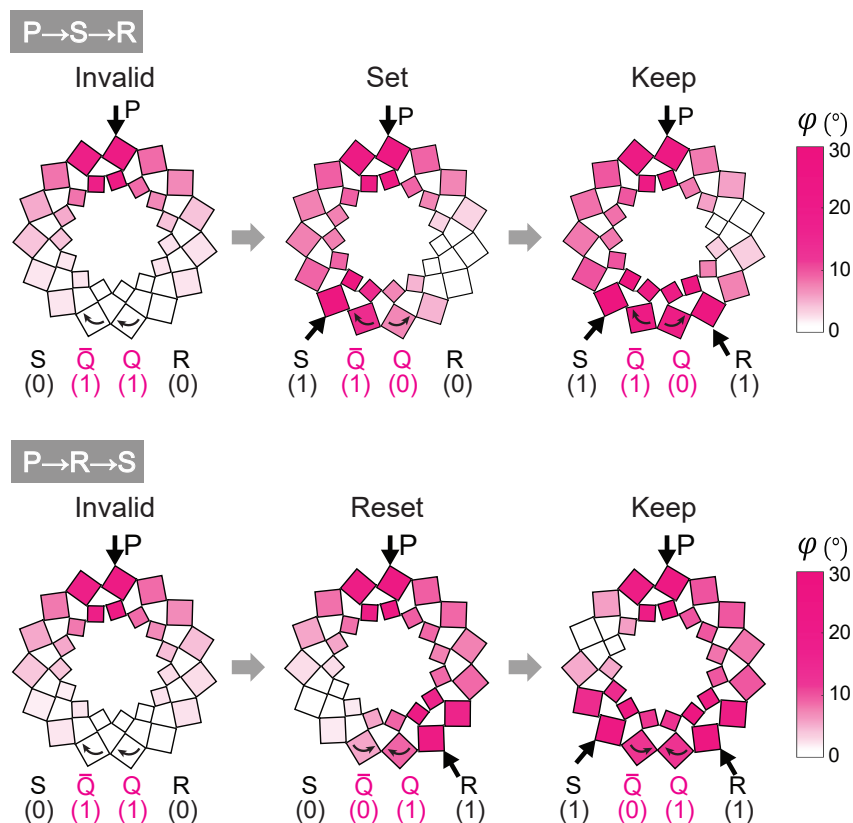


Figure 4.27: **Mechanical sequential logic gate using the non-commutative response of an odd metaring.** The load P is a pre-load and always exists during the whole process. Loads S and R are two inputs. The inputs are 1 when a load is applied and 0 otherwise. The rotation angles \bar{Q} and Q are two outputs. The outputs are 1 for clockwise rotations and 0 for counterclockwise rotations. The non-commutative response of an odd metaring conforms to the value table of a Set-Reset latch (Fig. 4.21c in the Main Text).

4.9 Supplementary Videos

Supplementary Video 1: Active liquid shows global frustration.

Supplementary Video 2: An odd metaring and an even metaring are compressed homogeneously by a vacuum bag.

Supplementary Video 3: A Möbius band and a cylinder are compressed homogeneously by a vacuum bag.

Supplementary Video 4: Tori with different parities of the number of lozenges along toroidal and poloidal directions are compressed homogeneously by a vacuum bag.

Supplementary Video 5: Under two different loading sequences, an odd metaring shows non-commutative response.

Supplementary Video 6: A mechanical sequential logic gate realises all the Set-Reset latch operations.

Supplementary Video 7: Numerical simulations of an odd-odd metatorus under different sequences of identical point loads.

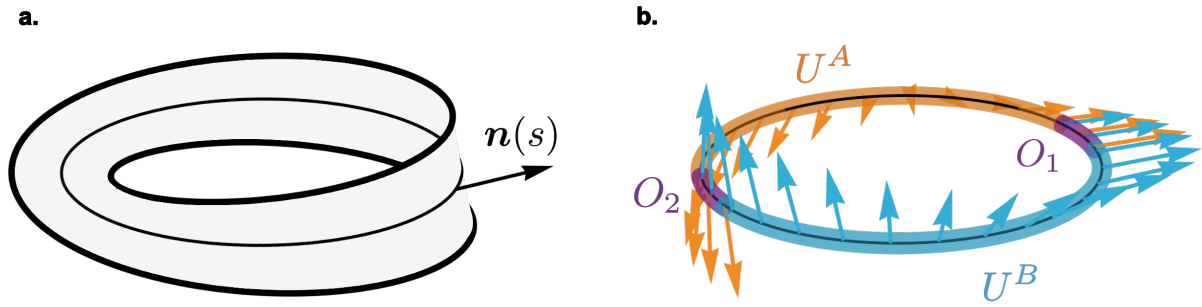


Figure 4.28: **Möbius strips are non-orientable.** **a.** Ruled surface having the shape of a Möbius strip, and definition of the normal vector $\mathbf{n}(s)$. **b.** It is impossible to define a consistent choice of a continuous normal-vector field on a Möbius strip. Considering two open sets covering the base circle S_1 , the product of the transition functions over the two open overlaps O_1 and O_2 is equal to -1 .

4.10 Supplementary Information

4.10.1 Bending mechanics of Möbius strips and non-orientable deformation bundles

A Möbius strip is a non-orientable surface

Fig. 4.28a shows a Möbius strip defined as a ruled surface of constant width w . We note s the curvilinear coordinate along the circular centerline of unit length, and $\mathbf{n}(s)$ the unit vector normal to the surface at s . The Möbius strip provides a prototypical example of a non-orientable manifold: it is impossible to coherently define a smooth normal vector field over the whole strip. At best, we can define smooth unit normal vectors n_A and n_B over two overlapping open intervals U^A and U^B , as illustrated in Fig. 4.28b. In each of the two overlap regions O_1 and O_2 , we can define a transition function $\eta_{1,2}$ which relates the two orientation conventions \mathbf{n}^A and \mathbf{n}^B : $\mathbf{n}^A = \eta_1^{AB} \mathbf{n}^B$ in O_1 and $\mathbf{n}^A = \eta_2^{AB} \mathbf{n}^B$ in O_2 . Non-orientability translates in the relation [131]:

$$\eta_1^{AB} \eta_2^{AB} = -1, \quad (4.28)$$

which prevents the definition of a smooth unit-vector field $\mathbf{n}(s)$ over $U^A \cup U^B$ [132, 179]. We explain below that the non-orientability of soft Möbius strip's results in a non-trivial topology of their bending deformations bundle.

The bending-deformation bundle of a Möbius strip is non-orientable

To single out the impact of non-orientability on buckling deformations, we use a low-energy description of the bending deformations. More specifically, we consider a single bending angle $\theta(s)$ associated to a displacement $\delta \mathbf{R}^*(s)/w = \frac{1}{2} \sin \theta(s) \mathbf{n}(s) \sim \frac{1}{2} \theta(s)$ along the local normal vector, see Fig. 4.29a. The bending deformations fields $\theta(s)$ define a real line bundle over S_1 . We now show that its topology is non trivial.

We first note that, as $\mathbf{n}(s)$ must be defined separately on the two open sets U^A and U^B , we also have to assign two consistent sign conventions for the bending angle (θ_A

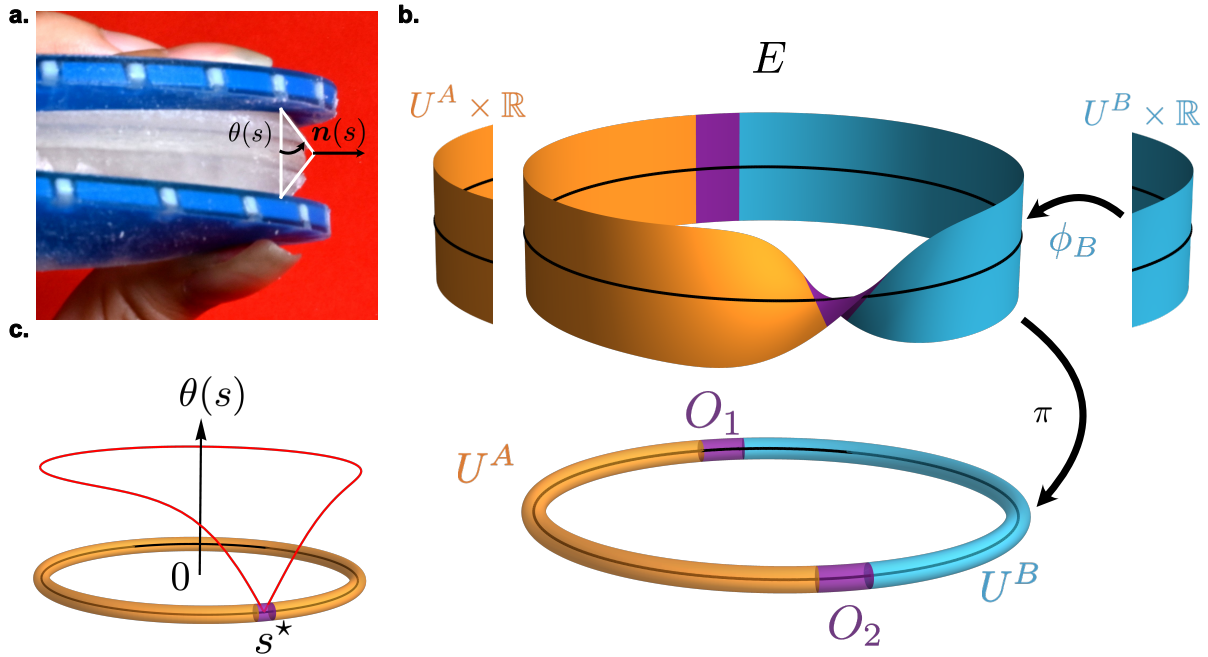


Figure 4.29: **Bending-deformation bundle of an elastic Möbius strip.** **a.** Picture of a buckled Möbius strip described in the Methods. In our simplified picture, the bending elasticity is captured by a single bending angle $\theta(s)$, the resulting local displacement vector is $\delta\mathbf{R}^*(s) = \sin\theta(s)\mathbf{n}(s)$. **b.** Sketch of the line bundle structure. The total space E is locally isomorphic to a cylinder ($\mathbb{R} \times S_1$) but not globally. The two sections θ_A and θ_B are defined on two overlapping open intervals U^A and U^B of the unit circle S_1 . **c.** Maximally large trivial section of the deformation bundle. It is defined over $U^A = S_1 \setminus \{s^*\}$, the non-orientability of the bundle structure implies that the deformation vanishes at s^* .

and θ_B). Conversely, the physical observable $\delta\mathbf{R}^*(s)$ is a displacement vector in our 3D Euclidian space, which does not depend on any local representation of the Möbius strip orientation. Therefore, when the orientation convention changes, the deformations must obey the same \mathbb{Z}_2 gauge transformation rule [?]:

$$\begin{cases} \mathbf{n}_{A/B} & \rightarrow & -\mathbf{n}_{A/B} \\ \theta_{A/B} & \rightarrow & -\theta_{A/B} \end{cases} \quad (4.29)$$

In all that follows $X_{A/B}$ stands for X_A or X_B . We can now describe the strip elasticity in term as a non-trivial line bundle, sketched in Fig. 4.29b, see [132, 179] for more mathematical details. The local deformation $\theta(s)$ belongs to a real fiber \mathbb{R}_s at each point s of the base manifold S_1 . By definition, the total space E of the deformations defines a fiber bundle. The scalar deformation fields $\theta_{A/B}(s)$ define two local sections of the deformation bundle. In an open neighborhood U_s of s , the deformations $\theta(s)$ is defined by a local choice of orientation. In more mathematical terms, this defines a local trivialization $\pi^{-1}(U_s) = \Phi_s(U_s \times \mathbb{R})$, where Φ_s is a smooth mapping, and where π is the local projection $E \xrightarrow{\pi} S_1$. Finally, the local choice of the orientation of the Möbius strip, discussed in Section 4.10.1, naturally associates a \mathbb{Z}_2 structure group (Eq. (4.29)) to the bundle definition, see also [?].

We can see that the deformation bundle is non-trivial by using the two bundle charts (U^A, Φ^A) and (U^B, Φ^B) sketched in Fig. 4.29b. In the open overlap O_1 , we can always choose the same orientation for the two charts, i.e. $(\Phi^A)^{-1} \circ \Phi^B(s, \theta) = (s, \theta)$ for all $s \in O_1$. However, given this choice, Eq. (4.28), and the independence of the real-space displacements $\delta \mathbf{R}^*(s)$ on the local orientation of the strip, imply that $(\Phi^B)^{-1} \circ \Phi^A(s, \theta) = (s, -\theta)$. The transition function $\Phi^B \circ (\Phi^A)^{-1}$ relating the two bundle charts in O_2 must have a negative Jacobian. This result defines a non-orientable line bundle: the bending deformations of a soft Möbius strip is non-orientable [132, 179]. An essential property of real line bundles is that non-orientability is equivalent to topological non-triviality. When a bundle is non-trivial, it is impossible to define a smooth non-vanishing section $\theta(s)$ over the whole base space S_1 . Regardless of the specifics of the elastic energy, non-orientability requires continuous bending deformations $\theta(s)$ to vanish at least at one point s^* along the strip. Simply put, Möbius strips are topologically protected against homogeneous buckling.

We close this section with three comments. Firstly, in the Main Text, and in all that follows, we avoid referring to the definition of two separate intervals by defining U^A as the maximally large open set over which the line bundle can be trivialized. Given the location of s^* , we define *a posteriori* $U^A = S_1 \setminus \{s^*\}$. We then drop the A index and $\theta_A(s) \equiv \theta(s)$. Given this definition of the bending deformations, $\theta(s)$ is continuous over the whole strip and vanishes at s^* , Fig 4.29c. Secondly, the definition of $\theta(s)$ does not require introducing a double covering of the Möbius strip [?]. The double-covering formulation is not in contradiction with the one used in this work. They represent two line-bundle representations of topologically constrained scalar fields defined over S_1 . Finally, our representation of the deformations of non-orientable manifolds are based on single-valued continuous fields. Therefore, it allows us to use a standard elastic energy:

$$\mathcal{E} = \frac{1}{2} \int_{S_1 \setminus \{s^*\}} (\partial_s \theta)^2 + 2V(\theta) ds, \quad (4.30)$$

where $V(\theta)$ is a potential parametrized by the magnitude of the axial load F . $V(\theta)$ is a symmetric bistable potential when F exceeds the Euler buckling threshold, see Fig. 1. The minimization of Eq. (4.30) in the specific case of a quartic potential was discussed in [?]. The comparison to our experimental measurements (Fig. 1d in the Main Text) demonstrates that the minimal model introduced in this section provides an excellent proxy of the full thin-sheet elasticity problem [180].

4.10.2 Non-orientable mechanics of anti-ferromagnetic mechanical metamaterials

Bending-Shearing model

The mechanical description of the metamaterials showed in Figs. 1 and 2 of the Main Text, is based on the bending-shearing model of Ref. [133]. This minimal model describes the deformations of a lattice of rigid lozenges connected by elastic hinges, see Fig. 4.30a. In this picture, the lozenges are squares of size L , their centers are separated by a distance a and the hinges' length is ℓ . The predominant deformations are the bending and shearing modes of the elastic hinges sketched in Fig. 4.30b. In the limit of small deformations, we

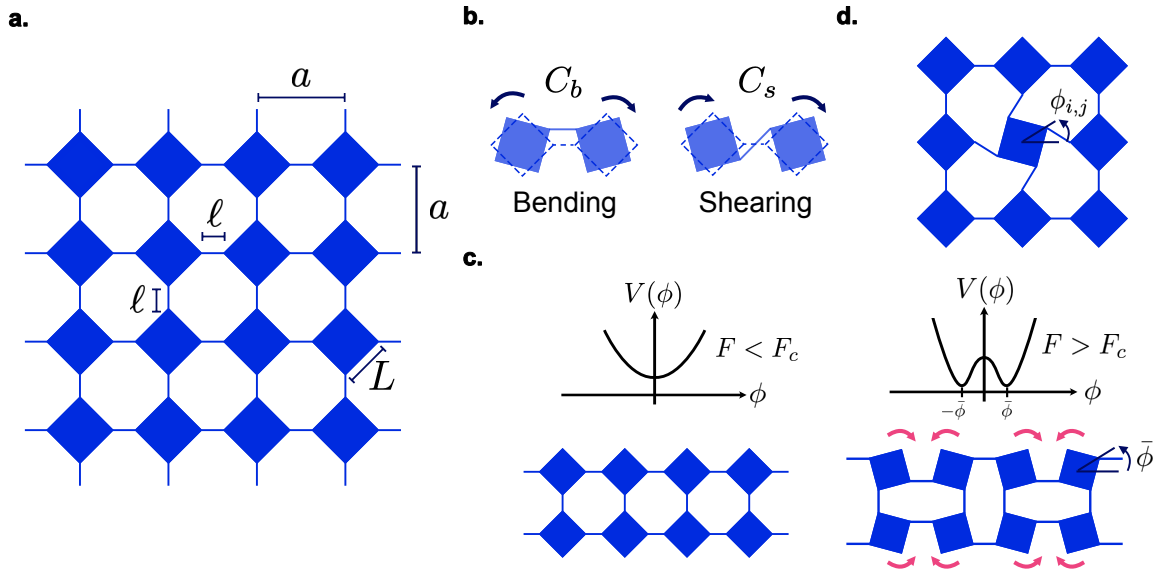


Figure 4.30: **Bending-Shearing model.** **a.** A square lattice of rigid squares connected by soft hinges. We note: a the lattice spacing, ℓ is the hinge length, and L the square size. **b.** Bending and shearing deformations of the filaments promote respectively the co-rotation and counter-rotation of adjacent squares. **c.** Each square is associated to a single degree of freedom ϕ corresponding to its rotation with respect to its equilibrium position. **d.** Total mechanical energy of the metamaterial under the action of a homogeneous compression load F . When $F < F_c$ the lattice is undeformed. When $F > F_c$, the lattice buckles in plane, and a global anti-ferromagnetic order emerges.

neglect the translation of the lozenge centers, and focus on their rotation. The Bending-Shearing model therefore consists in a competition between co-rotation of neighboring lozenges promoted by bending, and counter-rotation promoted by shearing, Fig. 4.30b.

Continuum mechanics of an open meta-chain

To gain some intuition, we consider first the simple case of an open meta-chain made of two rows of N squares. Within a harmonic approximation, and assuming mirror symmetry between the two rows, the elastic energy reduces to

$$E = 2 \sum_{i=1}^{N-1} \left[\frac{C_b}{2a} (\phi_{i+1} - \phi_i)^2 + \frac{C_s}{2a} (\phi_{i+1} + \phi_i)^2 \right] + \sum_{i=1}^N \frac{C_b}{2a} (2\phi_i)^2, \quad (4.31)$$

where the rotation ϕ is defined in Fig. 4.30. The first sum reflects the competition between co-rotation and counter-rotation. The two coupling constants are given by $C_b = k_b$ and $C_s = \frac{k_s}{4}(1 + \sqrt{2}L/\ell)$, where k_b and k_s are the bending and shearing stiffness of the hinges, see [133]. The second sum in Eq. (4.31) arises from the couplings between the two symmetric rows, and hinders the rotation of each individual square.

The mechanics of the metamaterial has an obvious magnetic analogy. The first sum in Eq. (4.31) mirrors the competition between ferromagnetic and anti-ferromagnetic interactions in a collection of XY spins, within a spin wave-approximation. The second

sum mirrors the role of a homogeneous magnetic field. All of our experimental results correspond to situations where $C_b \ll C_s$, we therefore limit our analysis to this case, and dub our mechanical systems anti-ferromagnetic metamaterials.

In addition to the elastic energy, the mechanical work W of an axial load F contributes to the total buckling energy $\mathcal{E} = E + W$ as

$$W = Fa \sum_i (\cos \phi_i - 1), \quad (4.32)$$

When $F < F_c$, with $F_c = 12C_b/a^2$, the total energy \mathcal{E} has a single minimum which corresponds to a homogeneous state with $\phi_i = 0$, Fig. 4.30c. But, when F exceeds F_c , the homogeneous rest state becomes unstable, the squares rotate to form a staggered structure depicted Fig. 4.30d. The metamaterial undergoes an anti-ferromagnetic transition.

To describe the low energy excitations of an open chain, we naturally introduce the local anti-ferromagnetic order parameter $\varphi_i = \epsilon(-1)^i \phi_i$, where $\epsilon = \pm 1$ is an arbitrary sign convention for the rotation direction. Close to the onset of the anti-ferromagnetic transition, we can expand the cosine function up to quartic order in Eq. (4.32), and write \mathcal{E} in the canonical form:

$$\mathcal{E} = \sum_i \left[\frac{K}{2a} (\varphi_{i+1} - \varphi_i)^2 + aV(\varphi_i) + \frac{2C_b}{a} (\varphi_{i+1}^2 - \varphi_i^2) \right], \quad (4.33)$$

with $K = 2(C_s - C_b)$ is the anti-ferromagnetic stiffness, and $V(\varphi) = K/\xi^2 (\varphi^2 - \varphi_0^2)^2$, with $\xi^2 = 24K/F$ and $\varphi_0^2 = 6(1 - F_c/F)$. In the last expression we have highlighted the anti-ferromagnetic interactions while accommodating the ferromagnetic part in the last two terms. In the long wave-length limit, only the first two components remain and we can therefore describe the anti-ferromagnetic transition in terms of a canonical φ^4 model:

$$\mathcal{E} = \int ds \frac{K}{2} (\partial_s \varphi)^2 + V(\varphi), \quad (4.34)$$

where s is the curvilinear coordinate along the chain and $\varphi(s)$ is a smooth staggered rotation field.

Non-orientable mechanics of closed meta-chains

When defining the phonon elasticity of a periodic lattice, taking the continuum limit does not require caring about the parity of the number of atoms. In stark contrast, the long wavelength excitations of closed mechanical anti-ferromagnets crucially depends on the parity of N . As illustrated in Fig. 4.31a, a metaring with an odd number of lozenges frustrates global anti-ferromagnetic order.

We now show that the geometrical frustration of mechanical deformations translates in the non-orientability of their associate bundle. As illustrated in Fig. 4.31b, we cover the closed chain by two overlapping open sets U^A and U^B corresponding to two arbitrary orientation conventions $\epsilon^A = \pm 1$ and $\epsilon^B = \pm 1$ defining two staggered-rotations fields: $\varphi_i^{A/B} = \epsilon^{A/B} (-1)^i \phi_i$. The local deformation ϕ_i is defined unambiguously with respect to the vector normal to the planar metamaterial. Therefore, the orientation and staggered rotation variables obey the same \mathbb{Z}_2 transformation rule as in Eq. (4.29):

$$\begin{cases} \epsilon^{A/B} & \rightarrow & -\epsilon^{A/B}, \\ \varphi^{A/B} & \rightarrow & -\varphi^{A/B}. \end{cases} \quad (4.35)$$

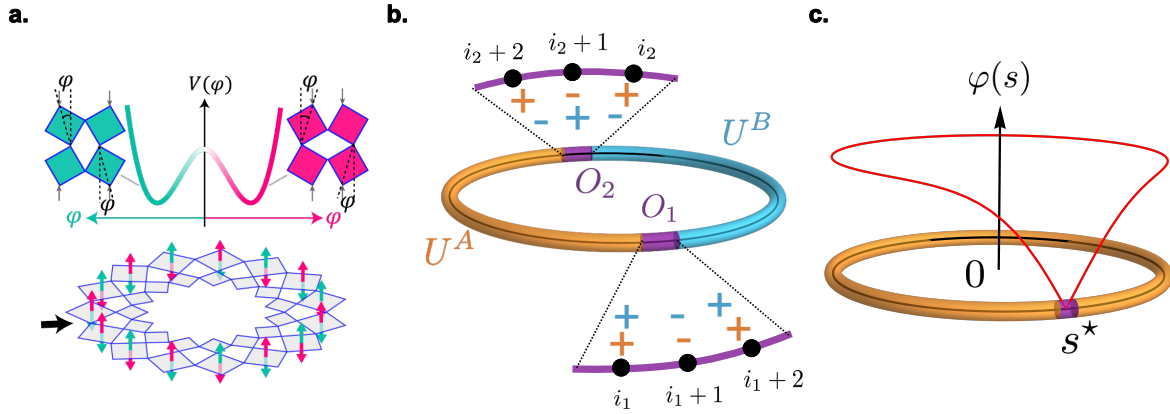


Figure 4.31: **frustration induced non-orientability of odd metarings.** **a.** In a closed metaring, anti-ferromagnetic order is frustrated when the number N of lozenges is odd. **b.** We can cover the ring of lozenges by two overlapping sets where we define two orientations ϵ_A and ϵ_B of the staggered angles $\varphi_i^{A/B}$. The global frustration of the anti-ferromagnetic order implies that the transition functions η cannot be all equal to 1 in the two overlap sets O_1 and O_2 . **c.** Continuum limit. The largest open set over which the elastic-deformation bundle can be trivialized is $S_1/\{s^*\}$. At the position s^* the non-triviality of the deformation bundle imposes $\varphi(s^*) = 0$.

We can always choose $\epsilon_A = \epsilon_B$ in the first overlapping region O_1 via e.g. a redefinition of the sign of φ^B . However, in O_2 the transition function which relates the two staggered rotations is determined by the parity of N . A direct count of the number of sites separating the two overlap regions yields: $\epsilon_A \varphi_i^A = (-1)^N \epsilon_B \varphi_i^B$, for $i \in O_2$. When N is even there is no obstruction to trivialize the deformation bundle into $S_1 \times \mathbb{R}$, and the long wavelength elastic energy is given by Eq. (4.34). By contrast, taking the continuum limit $N \rightarrow \infty$ and keeping N odd, defines a non-orientable deformation bundle. Following the exact same reasoning as in Section 4.10.1, we find that the staggered-rotation bundle $E \xrightarrow{\pi} S_1$ is topologically identical to the bending-deformation bundle of a continuous Möbius strip: the staggered-rotation bundle has an emergent non-orientable topology although the metamaterial itself is obviously orientable. Non-orientable real line bundles are non-trivial, as a consequence we cannot define a smooth non-vanishing field $\varphi(s)$ over the entire chain when N is odd, Fig. 4.31.

Following the same reasoning as in Section 4.10.1, in the Main Text we consider the largest possible trivialization of $E \xrightarrow{\pi} S_1$, see Fig. 4.31c. We define φ over the interval $U = S_1 \setminus \{s^*\}$, where s^* is the point where the deformation must vanish, Fig. 4.31c:

$$\varphi(s^*) = 0. \quad (4.36)$$

We stress that the location of the zero-deformation node is not prescribed *a priori*, and this additional (gauge) degree of freedom needs to be dealt with when minimizing the elastic energy, Eq. (4.34), of odd metamaterials.

Zero-deformation node on frustrated rings: a pedestrian demonstration

In this section we provide an alternative demonstration of Eqs. (4.34) and (4.36). This more pedestrian approach starts with the lattice model defined by Eq. (4.33). As in the continuum approach, we define two sets of lattice points U^A and U^B to cover the ring, Fig. 4.31b. We can write the anti-ferromagnetic part of the mechanical energy by keeping track of the regions over which the staggered deformations are defined:

$$E_{\text{AF}} = \sum_{i \in S_A \setminus \{i_1\}} \frac{K}{2a} (\varphi_i^A - \varphi_{i+1}^A)^2 + aV(\varphi_i^A) + \sum_{i \in S_B \setminus \{i_2\}} \frac{K}{2a} (\varphi_i^B - \varphi_{i+1}^B)^2 + aV(\varphi_i^B). \quad (4.37)$$

We can always find a couple of orientations $\{\epsilon^A, \epsilon^B\}$ so that $\varphi^A(i_1) = \varphi^B(i_1)$, in the overlap O_1 . However, this choice implies that $\varphi^A(i_2) = (-1)^N \varphi^B(i_2)$ in O_2 . Given this observation, we can drop the A/B indices and express Eq. (4.38) in term of a single deformation variable φ_i as

$$E_{\text{AF}} = \sum_{S_A \cup S_B \setminus \{i_2\}} \frac{K}{2a} (\varphi_i - \varphi_{i+1})^2 + aV(\varphi_i) + \frac{K}{2a} (\varphi_{i_2} + \varphi_{i_2+1})^2. \quad (4.38)$$

We then define $w_1 = \frac{1}{2}[1 - (-1)^N]$ and recast the above expression into

$$E_{\text{AF}} = \sum_i \frac{K}{2a} (\varphi_i^A - \varphi_{i+1}^A)^2 + aV(\varphi_i) + 4w_1 \frac{K}{a} \varphi_{i_G}^A \varphi_{i_G+1}^A, \quad (4.39)$$

where $a = 1/N$ for a ring of unit length. We can now take the continuum limit ($N \rightarrow \infty$) keeping the parity of N constant, see Fig. 4.31b. The long wave-length description of anti-ferromagnetic chains then takes the compact form:

$$\mathcal{E} = \int \left[\frac{K}{2} (\partial_s \varphi)^2 + V(\varphi) \right] ds + 4Kw_1 \lim_{N \rightarrow \infty} N \varphi^2(s^*), \quad (4.40)$$

where $s^* = i_2/N$. The second term of Eq. (4.40) originates from the topology of the deformation bundle. When N is even, the deformations are orientable, $w_1 = 0$ and Eq. (4.40) reduces to the linear low-energy description of 1D elastic materials (Eq. (4.34)). Conversely, when N is odd, mechanics is non-orientable, $w_1 = 1$ and the last term of Eq. (4.40) constrains any continuous deformation field $\varphi(s)$ to vanish at $s = s^*$. From a more formal perspective w_1 corresponds to the first Stieffel-Whitney class of the elastic deformation bundle. It defines an obstruction to its trivialization [132].

We showed in the previous section that the staggered deformations of frustrated odd chains are topologically identical to the bending modes of a soft Möbius strip. This result is further confirmed by the structure of Eq. (4.40) which includes the same topological term as in the minimal model of a Möbius strip introduced in [?].

Buckling patterns of 1D metarings: comparison to experiments

We find the response of odd metarings under the action of a homogeneous axial load by minimizing Eq. (4.34) with the constraint $\varphi(s^*) = 0$. This tedious minimization is discussed in [?]. The solution corresponds to two symmetric half ϕ^4 kinks continuously

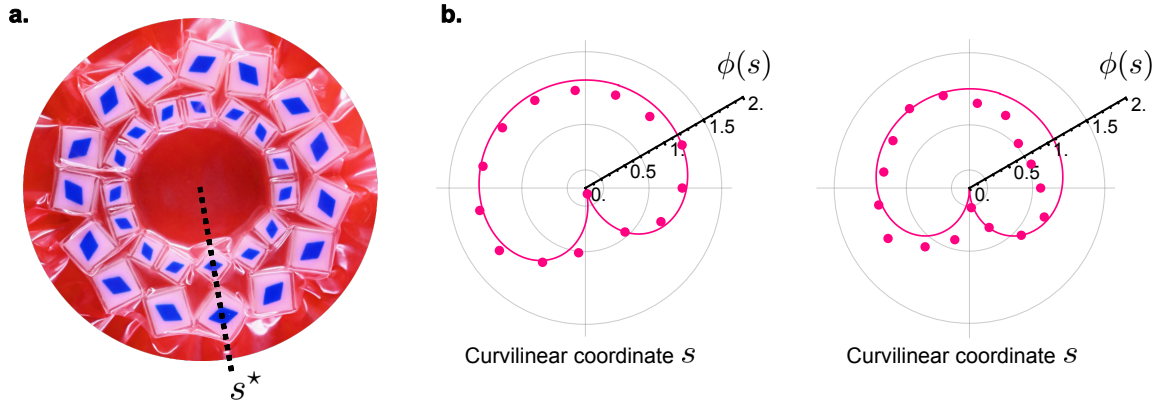


Figure 4.32: **Homogeneous compression of odd metachains.** **a.** Picture of a metaring pressurized in a vacuum bag ($N = 15$) described in the Methods. **b.** Plots of the measured staggered rotation angle for two different rings of lengths $N = 15$ and $N = 17$ (symbols) and best fit from our continuum theory, Eq. (4.41). We measure a maximum deformation angle $\varphi_{\max} = 1.19$ rad and find $\xi_{15} = 3.76 \pm 0.60 a_{15}$ and $\xi_{17} = 2.21 \pm 0.13 a_{17}$ where the lattice spacings are $a_{15} \approx 12.6$ mm and $a_{17} \approx 11.1$ mm.

connected on the unit circle, see Fig. 4.32. The analytical expression of the deformation profile takes a simple form only when expressed in an implicit form:

$$\varphi(s)/\varphi_{\max} = \pm \left| \sin \left(J \left[\frac{\sqrt{2}\varphi_{\max}}{\xi} (s - s^*), 1 \right] \right) \right|, \quad (4.41)$$

where $J[u, k]$ is the inverse of the elliptic integral function of the first kind, also known as the Jacobi Amplitude, and φ_{\max} is the maximum deformation angle. This expression depends on the metamaterial parameters only through the characteristic length ξ . We stress that this solution is singular at the location s^* and spontaneously breaks the translational invariance of Eq. (4.34). As a result, the location of s^* is not prescribed and its translation along the base circle corresponds to zero-energy deformations. Fig. 4.32 reveals that our minimal theory expressed in term of a single scalar order parameter correctly accounts for our experimental findings. Eq. (4.41) can therefore be effectively used to measure the elastic constant K of pressurized metarings.

4.10.3 Non-orientable mechanics of toroidal metamaterials

We now consider a metatorus made of a square lattice of 2D lozenges with anti-ferromagnetic couplings along both directions, Fig. 4.33a. We note N_p and N_t the number of lozenges in the poloidal and toroidal directions. In this section, we first show that all metatori including an odd number of units in at least one direction feature a non-orientable mechanics. We then demonstrate that non-orientability results in the topological protection of a zero-deformation loop under isotropic load. We finally show that the morphology of the zero-deformations loops are curves of minimal length that wind around the torus.

Non-orientable deformation bundles and zero-deformation loops

As in the Main Text, we consider the limit of very large tori and neglect all geometrical corrections arising from finite curvature. In the long wave-length limit the elastic energy of a finite portion U of the metatorus then generalizes Eq. (4.34) as:

$$\mathcal{E} = \int_U \frac{K}{2} [\nabla \varphi(x, y)]^2 + V(\varphi) dx dy, \quad (4.42)$$

where x and y are the toroidal and poloidal coordinates, and V is the bistable quartic potential defined in Eq. (4.34). Following the same analysis as for one-dimensional rings, we know that if number of lozenges is odd along one, or two, directions then homogeneous anti-ferromagnetic order is frustrated. We show below that this geometrical frustration translates again in the non-orientability of the staggered-deformation bundle.

For the sake of clarity, in Fig. 4.33 we represent the torus T^2 as a unit square with opposite edges identified, Fig. 4.33b. We consider two open sets U^A and U^B that overlap and cover T^2 . U^A and U^B are associated to two orientations ϵ^A and ϵ^B , which define two staggered rotation fields $\varphi^A(\mathbf{r})$ and $\varphi^B(\mathbf{r})$. Any loop on the torus effectively realizes a 1D metaring. Hence when N_t is odd, U^A and U^B should not include any loop winding in the toroidal direction. Repeating the same reasoning we identify the three types of possible coverings sketched in Fig. 4.33b depending on the parity of N_p and N_t . Let us now assume that there exists a smooth staggered-rotation field in the limit $N_p, N_t \gg 1$ (keeping the parity of the number of lozenges unchanged). In the two overlaps O_1 and O_2 , the local rotation angle $\phi(x, y)$ is unambiguously defined with respect to the normal of the torus. It is related to $\varphi^{A/B}$ as $\phi(x, y) = \epsilon^A \varphi^A(x, y) = \epsilon^B \varphi^B(x, y)$ in the two overlap regions. We can always choose $\epsilon^A = \epsilon^B$ in O_1 via a mere redefinition of the sign of φ^B . A direct count of the number of sites separating O_1 and O_2 along the odd directions then implies that $\epsilon^A \varphi^A(x, y) = -\epsilon^B \varphi^B(x, y)$ in O_2 . In other words, there is an obstruction to define smooth staggered deformations of constant sign over the whole torus. The $\varphi(x, y)$ fields define a non-orientable real line bundle $E \xrightarrow{\pi} T^2$ [132, 179].

Generalizing the analysis done for one-dimensional rings in Sec 4.10.2, we deduce that the largest open sets over which we can trivialize the deformations is $T^2 \setminus \mathcal{L}$, where \mathcal{L} is a closed loop winding once around the torus, see Fig. 4.33d. As $E \xrightarrow{\pi} T^2$ is non-orientable, φ must vanish along \mathcal{L} . We conclude that the mechanics of frustrated toroidal metamaterials is defined by the combination of their elastic energy Eq. (4.42), and of the topological constraint:

$$\varphi(\mathbf{R}^*(\sigma)) = 0, \quad (4.43)$$

where $\mathbf{R}^*(\sigma)$ is a parametrization of \mathcal{L} with respect to its curvilinear coordinate σ . The deformation modes of the \mathcal{L} loop add a number of degrees of freedom to the staggered rotation variables. They must be dealt with when computing the equilibrium deformation patterns, which minimize the elastic energy Eqs. (4.42) and (4.43). Remarkably, without explicitly solving this constrained minimization problem, we already know that in the case where both N_p and N_t are odd, \mathcal{L} must wind around both principal directions. As a result, mechanical equilibrium spontaneously breaks two mirror symmetries: the emergent buckling patterns of odd-odd tori compressed by isotropic loads are chiral, Fig. 4.33c.

An alternative demonstration of the topological protection of the \mathcal{L} loops can be done following the reasoning of Sec. 4.10.2. Consider for instance the case where N_t is odd and

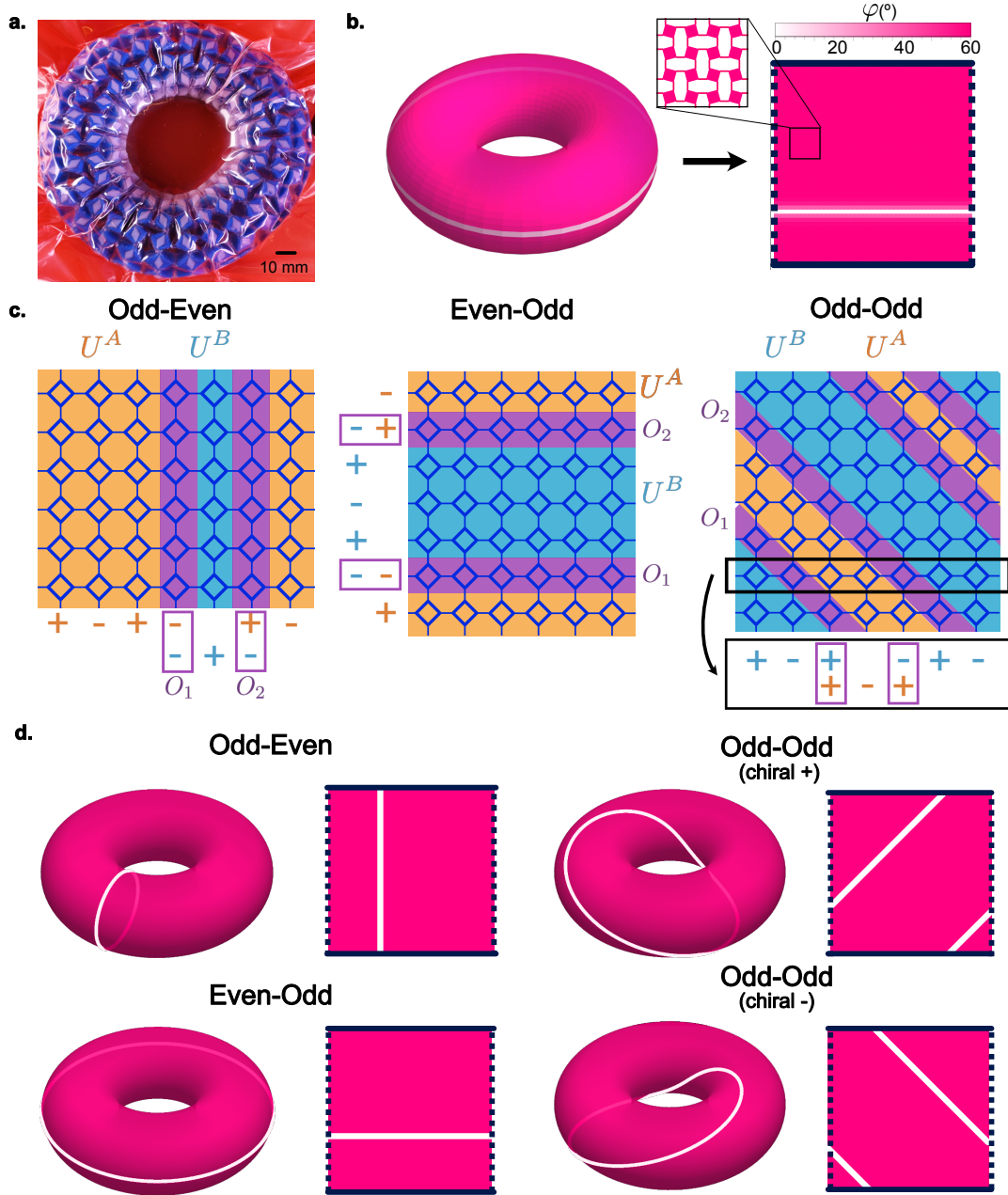


Figure 4.33: **Non-orientable mechanics of frustrated metatopori.** In all the figures N_p and, or, N_t are odd. **a.** Photograph of a toroidal metamaterial isotropically compressed in a vacuum bag ($N_p = 11$, $N_t = 27$). **b.** Planar representation of the torus. The heat map indicates the staggered deformation field on its planar representation, a square where the two pairs of opposite edges are identified. The deformations correspond to the minimization of the elastic energy Eq. (4.42) with the constraint Eq. (4.43) when N_p is odd and N_t is even. **c.** Two overlapping open sets U^A and U^B cover T^2 . The definition of smooth staggered deformations on both U^A and U^B constrains the topology of the two sets. $U^{A/B}$ cannot include any closed loop winding along one direction where the number of lozenges is odd. We can always choose the orientation and the staggered-rotation fields $\varphi^{A/B}$ to coincide on the overlap region O_1 . However, the parity of N_p and/or N_t forbids the equality $\varphi^A(x, y) = \varphi^B(x, y)$ when $(x, y) \in O_2$. No smooth anti-ferromagnetic order parameter having a constant sign can be defined on T^2 . The staggered deformations define a non-orientable line bundle. **d.** Topology and geometry of the zero-deformation line \mathcal{L} . When both N_p and N_t are odd \mathcal{L} winds along both directions and must spontaneously break two mirror symmetries. The shape of the \mathcal{L} loops in the three plots corresponds to the minimum of the elastic energy. The loops are curved of minimal length which satisfies

N_t even. Starting from an anti-ferromagnetic lattice model defined on two overlapping sets of sites, we can take the continuous limit and find

$$\mathcal{E}_{\text{odd--even}} = \int_{T^2} \left[\frac{K}{2} (\nabla\varphi)^2 + V(\varphi) \right] dx dy + \lim_{N_t, N_p \rightarrow +\infty} 4K N_t N_p \int_{S_1} \varphi^2(x^*(y), y) dy. \quad (4.44)$$

A loop \mathcal{L} lassoing the torus along the poloidal direction (y) is topologically protected against deformations irrespective of the magnitude of the load. $\mathcal{L} = \{\mathbf{R}^*(y)\}$ is here parametrized in the Monge gauge: $\mathbf{R}^* = (x^*(y), y)$

We close this section by noting that the same analysis can be formally extended to higher dimensional tori S_1^n where anti-ferromagnetic frustration results in the topological protection of vanishing deformations on $n - 1$ dimensional manifolds.

Geometry of the zero-deformation loops

As described in the Main Text, when frustrated, toroidal metamaterials are lassoed by zero-deformation loops \mathcal{L} . Their winding is determined by the underlying non-orientability of the deformation bundle. The bundle topology, however, does not prescribe the loop geometry, which depends on the specifics of the load distribution and of the elastic energy. In this section, we show that under the action of isotropic loads F , the set of zero-deformation points form loops of minimal length and compute their associated line tension.

Deep in the frustrated state, when $F \gg F_c$, the rotation of the squares are localized over a characteristic length $\xi = \sqrt{24Ka/F}$ around \mathcal{L} . This screening of the elastic deformations allows us to simplify the elastic energy. We first write $(\nabla\varphi)^2 = (\partial_{\parallel}\varphi)^2 + (\partial_{\perp}\varphi)^2$, where ∂_{\parallel} and ∂_{\perp} are the derivatives in the directions longitudinal and normal to \mathcal{L} . The large-scale variations of φ then reduce to $(\nabla\varphi)^2 \approx \varphi_0^2/\xi^2$, where we recall that φ_0 is the amplitude of the energy barrier separating the two minima of the quartic potential, Fig. 4.30. The total energy \mathcal{E} then takes the compact form:

$$\mathcal{E} \sim 2\xi \int d\sigma \left(\frac{K}{2} \frac{\varphi_0^2}{\xi^2} + \frac{K}{\xi^2} \varphi_0^4 \right) \equiv \gamma \int d\sigma, \quad (4.45)$$

with σ the curvilinear coordinate along \mathcal{L} , and $\gamma = K\varphi_0^2(1 + 2\varphi_0^2)/(2\xi)$ the effective line tension. In Eq. (4.45), we have effectively integrated out all the deformations degrees of freedom φ . We are thus left with the residual degrees of freedom associated to the shape of the \mathcal{L} loop. We find that under a homogeneous load they are lines of minimal length topologically constrained to wind around the torus. Their three possible shapes are shown in fig. 4.33d. In the odd-even and even-odd cases \mathcal{L} are circles (geodesics), whereas in the odd-odd case, \mathcal{L} is chiral and forms a helix of minimal length, which lassos the torus both in the toroidal and poloidal directions. These predictions are in excellent agreement with our experimental findings reported in Fig. 2 (Main Text).

4.10.4 Response to heterogeneous loads

In this last section we detail the mechanical response of frustrated metamaterials under the action of heterogeneous loads. We first focus on one-dimensional rings including an odd number of units and show how memory naturally emerges from non-orientable mechanics. We then compute the effective elasticity of the zero deformation loops arising from pointwise loads applied to metatori.

Mechanical memory of one-dimensional metaring

In the Main Text, we demonstrate the realisation of a Set-Reset Latch memory by applying localised axial loads to odd metarings. Here we show that the possibility to read, write and erase mechanical bits stems from a multistable effective potential ruling the position s^* of the zero-energy node.

We start from the continuum description of the odd metaring, and write the total energy

$$\mathcal{E} = \int ds \frac{K}{2} (\partial_s \varphi)^2 + \frac{6C_b}{a^2} \varphi^2. \quad (4.46)$$

We then readily find that the deformations of minimal energy satisfies

$$\lambda^2 \partial_s^2 \varphi - \varphi = 0, \quad (4.47)$$

with $\lambda^2 = a^2 K / (12C_b)$ and $\varphi(s^*) = 0$. To investigate the response to an imposed deformation at $s = 0$. We add the extra constraint $\varphi(0) = \varphi(1) = \bar{\varphi}$ on the periodic field. The deformation profile then takes the simple form:

$$\varphi(s; s^*) = \begin{cases} Ae^{s/\lambda} + Be^{-s/\lambda} & s \in [0, s^*] \\ Ce^{s/\lambda} + De^{-s/\lambda} & s \in [s^*, 1] \end{cases}, \quad (4.48)$$

with

$$\begin{pmatrix} A \\ B \end{pmatrix} = \frac{\bar{\varphi}}{2 \sinh(s^*/\lambda)} \begin{pmatrix} -e^{-s^*/\lambda} \\ e^{s^*/\lambda} \end{pmatrix}, \\ \begin{pmatrix} C \\ D \end{pmatrix} = \frac{\bar{\varphi}}{2 \sinh((s^* - 1)/\lambda)} \begin{pmatrix} -e^{-s^*/\lambda} \\ e^{s^*/\lambda} \end{pmatrix}. \quad (4.49)$$

We stress that the position s^* is yet to be determined. Inserting the deformation field $\varphi(s; s^*)$ back in the elastic energy \mathcal{E} leads to the effective potential:

$$\mathcal{U}(s^*) = \mathcal{E}[\varphi(s; s^*)] = \frac{K \bar{\varphi}^2}{2\lambda} \frac{\sinh(1/\lambda)}{\sinh((1 - s^*)/\lambda) \sinh(s^*/\lambda)}. \quad (4.50)$$

The location of the zero-energy node corresponds to the minimum of \mathcal{U} . When the ring is deformed by a single point load at $s = 0$, s^* is diametrically opposed to the source of deformation, $s^* = 1/2$, see Figs. 4.34a, 4.34b.

The above result is readily generalised to a set of local deformations $\{\bar{\varphi}_n\}$ imposed at $\{s_n\}$. To ease the notation we also include the topological restriction $\varphi(s^*) = 0$ as one of the imposed deformations. For each interval $[s_n, s_{n+1}]$, we have a solution $\varphi_n(s) = A_n e^{s/\lambda} + B_n e^{-s/\lambda}$, with

$$\begin{pmatrix} A_n \\ B_n \end{pmatrix} = M_n^{-1} \begin{pmatrix} \bar{\varphi}_n \\ \bar{\varphi}_{n+1} \end{pmatrix}, \quad M_n = \begin{pmatrix} e^{s_n/\lambda} & e^{-s_n/\lambda} \\ e^{s_{n+1}/\lambda} & e^{-s_{n+1}/\lambda} \end{pmatrix}. \quad (4.51)$$

As before, the determination of s^* follows directly from the minimisation of the effective potential $\mathcal{U}(s^*) = \mathcal{E}[\{\varphi_n\}]$. If, for instance, $s_n = s^*$ is located between s_{n-1} and s_{n+1} , its exact position between both local deformations is given by

$$s^* = \frac{1}{2}(s_{n-1} + s_{n+1}) + \frac{1}{2}\lambda \ln \left| \frac{e^{s_{n+1}/\lambda} \bar{\varphi}_{n-1} + e^{s_{n-1}/\lambda} \bar{\varphi}_{n+1}}{e^{s_{n-1}/\lambda} \bar{\varphi}_{n-1} + e^{s_{n+1}/\lambda} \bar{\varphi}_{n+1}} \right|. \quad (4.52)$$

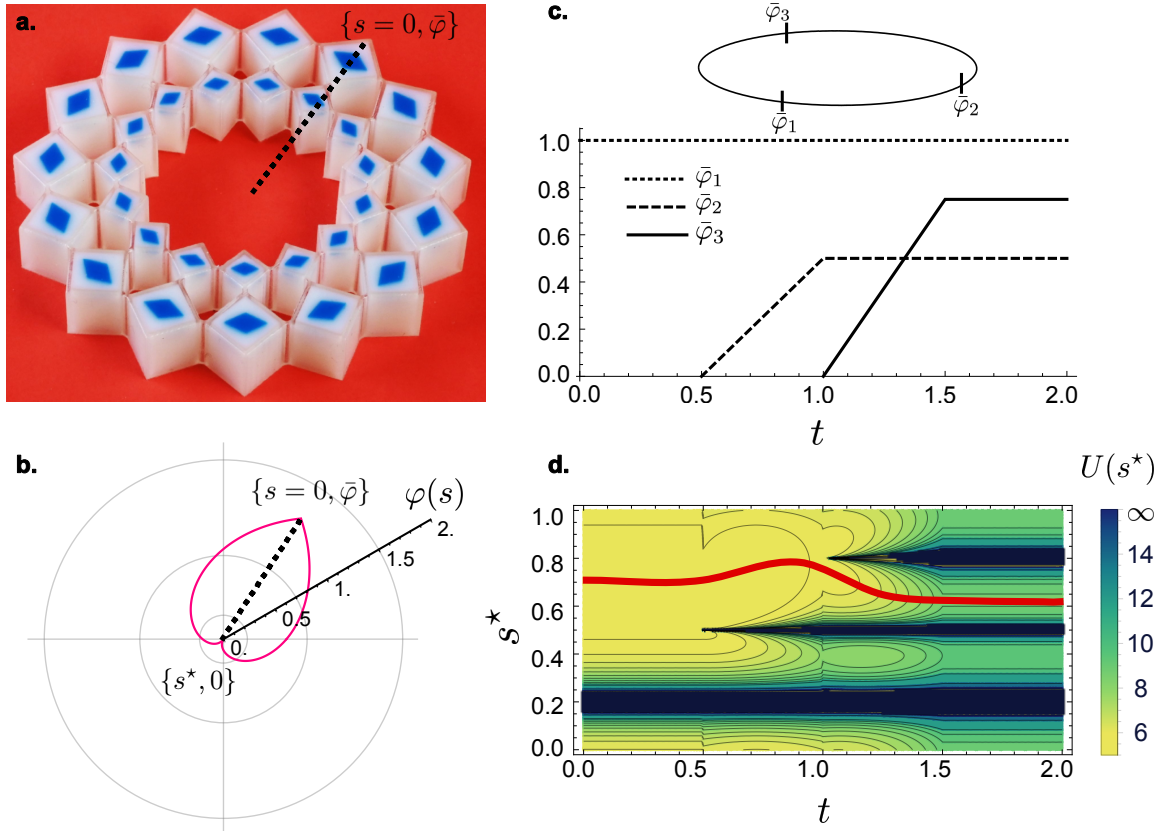


Figure 4.34: **Mechanical memory of one-dimensional metarings.** **a.** Response of a metaring (described in the Methods) to locally imposed deformations. Same experiments as in the Main Text. **b.** Polar plot of the deformations induced by a point load located at s_A . The deformation vanishes at s^* , the point opposite to s_1 . **c.** Three local rotations are imposed sequentially ($\bar{\varphi}_1, \bar{\varphi}_2, \bar{\varphi}_3$) at positions $s_1 = 0.2, s_2 = 0.5, s_3 = 0.8$, respectively, in a metaring consisting of an odd number of units. **d.** The potential energy $U(s^*)$ (heat map) evolves in time and becomes tri-stable when the three deformations are imposed. The red curve indicates how the position of the zero-deformation node evolves in time as the deformations are sequentially applied.

For each interval $[s_n, s_{n+1}]$, the corresponding elastic energy is

$$E_n = \int ds \frac{K}{\lambda^2} (A_n^2 e^{2s/\lambda} + B_n^2 e^{-2s/\lambda}). \quad (4.53)$$

When more than one compressive load F_n is applied, the mechanical work is $W = \sum F_n 2a(\cos\bar{\varphi}_n - 1) = \sum \bar{F}_n(\cos\bar{\varphi}_n - 1)$ and the total energy is $\mathcal{E} = \sum E_n + W$. Using the principle of minimum energy, $\partial\mathcal{E}/\partial\bar{\varphi}_n = 0$, we can get multiple equilibria. This property lies at the core of the memory effect in odd metarings. As illustrated in Fig. 4.34c and d, the sequential application of local deformations leads to the programmed selection of a single minimum corresponding to one deformation pattern. This property echoes the mechanical response of non-orientable surfaces to shear stresses predicted in [?]. Unlike in non-orientable surfaces, mechanical memory can be easily read given the planar geometry of the rings, and simply extended to higher dimensional meta-structures.

Shape memory of the \mathcal{L} loops.

We now determine the shape of the \mathcal{L} loop for frustrated metatopi deformed by a collection of point stresses. The intrinsic non-orientability of the staggered-rotation bundle $E \xrightarrow{\pi} T^2$ imposes the existence of zero deformation loops \mathcal{L} . When the applied load is homogeneous, elasticity minimises the length of \mathcal{L} , see Sec. 4.10.3. Under the action of localised sources of stress and deformations, the morphology of \mathcal{L} is more difficult to anticipate. In this last section, we derive the effective elasticity of \mathcal{L} loops caused by heterogeneous distributions of localised loads and shed light on their intrinsic multistability.

We consider a generic load distribution defined by the scalar field $F(\mathbf{r}) = \sum_\alpha F_\alpha \delta(\mathbf{r} - \mathbf{r}_\alpha)$. At mechanical equilibrium φ minimises the total energy functional which takes the generic form

$$\mathcal{E} = \int d^2r \left(\frac{K}{2} (\nabla\varphi)^2 + \frac{m^2}{2} \varphi^2 \right) - \int d\mathbf{r} F(\mathbf{r}) \varphi. \quad (4.54)$$

Non-orientability adds the topological constraint $\varphi(\mathbf{R}^*(\sigma)) = 0$. We stress that the minimisation of Eq. (4.54) involves two coupled fields: (i) the staggered deformations, $\varphi(\mathbf{R}^*)$, and the loop's shape $\mathbf{R}^*(\sigma)$.

To define the effective elasticity of \mathcal{L} , we solve a seemingly more complex problem. We consider the case where the structure could also be subject to thermal fluctuations [181], and introduce the partition function:

$$\mathcal{Z} = \int \mathcal{D}\varphi \int \mathcal{D}\mathbf{R}^* \left(\prod_\sigma \delta(\varphi(\mathbf{R}^*(\sigma))) \right) e^{-\beta\mathcal{E}[\varphi, \mathbf{R}^*]}. \quad (4.55)$$

This formulation allows us to compute the effective energy of the \mathcal{L} loop by integrating out the Gaussian fluctuations of $\varphi(\mathbf{R}^*)$. To proceed, we first express the topological constraint using a Lagrange multiplier $\lambda(\sigma)$. Noting, $G[\mathbf{r}, \mathbf{r}']$ the Green function defined

by $\beta(m^2 - \kappa\nabla^2)G[\mathbf{r}, \mathbf{r}'] = \delta(\mathbf{r} - \mathbf{r}')$, we have

$$\begin{aligned} \mathcal{Z} &= \int \mathcal{D}\mathbf{R}^* \int \mathcal{D}\lambda \int \mathcal{D}\varphi \exp \left[-\frac{1}{2} \int d\mathbf{r} d\mathbf{r}' \varphi(\mathbf{r}) G^{-1}(\mathbf{r}, \mathbf{r}') \varphi(\mathbf{r}') + \int d\mathbf{r} F(\mathbf{r}) \varphi(\mathbf{r}) \right. \\ &\quad \left. + i \int d\sigma \lambda(\sigma) \varphi(\mathbf{R}^*(\sigma)) \right] \end{aligned} \quad (4.56)$$

$$\begin{aligned} &= C_0 \int \mathcal{D}\mathbf{R}^* \int \mathcal{D}\lambda \exp \left[-\frac{1}{2} \int d\sigma d\sigma' \lambda(\sigma) G[\mathbf{R}^*(\sigma), \mathbf{R}^*(\sigma')] \lambda(\sigma') \right. \\ &\quad \left. - i\beta \int d\sigma \int d^2\mathbf{r} \lambda(\sigma) G[\mathbf{R}^*(\sigma), \mathbf{r}] F(\mathbf{r}) \right] \end{aligned} \quad (4.57)$$

$$= C_1 \int \mathcal{D}\mathbf{R}^* \exp(-\mathcal{U}[\mathbf{R}^*]), \quad (4.58)$$

where C_0, C_1 are constants independent on $\mathbf{R}^*(s)$ and the line effective energy in the presence of external forces reads

$$\mathcal{U}[\mathbf{R}^*] = \frac{\beta^2}{2} \int d\sigma d\sigma' \int d^2\mathbf{r} d^2\mathbf{r}' F(\mathbf{r}) G[\mathbf{r}, \mathbf{R}^*(\sigma)] \tilde{G}^{-1}[\mathbf{R}^*(\sigma), \mathbf{R}^*(\sigma')] G[\mathbf{R}^*(\sigma'), \mathbf{r}'] F(\mathbf{r}'), \quad (4.59)$$

where \tilde{G}^{-1} is defined by $\int d\sigma' G[\mathbf{R}^*(\sigma), \mathbf{R}^*(\sigma')] \tilde{G}^{-1}[\mathbf{R}^*(\sigma'), \mathbf{R}^*(\sigma'')] = \delta(\sigma - \sigma'')$. The case of a single force of amplitude F_0 applied at \mathbf{r}_0 corresponds to the simpler potential

$$\mathcal{U}_0[\mathbf{R}^*] = \frac{\beta^2 F_0^2}{2} \int d\sigma d\sigma' G[\mathbf{r}_0, \mathbf{R}^*(\sigma)] \tilde{G}^{-1}[\mathbf{R}^*(\sigma), \mathbf{R}^*(\sigma')] G[\mathbf{R}^*(\sigma'), \mathbf{r}_0]. \quad (4.60)$$

Equation (4.60) although exact, is not handy since it requires the inverse of the non-local operator \tilde{G} . To gain more insight on the long wave-length limit, we approximate the Green's function on the torus G by its expression on the \mathbb{R}^2 plane: $G(\mathbf{r}, \mathbf{r}') = g(|\mathbf{r} - \mathbf{r}'|) = \frac{1}{2\pi\beta} K_0(m|\mathbf{r} - \mathbf{r}'|)$, with K_n the modified Bessel function of the second kind.

In response to a single point load, elastic energy is clearly minimized when placing \mathcal{L} at a maximal distance from the load. This elementary reasoning is confirmed by our experiments and simulations. We hence make the following ansatz for the loop shape $\mathbf{R}_0^*(\sigma) = \hat{\mathbf{t}}\sigma + \mathbf{p}$, where $\hat{\mathbf{t}}$ is a unitary tangent vector, and \mathbf{p} a point of reference. Subject to additional local forces, \mathcal{L} undergoes transverse deformations. We parametrize its shape as $\mathbf{R}^*(\sigma) = \mathbf{R}_0^*(\sigma) + \epsilon \mathbf{R}_1^*(\sigma)$, with $\mathbf{R}_1^*(\sigma) = f(\sigma) \hat{\mathbf{n}}$, $\hat{\mathbf{n}}$ the normal vector, and ϵ the magnitude of the transverse fluctuation.

To quadratic order in ϵ we have

$$G[\mathbf{r}_0, \mathbf{R}^*(\sigma)] = G_0 + \epsilon f(\sigma) G_1 + \epsilon^2 f^2(\sigma) G_2 + \mathcal{O}(\epsilon^3) \quad (4.61)$$

where

$$\begin{aligned} G_0[\mathbf{r}_0, \mathbf{R}^*(\sigma)] &= g(|\hat{\mathbf{t}}\sigma + \mathbf{p} - \mathbf{r}_0|) \\ G_1[\mathbf{r}_0, \mathbf{R}^*(\sigma)] &= \frac{\hat{\mathbf{n}} \cdot (\mathbf{p} - \mathbf{r}_0)}{|\hat{\mathbf{t}}\sigma + \mathbf{p} - \mathbf{r}_0|} g'(|\hat{\mathbf{t}}\sigma + \mathbf{p} - \mathbf{r}_0|) \\ G_2[\mathbf{r}_0, \mathbf{R}^*(\sigma)] &= \left[\left(\frac{|\hat{\mathbf{t}}\sigma + \mathbf{p} - \mathbf{r}_0|^2 - (\hat{\mathbf{n}} \cdot (\mathbf{p} - \mathbf{r}_0))^2}{4|\hat{\mathbf{t}}\sigma + \mathbf{p} - \mathbf{r}_0|^3} \right) g'(|\hat{\mathbf{t}}\sigma + \mathbf{p} - \mathbf{r}_0|) \right. \\ &\quad \left. + \frac{(\hat{\mathbf{n}} \cdot (\mathbf{p} - \mathbf{r}_0))^2}{4|\hat{\mathbf{t}}\sigma + \mathbf{p} - \mathbf{r}_0|^2} g''(|\hat{\mathbf{t}}\sigma + \mathbf{p} - \mathbf{r}_0|) \right]. \end{aligned} \quad (4.62)$$

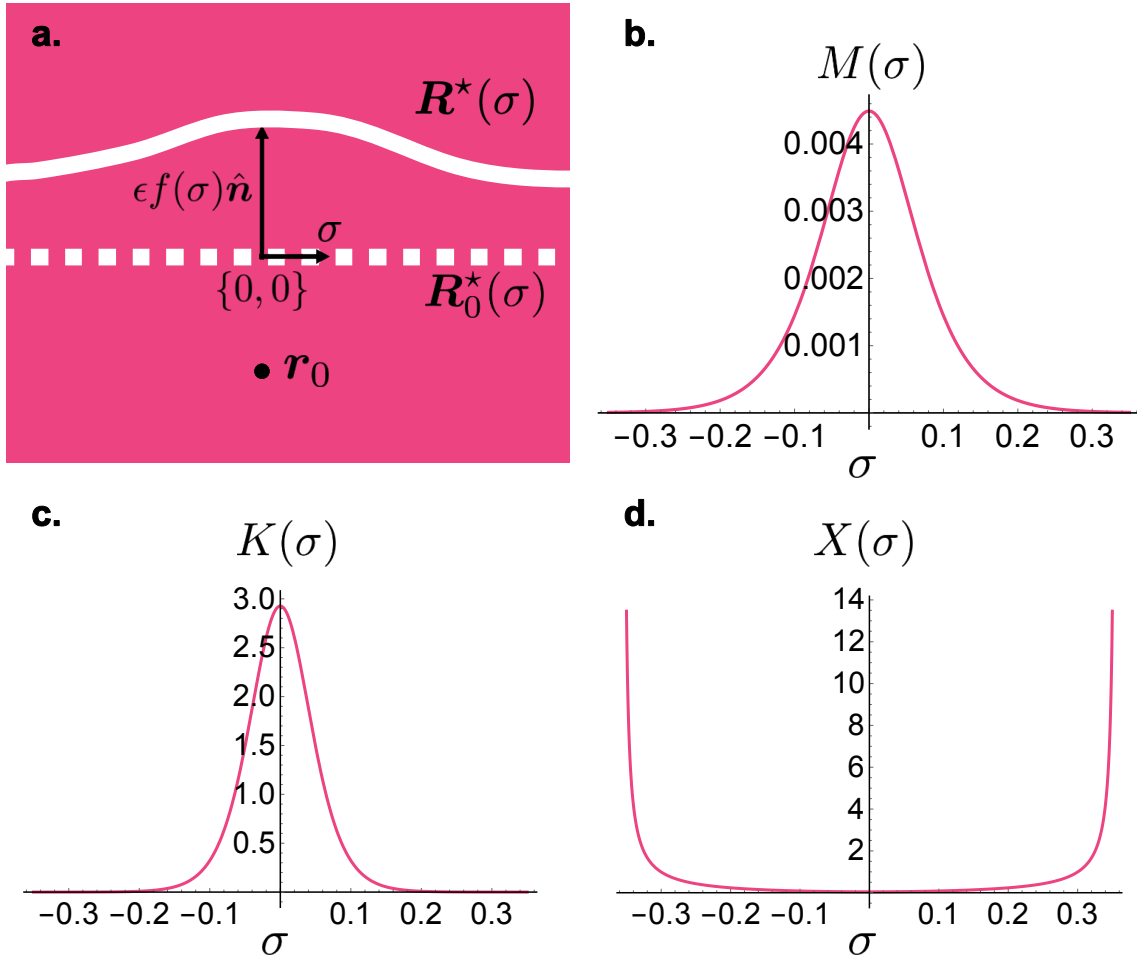


Figure 4.35: **Line repulsion from one point stress.** **a.** Sketch of the unperturbed zero line $\mathbf{R}_0^*(\sigma) = \hat{\mathbf{t}}\sigma + \mathbf{p}$ (dashed white line) and the deformed line $\mathbf{R}^*(\sigma) = \mathbf{R}_0^*(\sigma) + \epsilon f(\sigma) \hat{\mathbf{n}}$ (solid white line), where $\hat{\mathbf{t}} = \{1, 0\}$, and $\mathbf{p} = \{0, 0\}$. The point stress is applied at $\mathbf{r}_0 = \{0, -0.1\}$. **b, c, d.** Expansion terms from the one-source potential \mathcal{U}_0 for $m = 10$: effective line tension $M(\sigma)$, repulsion term $K(\sigma)$, and shift term $X(\sigma)$, respectively.

Analogously we have

$$\tilde{G}[\sigma, \sigma'] = \tilde{G}_0 + \epsilon \tilde{G}_1 + \epsilon^2 \tilde{G}_2 + \mathcal{O}(\epsilon^3), \quad (4.63)$$

with

$$\begin{aligned} \tilde{G}_0[\sigma, \sigma'] &= g(|\sigma - \sigma'|) \\ \tilde{G}_1[\sigma, \sigma'] &= \hat{\mathbf{t}} \cdot \hat{\mathbf{n}} \frac{(f(\sigma) - f(\sigma'))(\sigma - \sigma')}{|\sigma - \sigma'|} g'(|\sigma - \sigma'|) = 0 \\ \tilde{G}_2[\sigma, \sigma'] &= \frac{(f(\sigma) - f(\sigma'))^2}{2|\sigma - \sigma'|} g'(|\sigma - \sigma'|). \end{aligned} \quad (4.64)$$

Notice that the operator \tilde{G} is non-local. In order to have a local potential \mathcal{U} we employ the last approximation: $ml \gg 1$, where l is the characteristic separation between two neighboring sites. Under this regime, $g(\sigma) \sim \delta(\sigma)$ rendering both \tilde{G} and \tilde{G}^{-1} local functions of σ .

All in all, after eliminating unnecessary constant shifts in energy, the potential of eq. (4.60) reads

$$\mathcal{U}_0[\mathbf{R}^*] = -\epsilon \int d\sigma f(\sigma) K(\sigma) X(\sigma) + \epsilon^2 \int d\sigma \left[\frac{M(\sigma)}{2} \left(\frac{df}{d\sigma} \right)^2 + \frac{K(\sigma)}{2} f^2(\sigma) \right], \quad (4.65)$$

where

$$\begin{aligned} M(\sigma) &= G_0^2, \\ K(\sigma) &= 2(G_1^2 + 2G_0G_2), \\ X(\sigma) &= -\frac{G_1G_0}{G_1^2 + 2G_0G_2}, \end{aligned}$$

and the arguments of the G function are implicitly given by $[\mathbf{r}_0, \mathbf{R}^*(s)]$. These three functions are plotted in Fig. 4.35

We can now qualitatively understand the response of the \mathcal{L} loop to a point-wise stress applied to the metarings. At first order in ϵ , Eq. (4.65) indicates that the repulsion from the source of stress is minimised when the loop is at a maximal distance from the source. \mathcal{L} loops are repelled by point stresses. At second order in ϵ , Eq. (4.65) translates the effective elasticity of the \mathcal{L} loop. The first term of order ϵ^2 acts as an effective line tension. Unlike in the case of homogeneous load, the line tension is here heterogeneous. The second and last term of order ϵ^2 modulates the repulsive force from the source.

Simply put \mathcal{L} loops have a finite line tension and are repelled from point stresses. These two ingredients shed light on the pattern dynamics showed in Fig. 3 in the Main Text, where we see the zero deformation loop moving and bending away from the applied perturbations.

4.10.5 Experimental Methods

Sample designs

Metarings We design metarings, formed of 15, 17, 16 and 18 pairs of squares connected by short hinges connecting their corners, see Fig. 2a and d of the Main Text and Fig. 4.36a.

The high contrast in stiffness between the squares and the hinges and the geometry of the soft hinges ensure that the shearing stiffness is larger than the bending stiffness. This implies that counter-rotations of adjacent squares is more energetically favourable than co-rotation [133]. In other words antiferromagnetic order develops over long distances.

Flexible twisted bands We design four types of twisted bands that have 0, 1, 2 and 3 half twists and that form closed loops, see Fig. 2f and i of the Main Text. Since we are interested in their out-of-plane buckling under homogeneous compression, we design the cross section of the twisted band in the shape of the “I” letter, see Fig. 4.36c. The top and bottom parts of the I are made of a stiff material and are used for applying compressive loads. The middle part of the twisted band is made of a soft material and its dimensions are suitably designed such that it features a single buckling mode.

Connected metarings We rigidly connect a pair of lozenges of two metarings. One metaring has 15 pairs of lozenges, the other has 16 pairs of lozenges. See Fig. 3b of the Main Text and Fig. 4.36e.

Möbius shorts We design a Möbius shorts composed of two rigidly connected bands: a cylinder and a Möbius band, see Fig. 3b of the Main Text and Fig. 4.36f.

Metatori The geometry of the metatori is that of toroidal shells formed of a square lattices of lozenges connected via their corners, see Fig. 3h of the Main Text, Extended Data Fig.2 and Fig. 4.36g. We design three types of metatori. They correspond to lattices including numbers of lozenges in the toroidals and poloidal directions with all possible parities. We again use a stiff material for the lozenges and a soft material for the hinges. This design promotes antiferromagnetic order under compression.

Sample fabrication

We produce all the samples by additive manufacturing using a PolyJet 3D printer (Stratasys Object500 Connex3). The central parts of the twisted bands and of the hinges of metarings and metatori are made of a flexible photopolymer (Stratasys Agilus30, Young’s modulus $E \approx 1$ MPa, see Fig. 4.37 for a calibration of the elastic properties). The other parts, the top and bottom part of the twisted bands and the lozenges forming the metarings and metatori, are made of a stiffer material (Stratasys Vero, Young’s modulus $E \approx 2500$ MPa).

Experimental setup

hydrostatic pressure In Fig. 2 and Fig. 3 of the Main Text, we test our structures under hydrostatic compression. To this end, the samples are placed into a seal plastic bag connected to a vacuum pump (KNF Neuberger N022.AN.18) and a vacuum regulator (SMC IRV series). We use this device to apply a pressure difference of ~ 20 kPa, such that the bag applies a constant pressure on the structures.

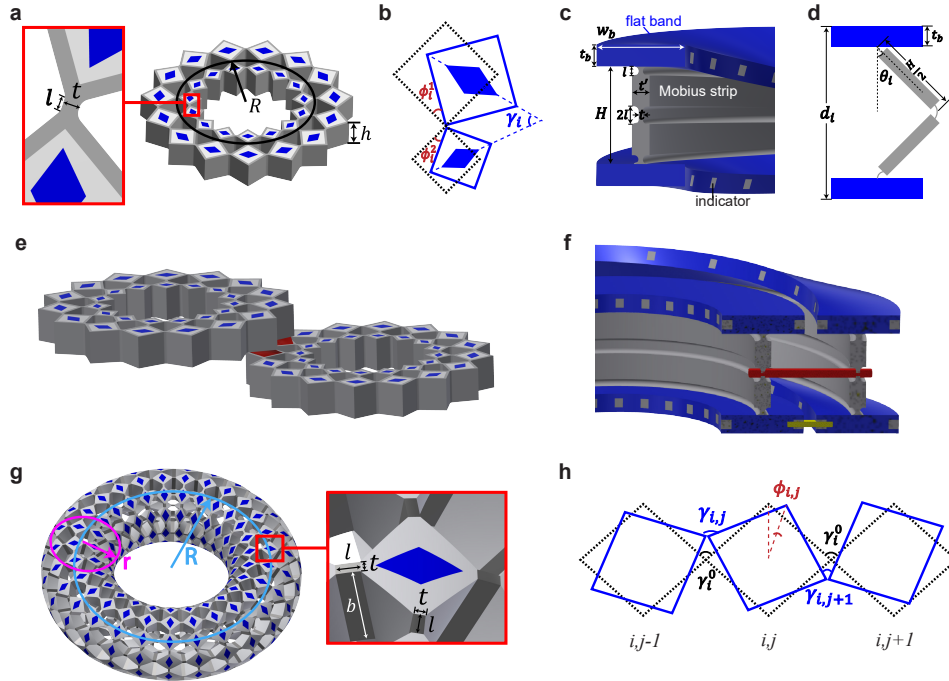
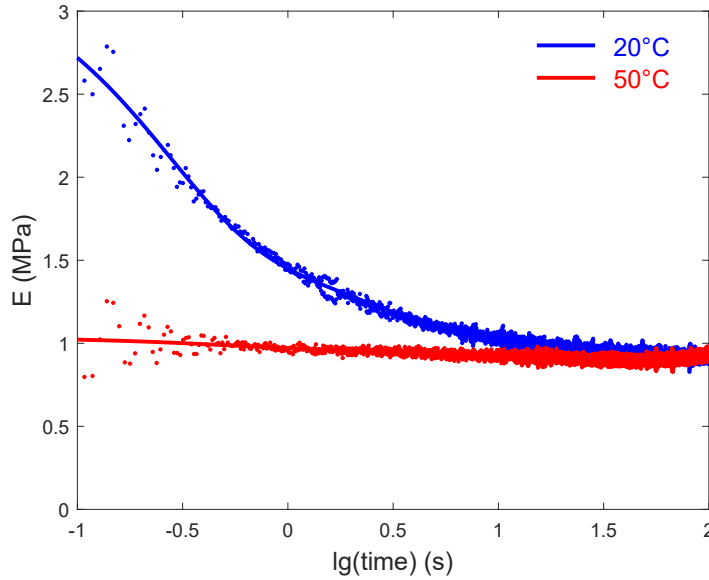


Figure 4.36: **Geometry and data acquisition.** **a.** Geometry design of a metaring, where $R = 30$ mm, $h = 12$ mm, $t = 1$ mm and $l \approx 1$ mm. Squares are marked by diamond marks to track their position and rotation. **b.** Definition of the rotation angle of a metaring's unit cell $\phi_i = (\phi_i^1 + \phi_i^2) = \gamma_i$. **c.** Cross section of twisted bands, where $w_b = 20$ mm, $t_b = 5$ mm, $H = 22$ mm, $t = 1$ mm, $l = 2$ mm and $t' = 4$ mm. The radius of twisted bands is 50 mm. A coating of flexible material (Stratasys Agilus30) encloses the flat band in order to make the junction more durable. **d.** Bending angle of a twisted band $\theta_i = \arccos((d_i - 2t_b)/H)$. **e.** Design of connected metarings. A pair of lozenges of are rigidly connected (red). The connected lozenges have the same rotation. **f.** Geometry design of a Möbius shorts. A Möbius band and a cylinder band are rigidly connected by a rigid yellow bar. The soft strips (grey) are connected at one point by a rigid red bar. The bending angles of the Möbius band and the cylinder band are the same at the connected point. The radius of the Möbius band is 65 mm and the radius of the cylinder band is 34 mm. Other geometrical parameters are the same as single twisted bands (see **c**). **g.** Geometry design of toroidal metamaterials, where $R = 51$ mm, $r = 20$ mm, $l = 2$ mm, $t = 1$ mm and $b = 8$ mm. **h.** Definition of the rotation angle of a metatorus' unit cell $\phi_{i,j} = \frac{1}{2}[(\gamma_{i,j} - \gamma_i^0) - (\gamma_{i,j+1} - \gamma_i^0)]$. A coating of flexible material (Stratasys Agilus30) encloses the squares in order to make the hinge more durable.



$$E(t) = E_0 \left(1 - \sum_{n=1}^3 \eta_n (1 - e^{-t/\tau_n}) \right)$$

	E_0 (MPa)	η_1	η_2	η_3	τ_1 (s)	τ_2 (s)	τ_3 (s)
20°C	3.282	0.506	0.164	0.0507	0.255	2.181	19.39
50°C	1.035	0.057	0.063	\	0.426	5.637	\

Figure 4.37: **High temperature weakens the viscoelasticity of Agilus.** The sample was stretched under a high strain rate of 4/s up to strain $\epsilon = 0.2$ and held fixed for 100 s. The effective section of the standard sample has a length $L = 80$ mm, depth $d = 4$ mm and width $w = 20$ mm. The Young's modulus is obtained by the neo-Hookean material model, $E(t) = 3F/[(\lambda - \lambda^{-1})wd]$, where λ is the applied stretch ratio and F is the measured force. The solid lines are fits of the Maxwell–Wiechert viscoelastic material model to the data, given by $E(t) = E_0(1 - \sum_{n=1}^3 \eta_n(1 - e^{-t/\tau_n}))$, where E_0 is the peak Young's modulus under instantaneous load, η_n is the dimensionless relaxation strength and τ_n is the timescale. At room temperature (20°C), the effective Young's modulus drops by 70% in 20s. While at 50°C, the effective Young's modulus only drops by up to 11%.

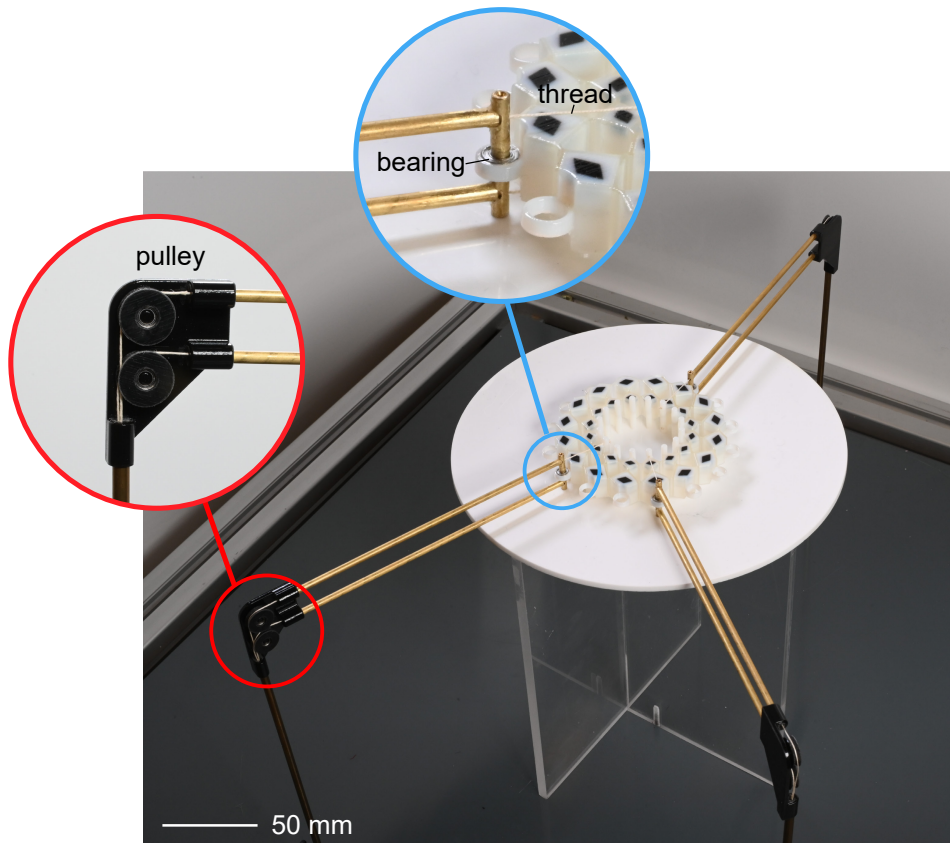


Figure 4.38: **Setup of applying local forces on a metaring.**

Local compressive loads To demonstrate non-commutative mechanics and the mechanical sequential logic gates displayed in Fig. 4 of the Main Text and in Extended Data Fig.3, we designed a second setup shown in Fig. 4.38. The setup allows us to apply local compressive forces using pulleys and weights. To minimize the effect of unwanted external torques that would bias our measurements, we attached ball bearings to the metaring. In the non-commutative mechanics experiments (Fig. 4b of the Main Text and Extended Data Fig.3), we use an odd (even) metaring made of 15 (16) pairs of squares, and apply three forces P , S and R having the same magnitude (2.75 N). The point of applications of the loads are $i_P = 1$, $i_S = 7$ and $i_R = 11$ ($i_P = 1$, $i_S = 8$ and $i_R = 12$).

In the mechanical Set-Reset latch experiment (Fig. 4d of the Main Text), we use the same points of applications of the three loads P , R , S as above, but we slightly adjust the experimental protocol to ensure that the hinges can snap back during the unloading steps: (i) we use smaller P , S and R loads of 1.65N, 1.05N and 1.65N; (ii) we work at a temperature of 50°C by using a heat gun and a thermometer (Fluke 62 Mini). At room temperature, the flexible photopolymer (Agilus30) features a strong viscoelastic stress relaxation, which typically prevents snap back [182]. As shown in Fig. 4.37, a temperature of 50°C speeds up the viscoelastic stress relaxation by orders of magnitude and limit the fluctuations of the Young modulus .

Data acquisition

Metarings The experiments on the metarings are recorded with a high-resolution camera (Nikon D780 with Micro-Nikkor 105mm lens, resolution 6048 px \times 4024 px). By tracking the diamond markers on the squares using particle detection and tracking (ImageJ), we measure the position and angle of each square. The accuracy of the measured rotation angles is 0.3 deg. From the rotation of each square, we extract the average rotation of the pairs of squares i $\phi_i = (\phi_i^1 + \phi_i^2)$, see Fig. 4.36b, from which we compute the staggered variable φ_i . The data is shown in Fig. 2d and e of the Main Text, Fig. 4b and d of the Main Text, Extended Data Fig.1 and in Supplementary Videos 2, 5 and 6.

Flexible twisted bands The distances d_i between the white square markers on the deformed flexible twisted bands are measured by a digital caliper (Mitutoyo CD-15APX). The buckling angle is then computed from the distances d_i and from the dimensions of the specimen using the formula $\theta_i = \arccos((d_i - 2t_b)/H)$, see Fig. 4.36d. Error propagation on all these measurements give a typical measurement error of 5 degrees for the buckling angle. The data is used in Fig. 2i and j of the Main Text.

Metatori The data from the experiments of toroidal metamaterials correspond to measurements performed with a digital protractor (Wixey WR41). The error is around 5 degrees. By measuring the angle $\gamma_{i,j}$ between adjacent lozenges, the rotation of each square $\phi_{i,j} = \frac{1}{2}[(\gamma_{i,j} - \gamma_i^0) - (\gamma_{i,j+1} - \gamma_i^0)]$ is obtained, see Fig. 4.36h. The data are plotted in Fig. 3i of the Main Text, Extended Data Fig.2 and shown in Supplementary Video 4.

Numerical simulations

The numerical results shown in Fig. 4e of the Main Text and in the Supplementary Video 7 correspond to Brownian dynamics simulations over the angle variables $\phi_{i,j}$ indexed by the coordinates i, j of the sites:

$$\eta \frac{d\phi_{i,j}}{dt} = - \sum_{i',j'} \mathcal{D}_{i,j,i',j'} \phi_{i',j'} - f_{i,j}(t) \phi_{i,j} (\phi_{i,j}^2 - \phi_0^2) + w(t), \quad (4.66)$$

where η is the friction coefficient, $f_{i,j}(t)$ corresponds to the force applied at the site i, j at a time t , $w(t)$ is a white noise signal of small amplitude (0.01), and the dynamical matrix \mathcal{D} is directly obtained as the Hessian of the discrete elastic energy

$$E = \sum_{i,j} \left[\frac{C_s}{2a} (\phi_{i+1,j} + \phi_{i,j})^2 + \frac{C_s}{2a} (\phi_{i,j+1} + \phi_{i,j})^2 \right] + \sum_{i,j} \left[\frac{C_b}{2a} (\phi_{i+1,j} - \phi_{i,j})^2 + \frac{C_b}{2a} (\phi_{i,j+1} - \phi_{i,j})^2 \right], \quad (4.67)$$

satisfying $\mathcal{D}_{i,j,i',j'} = \partial E / \partial \phi_{i,j} \partial \phi_{i',j'}$. The white noise is used to ensure that a stable equilibrium is reached but none of the results depend on its magnitude.

Eq. (4.66) was solved with the software *Mathematica* using a LSODA scheme, which automatically detects stiff and non-stiff regions, adapting the solver as needed [183].

The simulations were performed on systems with periodic boundary conditions of sizes 48x49, 49x48, and 49x49 for the even-odd, odd-even, and odd-odd cases respectively.

The simulations involving a homogeneous compression of the metatopi (Fig. 4.33) were performed by setting $\eta = 2$, $a = 1$, $\phi_0 = 1$, $C_s = 3$, $C_b = 0.01$, and $f_{i,j}(t) = 1 \ \forall i, j, t$ and a total simulation time $T = 100$. The choice of bending and shearing stiffness ensures a strong anti-ferromagnetic order ($C_s/C_b \gg 1$).

For the localised loading case shown in Fig. 4e of the Main Text, we used $\eta = 1$, $a = 1$, $\phi_0 = 1$, $C_s = 1$, $C_b = 0.001$, and the magnitude of the loading forces were kept constant in each simulation: $|f_{i,j}^t(t)| = 70$. We used a total simulation time of $T = 1050$. As initial conditions we used configurations with predefined zero-deformation lines. We then let the system relax for a time $t^{\text{relaxation}_1} = 30$ in both cases, reaching an equilibrium configuration (bottom row of each subfigure). Then the applied sources are braided in as follows: exchange of local loads for a duration of $\tau = 400$, relaxation of $t^{\text{relaxation}_2} = 20$, new exchange of $\tau = 400$ and a final relaxation of $t^{\text{relaxation}_3} = 200$.

Bibliography

- [1] A. Seguin and J. Crassous, “Twist-controlled force amplification and spinning tension transition in yarn,” *Phys. Rev. Lett.*, vol. 128, p. 078002, Feb 2022.
- [2] R. A. Shelby, D. R. Smith, and S. Schultz, “Experimental verification of a negative index of refraction,” *Science*, vol. 292, no. 5514, pp. 77–79, 2001.
- [3] H. Chen, C. T. Chan, and P. Sheng, “Transformation optics and metamaterials,” *Nature Materials*, vol. 9, no. 5, pp. 387–396, 2010.
- [4] G. W. Milton and A. V. Cherkaev, “Which Elasticity Tensors are Realizable?,” *Journal of Engineering Materials and Technology*, vol. 117, pp. 483–493, 10 1995.
- [5] M. Kadic, T. Bückmann, N. Stenger, M. Thiel, and M. Wegener, “On the practicality of pentamode mechanical metamaterials,” *Applied Physics Letters*, vol. 100, no. 19, p. 191901, 2012.
- [6] J. N. Grima and K. E. Evans, “Auxetic behavior from rotating squares,” *Journal of Materials Science Letters*, vol. 19, no. 17, pp. 1563–1565, 2000.
- [7] B. Orazbayev and R. Fleury, “Far-field subwavelength acoustic imaging by deep learning,” *Phys. Rev. X*, vol. 10, p. 031029, Aug 2020.
- [8] R. Fleury, D. L. Sounas, C. F. Sieck, M. R. Haberman, and A. Alù, “Sound isolation and giant linear nonreciprocity in a compact acoustic circulator,” *Science*, vol. 343, no. 6170, pp. 516–519, 2014.
- [9] M. Kadic, G. W. Milton, M. van Hecke, and M. Wegener, “3d metamaterials,” *Nature Reviews Physics*, vol. 1, no. 3, pp. 198–210, 2019.
- [10] K. Bertoldi, P. M. Reis, S. Willshaw, and T. Mullin, “Negative poisson’s ratio behavior induced by an elastic instability,” *Advanced Materials*, vol. 22, no. 3, pp. 361–366, 2010.
- [11] J. Li and J. B. Pendry, “Hiding under the carpet: A new strategy for cloaking,” *Phys. Rev. Lett.*, vol. 101, p. 203901, Nov 2008.
- [12] W. Cai, U. K. Chettiar, A. V. Kildishev, and V. M. Shalaev, “Optical cloaking with metamaterials,” *Nature Photonics*, vol. 1, no. 4, pp. 224–227, 2007.

- [13] T. Ergin, N. Stenger, P. Brenner, J. B. Pendry, and M. Wegener, “Three-dimensional invisibility cloak at optical wavelengths,” *Science*, vol. 328, no. 5976, pp. 337–339, 2010.
- [14] T. Bückmann, M. Thiel, M. Kadic, R. Schittny, and M. Wegener, “An elasto-mechanical unfeelability cloak made of pentamode metamaterials,” *Nature Communications*, vol. 5, no. 1, p. 4130, 2014.
- [15] S. Zhang, C. Xia, and N. Fang, “Broadband acoustic cloak for ultrasound waves,” *Phys. Rev. Lett.*, vol. 106, p. 024301, Jan 2011.
- [16] Y. Wang, L. Li, D. Hofmann, J. Andrade, and C. Daraio, “Structured fabrics with tunable mechanical properties,” *Nature*, vol. 596, no. 7871, pp. 238–243, 2021.
- [17] A. Shanian, F.-X. Jette, M. Salehii, M. Q. Pham, M. Schaenzer, G. Bourgeois, K. Bertoldi, A. Gross, F. Javid, D. Backman, S. Yandt, M. Gerendas, T. Meis, K. Knobloch, F. Bake, and D. Peitsch, “Application of multifunctional mechanical metamaterials,” *Advanced Engineering Materials*, vol. 21, no. 7, p. 1900084, 2019.
- [18] K. Bertoldi, V. Vitelli, J. Christensen, and M. Van Hecke, “Flexible mechanical metamaterials,” *Nature Reviews Materials*, vol. 2, no. 11, pp. 1–11, 2017.
- [19] M. Kim, Z. Jacob, and J. Rho, “Recent advances in 2d, 3d and higher-order topological photonics,” *Light: Science & Applications*, vol. 9, no. 1, p. 130, 2020.
- [20] M. Z. Hasan and C. L. Kane, “Colloquium: Topological insulators,” *Rev. Mod. Phys.*, vol. 82, pp. 3045–3067, Nov 2010.
- [21] N. Shahrubudin, T. Lee, and R. Ramlan, “An overview on 3d printing technology: Technological, materials, and applications,” *Procedia Manufacturing*, vol. 35, pp. 1286–1296, 2019. The 2nd International Conference on Sustainable Materials Processing and Manufacturing, SMPM 2019, 8-10 March 2019, Sun City, South Africa.
- [22] L. M. Nash, D. Kleckner, A. Read, V. Vitelli, A. M. Turner, and W. T. M. Irvine, “Topological mechanics of gyroscopic metamaterials,” *Proceedings of the National Academy of Sciences*, vol. 112, no. 47, pp. 14495–14500, 2015.
- [23] R. Süssstrunk and S. D. Huber, “Observation of phononic helical edge states in a mechanical topological insulator,” *Science*, vol. 349, no. 6243, pp. 47–50, 2015.
- [24] J. Paulose, A. S. Meeussen, and V. Vitelli, “Selective buckling via states of self-stress in topological metamaterials,” *Proceedings of the National Academy of Sciences*, vol. 112, no. 25, pp. 7639–7644, 2015.
- [25] J. Paulose, B. G.-g. Chen, and V. Vitelli, “Topological modes bound to dislocations in mechanical metamaterials,” *Nature Physics*, vol. 11, no. 2, pp. 153–156, 2015.
- [26] X. Mao and T. C. Lubensky, “Maxwell lattices and topological mechanics,” *Annual Review of Condensed Matter Physics*, vol. 9, no. 1, pp. 413–433, 2018.

-
- [27] C. Calladine, “Buckminster fuller’s “tensegrity” structures and clerk maxwell’s rules for the construction of stiff frames,” *International Journal of Solids and Structures*, vol. 14, no. 2, pp. 161–172, 1978.
- [28] J. C. Maxwell, “L. on the calculation of the equilibrium and stiffness of frames,” *The London, Edinburgh, and Dublin Philosophical Magazine and Journal of Science*, vol. 27, no. 182, pp. 294–299, 1864.
- [29] C. L. Kane and T. C. Lubensky, “Topological boundary modes in isostatic lattices,” *Nature Physics*, vol. 10, no. 1, pp. 39–45, 2014.
- [30] B. G.-g. Chen, N. Upadhyaya, and V. Vitelli, “Nonlinear conduction via solitons in a topological mechanical insulator,” *Proceedings of the National Academy of Sciences*, vol. 111, no. 36, pp. 13004–13009, 2014.
- [31] M. Guzmán, D. Bartolo, and D. Carpentier, “Geometry and Topology Tango in Ordered and Amorphous Chiral Matter,” *SciPost Phys.*, vol. 12, p. 38, 2022.
- [32] S. Ryu, A. P. Schnyder, A. Furusaki, and A. W. W. Ludwig, “Topological insulators and superconductors: tenfold way and dimensional hierarchy,” *New Journal of Physics*, vol. 12, p. 065010, jun 2010.
- [33] J.-W. Rhim, J. Behrends, and J. H. Bardarson, “Bulk-boundary correspondence from the intercellular zak phase,” *Phys. Rev. B*, vol. 95, p. 035421, Jan 2017.
- [34] B. G.-g. Chen, B. Liu, A. A. Evans, J. Paulose, I. Cohen, V. Vitelli, and C. D. Santangelo, “Topological mechanics of origami and kirigami,” *Phys. Rev. Lett.*, vol. 116, p. 135501, Mar 2016.
- [35] S. Guest and J. Hutchinson, “On the determinacy of repetitive structures,” *Journal of the Mechanics and Physics of Solids*, vol. 51, no. 3, pp. 383–391, 2003.
- [36] T. C. Lubensky, C. L. Kane, X. Mao, A. Souslov, and K. Sun, “Phonons and elasticity in critically coordinated lattices,” *Reports on Progress in Physics*, vol. 78, p. 073901, jun 2015.
- [37] D. Z. Rocklin, S. Zhou, K. Sun, and X. Mao, “Transformable topological mechanical metamaterials,” *Nature Communications*, vol. 8, no. 1, p. 14201, 2017.
- [38] A. J. Heeger, S. Kivelson, J. R. Schrieffer, and W. P. Su, “Solitons in conducting polymers,” *Rev. Mod. Phys.*, vol. 60, pp. 781–850, Jul 1988.
- [39] C. W. Peterson, W. A. Benalcazar, T. L. Hughes, and G. Bahl, “A quantized microwave quadrupole insulator with topologically protected corner states,” *Nature*, vol. 555, no. 7696, pp. 346–350, 2018.
- [40] X. Ni, M. Weiner, A. Alù, and A. B. Khanikaev, “Observation of higher-order topological acoustic states protected by generalized chiral symmetry,” *Nature Materials*, vol. 18, no. 2, pp. 113–120, 2019.

- [41] X. Ni, M. Li, M. Weiner, A. Alù, and A. B. Khanikaev, “Demonstration of a quantized acoustic octupole topological insulator,” *Nature Communications*, vol. 11, no. 1, p. 2108, 2020.
- [42] M. Bellec, U. Kuhl, G. Montambaux, and F. Mortessagne, “Manipulation of edge states in microwave artificial graphene,” *New Journal of Physics*, vol. 16, p. 113023, nov 2014.
- [43] S. Imhof, C. Berger, F. Bayer, J. Brehm, L. W. Molenkamp, T. Kiessling, F. Schindler, C. H. Lee, M. Greiter, T. Neupert, and R. Thomale, “Topoelectrical-circuit realization of topological corner modes,” *Nature Physics*, vol. 14, no. 9, pp. 925–929, 2018.
- [44] P. St-Jean, V. Goblot, E. Galopin, A. Lemaître, T. Ozawa, L. Le Gratiet, I. Sagnes, J. Bloch, and A. Amo, “Lasing in topological edge states of a one-dimensional lattice,” *Nature Photonics*, vol. 11, no. 10, pp. 651–656, 2017.
- [45] A. Altland and M. R. Zirnbauer, “Nonstandard symmetry classes in mesoscopic normal-superconducting hybrid structures,” *Phys. Rev. B*, vol. 55, pp. 1142–1161, Jan 1997.
- [46] R. Süsstrunk and S. D. Huber, “Classification of topological phonons in linear mechanical metamaterials,” *Proceedings of the National Academy of Sciences*, vol. 113, no. 33, pp. E4767–E4775, 2016.
- [47] S. D. Huber, “Topological mechanics,” *Nature Physics*, vol. 12, no. 7, pp. 621–623, 2016.
- [48] Y. Barlas and E. Prodan, “Topological classification table implemented with classical passive metamaterials,” *Phys. Rev. B*, vol. 98, p. 094310, Sep 2018.
- [49] H. Wakao, T. Yoshida, H. Araki, T. Mizoguchi, and Y. Hatsugai, “Higher-order topological phases in a spring-mass model on a breathing kagome lattice,” *Phys. Rev. B*, vol. 101, p. 094107, Mar 2020.
- [50] M. E. Cage, K. Klitzing, A. Chang, F. Duncan, M. Haldane, R. B. Laughlin, A. Pruisken, and D. Thouless, *The quantum Hall effect*. Springer Science & Business Media, 2012.
- [51] N. P. Mitchell, L. M. Nash, D. Hexner, A. M. Turner, and W. T. M. Irvine, “Amorphous topological insulators constructed from random point sets,” *Nature Physics*, vol. 14, no. 4, pp. 380–385, 2018.
- [52] W. A. Benalcazar, B. A. Bernevig, and T. L. Hughes, “Quantized electric multipole insulators,” *Science*, vol. 357, no. 6346, pp. 61–66, 2017.
- [53] W. A. Benalcazar, B. A. Bernevig, and T. L. Hughes, “Electric multipole moments, topological multipole moment pumping, and chiral hinge states in crystalline insulators,” *Phys. Rev. B*, vol. 96, p. 245115, Dec 2017.

-
- [54] M. Serra-Garcia, V. Peri, R. Süsstrunk, O. R. Bilal, T. Larsen, L. G. Villanueva, and S. D. Huber, “Observation of a phononic quadrupole topological insulator,” *Nature*, vol. 555, no. 7696, pp. 342–345, 2018.
- [55] X. Guo, M. Guzman, D. Carpentier, D. Bartolo, and C. Coulais, “Non-orientable order and non-abelian response in frustrated metamaterials,” 2021.
- [56] J. C. Maxwell, “L. on the calculation of the equilibrium and stiffness of frames,” *The London, Edinburgh, and Dublin Philosophical Magazine and Journal of Science*, vol. 27, no. 182, pp. 294–299, 1864.
- [57] B. Schulze, C. Millar, A. Mazurek, and W. Baker, “States of self-stress in symmetric frameworks and applications,” *International Journal of Solids and Structures*, vol. 234-235, p. 111238, 2022.
- [58] J.-N. Fuchs and F. Piéchon, “Orbital embedding and topology of one-dimensional two-band insulators,” *Phys. Rev. B*, vol. 104, p. 235428, Dec 2021.
- [59] J. K. Asbóth, L. Oroszlány, and A. Pályi, “A short course on topological insulators,” *Lecture notes in physics*, vol. 919, p. 166, 2016.
- [60] L. Xin, Y. Siyuan, L. Harry, L. Minghui, and C. Yanfeng, “Topological mechanical metamaterials: A brief review,” *Current Opinion in Solid State and Materials Science*, vol. 24, no. 5, p. 100853, 2020.
- [61] M. V. Berry, “Quantal phase factors accompanying adiabatic changes,” *Proceedings of the Royal Society of London. A. Mathematical and Physical Sciences*, vol. 392, no. 1802, pp. 45–57, 1984.
- [62] J. Zak, “Berry’s phase for energy bands in solids,” *Physical review letters*, vol. 62, no. 23, p. 2747, 1989.
- [63] D. Vanderbilt and R. D. King-Smith, “Electric polarization as a bulk quantity and its relation to surface charge,” *Phys. Rev. B*, vol. 48, pp. 4442–4455, Aug 1993.
- [64] A. G. Grushin, “Topological phases of amorphous matter,” 2020.
- [65] D. Vanderbilt, *Berry phases in electronic structure theory: electric polarization, orbital magnetization and topological insulators*. Cambridge University Press, 2018.
- [66] T. Neupert and F. Schindler, “Topological crystalline insulators,” in *Topological Matter*, pp. 31–61, Springer, 2018.
- [67] N. Marzari and D. Vanderbilt, “Maximally localized generalized wannier functions for composite energy bands,” *Phys. Rev. B*, vol. 56, pp. 12847–12865, Nov 1997.
- [68] F. Bloch, “Über die quantenmechanik der elektronen in kristallgittern,” *Zeitschrift fur Physik*, vol. 52, p. 555, 1929.
- [69] X.-L. Qi, T. L. Hughes, and S.-C. Zhang, “Topological field theory of time-reversal invariant insulators,” *Phys. Rev. B*, vol. 78, p. 195424, Nov 2008.

- [70] B.A.Bernevig and T.L.Hughes, *Topological insulators and topological superconductors*. Princeton University Press, 2013.
- [71] M. Franz and L. Molenkamp, eds., *Topological Insulators*, vol. 6 of *Contemporary Concepts of Condensed Matter Science*. Elsevier,, 2013.
- [72] J. K. Asbóth, L. Oroszlány, and A. Pályi, “A short course on topological insulators,” *Lecture Notes in Physics*, 2016.
- [73] N. P. Armitage, E. J. Mele, and A. Vishwanath, “Weyl and dirac semimetals in three-dimensional solids,” *Rev. Mod. Phys.*, vol. 90, p. 015001, Jan 2018.
- [74] A. P. Schnyder, S. Ryu, A. Furusaki, and A. W. W. Ludwig, “Classification of topological insulators and superconductors in three spatial dimensions,” *Phys. Rev. B*, vol. 78, p. 195125, Nov 2008.
- [75] A. Kitaev, “Periodic table for topological insulators and superconductors,” in *AIP conference proceedings*, vol. 1134, pp. 22–30, American Institute of Physics, 2009.
- [76] L. Fidkowski, T. S. Jackson, and I. Klich, “Model characterization of gapless edge modes of topological insulators using intermediate brillouin-zone functions,” *Phys. Rev. Lett.*, vol. 107, p. 036601, Jul 2011.
- [77] A. Alexandradinata, X. Dai, and B. A. Bernevig, “Wilson-loop characterization of inversion-symmetric topological insulators,” *Phys. Rev. B*, vol. 89, p. 155114, Apr 2014.
- [78] M. Taherinejad, K. F. Garrity, and D. Vanderbilt, “Wannier center sheets in topological insulators,” *Phys. Rev. B*, vol. 89, p. 115102, Mar 2014.
- [79] A. Alexandradinata, Z. Wang, and B. A. Bernevig, “Topological insulators from group cohomology,” *Phys. Rev. X*, vol. 6, p. 021008, Apr 2016.
- [80] A. Alexandradinata and B. A. Bernevig, “Berry-phase description of topological crystalline insulators,” *Phys. Rev. B*, vol. 93, p. 205104, May 2016.
- [81] R. Jackiw and C. Rebbi, “Solitons with fermion number $1/2$,” *Phys. Rev. D*, vol. 13, pp. 3398–3409, Jun 1976.
- [82] B. Volkov and O. Pankratov, “Two-dimensional massless electrons in an inverted contact,” *Soviet Journal of Experimental and Theoretical Physics Letters*, vol. 42, p. 178, 1985.
- [83] E. Fradkin, E. Dagotto, and D. Boyanovsky, “Physical realization of the parity anomaly in condensed matter physics,” *Phys. Rev. Lett.*, vol. 57, pp. 2967–2970, Dec 1986.
- [84] Y. Hatsugai, “Chern number and edge states in the integer quantum hall effect,” *Phys. Rev. Lett.*, vol. 71, pp. 3697–3700, Nov 1993.

-
- [85] T. Ozawa, H. M. Price, A. Amo, N. Goldman, M. Hafezi, L. Lu, M. C. Rechtsman, D. Schuster, J. Simon, O. Zilberberg, and I. Carusotto, “Topological photonics,” *Rev. Mod. Phys.*, vol. 91, p. 015006, Mar 2019.
- [86] V. Gurarie and J. T. Chalker, “Some generic aspects of bosonic excitations in disordered systems,” *Phys. Rev. Lett.*, vol. 89, p. 136801, Sep 2002.
- [87] V. Gurarie and J. T. Chalker, “Bosonic excitations in random media,” *Phys. Rev. B*, vol. 68, p. 134207, Oct 2003.
- [88] D. Vanderbilt, *Berry Phases in Electronic Structure Theory*. Cambridge University Press, 2018.
- [89] R. D. King-Smith and D. Vanderbilt, “Theory of polarization of crystalline solids,” *Phys. Rev. B*, vol. 47, pp. 1651–1654, Jan 1993.
- [90] L. Fu and C. L. Kane, “Time reversal polarization and a Z_2 adiabatic spin pump,” *Phys. Rev. B*, vol. 74, p. 195312, Nov 2006.
- [91] T. Louvet, P. Delplace, A. A. Fedorenko, and D. Carpentier, “On the origin of minimal conductivity at a band crossing,” *Phys. Rev. B*, vol. 92, p. 155116, Oct 2015.
- [92] B. Sutherland, “Localization of electronic wave functions due to local topology,” *Phys. Rev. B*, vol. 34, pp. 5208–5211, Oct 1986.
- [93] I. Mondragon-Shem, T. L. Hughes, J. Song, and E. Prodan, “Topological criticality in the chiral-symmetric aiii class at strong disorder,” *Phys. Rev. Lett.*, vol. 113, p. 046802, Jul 2014.
- [94] T. Rakovszky, J. K. Asbóth, and A. Alberti, “Detecting topological invariants in chiral symmetric insulators via losses,” *Phys. Rev. B*, vol. 95, p. 201407, May 2017.
- [95] F. Cardano, A. D’Errico, A. Dauphin, M. Maffei, B. Piccirillo, C. de Lisio, G. De Filippis, V. Cataudella, E. Santamato, L. Marrucci, M. Lewenstein, and P. Massignan, “Detection of zak phases and topological invariants in a chiral quantum walk of twisted photons,” *Nature Communications*, vol. 8, no. 1, p. 15516, 2017.
- [96] D. Z. Rocklin, “Directional mechanical response in the bulk of topological metamaterials,” *New Journal of Physics*, vol. 19, p. 065004, jun 2017.
- [97] O. R. Bilal, R. Süsstrunk, C. Daraio, and S. D. Huber, “Intrinsically polar elastic metamaterials,” *Advanced Materials*, vol. 29, no. 26, p. 1700540, 2017.
- [98] E. Blount, “Formalisms of band theory,” vol. 13 of *Solid State Physics*, pp. 305–373, Academic Press, 1962.
- [99] T. Neupert and F. Schindler, “Topological crystalline insulators,” in *Topological Matter*, pp. 31–61, Springer, 2018.
- [100] J. Jiang and S. G. Louie, “Topology classification using chiral symmetry and spin correlations in graphene nanoribbons,” *Nano Letters*, vol. 21, pp. 197–202, 01 2021.

- [101] B. Bradlyn, L. Elcoro, J. Cano, M. G. Vergniory, Z. Wang, C. Felser, M. I. Aroyo, and B. A. Bernevig, “Topological quantum chemistry,” *Nature*, vol. 547, no. 7663, pp. 298–305, 2017.
- [102] X. Zhang, M. Xiao, Y. Cheng, M.-H. Lu, and J. Christensen, “Topological sound,” *Communications Physics*, vol. 1, no. 1, p. 97, 2018.
- [103] M. Xiao and S. Fan, “Photonic chern insulator through homogenization of an array of particles,” *Phys. Rev. B*, vol. 96, p. 100202, Sep 2017.
- [104] A. Agarwala and V. B. Shenoy, “Topological insulators in amorphous systems,” *Phys. Rev. Lett.*, vol. 118, p. 236402, Jun 2017.
- [105] Q. Marsal, D. Varjas, and A. G. Grushin, “Topological weaire–thorpe models of amorphous matter,” *Proceedings of the National Academy of Sciences*, vol. 117, no. 48, pp. 30260–30265, 2020.
- [106] E. J. Meier, F. A. An, A. Dauphin, M. Maffei, P. Massignan, T. L. Hughes, and B. Gadway, “Observation of the topological anderson insulator in disordered atomic wires,” *Science*, vol. 362, no. 6417, pp. 929–933, 2018.
- [107] M. Bellec, U. Kuhl, G. Montambaux, and F. Mortessagne, “Topological transition of dirac points in a microwave experiment,” *Phys. Rev. Lett.*, vol. 110, p. 033902, Jan 2013.
- [108] A. Agarwala, V. Juričić, and B. Roy, “Higher-order topological insulators in amorphous solids,” *Phys. Rev. Research*, vol. 2, p. 012067, Mar 2020.
- [109] M. Maffei, A. Dauphin, F. Cardano, M. Lewenstein, and P. Massignan, “Topological characterization of chiral models through their long time dynamics,” *New Journal of Physics*, vol. 20, p. 013023, jan 2018.
- [110] P. St-Jean, A. Dauphin, P. Massignan, B. Real, O. Jamadi, M. Milicevic, A. Lemaître, A. Harouri, L. Le Gratiet, I. Sagnes, S. Ravets, J. Bloch, and A. Amo, “Measuring topological invariants in a polaritonic analog of graphene,” *Phys. Rev. Lett.*, vol. 126, p. 127403, Mar 2021.
- [111] A. D’Errico, F. Di Colandrea, R. Barboza, A. Dauphin, M. Lewenstein, P. Massignan, L. Marrucci, and F. Cardano, “Bulk detection of time-dependent topological transitions in quenched chiral models,” *Phys. Rev. Research*, vol. 2, p. 023119, May 2020.
- [112] J. Kruthoff, J. de Boer, J. van Wezel, C. L. Kane, and R.-J. Slager, “Topological classification of crystalline insulators through band structure combinatorics,” *Phys. Rev. X*, vol. 7, p. 041069, Dec 2017.
- [113] F. Tang, H. C. Po, A. Vishwanath, and X. Wan, “Comprehensive search for topological materials using symmetry indicators,” *Nature*, vol. 566, no. 7745, pp. 486–489, 2019.

-
- [114] T. Zhang, Y. Jiang, Z. Song, H. Huang, Y. He, Z. Fang, H. Weng, and C. Fang, “Catalogue of topological electronic materials,” *Nature*, vol. 566, no. 7745, pp. 475–479, 2019.
- [115] K. Kawabata, K. Shiozaki, M. Ueda, and M. Sato, “Symmetry and topology in non-hermitian physics,” *Phys. Rev. X*, vol. 9, p. 041015, Oct 2019.
- [116] C. Bena and G. Montambaux, “Remarks on the tight-binding model of graphene,” *New Journal of Physics*, vol. 11, p. 095003, sep 2009.
- [117] J. N. Fuchs, F. Piéchon, M. O. Goerbig, and G. Montambaux, “Topological berry phase and semiclassical quantization of cyclotron orbits for two dimensional electrons in coupled band models,” *The European Physical Journal B*, vol. 77, no. 3, pp. 351–362, 2010.
- [118] M. Fruchart, D. Carpentier, and K. Gawedzki, “Parallel transport and band theory in crystals,” *EPL (Europhysics Letters)*, vol. 106, p. 60002, jun 2014.
- [119] N. Marzari, A. A. Mostofi, J. R. Yates, I. Souza, and D. Vanderbilt, “Maximally localized wannier functions: Theory and applications,” *Rev. Mod. Phys.*, vol. 84, pp. 1419–1475, Oct 2012.
- [120] K. D. Ikramov, “Matrix pencils: Theory, applications, and numerical methods,” *Journal of Soviet Mathematics*, vol. 64, no. 2, pp. 783–853, 1993.
- [121] G. H. Golub and C. F. Van Loan, *Matrix computations*, vol. 3. JHU press, 2013.
- [122] W. T. B. Kelvin, *Popular lectures and addresses*, vol. 3. Macmillan and Company, 1891.
- [123] M. D. Caio, G. Möller, N. R. Cooper, and M. J. Bhaseen, “Topological marker currents in chern insulators,” *Nature Physics*, vol. 15, no. 3, pp. 257–261, 2019.
- [124] T. A. Loring, “A guide to the bott index and localizer index,” *arXiv preprint arXiv:1907.11791*, 2019.
- [125] M. Tarnowski, F. N. Ünal, N. Fläschner, B. S. Rem, A. Eckardt, K. Sengstock, and C. Weitenberg, “Measuring topology from dynamics by obtaining the chern number from a linking number,” *Nature Communications*, vol. 10, no. 1, p. 1728, 2019.
- [126] A. Dauphin and N. Goldman, “Extracting the chern number from the dynamics of a fermi gas: Implementing a quantum hall bar for cold atoms,” *Phys. Rev. Lett.*, vol. 111, p. 135302, Sep 2013.
- [127] J. E. S. Socolar, T. C. Lubensky, and C. L. Kane, “Mechanical graphene,” *New Journal of Physics*, vol. 19, p. 025003, feb 2017.
- [128] S. Yves, G. Lerosey, and F. Lemoult, “Inducing topology in a wire medium based metamaterial,” *Opt. Mater. Express*, vol. 11, pp. 821–841, Mar 2021.

- [129] M. Di Ventra, Y. V. Pershin, and C.-C. Chien, “Custodial chiral symmetry in a su-schrieffer-heeger electrical circuit with memory,” *Phys. Rev. Lett.*, vol. 128, p. 097701, Mar 2022.
- [130] M. Weiner, X. Ni, M. Li, A. Alù, and A. B. Khanikaev, “Demonstration of a third-order hierarchy of topological states in a three-dimensional acoustic metamaterial,” *Science Advances*, vol. 6, no. 13, p. eaay4166, 2020.
- [131] D. Bartolo and D. Carpentier, “Topological elasticity of nonorientable ribbons,” *Physical Review X*, vol. 9, p. 041058, dec 2019.
- [132] A. Hatcher, *Algebraic topology*. Cambridge University Press, 2002.
- [133] C. Coulais, C. Kettenis, and M. van Hecke, “A characteristic length scale causes anomalous size effects and boundary programmability in mechanical metamaterials,” *Nature Physics*, vol. 14, pp. 40–44, sep 2017.
- [134] M. L. Baker, G. A. Timco, S. Piligkos, J. S. Mathieson, H. Mutka, F. Tuna, P. Kozłowski, M. Antkowiak, T. Guidi, T. Gupta, H. Rath, R. J. Woolfson, G. Kamieniarz, R. G. Pritchard, H. Weihe, L. Cronin, G. Rajaraman, D. Colli-son, E. J. L. McInnes, and R. E. P. Winpenny, “A classification of spin frustration in molecular magnets from a physical study of large odd-numbered-metal, odd electron rings,” *Proceedings of the National Academy of Sciences*, vol. 109, no. 47, pp. 19113–19118, 2012.
- [135] A. Chardac, L. A. Hoffmann, Y. Poupard, L. Giomi, and D. Bartolo, “Topology-driven ordering of flocking matter,” *Physical Review X*, vol. 11, p. 031069, Sep 2021.
- [136] S. Tanda, T. Tsuneta, Y. Okajima, K. Inagaki, K. Yamaya, and N. Hatakenaka, “A möbius strip of single crystals,” *Nature*, vol. 417, no. 6887, pp. 397–398, 2002.
- [137] J.-H. Chung and J.-D. Chai, “Electronic properties of möbius cyclacenes studied by thermally-assisted-occupation density functional theory,” *Scientific Reports*, vol. 9, no. 1, p. 2907, 2019.
- [138] G. Ouyang, L. Ji, Y. Jiang, F. Würthner, and M. Liu, “Self-assembled möbius strips with controlled helicity,” *Nature Communications*, vol. 11, no. 1, p. 5910, 2020.
- [139] Y. Segawa, T. Watanabe, K. Yamanoue, M. Kuwayama, K. Watanabe, J. Pirillo, Y. Hijikata, and K. Itami, “Synthesis of a möbius carbon nanobelt,” *Nature Synthesis*, 2022.
- [140] G. R. Schaller, F. Topić, K. Rissanen, Y. Okamoto, J. Shen, and R. Herges, “Design and synthesis of the first triply twisted möbius annulene,” *Nature Chemistry*, vol. 6, no. 7, pp. 608–613, 2014.
- [141] Y. Wang, H. M. Price, B. Zhang, and Y. D. Chong, “Circuit implementation of a four-dimensional topological insulator,” *Nature Communications*, vol. 11, no. 1, p. 2356, 2020.

-
- [142] L. D. Landau, “On the theory of phase transitions,” *Zh. Eksp. Teor. Fiz.*, vol. 7, pp. 19–32, 1937.
- [143] P. M. Chaikin and T. C. Lubensky, *Principles of condensed matter physics*. Cambridge university press Cambridge, 1995.
- [144] J. Toner, Y. Tu, and S. Ramaswamy, “Hydrodynamics and phases of flocks,” *Annals of Physics*, vol. 318, no. 1, pp. 170–244, 2005.
- [145] A. Cavagna and I. Giardina, “Bird flocks as condensed matter,” *Annu. Rev. Condens. Matter Phys.*, vol. 5, no. 1, pp. 183–207, 2014.
- [146] X.-G. Wen, “Colloquium: Zoo of quantum-topological phases of matter,” *Rev. Mod. Phys.*, vol. 89, p. 041004, Dec 2017.
- [147] R. Bondesan and Z. Ringel, “Classical topological paramagnetism,” *Phys. Rev. B*, vol. 95, p. 174418, May 2017.
- [148] B. Trembl, A. Gillman, P. Buskohl, and R. Vaia, “Origami mechanologic,” *Proceedings of the National Academy of Sciences*, vol. 115, no. 27, pp. 6916–6921, 2018.
- [149] N. C. Keim, J. D. Paulsen, Z. Zeravcic, S. Sastry, and S. R. Nagel, “Memory formation in matter,” *Reviews of Modern Physics*, vol. 91, no. 3, p. 035002, 2019.
- [150] J. A. Faber, J. P. Udani, K. S. Riley, A. R. Studart, and A. F. Arrieta, “Dome-patterned metamaterial sheets,” *Advanced Science*, vol. 7, no. 22, p. 2001955, 2020.
- [151] T. Chen, M. Pauly, and P. M. Reis, “A reprogrammable mechanical metamaterial with stable memory,” *Nature*, vol. 589, no. 7842, pp. 386–390, 2021.
- [152] C. Merrigan, C. Nisoli, and Y. Shokef, “Topologically protected steady cycles in an icelike mechanical metamaterial,” *Physical Review Research*, vol. 3, no. 2, p. 023174, 2021.
- [153] T. Jules, A. Reid, K. E. Daniels, M. Mungan, and F. Lechenault, “The delicate memory structure of coupled origami switches,” *arXiv:2106.08243*, 2021.
- [154] H. Bense and M. van Hecke, “Complex pathways and memory in compressed corrugated sheets,” *arXiv:2106.14441*, 2021.
- [155] G. Toulouse *et al.*, “Theory of the frustration effect in spin glasses: I,” *Spin Glass Theory and Beyond: An Introduction to the Replica Method and Its Applications*, vol. 9, p. 99, 1987.
- [156] R. Moessner and A. P. Ramirez, “Geometrical frustration,” *Physics Today*, vol. 59, no. 2, p. 24, 2006.
- [157] L. Balents, “Spin liquids in frustrated magnets,” *Nature*, vol. 464, no. 7286, pp. 199–208, 2010.

- [158] C. Nisoli, R. Moessner, and P. Schiffer, “Colloquium: Artificial spin ice: Designing and imaging magnetic frustration,” *Reviews of Modern Physics*, vol. 85, pp. 1473–1490, Oct 2013.
- [159] H. Wioland, F. G. Woodhouse, J. Dunkel, and R. E. Goldstein, “Ferromagnetic and antiferromagnetic order in bacterial vortex lattices,” *Nature physics*, vol. 12, no. 4, pp. 341–345, 2016.
- [160] K.-T. Wu, J. B. Hishamunda, D. T. Chen, S. J. DeCamp, Y.-W. Chang, A. Fernández-Nieves, S. Fraden, and Z. Dogic, “Transition from turbulent to coherent flows in confined three-dimensional active fluids,” *Science*, vol. 355, no. 6331, 2017.
- [161] A. Forrow, F. G. Woodhouse, and J. Dunkel, “Mode selection in compressible active flow networks,” *Physical Review Letters*, vol. 119, p. 028102, Jul 2017.
- [162] Y. Han, Y. Shokef, A. M. Alsayed, P. Yunker, T. C. Lubensky, and A. G. Yodh, “Geometric frustration in buckled colloidal monolayers,” *Nature*, vol. 456, no. 7224, pp. 898–903, 2008.
- [163] A. Ortiz-Ambriz, C. Nisoli, C. Reichhardt, C. J. O. Reichhardt, and P. Tierno, “Colloquium: Ice rule and emergent frustration in particle ice and beyond,” *Reviews of Modern Physics*, vol. 91, p. 041003, Dec 2019.
- [164] A. Molina, S. Kumar, S. Karpitschka, and M. Prakash, “Droplet tilings for rapid exploration of spatially constrained many-body systems,” *Proceedings of the National Academy of Sciences*, vol. 118, no. 34, 2021.
- [165] S. H. Kang, S. Shan, A. Košmrlj, W. L. Noorduin, S. Shian, J. C. Weaver, D. R. Clarke, and K. Bertoldi, “Complex ordered patterns in mechanical instability induced geometrically frustrated triangular cellular structures,” *Physical Review Letters*, vol. 112, no. 9, p. 098701, 2014.
- [166] P. Celli, C. McMahan, B. Ramirez, A. Bauhofer, C. Naify, D. Hofmann, B. Audoly, and C. Daraio, “Shape-morphing architected sheets with non-periodic cut patterns,” *Soft Matter*, vol. 14, no. 48, pp. 9744–9749, 2018.
- [167] A. S. Meeussen, E. C. Oğuz, Y. Shokef, and M. van Hecke, “Topological defects produce exotic mechanics in complex metamaterials,” *Nature Physics*, vol. 16, no. 3, pp. 307–311, 2020.
- [168] B. Deng, S. Yu, A. E. Forte, V. Tournat, and K. Bertoldi, “Characterization, stability, and application of domain walls in flexible mechanical metamaterials,” *Proceedings of the National Academy of Sciences*, vol. 117, pp. 31002–31009, nov 2020.
- [169] G. P. Choi, L. H. Dudte, and L. Mahadevan, “Programming shape using kirigami tessellations,” *Nature Materials*, vol. 18, no. 9, pp. 999–1004, 2019.
- [170] Y. Zhang, B. Li, Q. Zheng, G. M. Genin, and C. Chen, “Programmable and robust static topological solitons in mechanical metamaterials,” *Nature Communications*, vol. 10, no. 1, pp. 1–8, 2019.

- [171] A. Hatcher, “Vector bundles and K-theory,” *available at <http://www.math.cornell.edu/~hatcher>*, 2017.
- [172] Z. P. Bazant and L. Cedolin, *Stability of structures: elastic, inelastic, fracture and damage theories*. World Scientific, 2010.
- [173] M. Z. Hasan and C. L. Kane, “Colloquium: topological insulators,” *Reviews of modern physics*, vol. 82, no. 4, p. 3045, 2010.
- [174] R. P. Boas Jr, “Möbius shorts,” *Mathematics Magazine*, vol. 68, no. 2, pp. 127–127, 1995.
- [175] M. Fruchart, Y. Zhou, and V. Vitelli, “Dualities and non-abelian mechanics,” *Nature*, vol. 577, no. 7792, pp. 636–640, 2020.
- [176] P. Horowitz, W. Hill, and I. Robinson, *The art of electronics*, vol. 2. Cambridge university press Cambridge, 1989.
- [177] P. Zanardi and M. Rasetti, “Holonomic quantum computation,” *Physics Letters A*, vol. 264, no. 2-3, pp. 94–99, 1999.
- [178] J. Alicea, Y. Oreg, G. Refael, F. Von Oppen, and M. P. Fisher, “Non-abelian statistics and topological quantum information processing in 1d wire networks,” *Nature Physics*, vol. 7, no. 5, pp. 412–417, 2011.
- [179] A. Gramain, *Topologie des Surfaces*. Presses Universitaires de France, 1971.
- [180] B. Audoly and Y. Pomeau, *Elasticity and geometry: from hair curls to the non-linear response of shells*. Oxford university press, 2010.
- [181] D. Bartolo and J.-B. Fournier, “Elastic interaction between "hard" or "soft" pointwise inclusions on biological membranes,” *The European Physical Journal E*, vol. 11, no. 2, pp. 141–146, 2003.
- [182] D. M. Dykstra, J. Busink, B. Ennis, and C. Coulais, “Viscoelastic snapping metamaterials,” *Journal of Applied Mechanics*, vol. 86, no. 11, 2019.
- [183] A. C. Hindmarsh, “Odepack, a systematized collection of ode solvers,” *Scientific computing*, pp. 55–64, 1983.

Abstract:

What explains the rigidity of a material? The answer, in most cases, lies in the microscopic stiffness of their components. However, in the 18th century, Maxwell understood that materials made of stiff constituents may exhibit soft modes depending on a macroscopic quantity: the number of degrees of freedom and constraints. Two centuries later we can understand this softness as a topological property.

This thesis explores the concept of rigidity from a topological lens. First, I explore the consequences of Maxwell's realization on networks of beads and springs. These systems enjoy an often overlooked symmetry known as chiral symmetry. I exploit this symmetry to define a new material property, the chiral polarization, encoding both the geometry and topology of the material. It distinguishes between distinct topological phases and also probes their softness by locating zero-energy modes. We confirm these findings by experimentally measuring the chiral polarization on several mechanical metamaterials, without resorting to any low-energy model.

In the second part, I analyze the connection between a different topological property, non-orientability, and the location of highly stiff regions in an otherwise homogeneous system. Inspired by the relation between global frustration and non-orientability, I describe a unifying framework explaining the topological origin of the rigidity of non-orientable soft surfaces and frustrated mechanical metamaterials. Their common denominator corresponds to the non-orientability of their deformation bundles. Through experiments and simulations, we confirm the existence of topologically protected undeformable nodes and lines, and explore their non-commutative responses, paving the way to designing robust and functional mechanical metamaterials.

Résumé :

Comment expliquer la rigidité d'un matériau? Dans la plupart des cas grâce à la raideur microscopique de ses composants. Néanmoins, au 18ème siècle, Maxwell comprit que certains matériaux construits à partir de constituents rigides, peuvent posséder des modes de déformations mous. Il en fait le comptage à partir d'une quantité macroscopique: le nombre de degrés de liberté et de restrictions. Deux siècles plus tard, nous comprenons cette souplesse comme une propriété topologique.

Cette thèse explore le concept de rigidité du point de vue topologique. Premièrement, j'explore les conséquences de la réalisation de Maxwell sur des réseaux de billes et ressorts. Ces systèmes possèdent une symétrie souvent négligée: la symétrie chirale. J'exploite cette symétrie pour définir une nouvelle propriété de matériau, la polarisation chirale, codant à la fois la géométrie et la topologie du système. Cette polarisation distingue des phases topologiques distinctes et permet de sonder leur souplesse en localisant les modes d'énergie nulle. Nous confirmons ces résultats grâce à des mesures expérimentales de la polarisation chirale sur plusieurs métamatériaux mécaniques sans recourir à aucun modèle de basse énergie.

Dans la deuxième partie, j'analyse le rapport entre non-orientabilité et la rigidité des certains métamatériaux. J'établis un lien étroit entre non-orientabilité et frustration, et décris un cadre général permettant d'expliquer l'origine topologique de la rigidité des surfaces élastiques non-orientables et des métamatériaux frustrés. Leur point commun est la non-orientabilité des leurs fibrés de déformations. En utilisant des expériences et des simulations, nous confirmons l'existence de points et lignes rigides topologiquement protégés, et nous explorons leurs réponses non-commutatives, ouvrant la voie à la conception de métamatériaux mécaniques robustes et fonctionnels.